CHEMICAL REVIEWS

pubs.acs.org/CR Review

Noble-Metal Nanocrystals with Controlled Shapes for Catalytic and Electrocatalytic Applications

Yifeng Shi, Zhiheng Lyu, Ming Zhao, Ruhui Chen, Quynh N. Nguyen, and Younan Xia*

Cite This: https://dx.doi.org/10.1021/acs.chemrev.0c00454

Read Online

ACCESS | Metrics & More | Article Recommendations

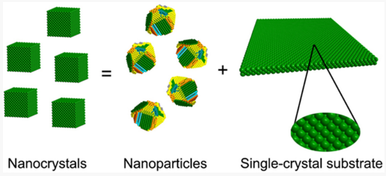

ABSTRACT: The successful synthesis of noble-metal nanocrystals with controlled shapes offers many opportunities to not only maneuver their physicochemical properties but also optimize their figures of merit in a wide variety of applications. In particular, heterogeneous catalysis and surface science have benefited enormously from the availability of this new class of nanomaterials as the atomic structure presented on the surface of a nanocrystal is ultimately determined by its geometric shape. The immediate advantages may include significant enhancement in catalytic activity and/or selectivity and substantial reduction in materials cost while providing a well-defined model system for mechanistic study. With a focus on the monometallic system, this review article provides a comprehensive account of recent progress in the development of noble-metal nanocrystals with controlled shapes, in addition to their remarkable performance in a large number of catalytic and electrocatalytic reactions. We hope that this review article offers the impetus and roadmap for the development of next-generation catalysts vital to a broad range of industrial applications.

CONTENTS

Special Issue: Advanced Materials and Methods for Catalysis and Electrocatalysis by Transition Metals

Received: May 13, 2020

Downloaded via GEORGIA INST OF TECHNOLOGY on July 24, 2020 at 19:01:14 (UTC).
See https://pubs.acs.org/sharingguidelines for options on how to legitimately share published articles.

ACS Publications © XXXX American Chemical Society

1. INTRODUCTION

Heterogeneous catalysis is of critical importance to the world's economy as it is involved in more than 90% of the chemical processes.[1] Among various catalytic materials, noble metals easily stand out because of their ability to donate and accept electrons for catalyzing both reduction and oxidation reactions, as well as the capability to adopt different oxidation states depending on the reaction environment. Heterogeneous catalysts based on noble metals are indispensable for the production of numerous industrial chemicals and pharmaceuticals.[2] Notable examples include those based on Cu for methanol synthesis;[3−5] those based on Ru for the reduction of nitrogen and thus ammonia synthesis;[6−8] those based on Pd for Suzuki coupling[9] and hydrogenation reactions;[10] those based on Ag for the epoxidation of ethylene;[11,12] and those based on Pt for hydrogenation and dehydrogenation reactions.[13,14] The catalysts also play an essential role in protecting our environment as exemplified by those based on Pd, Rh, and/or Pt in catalytic converters;[15] those based on Pt for the operation of fuel cells;[16] and those based on Cu for the electrochemical reduction of CO_2.[17]

Although some of the noble-metal catalysts have been used for hundreds of years, essentially all of them are still prepared using a precipitation or impregnation method that typically involves the deposition of a salt precursor on a catalyst support, followed by pyrolysis and then reduction at an elevated temperature and under a proper gaseous environment for the generation of noble-metal nanoparticles well dispersed across the surface of the support.[18] By optimizing experimental conditions, particles as small as a few nanometers, and even down to the single-atom level,[19] have been prepared on an industrial scale through the use of such a simple method. Figure 1, panels A and B, shows the typical transmission electron microscopy (TEM) images of a commercial Pt/C catalyst, in which Pt nanoparticles are deposited on a carbon support to serve as an electrocatalyst toward oxygen reduction, a cathodic half-reaction key to the operation of proton-exchange membrane fuel cells (PEMFCs).[20,21] Although such nanoparticles can be made with an extremely small size to give a remarkable specific surface area, they are suboptimal for practical applications. For one thing, their broad distributions in terms of both size and shape make them highly susceptible

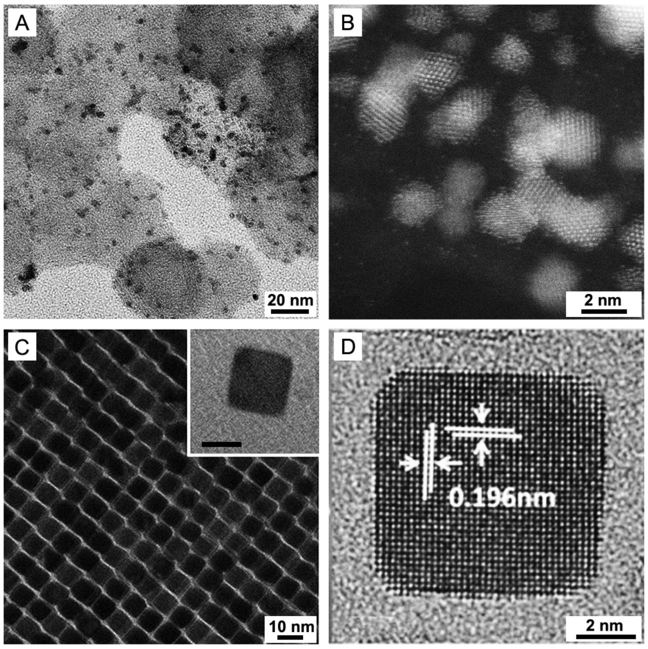

Figure 1. (A) TEM and (B) high-angle annular dark-field scanning transmission electron microscopy (HAADF-STEM) images of a commercial Pt/C catalyst (20 wt % Pt nanoparticles on Vulcan XC-72 carbon support; E-TEK), showing a broad size distribution along with poorly defined shapes and surface structures for the Pt nanoparticles. (C) TEM and (D) atomic-resolution TEM images of Pt cubic nanocrystals prepared using colloidal synthesis, demonstrating the marked uniformity in terms of size, shape, and surface structure. The inset in panel C shows an individual Pt cube (scale bar: 5 nm). (C) Reprinted with permission from ref 34. Copyright 2018 Elsevier. (D) Reprinted with permission from ref 35. Copyright 2013 American Chemical Society.

to Ostwald ripening,[22,23] a process that drives large particles to grow at the expense of small ones and eventually lead to a major loss in mass-specific activity.

The irregular, poorly defined shapes characteristic of the nanoparticles fabricated using the conventional protocol also make it difficult to develop new catalysts by leveraging the knowledge gained from fundamental studies in the framework of surface science. Using model catalysts built upon single-crystal substrates, both experimental and computational studies have clearly established that many catalytic reactions are highly sensitive to the exact arrangement of atoms on the surface. For example, it was reported that the formation of ammonia, from a stoichiometric mixture of N_2 and H_2, on Fe(111) surface occurred at a rate almost 20- and 420-fold faster than those on Fe(100) and Fe(110) surfaces, respectively.[24] For single-crystal Pt, it can selectively catalyze different types of reactions depending on the surface structure, with (100) and (210) being the most active toward reactions involving H_2 and CO, respectively.[25,26] When conducted in aqueous $HClO_4$, it was demonstrated that the area-specific activities of single-crystal Pt electrodes toward oxygen reduction decreased in the order of $(110) > (111) \gg (100)$.[27] Despite these and many other exciting developments, however, there exists a structure gap between the catalysts used in practice and the ideal systems identified through experimental and computational studies involving single-crystal substrates. To a large extent, this gap can be attributed to the conventional method used for catalyst preparation, which is only capable of generating metal nanoparticles with poorly defined shapes and thereby a mix of multiple types of facets on the surface.[18]

Recent demonstrations suggest that the aforementioned gap will vanish if we switch to noble-metal nanocrystals with controlled shapes.[28] When prepared through colloidal synthesis and with monodispersity in terms of both size and shape (Figure 1, panels C and D), the nanocrystals are able to bridge the gap by simultaneously providing the key features associated with the poorly defined nanoparticles found in industrial catalysts and the single-crystal substrates commonly used in surface science.[19,29] Specifically, the nanocrystals can be easily made as compact as the conventional catalytic nanoparticles to preserve the large specific surface area. More significantly, they can be synthesized with a controlled shape to present only one specific type of facet on the surface, for example, a cubic shape for the exposure of {100} facets that are equivalent to the (100) substrates employed in surface science. By simply replacing the conventional catalytic nanoparticles with uniform, shape-controlled nanocrystals, it is feasible to greatly enhance the performance of many catalytic systems in terms of activity, selectivity, and even stability. Most significantly, the results from fundamental studies in surface science can be directly transferred to applied catalysis. This concept, however, could not be explored until the early 2000s when it finally became feasible to produce noble-metal nanocrystals with well-defined and controllable shapes through colloidal syntheses.[30−33]

Now it is an exciting and rewarding time to rationally translate shape-controlled nanocrystals into catalysts with enhanced performance in a myriad of reactions by leveraging the results from mechanistic studies in surface science and the synthetic capability of materials chemistry. As a bridge between the conventional catalytic nanoparticles and single-crystal substrates, nanocrystals with controlled shapes have both high specific surface areas and well-defined surface structures. Their broad tunability in terms of elemental composition,[36−38] geometric shape,[39−42] and size[29,43] also greatly expands the diversity of catalytic materials. Many studies have demonstrated that controlling the shape of a monometallic nanocrystal and thus its surface structure and electronic properties is an effective strategy for optimizing the activity and/or selectivity of a heterogeneous catalyst.[29,44,45] The effect of size, which cannot be investigated at all using the single-crystal substrates, can also be readily scrutinized using nanocrystals.[29,43,46] In addition, the well-defined and, in many cases, a single type of surface structure on the shape-controlled nanocrystals has further enabled new characterization techniques for probing the surface properties and catalytic reactions.[47−49] In principle, nanocrystals with controlled shapes can serve as a new platform for investigating the mechanism of a catalytic reaction under the practical conditions. Eventually, such studies might be able to shed light on the rational development of the next-generation catalysts.

With a focus on the monometallic system, this article offers a comprehensive review on the development of noble-metal nanocrystals with controlled shapes for catalytic and electrocatalytic applications. We begin with a brief introduction to the correlation between the surface structure and geometric shape of a nanocrystal made of a face-centered cubic (fcc) metal. We then discuss the concepts and methodologies involved in the colloidal synthesis of noble-metal nanocrystals with diverse but well-controlled shapes, followed by an extensive presentation of examples pertaining to all the noble metals. Using the most relevant systems, we also highlight the major advantages and advancements brought into heterogeneous catalysis and electrocatalysis by these nanocrystals. At the end, we offer a brief summary, together with perspectives on the challenges, opportunities, and new directions for future development. It is hoped this article provides not only a comprehensive review of the current status of this exciting and rapidly evolving field but also the necessary knowledge, and more importantly, the inspiration for people to push this research one step closer to commercial success.

2. CORRELATION BETWEEN THE SURFACE STRUCTURE AND SHAPE OF NANOCRYSTALS

Noble-metal nanocrystals with controlled shapes play an important role in bridging the structure gap between the conventional catalytic nanoparticles and single-crystal substrates. In this section, we discuss how to engineer the surface structure of noble-metal nanocrystals by controlling their geometric shapes, including the types of facets expressed as side faces on the nanocrystals bearing different shapes, the easy creation of high-index facets on nanocrystals, and the inclusion of twin defects in nanocrystals for the generation of surface strains. We also discuss the impact of particle size on the inhomogeneity in surface structure for a nanocrystal, as well as the new characterization capabilities brought to heterogeneous catalysis and surface science by the metal nanocrystals with well-defined and controllable surface structures. At the end, we briefly discuss the stability and sintering issues of the shape-controlled nanocrystals as most of them are kinetic products and thus not favorable in terms of thermodynamics.

2.1. Surface Structure

It is well-established that the activity of a heterogeneous catalyst strongly depends on how its surface atoms interact with the intermediate(s) involved in the rate-determining step, as illustrated by the Sabatier principle (Figure 2A).[50] Based on this principle, the interaction corresponding to the most active catalyst should be at an optimal strength, neither too weak nor too strong. If the interaction is too weak, no reaction will be able to occur. On the other hand, the catalyst will be poisoned when the interaction is too strong as the intermediate(s) will fail to dissociate from the surface. When the reaction rate is plotted as a function of the reaction property such as the heat of adsorption of an intermediate involved in the rate-limiting step, a volcano shape will be obtained, with the apex corresponding to the most active catalyst.[51]

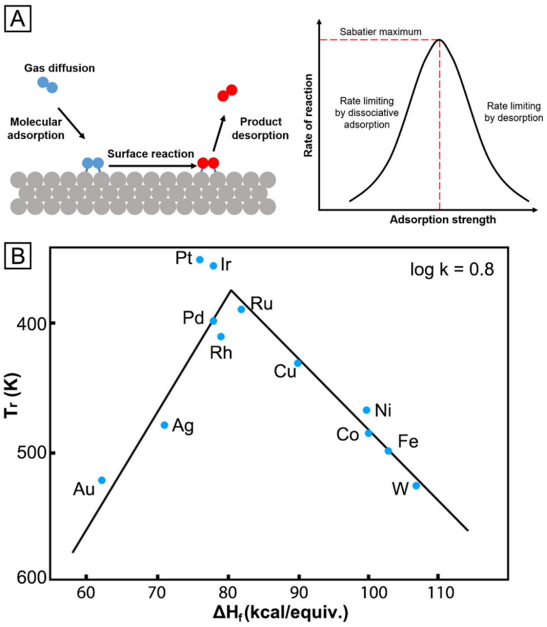

Figure 2. (A) Elementary steps involved in a typical heterogeneous catalytic reaction (left) and a volcano plot illustrating the Sabatier principle (right). (B) Volcano plot for the decomposition of formic acid on different transition metals. The reaction rate is expressed by T_r, at which the rate constant k reaches a fixed value (log k = 0.8). The adsorption strength is represented by the heat of formation of the metal formate (ΔH_f). (B) Modified with permission from ref 57. Copyright 1960 Walter de Gruyter.

One effective strategy for manipulating the interaction strength is to modulate the electronic structure of a catalyst's surface. According to the *d*-band center model, the binding energy of an adsorbate has a strong correlation with the location of the *d*-band center.[52−54] A higher *d*-band center (i.e., a smaller energy difference between *d*-band center and Fermi level) suggests a stronger binding for the adsorbate and vice versa. By engineering the attributes of metal nanocrystals, including the elemental composition, type of facet, twin structure, and particle size, the *d*-band center and thereby the catalytic activity of a catalyst can be effectively optimized.[55,56] When developing a catalyst, the elemental composition should be taken into consideration in the first place as it plays the most important role in determining the catalytic activity. Figure 2B shows a typical volcano plot for the decomposition of formic acid on different transition metals.[57] In this case, the horizontal axis is represented by the heat of formation (ΔH_f) of the corresponding metal formate salt because surface formate has been experimentally identified as an intermediate for this. The temperature at which the reaction reaches a specific rate is used for the vertical axis and it is plotted in reverse to display the conventional volcano shape. When the value of ΔH_f is low (i.e., the left half of the plot), the reaction is slow as it requires a high temperature to achieve the specified

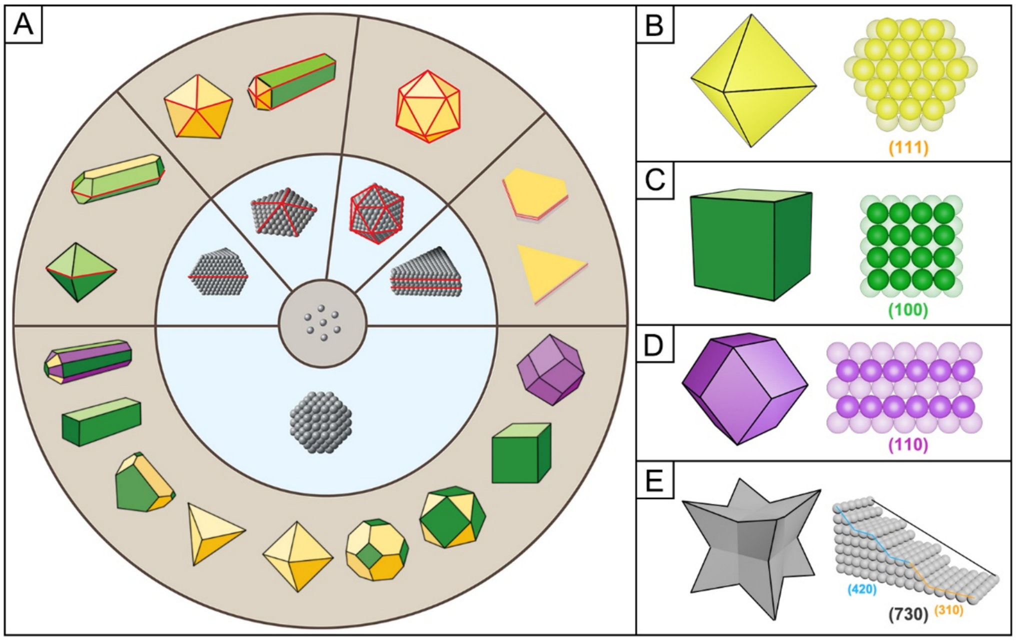

Figure 3. Correlation between the shape and type of facet for nanocrystals made of an fcc metal. (A) Examples of nanocrystals with different shapes (outer ring) and their corresponding seeds with five types of internal structures (middle ring) that are generated during the nucleation of metal atoms (center). (B−D) Models of octahedral, cubic, and rhombic dodecahedral nanocrystals and the corresponding atom arrangements on their side faces. (E) A concave cube terminated in high-index {730} facets. The atomic model indicates that the (730) surface contains a high density of steps. (A) Reprinted with permission from ref 45. Copyright 2016 Annual Reviews.

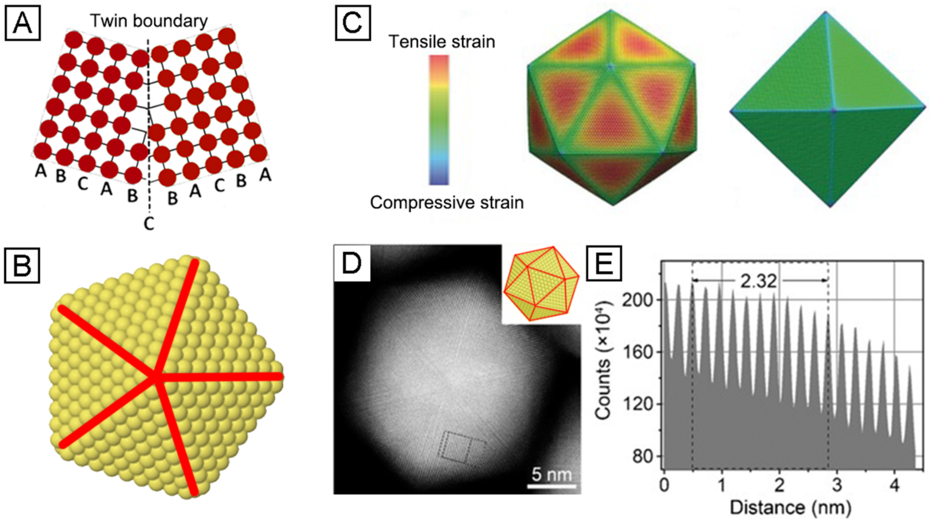

Figure 4. Twin defect and surface strain. (A) Schematic illustration of the disrupted arrangement of atoms in a twin boundary. (B) The penta-twinned structure taken by a decahedral nanocrystal. The red lines are indicative of the twin boundaries. (C) Calculated surface strain fields for Pd icosahedral and octahedral nanocrystals, respectively. Different colors indicate various degrees of strain labeled in the color map. (D) HAADF-STEM image of a Pd icosahedron and (E) intensity profiles recorded from the area marked in the rectangular box in panel D. The inset in panel D shows the corresponding atomic model of an icosahedron. (A) Modified with permission from ref 68. Copyright 2019 Multidisciplinary Digital Publishing Institute. (B) Modified with permission from ref 76. Copyright 2019 IOP Publishing. (C−E) Modified with permission from ref 74. Copyright 2017 Wiley-VCH.

reaction rate. In this case, the adsorption is slow and rate-determining. As the value of ΔH_f is increased to the right half of the plot, desorption becomes the rate-limiting step. Taken together, it is not difficult to understand why the prime catalysts for formic acid decomposition are all based on the platinum group metals (PGMs). Because of their intermediate values of ΔH_f, the net reaction rate is determined by an optimal combination of the rate of adsorption and the rate of desorption.

Once the elemental composition is fixed, one can still tune the interaction between a catalyst and the intermediate(s) by altering its surface structure, that is, the spatial arrangement or packing of atoms situated on the surface. The surface structure can be quantitatively described using the coordination number (CN), which refers to the number of bonds that the atom of interest forms with adjacent atoms, or simply put, the number of its nearest neighbors. The CN can directly affect the performance, including both activity and selectivity, of a heterogeneous catalyst by changing the adsorption and dissociation energies of reactant molecules on a metal surface.[58] For a perfect crystal, CN is mainly determined by the lattice structure and the type of facet, with the latter having a strong correlation with the shape taken by a nanocrystal. As a result, one can engineer the shape of noble-metal nanocrystals for the development of advanced catalysts by leveraging the facet dependence of both catalytic activity and selectivity.

2.2. Facet and Shape

Thanks to the efforts from many research groups, colloidal synthesis has been successfully applied to produce noble-metal nanocrystals bearing a wide variety of shapes (Figure 3A).[28,40−42,45,59−61] Naturally, the distinct shapes lead to the expression of different types of facets as the side faces on the nanocrystals. Figure 3B−D, shows schematic illustrations of octahedral, cubic, and rhombic dodecahedral nanocrystals made of an fcc metal, with their side faces enclosed by a single type of facet, that is, {111}, {100}, and {110}, respectively. Note that the atoms located at these side faces have CNs of 9, 8, and 7, respectively, identical to those of (111), (100), and (110) surfaces for single-crystal substrates. Of course, the same type of facet can be found in nanocrystals with a number of different shapes. For example, in addition to cubes, the side faces of rectangular bars and right bipyramids (RBPs) are also terminated in {100} facets. Even for penta-twinned rods and wires, their side surface is also enclosed by {100} facets. Such a one-to-multiple correlation is advantageous as it allows one to access a specific type of facet through the use of nanocrystals with different shapes depending on the availability of synthetic protocols. For nanocrystals that share the same type of facet but differ in geometric shape, they may show different catalytic performance because of the variation in surface-to-volume ratio and/or the presence of additional features such as twin boundaries (see section 2.3).

As a major difference from a bulk crystal, it is easier to generate high-index facets on the surface of a nanoscale crystal, leading to the production of low-coordination atoms at a high density on the surface. Such atoms with low CNs can be highly active in catalyzing chemical reactions. High-index facets, denoted by a set of Miller indices {*hkl*} with at least one of the indices being greater than unity, are well-known for the presence of surface steps, kinks, and edges in high densities.[39] They can be easily found on nanocrystals with a concave or convex surface. Figure 3E shows the schematic illustration of a typical example: a concave cube enclosed by {730} high-index facets. Such nanocrystals are usually obtained under kinetically controlled growth and they are intrinsically higher in total surface free energy relative to their platonic counterparts (see section 4.3). Although metal nanocrystals encased by high-index facets are promising candidates for a variety of catalytic applications,[62,63] their synthesis and utilization are still limited at the current stage of development, primarily due to their intrinsic instability and the lack of effective capping agents for high-index facets.[64,65]

The shape of a nanocrystal can also affect the coordination environment of a surface atom from other aspects, including its second-nearest neighbors and surface curvature. According to a computational study, the arrangement of the second-nearest neighbors surrounding a surface Pt atom also played an important role in determining its activity toward oxygen reduction.[66] The authors proposed the use of "weighted average CN" as a function of both the first- and the second-nearest neighbors. Their simulation result indicated that the optimal Pt catalyst should have a "weighted average CN" of 8.3. For Pt(111) surface, the "weighted average CN" is only 7.5, and this number can be increased by modifying the second-nearest neighbors. The same group also demonstrated that despite being identical in terms of CN, the surface curvature of a Pt nanocrystal could make additional contribution to the enhancement in activity toward oxygen reduction.[67] According to their model, the surface with a concave structure could surpass the activity of the Pt(111) surface, while a convex surface would become rather inactive toward this reaction.

2.3. Twin Defect and Surface Strain

As noted above, noble-metal nanocrystals enclosed by the same type of facet can still exhibit different catalytic activities due to the involvement of twin defect and surface strain. In the case of monometallic system, twin defect and surface strain are often correlated with each other. However, their explicit impacts on the catalytic performance are based on different mechanisms and deserve to be discussed separately.

A twin defect emerges when the crystal lattices on either side of a plane are mirror images of each other (Figure 4A). The atomic plane, known as the twin plane, will disrupt the ideal stacking sequence of the crystal lattice.[45,68] Noble metals are well-known for their easiness in producing twin defects during crystallization because of the relative small penalty in energy when such a planar defect is introduced into the otherwise single-crystal fcc lattice. Based on the number of twin defects contained in the nanocrystals, they can be divided into singly twinned or multiply twinned structures.[69,70] For the multiply twinned structures, the defects can be arranged as twin planes parallel to each other, but it is more often to observe them arranged in a radial fashion, as shown by the penta-twinned structure found in a decahedral or icosahedral nanocrystal (Figure 4B).[60,61] The penta-twinned structure in a decahedral nanocrystal can be considered as an assembly of five single-crystal, tetrahedral subunits by sharing one common edge. In these cases, each twin defect involves more than one atomic plane and evolves into a "twin boundary", in which the atoms are arranged in a more or less disordered form.

The contributions from twin defects to the activity of nanocrystals toward a catalytic reaction can come from two different sources: (i) the surface atoms situated at the twin plane or boundary, which often have a coordination environment different from those associated with the atoms on faces and thereby show different capabilities in activating reactant molecules and (ii) the surface strain exerting on the face atoms as induced by the twin defects. A good example for the first contribution can be found in the use of Pd RBPs as a catalyst toward formic acid oxidation (FAO).[71] As described in a report, the six isosceles right triangles on the surface of a Pd RBP could be indexed as {100} facets, while the single twin boundary could be assigned to the high-index {211} facet. The atoms in the twin boundary or on the high-index facets were believed to be responsible for the enhanced area-specific catalytic activity toward FAO when compared with that of Pd cubic nanocrystals whose surface was also enclosed by {100} facets but free of the twin boundary.

In the context of nanocrystals, surface strain is related to the slight displacement of an atom from its original position in a crystal lattice. It is a direct measure of the lattice distortion arising from the imperfection of a crystal. The atoms under strain can be either compressed or expanded, and the corresponding strains are termed compressive and tensile, respectively.[55] Strain represents another important surface attribute that plays an important role in determining the area-specific activity of a catalyst. Both experimental and computational studies have demonstrated that it can change the electronic structure and thus activity of a metal surface.[55,56,72] One popular explanation lies in that the change in atomic separation will affect the position of the *d*-band center of a surface, and therefore, alters its interaction with the adsorbates.[52,56] Specifically, when the atoms are under tensile strain, the overlap of the *d*-band states between neighboring atoms decreases. As a result, the *d*-bandwidth decreases correspondingly, and the *d*-band center has to shift upward relative to the Fermi level to maintain the degree of *d*-occupancy. Similarly, when the separation between atoms is narrowed, the *d*-bandwidth increases, and *d*-band center will be shifted downward. The upshift in *d*-band center will strengthen the adsorption of the reaction intermediate and vice versa. This argument is the primary principle behind the strain-dependent catalytic properties.[73]

For studies involving single-crystal substrates, the strain of a metal surface is often tuned by depositing a monolayer of the metal atoms on a substrate with a different lattice constant.[55] When switched to monometallic nanocrystals, strain could also be generated by simply controlling their shapes. Typical examples of nanocrystals featuring tensile strains include those with a decahedral or icosahedral shape and thus a penta-twinned structure. In these cases, there is an intrinsic strain on the side face of each tetrahedral subunit as a result of the twin boundaries.[60,61] Figure 4C shows a comparison of the surface strain fields calculated for Pd icosahedral and octahedral nanocrystals. While both nanocrystals are enclosed by {111} facets, tensile strain was only observed on the side faces of the icosahedral nanocrystal.[74] This result was verified by a higher interlayer spacing recorded from the intensity profile of the atomic-resolution scanning transmission electron microscopy (STEM) image (Figure 4D,E). The normal interlayer spacing of Pd(111) planes is 2.24 Å, but the spacing increased to 2.32 Å for Pd icosahedral nanocrystals. When these nanocrystals were tested as catalysts for the electrochemical reduction of CO_2, the tensile strain in icosahedral nanocrystals led to 1.7-fold enhancement in the maximum faradaic efficiency (FE) for CO relative to that of octahedral nanocrystals. According to density functional theory (DFT) and molecular dynamics (MD) calculations, the tensile strain on the surface of a Pd icosahedral nanocrystal induced an upshift for the *d*-band center, increasing the adsorption strength of the key intermediate COOH* for the easier reduction of CO_2 to CO.[74] It should be pointed out that nanocrystals characterized by the penta-twinned structure are only thermodynamically favorable when their sizes are relatively small.[75] As the size is increased, their stability will decrease because of the increase in surface strain. On the other hand, when the size is reduced, the number of atoms situated on the side faces and thus exposed to the tensile strain will decrease. Taken together, when developing effective catalysts based on penta-twinned nanocrystals, the size should be optimized.

Unlike the tensile strain generated in a penta-twinned structure, compressive strain is observed in plates or sheets lined with planar defects. A recent study suggested that Pd sheets with a thickness of 1−12 monolayers exhibited tunable compressive strains up to 10%.[77] Their results also indicated that a thinner sheet was correlated with a greater compressive strain. When applied as catalysts toward oxygen reduction and hydrogen evolution, the area-specific activity of Pd sheets was more than 10 times greater than that of the conventional Pd nanoparticles.

2.4. Particle Size

In addition to geometric shape, we also need to pay close attention to the size of nanocrystals when developing them into effective catalysts.[29,43,46] For one thing, the mass-specific activity of a catalyst is directly controlled by particle size because of its impact on the specific surface area, which refers to the total surface area per unit mass of a catalytic material, with a unit of m^2 g^{-1}. As shown in Figure 5A, the specific surface area of a Pt spherical particle is inversely proportional to its size, with the impact becoming most significant as the size drops below about 5 nm. This explains why the industrial catalysts are usually based on particles with sizes in the range of 1−10 nm for the achievement of the most effective catalyst in terms of mass-specific activity.[19] In some cases, the dependence of catalytic activity on particle size cannot be simply explained through its impact on the specific surface area. For example, it is well documented that Au nanocrystals are only able to catalyze CO oxidation at room temperature with their sizes dropping below 6 nm.[78] Other experiments also demonstrated that the variation in particle size could cause changes to the area-specific activity and selectivity of a catalyst although both of them are supposed to be independent of the specific surface area.[79−82] These reports indicate that the variation in particle size can alter the surface structure of a noble-metal catalyst from an electronic perspective rather than the specific surface area. Now it is generally accepted that the variation in particle size can affect the catalytic performance of metal nanocrystals through two other mechanisms: (i) modification to the electronic structure of the surface atoms and (ii) alteration to the inhomogeneity of a surface by affecting the fractions of atoms situated at vertices and edges. For these reasons, variation in particle size may cause changes to both catalytic activity and selectivity when a structure-sensitive reaction is involved.

The size-dependent catalytic activity of Au nanocrystals toward CO oxidation can be ascribed to the weakened strength of the metallic bond as the size is reduced. The weaker interaction among the Au atoms allows them to interact with oxygen more strongly, helping activate the double bonds in O_2.[83] However, if the size of the catalytic particles is further reduced down to a threshold value of 1−2 nm to reach the cluster regime, the band structure will change significantly and the particle will start to exhibit nonmetallic properties. Specifically, it was shown that the separation between electronic bands will become appreciable when a Au nanoparticle is downsized to 1 nm (or about 40 atoms).[84] In general, the bands observed in large nanoparticles will become discrete levels in small nanoparticles, and the particles eventually will exhibit molecule-like properties when their size is reduced down to the cluster level.[2]

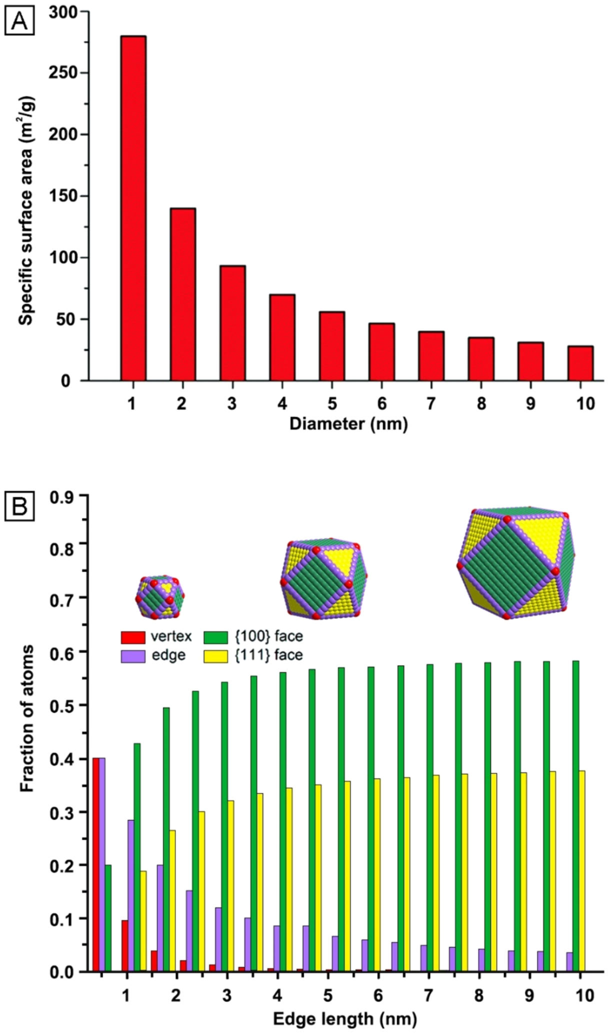

Figure 5. Effects of particle size on the surface properties of nanocrystals. (A) The specific surface area of a Pt spherical particle as a function of its diameter. (B) The fractions of surface atoms situated at vertices, edges, {100} facets, and {111} facets of a Au cuboctahedron as a function of edge length. (A) Reprinted with permission from ref 23. Copyright 2018 Royal Society of Chemistry. (B) Modified with permission from ref 43. Copyright 2013 Elsevier.

As a major difference from that of a bulk crystal, the surface of a nanocrystal is inherently heterogeneous as it contains atoms situated at vertices and edges, in addition to those on the faces. The fractions of these different types of atoms on a surface are dependent on the particle size. Such dependence can be easily quantified for metal nanocrystals with a known crystal structure and in a well-defined shape. Figure 5B shows the fractions of surface atoms situated at vertices, edges, {111} facets, and {100} facets for a Au cuboctahedral nanocrystal made of an fcc metal when its edge length is increased from 0.5 to 10 nm. For atoms situated at vertices and edges, they tend to have low CNs relative to those on the facets. Their presence on the surface at large proportions can potentially affect the catalytic performance of metal nanocrystals. This phenomenon was observed when investigating the catalytic activity of Au cuboctahedra toward CO oxidation.[85] When the size of the catalytic particle was reduced from 6 to 3 nm, the conversion of CO to CO_2 was increased from 1% to 99% at 50 °C. The improvement in catalytic activity was attributed to the increase in proportion of low-coordination Au atoms situated at vertices and edges. For nanocrystals with twin boundaries, the surface strain will decrease correspondingly as the particle size is reduced.[75,86]

The plot in Figure 5B clearly indicates that the fractions of atoms situated at vertices and edges can no longer be neglected when the particle size drops below 5 nm. In other words, we have to focus on nanocrystals with sizes greater than 5 nm in order to maximize the fractions of atoms situated on side faces for the achievement of a precise control over the surface structure. When combined with the requirement from specific surface area and mass-specific activity, the shape-controlled nanocrystals for most catalytic applications should take an optimal size around 5 nm to balance the mass-specific activity and expression of surface structure. At the current stage of development, it is still a grand challenge to obtain noble-metal nanocrystals with nonspherical shapes through colloidal synthesis when their sizes are below 10 nm. Most of the protocols reported in literature are only able to provide shape-controlled nanocrystals with dimensions much greater than 10 nm.

2.5. New Characterization Capabilities

The availability of uniform nanocrystals with well-defined and controllable surface structures has also enabled new capabilities for investigating surface science and catalysis. For the conventional nanoparticles with poorly defined shapes and a broad size distribution, it is very difficult or almost impossible to precisely describe their surface structures. Although some information can be obtained through the use of advanced techniques such as atomic-resolution electron microscopy, one can only capture the images from a limited number of particles and the data cannot really be considered to be representative.[87] Alternatively, the availability of nanocrystals with a single type of surface structure allows one to use simple characterization techniques to analyze the structure−property relationships. For example, infrared (IR) spectroscopy is a nondestructive technique that can be applied to quantitatively analyze the types of facets on metal nanocrystals through the use of probe molecules such as CO, NO, C_2H_2, and CO_2. Studies involving single-crystal substrates have established that the vibrational frequency of CO is sensitive to the surface structure, strain, and elemental composition when it binds to the metal surface.[88−90] Taking Pd single-crystal substrate as an example, the vibrational frequency of the CO adsorbed on (100) and (111) surfaces are quite different from each other (Figure 6A). However, it is not easy to acquire enough signals due to the relatively low specific surface area intrinsically associated with a single-crystal substrate. This technical issue will disappear when switching to metal nanocrystals because of the significant increase in specific surface area. In recent years, IR has been increasingly utilized to characterize the elemental composition and even surface structure of metal nanoparticles.[48] When applied to monometallic nanocrystals with controlled shapes, it is also possible to analyze catalytic reactions in situ and under operando conditions for achieving an unprecedented understanding of the effects from the type of facet, twin boundary, and/or surface strain.

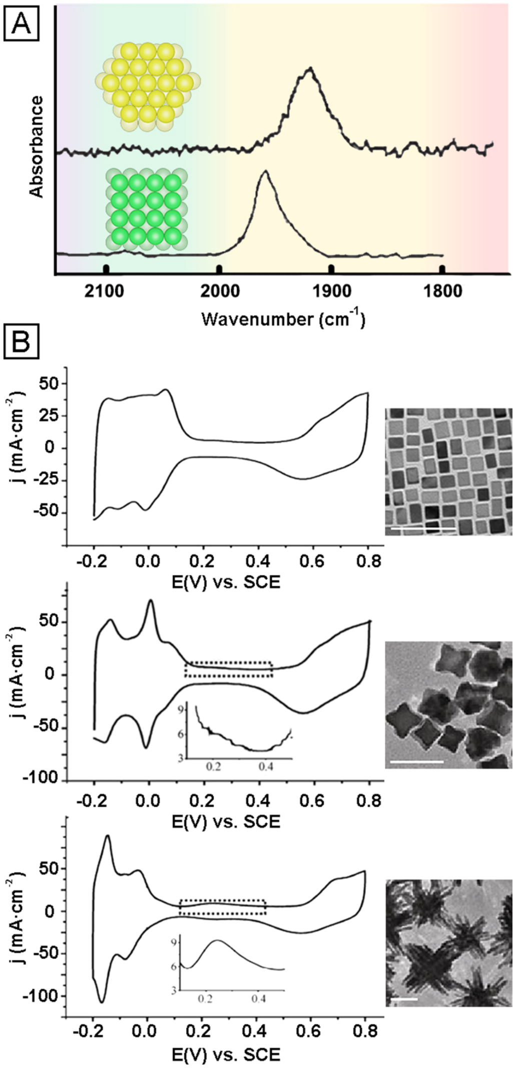

Figure 6. New characterization techniques enabled by nanocrystals with well-defined surface structures. (A) IR spectra of CO on Pd(111) and Pd(100) single-crystal substrates at 400 °C under a CO pressure of 10^{-6} Torr. (B) CV curves of Pt cubes, concave cubes, and multipods obtained in 0.5 M H_2SO_4 at a scan rate of 50 mV s^{-1}. Insets in the CV curves show the maginified plots marked in dashed boxes. A typical TEM image of each nanocrystal is shown to the right of the CV curve (scale bars: 50 nm). (A) Modified with permission from ref 89. Copyright 1993 AIP Publishing. (B) Modified with permission from ref 47. Copyright 2012 Springer Nature.

Electrochemical measurements offer another facile and sensitive characterization technique for elucidating the surface properties of nanomaterials. When applied to metal nanocrystals with a single type of facet, it will be much easier to analyze the data for the establishment of structure−property relationship. To this end, the cyclic voltammetry (CV) has been utilized to characterize the initial surface properties of nanocrystals, including the type of facet and oxidation state. In one study, it was reported that the shapes of the hydrogen adsorption/desorption region in CV curves could be used to reveal the surface structures of Pt nanocrystals (Figure 6B).[47] When conducted in aqueous H_2SO_4, the CV curve of Pt cubes exhibited three peaks at −0.14, 0, and +0.08 V (vs saturated calomel electrode, SCE). The peaks at 0 and 0.08 V were indicative of the short- and long-range-ordered {100} facets, respectively. For Pt concave cubes, the peak at 0 V became much stronger, suggesting that the surface of the concave cubes contained more short-range-ordered {100} facets. At the same time, the intensity of the peak at 0.08 V decreased as a small shoulder peak, suggesting that the long-range-ordered

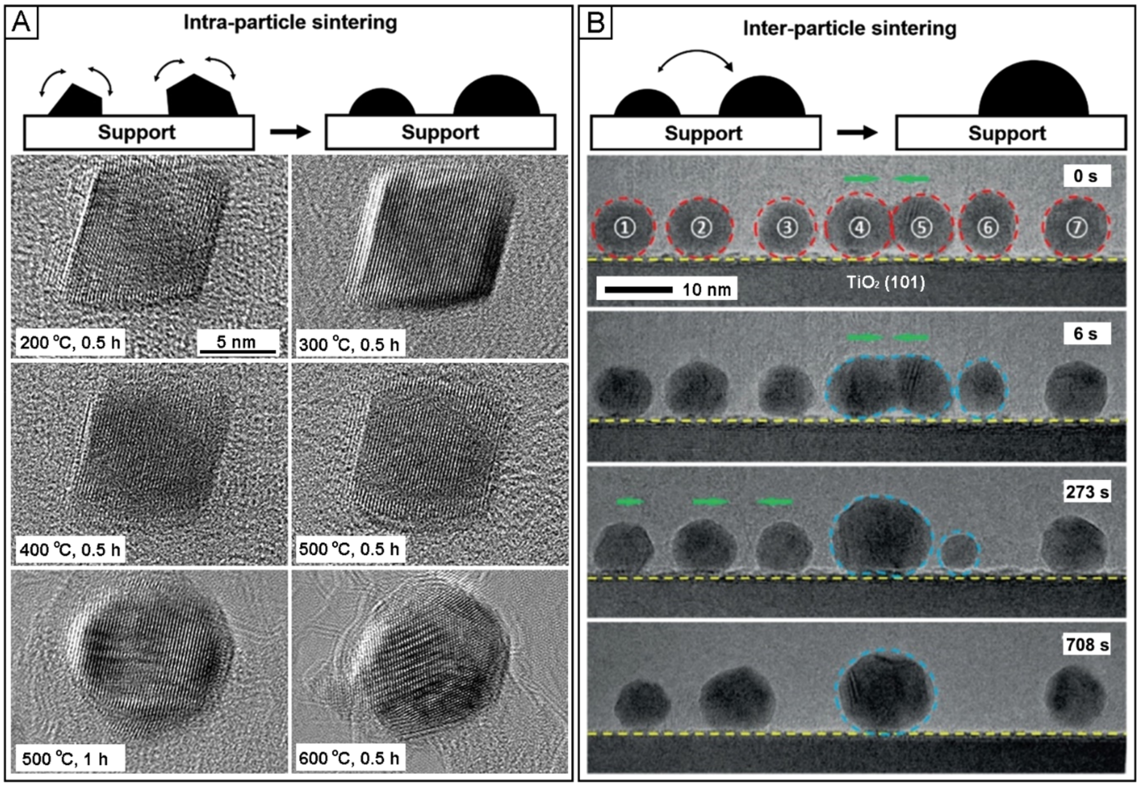

Figure 7. Schematics and in situ TEM images illustrating two types of catalyst sintering: (A) intraparticle and (B) interparticle sintering, respectively. The high-resolution TEM images in panel A were recorded from the same Ru octahedron heated at various temperatures for a certain period of time. The TEM images in panel B show the interparticle sintering behavior of Au spheres on $TiO_2(101)$ substrate when aged at 500 °C at a pressure of 5×10^{-2} Pa for oxygen. The red and blue dashed circles in panel B outline the Au spheres at the initial and sintering stages, respectively. Green arrows stand for the moving direction of the particles. The schematics in panels A and B were reprinted with permission from ref 23. Copyright 2018 Royal Society of Chemistry. The TEM images in panel A were reprinted with permission from ref 95. Copyright 2019 American Chemical Society. The TEM images in panel B were reprinted with permission from ref 96. Copyright 2018 Wiley-VCH.

{100} facets were no longer in dominance on the concave cubes. In comparison, the CV curves of Pt multipods showed two peaks at 0 and 2.4 V, corresponding to the short-range-ordered {100} facets and {111} surface domains, respectively. Such a structure−property correlation could only be achieved when the shape and size of the nanocrystals are highly uniform. For Pt nanoparticles with irregular shapes and poorly defined surface structures, the hydrogen adsorption/desorption region became less informative due to the absence of well-defined peaks.

In addition to IR and electrochemical characterizations, other techniques, such as surface-enhanced Raman scattering (SERS),[49] nuclear magnetic resonance (NMR),[91] and calorimetry,[92] have also been integrated with uniform metal nanocrystals bearing controlled shapes to investigate fundamental problems in both surface science and heterogeneous catalysis. Compared with the traditional tools commonly used for such studies, these characterization techniques are cheaper and more accessible to most research groups. They are also well-suited for providing high-quality and more representative data.

2.6. Catalytic Stability and Sintering

Similar to the conventional catalytic system, the activity and selectivity of a catalyst built upon shape-controlled nanocrystals tend to decay in the course of operation as a result of physical (i.e., sintering) or chemical (i.e., poisoning) changes. Here we only focus on the physical deactivation as chemical deactivation is highly dependent on the nature of the reaction rather than the intrinsic parameters of the nanocrystals. Sintering can be broadly defined as the loss of metal surface area during the use of a heterogeneous catalyst. For industrial processes involving high temperatures, such as steam reforming, automotive exhaust treatment, and catalytic combustion, sintering is always a major concern or challenge for the long-term use of heterogeneous catalysts without compromising their performance.

The general driving force for sintering is to reduce the total surface free energy, which can be achieved through two different pathways: intraparticle and interparticle sintering.[23] Intraparticle sintering refers to the migration of surface atoms on an individual particle for the reconstruction of surface structure, including the types of various facets and their area proportions. This is a spontaneous process driven and governed by thermodynamics as nanocrystals with a non-spherical shape are supposed to reach the equilibrium shape determined by the Wulff construction.[93,94] As a result, shape-controlled nanocrystals are intrinsically susceptible to intraparticle sintering and the shape transformation process will be greatly accelerated when the sample is subjected to a thermal stress (Figure 7A). If the catalytic activity and selectivity are dependent on the surface structure such as the type of facet, the transformation of shape or reconstruction of surface will lead to degradation in the performance of a catalyst.

Interparticle sintering refers to the growth of nanocrystals through particle coalescence and/or Ostwald ripening (Figure 7B).[97] Particle coalescence will likely occur when two particles are close to each other, in which one particle will migrate along the support to fuse with another particle. In Ostwald ripening, individual atoms or small clusters leave the surface of a smaller particle and migrate along the support or through the medium and are redeposited onto the surface of a larger particle. Because the strength of metal–metal bond in smaller particles is weaker than that in larger ones, small particles tend to dissolve and disappear, while energetically favorable large particles will keep growing. Ostwald ripening can even occur when the particles are well separated from each other on the support. These two mechanisms are usually coupled together, and sometimes it is hard to discriminate one from the other. Nevertheless, both of them will lead to an increase in particle size and thus a loss in specific surface area. For the catalysts prepared using the conventional methods, it is hard to control the size and shape uniformity of the resultant nanoparticles. On the other hand, for the nanocrystals prepared using colloidal synthesis, it has become a routine practice to obtain samples with high uniformity in terms of both size and shape. The well-defined facets on the nanocrystals should also help strengthen their interactions with the support, making it harder for the particles to migrate and coalesce. Taken together, it is anticipated that shape-controlled nanocrystals are more resistant against interparticle sintering because of their higher uniformity than the conventional nanoparticles. In this case, intraparticle sintering would be the major cause of the observed degradation in catalytic performance.

3. SHAPE-CONTROLLED SYNTHESIS OF NANOCRYSTALS

It takes several steps to convert a salt precursor into noble-metal nanocrystals with a specific shape, and each step plays a vital role in controlling the shape evolution process. In the simplest picture, a colloidal synthesis begins with the production of atoms from a salt precursor, followed by their aggregation or assembly into clusters known as nuclei. At this point, the nucleus probably does not have a fixed structure yet since the thermal energy involved in a typical synthesis can easily cause its structure to fluctuate among different configurations.[98,99] As the number of atoms is further increased, the structural fluctuation ceases and the nuclei evolve into seeds with diverse but fixed internal structures, including those characterized by single-crystal, singly twinned, multiply twinned, and stacking-fault-lined structures (see the examples shown in the middle ring of Figure 3A). Afterward, the seeds grow in size while evolving into nanocrystals with different shapes through atomic addition and/or oriented attachment.[100] In this section, we start with a brief introduction to two methods for the generation of atoms, followed by a discussion on their nucleation and growth into nanocrystals, with a focus on how to maneuver the shape under various thermodynamic and kinetic controls. Since most of the syntheses are conducted under ambient conditions, we also discuss the important role(s) of oxidative etching in affecting the distributions of seeds featuring different types of internal structures. We further highlight the use of seed-mediated synthesis for achieving an ultimate control over both the shape and size of noble-metal nanocrystals. At the end, we specifically talk about surface capping agents due to their essential roles in controlling the shape evolution of nanocrystals during the growth process.

3.1. From Precursor to Atom

The metal atoms that serve as the building blocks of nanocrystals are typically generated through the reduction and/or decomposition of a salt precursor.[28] Most of the protocols reported in the literature rely on chemical reduction, in which a salt precursor in a high oxidation state is reduced by reacting with a reductant to generate metal atoms. Many types of reductants have been successfully applied to the colloidal synthesis of noble-metal nanocrystals, and some of them only generate gases such as N_2 and H_2 as the products, helping prevent the surface of the obtained nanocrystals from contamination by unsolicited chemical species.[101] Alternatively, the atoms can be generated through the decomposition of a metal complex without involving a reductant. The decomposition process typically requires the assistance of heating and/or ultrasonication.[102] In some cases, both reduction and decomposition can be involved. A notable example can be found in the synthesis of Au nanocrystals through the thermal decomposition of a Au(I) halide, during which AuCl or AuBr was dissolved in chloroform in the presence of a stabilizer such as alkylamine, whose amine group can also act as a reductant.[103] As an advantage, the decomposition route offers a simple and effective route to the incorporation of different elements into bi- and even multimetallic nanocrystals with a tight control over the composition. In comparison, it is more challenging to accomplish such a control for the reduction route because of the difficulty in matching the reduction rates of different precursors.[42]

Regardless of reduction or decomposition, it is the initial reaction rate that plays the most important role in determining the internal structures of the seeds in the nucleation step.[69] As a major drawback of the decomposition route, it is difficult to precisely control the reaction kinetics as the rate of decomposition has an exponential dependence on the reaction temperature. In comparison, it is easier to control the kinetics of a reduction reaction as the rate of reduction (at least, the initial rate) is linearly proportional to the concentrations of the precursor and reductant. Immediately after the nucleation step, however, the reduction may proceed through an autocatalytic pathway on the surface of the seeds (see section 3.3), causing dramatic acceleration to the reduction kinetics. In general, the success of a synthesis critically depends on our ability to control the reduction kinetics, and the common practice includes the use of a proper combination of precursor and reductant,[104] as well as their molar concentrations. The temperature can also be leveraged to control the reduction rate, but it should be kept in mind that the relationship is exponential rather than linear.[105] In many cases, it is necessary to introduce a proper capping agent for the production of nanocrystals with a specific shape.[106,107]

3.2. Homogeneous Nucleation

Homogeneous nucleation refers to the aggregation or assembly of metal atoms into small clusters commonly known as nuclei. It is the very first step of any synthesis of nanocrystals that does not involve the introduction of preformed seeds. The general framework of homogeneous nucleation can be described using the LaMer model, which was formulated in the 1950s to account for the synthesis of sulfur colloids with a uniform distribution in size.[108] This model can also be extended to account for the synthesis of noble-metal nanocrystals (Figure 8). As soon as the salt precursor is reduced or decomposed, the

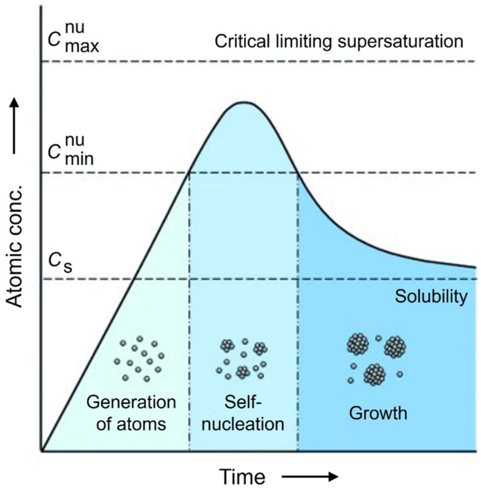

Figure 8. Plot of the concentration of atoms as a function of reaction time illustrating the major steps involved in a synthesis, including the generation of atoms, homogeneous nucleation, and growth. Reprinted with permission from ref 108. Copyright 1950 American Chemical Society.

concentration of metal atoms in the reaction solution is expected to increase as a function of time. Once the concentration of metal atoms exceeds the minimum value for nucleation (C^{nu}_{min}), nuclei will be formed spontaneously through aggregation or assembly of the atoms. Rapid consumption of the atoms in the solution will cause their concentration to decrease quickly. When the concentration drops below the minimum level for nucleation, homogeneous nucleation will cease. However, with a continuous supply of new metal atoms from the precursor, homogeneous nucleation can occur again if their concentration surpasses the minimum level. Such recurrence can repeat multiple times until most of the precursor in the solution has been depleted. In general, it is necessary to ensure that there is only one nucleation event per synthesis. Otherwise, the products will have a broad distribution in size as the seeds from different nucleation cycles will experience different durations of growth. In practice, the requirement for one nucleation event can be met by regulating the reaction kinetics of the synthesis through the choice of a right reductant or introduction of the precursor dropwise rather than in one shot.

Despite the lack of a quantitative analysis and many oversimplified assumptions, the LaMer model has been very successful in providing a qualitative understanding of the colloidal synthesis of metal nanocrystals. At least, it offers an insightful instruction about how to obtain nanocrystals with a uniform distribution in size. With the advancement in instrumentation and computational method, this simple model has been challenged in recent years due to the large discrepancy between the expected and actual observations. To this end, nonclassical mechanisms involving two or even multiple steps were proposed for nucleation, in which a dense, metastable liquid[109] or amorphous structure[110] is formed as the intermediate. Instead of the aggregation of metal atoms, it was also proposed that nucleation could be achieved by forming clusters from the partially reduced precursor. In one report, continuous flow was combined with in situ X-ray absorption fine structure (XAFS) spectroscopy to investigate the nucleation step involved in the synthesis of Au nanocrystals.[111] It was demonstrated that in the early stage of nucleation, partial reduction of $AuCl_4^-$ occurred, and Au−Au bonds were formed to generate $Cl_3Au\text{-}AuCl_3^-$ dimers and then larger clusters in the general format of Au_nCl_{n+x} under the mild reduction condition. So far, there are only a limited number of reports on the exploration of nonclassical nucleation involved in the colloidal synthesis of nanocrystals.

While it remains a grand challenge to uncover the atomistic detail involved in the very early stage of a synthesis, several methods have been developed for manipulating the fractions of seeds with different types of internal structures. The first method is computational modeling built upon the perspective of thermodynamics.[75] Figure 9A shows the phase diagram of Au seeds computed as functions of particle size and temperature, indicating that multiply twinned and single-crystal seeds are formed at relatively small and large sizes, respectively. Alternatively, it was established that the initial reduction rate of the precursor could serve as a quantitative knob for experimentally controlling the internal structure of the seeds.[69] Specifically, the initial reduction rates responsible for the generation of seeds with different internal structures increased in the order of stacking-fault-lined, multiply twinned, singly twinned, and single-crystal. Figure 9B shows the percentages of Pd seeds with different internal structures as a function of the initial rate for the reduction of $PdCl_4^{2-}$ by a polyol. Of particular interest is the existence of well-separated windows of initial reduction rates, which correlate well with the formation of seeds with different internal structures. In practice, the initial reduction rate can be experimentally controlled by adjusting the temperature, as well as both the type and concentration of precursor and reductant involved in a synthesis.[69,104,112,113]

In addition to these thermodynamic and kinetic controls, oxidative etching can be used to selectively remove multiply twinned seeds for the generation of single-crystal and/or singly twinned seeds.[114,115] As a process intrinsic to all metals, the etching typically involves a redox reaction between the highly energetic twin defects and an etchant consisting of an oxidant (e.g., the O_2 from air) and a ligand for the metal ions, including the halide from the salt precursor. One can even differentiate the seeds containing different numbers of twin defects by tuning the strength of the etchant through the use of different ligands at various concentrations.[71,116] During the polyol synthesis of Ag nanocrystals, for example, one can replace Cl^- with Br^- to only remove the multiply twinned seeds, leaving behind the singly twinned seeds for their further growth into RBPs.[116] For most noble metals, now it is feasible to produce all the four basic types of seeds shown in Figure 3A by carefully controlling the experimental conditions.

3.3. Growth

Growth is responsible for the increasingly enlarged size of a nanocrystal, in addition to faceting and shape development. As a result of the catalytic activity of most metal surfaces, the precursor can now be reduced to the elemental form through two different pathways (Figure 10A,B): solution reduction and surface reduction.[117] For the solution pathway, the precursor compound is still directly reduced in the solution phase through collision and electron transfer with the reductant molecule, just like what has happened during the homogeneous nucleation step. The atoms are then added onto the surface of a seed to facilitate its growth into a nanocrystal. In contrast, surface reduction relies on the assistance from the existing seed to greatly facilitate the production of metal atom:

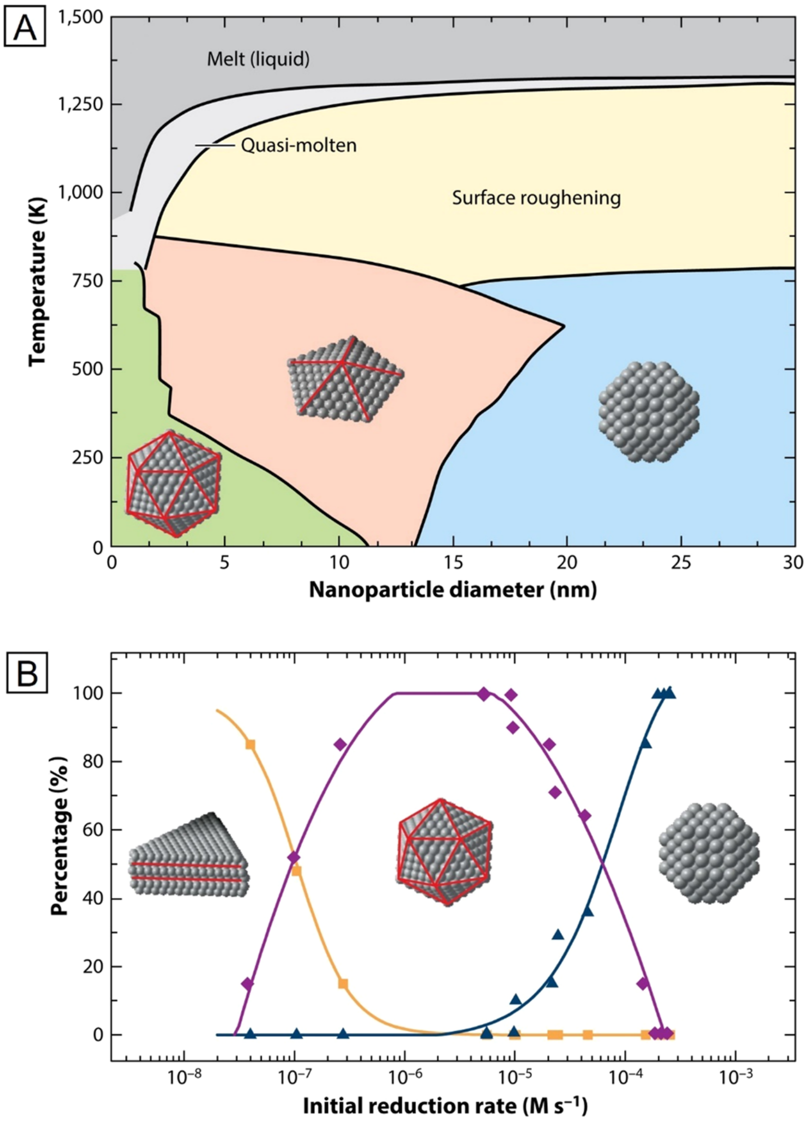

Figure 9. Thermodynamic and kinetic approaches to controlling the internal structure of seeds. (A) Phase diagram of Au seeds as functions of temperature and particle size. (B) Population of Pd nanocrystals as a function of the initial reduction rate, showing the formation of plates with stacking faults (orange line), multiply twinned icosahedra (purple line), and single-crystal cuboctahedra (blue line). (A) Modified with permission from ref 75. Copyright 2009 American Chemical Society. (B) Modified with permission from ref 69. Copyright 2015 American Chemical Society.

the precursor will adsorb onto the surface of a seed, followed by its reduction to an atom through an autocatalytic mechanism.[118] The activation energies for these two different reduction pathways differ significantly. In general, when the precursor undergoes surface reduction in the growth stage, the presence of a seed can significantly lower the energy barrier for the formation of an atom, as if the surface atoms of the seed act as a "catalyst" for the reduction process. This autocatalytic process was originally discovered when people were trying to understand the mechanistic details involved in the development of photographic films[119] and it has been observed during the colloidal syntheses of nanocrystals for essentially all noble metals.[120−124] As illustrated by the TEM images, it is critical to ensure the dominance of surface reduction pathway during the process (Figure 10C,D). Otherwise, the product will contain a second population of nanocrystals, typically, with a much smaller size, due to the involvement of additional homogeneous nucleation events rather than just growth.[117]

To obtain a quantitative understanding of the relative significance of the two distinct reduction pathways, one can measure the reduction kinetics and then use the Finke−Watzky model to fit the data.[122] According to this model, the colloidal synthesis of metal nanocrystals can be described using a two-step mechanism involving two pseudoelementary reactions:

$$\mathrm{A} \rightarrow \mathrm{B} \qquad \text{(I)}$$

$$\mathrm{A} + \mathrm{B}_{\mathrm{surface}} \rightarrow 2\mathrm{B} \qquad \text{(II)}$$

where A represents the precursor and $B_{surface}$ is the active site on the seed. Specifically, the first step is responsible for the relatively slow reduction pathway in the solution phase, whereas the second step corresponds to the faster, autocatalytic reduction pathway that involves the surface of a seed or growing nanocrystal. In general, homogeneous nucleation only involves solution reduction while both surface and solution reduction can participate in the growth process. Based on the Finke−Watzky model, one can quantify the

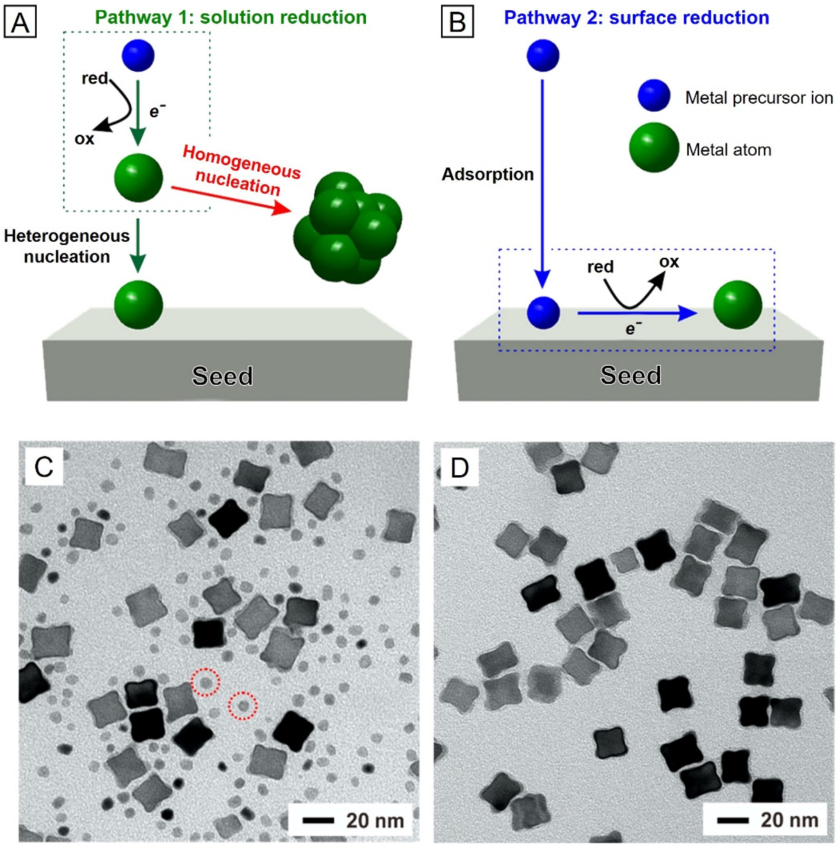

Figure 10. (A and B) Schematic illustrations of the two different reduction pathways involved in a colloidal synthesis of metal nanocrystals: (A) solution reduction and (B) surface reduction, respectively. (C and D) TEM images of the products obtained when (C) solution reduction or (D) surface reduction dominated the reduction of a Pd(II) precursor, in the presence of 18 nm Pd cubic seeds. The smaller particles marked in panel C were formed through homogeneous nucleation. Modified with permission from ref 117. Copyright 2017 American Chemical Society.

relative proportions of surface and solution reduction involved in a colloidal synthesis, offering mechanistic insights and guidelines for controlling the shape evolution of nanocrystals.[117,122,125,126] In general, the reduction kinetics has a strong correlation with the reduction pathway taken by the salt precursor, with the fast and slow ones favoring solution and surface reduction, respectively. There exists a transition point in the reduction rate for separating the two distinctive pathways.[127] Below the critical rate, surface reduction will take over the dominance in the generation of atoms whereas solution reduction will exert a major effect when the reduction rate is above the critical level. By finely tuning the reduction kinetics of a synthesis, it is feasible to achieve the preferred reduction pathway for the salt precursor and thereby obtain nanocrystals with the desired shape and other attributes.

3.4. Seed-Mediated Growth

Traditionally, colloidal synthesis of metal nanocrystals is conducted in the one-pot setting, and it is nontrivial to separate growth from homogeneous nucleation unless one can precisely control the instantaneous concentration of the atoms. In many cases, the optimal parameters for these two competing processes may differ substantially. This inherent drawback often results in nanocrystals featuring broad distributions in terms of size, shape, and internal structure. One can easily solve this problem by separating homogeneous nucleation and growth into two well-defined steps.[128] As a hallmark of seed-mediated growth, it circumvents homogeneous nucleation by directing the newly formed atoms to heterogeneously nucleate and then grow from the surface of a preformed seed featuring well-defined attributes. Seed-mediated growth of nanocrystals in a colloidal suspension can be considered as a nanoscale analogue of the Czochralski method as they are operated under the same principle.[129,130] In both cases, well-defined seeds (nanoscale or bulk size) are exposed to a supersaturated solution in a reaction vessel in an effort to promote growth on the preformed seeds. During the growth process, the internal structure is more or less fixed while the growth pattern and thereby the shape or surface structure taken by the resultant nanocrystals can be readily controlled by varying the experimental conditions.

In the presence of preformed seeds, heterogeneous nucleation will prevail over homogeneous nucleation. From the viewpoint of thermodynamics, the energy barrier to heterogeneous nucleation is always lower than that to homogeneous nucleation:[100]

$$\Delta G^{*}_{\mathrm{hetero}} = \left(\frac{2 - 3\cos\theta + \cos^{3}\theta}{4}\right)\Delta G^{*}_{\mathrm{homo}} \tag{1}$$

where θ is the contact angle formed by the nucleus in equilibrium with a surface. Since the θ-dependent term in the parentheses is limited to the range of 0−1, the energy barrier to heterogeneous nucleation cannot exceed that to homogeneous nucleation. As a result, heterogeneous nucleation can take place at a concentration well below the minimum needed for homogeneous nucleation. In other words, heterogeneous nucleation can occur under relatively milder reaction conditions, such as a lower reaction temperature or a lower concentration of the precursor.

In the setting of seed-mediated growth, one can easily eliminate homogeneous nucleation by ensuring that the atoms in the solution are kept below the minimum level needed for homogeneous nucleation. This goal can be easily achieved by titrating the precursor solution into a suspension of seeds through the assistance of a syringe pump. In this case, the instantaneous concentration of the precursor (C_t) at time t can be modeled using pseudo-first-order kinetics, with the reduction rate being solely determined by the precursor concentration.[131] If the volume of precursor solution added is negligible relative to the total volume of the growth solution, C_t can be calculated according to

$$\begin{aligned} C_t &= C_0 e^{-kt} + C_0 e^{-k(t-\tau)} + C_0 e^{-k(t-2\tau)} + ... + C_0 e^{-k(t-N\tau)} \\ &= C_0 e^{-kt} \frac{(1 - (e^{k\tau})^{N+1})}{1 - e^{k\tau}} \end{aligned} \tag{2}$$

where N represents the total number of droplets (with an initial concentration of C_0) that have been introduced periodically at a time increment of τ. The rate constant k depends on the nature of the precursor and reducing agent and it can be derived experimentally from measurements based on ultraviolet−visible (UV−vis) spectroscopy or inductively-coupled plasma mass spectrometry (ICP-MS). When plotted as a function of time, C_t quickly enters a steady state, in which it only oscillates between two limits, C_{low} and C_{up}. These two values can be calculated as

$$C_{\text{low}} = \frac{C_0 e^{-k\tau}}{1 - e^{-k\tau}} \tag{3}$$

$$C_{\text{up}} = \frac{C_0}{1 - e^{-k\tau}} \tag{4}$$

It is critical to maintain the upper limit (C_{up}) below the minimum level needed for homogeneous nucleation by judiciously choosing the initial concentration (C_0) and the injection frequency (τ) once the types of precursor and reducing agent are fixed.

The beauty of seed-mediated growth is that one can take any existing sample of nanocrystals, add a precursor, together with a reductant and/or capping agent, to obtain nanocrystals with a broad range of new shapes.[128] A classic example can be found in the growth of cubic seeds into octahedral nanocrystals through a series of intermediates, including truncated cubes/octahedra with different ratios between the areas of {100} and {111} facets.[132,133] With the use of seeds based on nanocrystals bearing well-defined attributes such as size, facet, and internal structure, one can also systematically investigate the correlations between autocatalytic surface reduction and these attributes.[118] Similar to the concept of facet-dependent catalysis, autocatalytic reduction is also supposed to be sensitive to the surface structure. As demonstrated in a recent study involving Pd, the activation energy barrier to autocatalytic surface reduction was highly dependent on both the type of facet and the presence of twin boundaries, following the order of {111} > {100} > vertex of a decahedron > vertex of an icosahedron.[118] As a result, the growth of atoms from these seeds may take completely different patterns, leading to the production of nanocrystals with diverse shapes.

3.5. Shape Evolution of Nanocrystals: Thermodynamic vs Kinetic Controls

The ultimate shape taken by a nanocrystal during its growth process is determined by the interplay between multiple thermodynamic and kinetic factors defined by the experimental conditions.[134] In essence, the thermodynamically controlled product should exhibit a global minimum in terms of total energy, including the contributions from surface, volume, defects, and strains (Figure 11A).[135] The thermodynamic shape can be considered as the equilibrium state defined by the experimental parameters involved in the synthesis, including temperature, pressure, and concentrations of all the chemical species.[134] When surrounded by vacuum, the equilibrium shape of a single-crystal nanocrystal can be derived using the Wulff construction. In this case, one only needs to consider the surface free energy, and the specific energy of a given facet should be in direct proportion to the distance from the center of the nanocrystal to the facet.[93,94] As predicted using the Wulff construction, the equilibrium shape of a single-crystal nanocrystal of an fcc metal is represented by a truncated octahedron enclosed by a mix of {111} and {100} facets at roughly the same proportion in terms of area. Of course, when

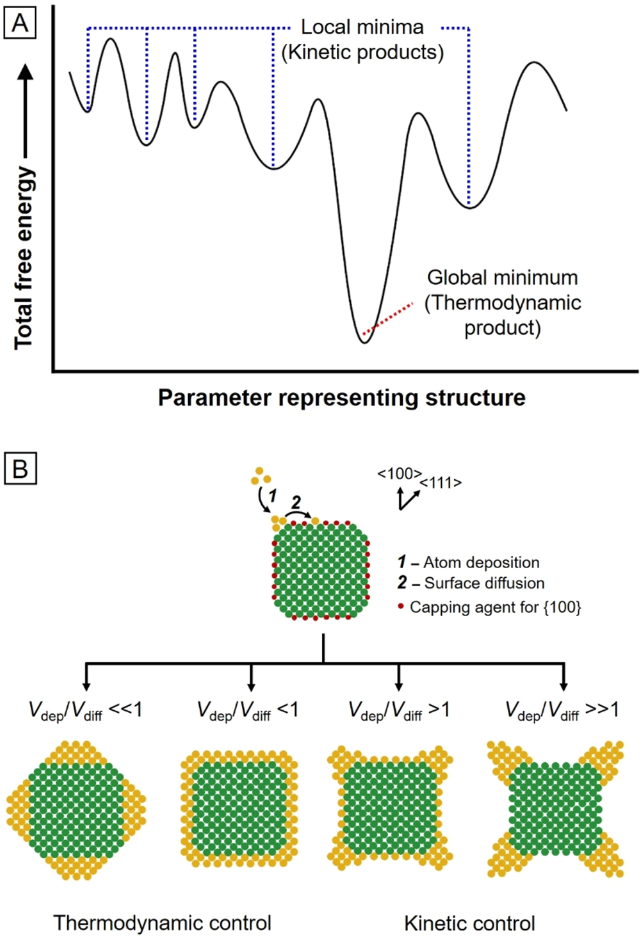

Figure 11. Schematic illustrations of (A) thermodynamic and kinetic controls that involve a series of sequential reactions and (B) the shape evolution of a cubic seed under four sets of experimental conditions. (A) Modified with permission from ref 134. Copyright 2015 American Chemical Society. (B) Modified with permission from ref 136. Copyright 2013 United States National Academy of Sciences.

we move the nanocrystal from vacuum into a solution (or even a gas), the equilibrium shape will be deviated from a truncated octahedron due to the variations in specific surface energy for the facets involved.

Although thermodynamics defines the final destinations that atoms should reach in attaining a global minimum in free energy, only a very limited number of shapes and surface structures could be obtained if the synthesis is conducted under the thermodynamic control. Accumulating evidence from experimental studies indicated that many nanocrystals would rather settle into structures that are thermodynamically less stable but locally stable, known as kinetically controlled products (Figure 11A).[134,135] For a colloidal synthesis of noble-metal nanocrystals, such a kinetic control is achieved by maneuvering the reduction rates involved in nucleation and growth. In the stage of nucleation, the initial reduction rate plays a vital role in controlling the internal structure of the seeds. By decreasing the initial reduction rate of a salt precursor, the internal structure could be tuned from single-crystal, singly twinned, multiply twinned, and further to stacking fault-lined.[69] Upon entering the stage of growth, manipulation of the reduction kinetics is essential to the control of faceting and thus shape evolution. The kinetic products can take a wide variety of shapes depending on the reaction conditions. Therefore, having a good understanding of kinetics offers more opportunities in synthesizing nanocrystals with diverse surface structures.

One can adjust the experimental parameters to apply either thermodynamic or kinetic control to a shape-controlled synthesis of nanocrystals. According to the Arrhenius equation (reaction rate constant = $A e^{-E_a/RT}$), the most effective way to promote a thermodynamically controlled synthesis is to raise the reaction temperature for overcoming the energy barriers more easily. This is because the thermodynamically controlled product is exclusively determined by the difference in Gibbs free energy rather than the reaction pathway. In contrast to the thermodynamic control, a relatively low temperature is more desired for a kinetically controlled synthesis because it allows one to finely tune the kinetic parameters such as atom deposition and surface diffusion rates (denoted as V_{dep} and V_{diff}, respectively) to reach local minima in terms of total free energy.[136] In general, V_{dep} is directly associated with the generation rate of atoms (i.e., the reduction rate of a salt precursor), which can be controlled through the selection of precursor and reductant, variation in reagent concentration, adjustment of reaction temperature, and the type of coordination ligand for the metal ions.[128,136] Regarding the surface diffusion, it is essentially determined by the reaction temperature and the energy barrier to diffusion (E_{diff}), with the latter related to the strength of the bond between the surface atom and the adatom, the crystallographic plane of the surface, the accessibility of the surface, and the chemical potential gradient.[137,138] As such, an effective means to control surface diffusion in a colloidal synthesis of nanocrystals relies on the variation in reaction temperature, the type of metal and its surface structure, as well as the addition of a capping agent for passivating a specific type of facet.[136,139,140]

In principle, whether the product is formed under thermodynamic or kinetic control is really determined by the surface diffusion rate. An exemplary illustration can be found in the growth of a cubic seed (Figure 11B), in which the surface energies of various sites on the cube increase in the order of side faces, corners, and edges owing to the difference in CN for the atoms and presence of a capping agent on the side faces. During deposition, atoms under thermodynamic control involve a much greater V_{diff} relative to V_{dep} and their behavior follows a "hit-then-diffuse" fashion across the surface of a seed, giving rise to the formation of nanocrystals featuring the Wulff shape. In contrast, atoms under kinetic control suggest a site-selected growth, producing diverse products including concave cubes and octapods as the ratio of V_{diff} and V_{dep} is decreased.[136] It should be pointed out that nanocrystals with a shape deviated from the Wulff shape, for example, the cubes in Figure 11B, could also be favored by thermodynamics, as long as there is enough capping agent in the reaction solution to effectively passivate and thereby stabilize the exposed facets.[107]

3.6. Capping Agents

Capping agents are extensively used in the colloidal synthesis of nanocrystals owing to their vital roles in controlling the shape and thus surface structure of the product.[106,107] A variety of capping agents have been reported, including those based on cationic/anionic species, small molecules, macromolecules, and biomolecules.[141−146] Through facet-selective adsorption, a capping agent is able to alter both the thermodynamic and kinetic factors responsible for controlling the shape evolution of nanocrystals. From the perspective of thermodynamics, the role of a capping agent is to selectively stabilize a certain type of facet on a nanocrystal by altering the landscape of surface free energies. Kinetically speaking, the capping agent chemisorbed on a facet can act as a physical barrier to impede or even prohibit the deposition of atoms on this facet, affecting the outcome of a colloidal synthesis of nanocrystals.[107] The adsorbed capping agent can also retard the surface diffusion of adatoms, promoting the formation of kinetic products.

When there is no capping agent, the thermodynamically favored shape of a nanocrystal made of an fcc metal is a cuboctahedron defined by the Wulff construction as the specific surface free energies increase in the order of $\gamma_{(111)} < \gamma_{(100)} < \gamma_{(110)}$. However, in the presence of a capping agent selective toward {100} facets, the capped {100} facets will have the lowest specific surface free energy and the order will become $\gamma_{(100)} < \gamma_{(111)} < \gamma_{(110)}$, leading to the formation of a nanocrystal that features a cubic shape to maximize the expression of {100} facets. Alternatively, the cubic shape can also be considered as the product of a kinetic process. When the capping agent selectively adsorbs onto {100} facets, the adsorbate layer will impede the direct deposition of atoms onto these facets while retarding the diffusion of adatoms from other regions to these facets. As a result, a majority of the atoms will be deposited on the corners and edges of a growing nanocrystal, followed by their slow diffusion to the side faces. If the deposition and diffusion rates of atoms are comparable, the surface of the product will be enclosed by {100} facets to give a cubic shape. The same argument also applies to the synthesis that is conducted in the presence of a capping agent selective toward {111} facets. In this case, an octahedral nanocrystal covered by eight {111} facets will be obtained.[107,134]

It should be pointed out that the presence of capping agents can also significantly affect the internal structure of the product, in addition to the surface structure. One compelling example can be found in the synthesis of Pd nanocrystals. When a Pd(II) precursor was reduced by ascorbic acid (AA) in a polyol system, single-crystal Pd nanocrystals were found to be dominant in the final product.[147] In sharp contrast, Pd wires

Table 1. Summary of Shapes That Have Been Successfully Obtained for Noble-Metal Nanocrystals

Internal Structure	Shapes	Models[a]	Metals	References
Single-crystal	Cube and truncated cube	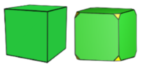	Cu	153−159
			Rh	104, 160−162
			Pd	132, 163−167
			Ag	168−181
			Pt	35, 141, 148, 182−193
			Au	32, 194−198
	Rectangular bar	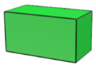	Pd	139, 199−201
			Ag	202−204
			Pt	139, 205
	Octahedron and truncated octahedron	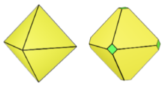	Cu	206
			Rh	104, 207
			Pd	132, 165, 208−212
			Ag	180, 181, 213, 214
			Pt	34, 35, 144, 187, 191, 215−217
			Au	32, 196, 218−220
	Tetrahedron		Cu	158
			Rh	221, 222
			Pd	210, 223
			Ag	224, 225
			Pt	141, 182, 183, 226
			Au	32, 227
	Rhombic dodecahedron	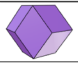	Pd	165, 228
			Au	229−231
	Plate or sheet		Rh	232, 233
			Au	234, 235
Singly-twinned	Bipyramid	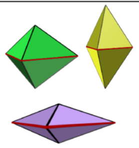	Pd	71, 236, 237
			Ag	116
			Pt	238
			Au	230
	Beam	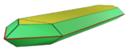	Ag	239
Multi-twinned	Decahedron		Cu	240
			Rh	241
			Pd	208, 242, 243
			Ag	224, 244
			Pt	245
			Au	102, 246−248
	Icosahedron		Rh	249
			Pd	208, 242
			Ag	175, 177, 250, 251
			Pt	35, 245, 252, 253
			Au	32, 103, 254, 255
	Penta-twinned rod or wire	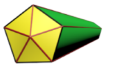	Cu	153, 256−263
			Pd	147, 237, 264−267
			Ag	268−290
			Au	291−296
	Hexagonal or triangular plate	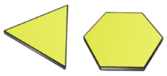	Cu	297−300
			Ru	301
			Rh	302, 303
			Pd	304−307
			Ag	305, 308−315
			Au	305, 316−319
	Twinned cube or bipyramid	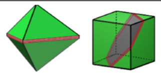	Cu	320
			Ag	321, 322
			Au	292, 323−325
High-index facets	Concave polyhedron		Pd	118, 223, 326−330
			Pt	34, 47, 62, 64, 331, 332
			Au	333−337
	Multipod	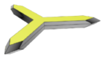	Pt	47, 338−340
			Au	341
	Convex polyhedron		Pt	63, 342
			Au	343−345
Others	Belt		Ag	346, 347
			Au	348−350
	Wavy wire	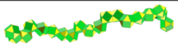	Ir	351
			Au	352, 353
Hollow	Cage	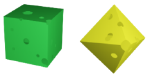	Ru	354−357
			Rh	358, 359
			Pd	360, 361
			Ir	362
			Pt	363−365
			Au	366−370

[a] For metals in fcc crystal structure, green, yellow, purple, and gray colors represent {100}, {111}, {110}, and high-index facets, respectively. The red lines are representative of twin planes/twin boundaries.

characterized by a penta-twinned structure and well-defined {100} facets on the side surface were produced when I^- ions were introduced into the synthesis.[147] Apart from the capping effect of I^- ions toward Pd{100}, kinetic measurements indicated that the presence of I^- ions could substantially slow down the reduction of the Pd(II) precursor by forming PdI_4^{2-}, moving the initial reduction rate into the window favorable for the formation of decahedral seeds, followed by their growth into penta-twinned wires.[147] In many cases, the halides that are commonly used as capping agents can also induce oxidative etching when the syntheses are carried out in air. If managed well, oxidative etching can be used to selectively eliminate twinned seeds, leaving behind single-crystal seeds for the production of cubic or octahedral nanocrystals in high purity. It is even feasible to produce singly twinned nanocrystals such as RBPs in high yields by carefully controlling the oxidative etching process.[71,116] These examples clearly illustrate the necessity to analyze all of the possible roles played by a capping agent in a colloidal synthesis of nanocrystals before a conclusion is drawn.

Despite its pivotal roles in a shape-controlled synthesis, the capping agent remaining on the surface of metal nanocrystals may compromise their performance in (electro)catalysis and other related applications. For example, it was reported that Pt−Ni octahedral catalyst with a capping layer based on poly(vinylpyrrolidone) (PVP) showed an electrochemically active surface area (ECSA) much lower than that of the same catalyst bearing a clean surface.[148] The deactivation was attributed to the blocking effect of PVP that tended to restrict the reactants from accessing the catalytic sites on a Pt−Ni octahedral nanocrystal. To this end, a number of methods have been developed for the postsynthesis removal of capping agents, including washing with a proper solvent, thermal annealing, UV-ozone (UVO) treatment, and ligand exchange (a more detailed discussion can be found in section 8.1).[149−151] In parallel, there is a strong interest in developing synthetic protocols involving no capping agent for the direct production of shape-controlled nanocrystals with a clean surface.[63,152]

4. EXAMPLES OF SHAPE-CONTROLLED NANOCRYSTALS

Built upon our general discussion in sections 2 and 3, this section provides some notable examples of monometallic nanocrystals with controlled shapes. The presentation is divided into different subsections according to the types of surface structures, and eight of the noble metals are discussed in the order of increasing atomic number. The nanocrystals are also summarized in Table 1. These nanocrystals not only offer a variety of well-defined surface structures for fundamental studies but also enable an array of applications related to catalysis and electrocatalysis (see sections 6 and 7).

4.1. Single-Crystal Nanocrystals Enclosed by Low-Index Facets

All the noble metals except Ru are crystallized in the fcc phase, where the specific surface energies of the low-index facets increase in the order of $\gamma_{\{111\}} < \gamma_{\{100\}} < \gamma_{\{110\}}$. As illustrated in Figure 3B–D, the representative nanocrystals with their surfaces enclosed by {111}, {100}, and {110} facets, respectively, are octahedron, cube, and RDD. Since these nanocrystals only expose one specific type of facet as the side faces, they are perfect candidates for studying the facet-property relationship without involving other structural factors.

4.1.1. Cubes and Bars. Cube is one of the most commonly observed shapes for single-crystal nanocrystals, with all the six side faces being identical and terminated in {100} facets. Compared to {111} facets, {100} facets are intrinsically greater in surface energy owing to a lower CN for the surface atoms (9 vs 8). As a result, the formation of cubes typically requires the involvement of a capping agent selective toward {100} facets to direct the shape evolution. In some cases, the cube can also be elongated or compressed along one (or two) of the three axes to yield a bar albeit the areas of adjacent side faces are different from each other. Similar to a cube, a bar has six side faces terminated in {100} facets, but shows an anisotropic shape and an aspect ratio greater than one. In terms of catalytic properties, the surface structures of these nanocrystals in two distinct shapes are almost identical, despite their slight difference in specific surface areas and the proportion of under-coordinated atoms located at corners and edges. The formation of bars typically involves symmetry breaking, which can be most conveniently achieved by slowing down the reduction kinetics and/or through localized oxidative etching. Figure 12 shows TEM images of some typical examples of noble-metal nanocrystals featuring a cubic or bar-like shape.

4.1.1.1. Copper. To generate Cu cubes with a single-crystal structure using an oil-phase method, an elevated temperature, a Cu(I) precursor, and a capping agent are typically required in order to block the growth of {100} facets.[154−157,159] In one example, Cu cubes were synthesized in high purity by reducing CuCl with oleylamine (OAm) in the presence of trioctylphosphine (TOP) and octadecylamine (ODA) at a temperature as high as 330 °C.[155] The cubes had an average edge length of 75.7 nm. It was speculated that TOP and ODA mainly contributed to the formation of single-crystal seeds and stabilization of {100} facets. Similarly, by replacing CuCl with CuBr and both TOP and ODA with trioctylphosphine oxide (TOPO), Cu cubes could be produced at a lower temperature of 260 °C.[154,156,157,159] By varying the reaction time and the amount of TOPO, the size of the cubes could be tuned in the range of 20−80 nm. It was proposed that the weak coordination effect of TOPO to Cu(I) led to a faster reduction of Cu(I) to atoms, enabling nucleation at a relatively lower temperature. Under this circumstance, the {100} facets could be effectively capped by the Br^- ions from the precursor due to the decelerated growth rate.[154] A further investigation into the OAm-based synthesis using in situ X-ray absorption spectroscopy (XAS) measurements indicated that the disproportionation of Cu(I) contributed to the formation of atoms and thus Cu nanocrystals.[158] The final shape of the products was determined by the rate of disproportionation. In the case of TOP, with reaction conducted at 260 °C, a gradual increase in Cu atom concentration was observed, indicating that the reaction was controlled by thermodynamics and quasi-spherical particles were obtained as the final products. When switched to TOPO, however, a sudden increase in Cu atom concentration was observed and cubic nanocrystals were obtained, suggesting that the synthesis was conducted under a kinetic control.

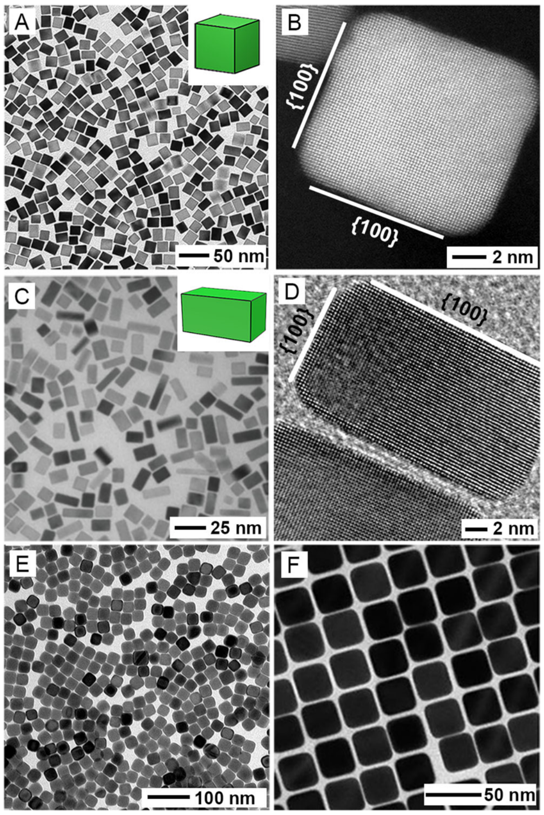

Figure 12. (A) TEM and (B) HAADF-STEM images of Pd cubes with the corresponding three-dimensional (3-D) model shown in the inset of panel A. (C) TEM and (D) high-resolution TEM images of Pd bars, showing the side faces enclosed by {100} facets. (E and F) TEM images of uniform Ag and Au cubes, respectively. (A) Reprinted with permission from ref 371. Copyright 2014 American Chemical Society. (B) Modified with permission from ref 199. Copyright 2010 Springer Nature. (C) Reprinted with permission from ref 201. Copyright 2009 Wiley-VCH. (D) Modified with permission from ref 139. Copyright 2007 American Chemical Society. (E) Reprinted with permission from ref 172. Copyright 2013 American Chemical Society. (F) Reprinted with permission from ref 198. Copyright 2018 American Chemical Society.

It is also feasible to produce Cu cubes using a water-based approach by reducing $CuCl_2$ with glucose in the presence of hexadecylamine (HDA).[153] A temperature as low as 100 °C was adequate for the synthesis, with oxidative etching and the capping effect from HDA and Cl^- ions regarded as the main factors contributing to the formation of cubes. In the presence of O_2 from air, twinned seeds with high surface energy were removed, leaving behind single-crystal seeds for their further growth into cubes. It should be mentioned that HDA, an additive commonly considered as a capping agent for Cu{100} facets in most reports, played an important role in the production of Cu cubes but its capping effect is still under debate.[372] This aspect is discussed in more detail for the synthesis of penta-twinned Cu wires (see section 4.2.3).

4.1.1.2. Rhodium. In comparison with other noble metals such as Pd, Pt, Ag, and Au, only limited success has been achieved for the synthesis of Rh nanocrystals with well-controlled shapes. The difficulty primarily arises from the high bond dissociation energy and surface free energy of Rh.[373] An early report demonstrated a seed-mediated method for the synthesis of Rh cubes with an average edge length of 12.7 nm. Smaller Rh nanocrystals (the seeds) were prepared through the reduction of $RhCl_3$ precursor by ethylene glycol (EG) in the presence of PVP, followed by growth at 190 °C to generate Rh cubes.[160] The Rh cubes reported in this study were mostly truncated, together with the presence of nanoparticles poorly defined in terms of shape. In addressing this issue, a polyol method was later reported to produce Rh cubes in a relative high yield, together with sizes smaller than 10 nm.[161] The key to the success of this synthesis was the presence of Br^- ions released from tetradecyltrimethylammonium bromide (TTAB), which could stabilize the {100} facets and direct the shape evolution to cubes. Later studies have also demonstrated Br^- ions as an effective capping agent toward Rh{100} facets.[162,374] When KBr was introduced into the polyol synthesis, uniform Rh cubes of 6−7 nm in edge length were obtained as well. It is worth noting that the choice of precursor and solvent played a critical role in controlling the final shape of the Rh nanocrystals.[104] It was reported that Rh cubes could be obtained in a higher purity when $RhBr_3$ was used as a precursor while EG, diethylene glycol (DEG), or triethylene glycol (TEG) could serve as a solvent and reducing agent. The size of the Rh cubes increased with the chain length of the polyol.

4.1.1.3. Palladium. Palladium cubes have been extensively explored due to the well-established protocols, in addition to the high purity and uniformity of the products (Figure 12A,B). A typical synthesis of Pd cubes involved the injection of aqueous Na_2PdCl_4 into an aqueous mixture containing AA, halide ions (Br^- and/or Cl^-), and PVP.[166] When applied in the wet-chemical synthesis of Pd nanocrystals, PVP mainly served as a stabilizer to prevent nanocrystals from aggregation. By adjusting the concentrations of Br^- and/or Cl^- ions added into the reaction solution, the size of the Pd cubes with sharp corners and edges could be tuned in the range of 6−18 nm.[166] Halide ions were of great significance in the formation of cubes, and their functions can be generally ascribed to (i) selectively capping of the Pd{100} facets, (ii) coordination to Pd(II) ions for the deceleration of reduction kinetics, and (iii) removal of the twinned seeds through oxidative etching in the presence of O_2.[115] Typically, increasing the concentration of Br^- would slow down the reduction of Pd(II) precursor, resulting in the formation of fewer seeds and thus cubes with larger sizes. From the viewpoint of synthetic approach, enlarging the cubes would need assistance from oxidative etching and/or seed-mediated overgrowth.[163,164,167]

By elongating the cubes along one axis, nanocrystals with a bar-like shape would be produced. A typical synthesis of Pd bars involved the reduction of Na_2PdCl_4 in a mixture of KBr, PVP, and EG or water (Figure 12C,D).[139,201] Here Br^- ions served as the capping agent, while PVP and EG could both act as reducing agents. Several mechanisms have been proposed to account for the anisotropic growth, including (i) localized oxidative etching and thus selective removal of Br^- ions from one specific side face on the cube, enabling atomic deposition onto this face and thus breaking of the cubic symmetry; (ii) oriented attachment of small Pd particles along one direction to minimize the total surface energy, followed by further growth via atomic addition into a bar;[199] and (iii) preferential overgrowth on one of the side faces under the kinetically controlled condition.[200,375]

4.1.1.4. Silver. Among the various types of Ag nanocrystals that have been reported, cubes have attracted much attention because of their use as a sacrificial template for the preparation of Pd, Pt, and Au boxes/cages.[376−378] Despite a few reports on the synthesis of Ag cubes in an aqueous phase,[173,174] polyol process still remains the most effective and robust method, in which a Ag(I) precursor is reduced by a heated polyol in the presence of a stabilizer and a capping agent. Ethylene glycol is the most commonly used polyol in this regard,[168−171,379] with others including DEG,[172] 1,3-butylene glycol,[178] and 1,5-pentanediol,[176] among others. It was reported that glycolaldehyde, a stronger reductant than EG, is produced when EG is heated in air,[168] as shown by the following reaction:

$$2HOCH_2CH_2OH + O_2 \rightarrow 2HOCH_2CHO + 2H_2O \tag{5}$$

In a typical synthesis of Ag cubes, $AgNO_3$ is reduced by EG at an elevated temperature in the presence of PVP.[170] Different from the synthesis of Pd cubes, here the PVP serves both as the stabilizer and capping agent for Ag{100} facets.[142] The morphologies of the products were reported to have a strong dependence on the concentration of $AgNO_3$ and the molar ratio of PVP to $AgNO_3$.[180,181] A higher concentration of PVP relative to $AgNO_3$ was typically required to ensure the stabilization of the {100} facets. However, this protocol typically suffered from low purity due to the inclusion of twinned particles in the final product.

To solve this problem, the protocol was further modified with the introduction of Cl^- ions from NaCl[175] or HCl[168] to enhance the oxidative etching, eliminating the twinned seeds initially formed and only leaving the single-crystal seeds to grow into cubes. Despite the improved purity, the synthesis took more than 1 day to complete due to the involvement of oxidative etching, imposing restriction on the scale of production. It was then discovered that the addition of sulfide or hydrosulfide could greatly speed up the synthesis of Ag cubes through the formation of Ag_2S clusters, which could then serve as seeds for the nucleation and growth of Ag.[169] As a result, Ag cubes with an edge length of 25−45 nm could be rapidly produced in 3−8 min. In a 1,5-pentanediol-based polyol synthesis, the introduction of a trace amount of $CuCl_2$ also promoted the formation of Ag cubes in about 6 min.[176] Although the role of $CuCl_2$ was not discussed in that report, the addition of Cl^- ions into the reaction system could probably lead to the rapid generation of Ag cubes through a similar mechanism.[380] The choice of Ag(I) precursor was also found to play a significant role in the synthesis of Ag cubes. Since the NO_3^- from $AgNO_3$ might decompose to produce ionic or gaseous species at an elevated temperature, it was demonstrated that using CF_3COOAg as a precursor could achieve a better control over the product quality and reproducibility (Figure 12E).[171,172,379]

Controlling the size of Ag cubes is of great significance not only because they are used as a sacrificial template to synthesize hollow nanocrystals made of other noble metals, but also because the size of Ag cubes plays an essential role in the ethylene epoxidation reaction (see section 6.5.1). To this end, different methods have been developed to prepare Ag cubes with variable sizes. Using a seed-mediated growth method that features single-crystal Ag nanocrystals with a spherical or cubic shape as the seeds, the as-obtained cubes could be readily tuned in the range of 30−200 nm.[170] Furthermore, by replacing the polyol with DEG, the size of the Ag cubes was turned down to 18 nm.[172] The higher viscosity and weaker reducing power of DEG enabled a burst of nucleation in the early stage of a synthesis and relatively slow growth thereafter, reducing the average size of the cubes. More recently, Ag cubes smaller than 15 nm, together with sharp corners and edges, were prepared through a EG-based polyol process with the introduction of NaSH, NaBr, and NaCl.[379] Instead of using HCl as a chloride source for oxidative etching, the employment of NaCl could exclude the introduction of protons and thus the consumption of SH^- additives to form H_2S. Hence, Ag^+ ions could react with SH^- rapidly to produce a large number of Ag_2S clusters for the heterogeneous nucleation of Ag atoms. The Br^- ions not only served as a more effective capping agent for the {100} facets on small Ag nanocrystals relative to PVP, but also kinetically regulated the growth by forming largely insoluble AgBr to limit the amount of Ag^+ ions available in the solution. Moreover, through the use of CF_3COOAg as a precursor,[171] addition of HCl as an etchant,[168] and protection of the NaHS-mediated polyol synthesis with Ar gas,[179] a number of reports have demonstrated the ability to scale up the synthesis to up to 0.25 g of solid sample per batch, making it feasible to apply Ag cubes to commercial catalytic tests.

Silver bars with a single-crystal structure and a rectangular cross section were also reported by several groups. In an early report, a seed-mediated method was reported to prepare Ag bars using spherical or cubic Ag nanocrystals as seeds.[203] A solution containing $AgNO_3$, EG, and a bromide compound was applied to produce Ag bars with various aspect ratios. The anisotropic growth was attributed to the presence of bromide species in the system. It was found that Ag bars with higher aspect ratios could be obtained when Ag spheres were used as seeds, and ionic bromides promoted the formation of bars more effectively than covalent bromides. Similar to Pd bars,[139] Br^- ions also played a crucial role in the synthesis of Ag bars because it induced the localized oxidative etching and activated one of the many equivalent facets for preferential atom deposition, resulting in symmetry breaking and thus the formation of bars. In another study, a solution of $AgNO_3$ in EG and another containing PVP and NaBr in EG were added dropwise into EG heated at 155 °C, producing a mixture of cubes and bars with an average aspect ratio of 2.7.[202] Moreover, in a recent study, Ag bars were prepared by tentatively slowing down the reduction kinetics in a seed-mediated synthesis.[204] During the synthesis, cetyltrimethylammonium chloride (CTAC) was used as a capping agent, and AgCl was formed via the reaction between Ag^+ and Cl^- ions to serve as a new source to elemental Ag. The limited supply of Ag atoms caused by the slow reduction of AgCl, and the strong capping of the cubic seeds by Cl^- ions confined the nucleation of Ag to one of the side faces, inducing anisotropic growth. It was suggested that localized oxidative etching might also be involved in the synthesis by activating one of the side faces for preferential atom deposition.

4.1.1.5. Platinum. Similar to the synthesis of Pd cubes, a fast reduction rate of Pt precursor and the use of proper capping agents are of great significance in generating single-crystal seeds for their subsequent evolution into a cubic shape. The first report on the synthesis of Pt cubes involved the reduction of K_2PtCl_4 by H_2 with sodium polyacrylate serving as a stabilizer.[182,183] The key factor in this synthesis was the concentration of sodium polyacrylate. By varying the concentration of sodium polyacrylate, Pt tetrahedra and truncated octahedra were also produced. However, the purity of the Pt cubes in this report was relatively low, and further modification to the protocol was necessary. Other capping agents such as CO, OAm, and oleic acid (OA) have been confirmed to be more effective in passivating Pt{100} facets. For example, also under the H_2 atmosphere, by decomposing Pt(II) acetylacetonate (acac) in the presence of OAm, Pt cubes in high purity were obtained albeit their sizes varied in the range of 10−100 nm.[184] In another example, uniform Pt cubes with an average size around 10 nm were obtained by reducing $Pt(acac)_2$ in a mixture of OA, OAm, $W(CO)_6$, and benzyl ether.[148] The stronger binding of CO, derived from the decomposition of $W(CO)_6$, to Pt{100} facets than to {111} facets greatly prevented the deposition of atoms on {100} facets, resulting in the formation of cubes.[148,185,381,382] It should be mentioned that the explicit role of metal carbonyl was still under debate. Besides the formation of CO for passivating the Pt surface, it was also proposed that metal ions served as the actual capping agent while CO served as a reducing agent.[35,188−190] In addition to the small organic/inorganic molecules mentioned above, other types of capping agents such as Ag^+ ions,[187] triblock copolymers,[186] and peptides[141] have also been demonstrated for the formation of Pt cubes.

Manipulating the reduction kinetics is another important factor in synthesizing Pt cubes, especially in the generation of single-crystal seeds. In one example, Pt cubes were prepared by reducing K_2PtCl_4 with H_2 generated in situ from $NaBH_4$, with TTAB serving as the surfactant.[192] However, when $NaBH_4$ was replaced with AA, a milder reducing agent, porous Pt nanocrystals with a polycrystalline structure were obtained, revealing the importance of fast reduction rate in generating single-crystal seeds.[193]

In terms of Pt bars, the successful syntheses were achieved from both localized etching and oriented attachment.[194] The strategy used for the synthesis of Pd bar could also be extended to the Pt system. In one report, bars were synthesized using localized oxidative etching to selectively remove some of the capping agents on one side face.[139] The addition of Pt atoms onto the cleaned face led to the formation of anisotropic bars with an aspect ratio of 2−3 and a yield above 90%. In the case of oriented attachment, a typical protocol involved the reduction of $Pt(acac)_2$ in the presence of benzyl alcohol, OAm, and HCHO.[205] Numerous small particles were generated in the early stage of the reaction, and the particles were then observed to coalesce along the ⟨100⟩ direction to form an elongated, rod-like shape, which further grew into bars in the presence of capping agents toward {100} facets.

4.1.1.6. Gold. The synthesis of Au cubes was first achieved using a polyol method, during which $HAuCl_4$ was reduced by EG in the presence of PVP as a colloidal stabilizer and $AgNO_3$ as an additive to regulate the shape.[32] Different from the Ag system, PVP did not exert a capping effect on Au{100} facets and could not be applied as a shape directing agent for the formation of Au cubes.[142] Instead, this report suggested that the addition of Ag^+ ions effectively enhanced the growth rate of Au{111} relative to Au{100}, generating Au cubes as the final product. The polyol method was later modified by replacing EG with 1,5-pentanediol to reduce $HAuCl_4$ more rapidly.[195] With an increase in the amount of $AgNO_3$ added into the solution, Au octahedra, truncated octahedra, cuboctahedra, and cubes were sequentially obtained, due to the selective deposition of Ag^+ ions on the seed, and thus preferential growth of {111} over {100} facets. This example further confirmed the capping effect of Ag^+ toward Au{100}. However, it was hard to precisely control the reaction kinetics in such a one-pot synthesis, leading to a relatively low uniformity for the final product. In addressing this issue, seed-mediated growth was applied as a powerful approach to the synthesis of Au cubes (Figure 12F).[198] Using 10 nm Au spheres as seeds, Au cubes with sizes ranging from 17−78 nm could be obtained with a narrow size distribution and purity as high as 99%. The precise control of both size and shape relied on the introduction of Au seeds, as well as the adjustment of the concentration of Br^- ions in the reaction mixture.

4.1.2. Octahedra and Tetrahedra. Both octahedron and tetrahedron are single-crystal structures enclosed by {111} facets. Similar to the case of cube versus bar, the major difference between octahedron and tetrahedron lies in the specific surface area, with that of a tetrahedron being greater than that of an octahedron. The larger surface-to-volume ratio relative to that of octahedra makes tetrahedra less favorable in terms of thermodynamics, and a fine control over the reduction kinetics is necessary for the synthesis of tetrahedral nanocrystals in high yield and purity. Figure 13 shows TEM images of some typical examples of noble-metal nanocrystals featuring an octahedral or tetrahedral shape.

4.1.2.1. Copper. Copper octahedra were synthesized using a reaction system containing CuCl, TOP, and OAm, similar to what was used for the synthesis of Cu cubes.[206] The protocol involved the disproportionation reaction of Cu(I) at 335 °C, by which Cu octahedra as large as 145 nm were obtained in high purity. It was reported that TOP molecules could attach to the surface of Cu nanocrystals and were speculated to serve as a capping agent toward Cu{111} facets. However, considering the relatively weak binding of TOP to Cu, the high temperature used, and the lower surface energy of {111} facets, it seems to be more reasonable to attribute the formation of an octahedral shape to thermodynamics instead of the capping effect from TOP. When lowering the temperature to 300 °C and injecting CuBr and TOPO into OAm solution, Cu tetrahedra could be synthesized and their formation was largely attributed to a kinetic control.[158]

4.1.2.2. Rhodium. Rhodium octahedra were obtained by modifying the protocol developed for the synthesis of Rh cubes.[104] By changing the precursor from $RhBr_3$ to $RhCl_3$, while switching the reducing agent from EG, DEG, or TEG to poly(ethylene glycol) with an average molecular weight of 300 (PEG300), Rh octahedra were produced with a yield around 70%. The type of polyol solvent played a crucial role in this shape-controlled synthesis, which could be ascribed to the change in the reduction kinetics. Similar to the strategy for the synthesis of Au cubes, the polyol method could be optimized with the incorporation of small amounts of metal ions into the reaction system. It was reported that by adding $AgNO_3$ into a reaction system containing $RhCl_3$, PVP, and EG, the yield of Rh octahedra could be increased to as high as 90%.[207] It should be pointed out that the high purity and quality claimed by the authors do not seem to be supported by the TEM images and further refinement or improvement of the protocol is still necessary.

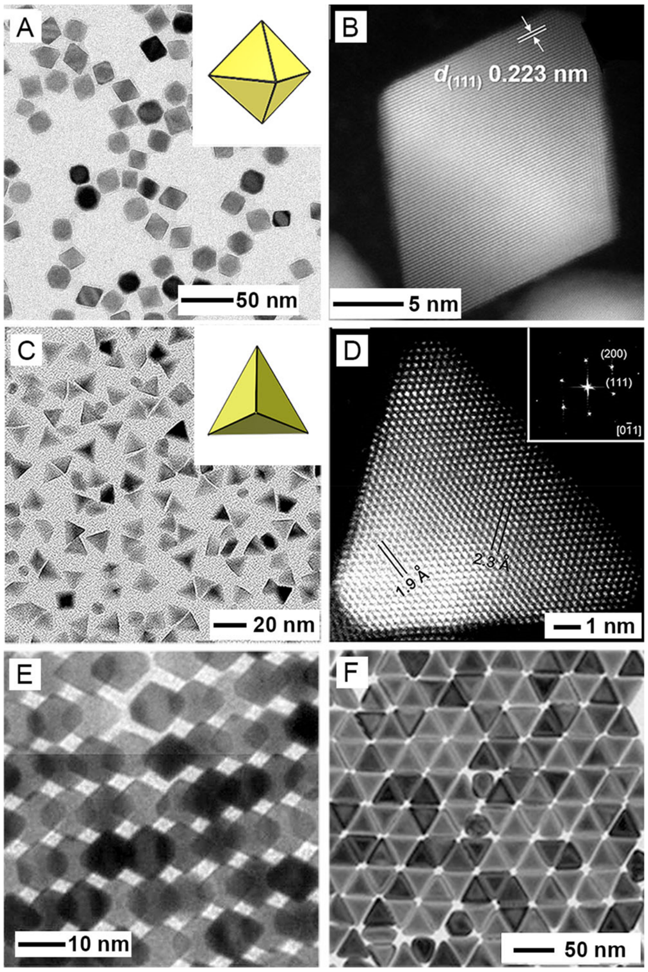

Figure 13. (A) TEM and (B) HAADF-STEM images of Pd octahedra. The inset in panel A shows a model of the octahedral nanocrystal. The lattice spacing of 0.223 nm can be indexed to the {111} planes of fcc-Pd. (C) TEM and (D) HAADF-STEM images of Pd tetrahedra. The insets show a model of the tetrahedral nanocrystal and the Fourier transform pattern, respectively. (E and F) TEM images of Pt octahedra and Au tetrahedra, respectively. (A) Reprinted with permission from ref 209. Copyright 2013 American Chemical Society. (B) Reprinted with permission from ref 383 Copyright 2020 American Chemical Society. (C and D) Reprinted with permission from ref 210. Copyright 2013 American Chemical Society. (E) Reprinted with permission from ref 35. Copyright 2013 American Chemical Society. (F) Reprinted with permission from ref 227. Copyright 2014 Wiley-VCH.

As for tetrahedra, an organometallic approach was proposed with rhodium carbonyl chloride as a precursor and OAm as a solvent to produce uniform Rh tetrahedra, whereas spherical nanocrystals were obtained when the precursor was changed to $Rh(acac)_3$.[221] Although the authors did not propose any specific mechanism to account for the formation of tetrahedra, the shape-controlled synthesis could likely be attributed to the change in reaction kinetics as induced by different stabilities of the precursors in the solvent. In another example, Rh tetrahedra were prepared by reducing Rh(III) acetate (ac) in a mixture containing glucose, *N*,*N*-dimethylformamide (DMF), and OAm.[222] The authors elucidated the roles played by DMF and glucose by carrying out a set of control experiments to vary the concentration of these two chemicals in the solution. However, no specific mechanism was presented in terms of how these two chemicals affected the shape evolution of Rh tetrahedra.

4.1.2.3. Palladium. Palladium octahedra could be produced using either one-pot approach or seed-mediated growth. Depending on the synthetic protocol, the products can take different ranges of sizes. Typically, larger octahedra are more suitable for analyzing facet-dependent properties while smaller octahedra offer a higher specific surface area.

Citric acid (CA) and citrate ions are mostly used as the capping agents in the synthesis of Pd octahedra. In one example, an aqueous solution containing Na_2PdCl_4, PVP, and CA was heated at 90 °C for 26 h to generate Pd octahedra with an average size of 20 nm.[208] The formation of an octahedral shape was mainly attributed to the selective binding of CA to Pd{111} facets, which stabilized these facets and blocked the addition of atoms to them. In addition to one-pot synthesis, Pd octahedra with different sizes could be produced through seed-mediated growth by employing Pd cubes as the seeds. In a typical synthesis, Na_2PdCl_4 was introduced into an aqueous solution containing PVP, HCHO, and Pd cubic seeds.[132,211] Without a capping agent in the solution, the surface free energy for low-index facets of an fcc metal follows the order: $\gamma\{111\} < \gamma\{100\} < \gamma\{110\}$. Thus, the newly formed Pd atoms would prefer to nucleate and grow from {100} facets for the generation of octahedral nanocrystals enclosed by {111} facets, which have a lower total surface free energy and are favored thermodynamically. By using cubes of 6, 10, and 18 nm in size as the seeds, Pd octahedra with edge lengths of 14, 21, and 37 nm, respectively, were obtained. During the growth, increasing the amount of Pd(II) precursor would give truncated cubes, cuboctahedra, truncated octahedra, and octahedra sequentially, with an increase in the area ratio between the {111} and {100} facets.

In addition to seed-mediated growth, oxidative etching offers another route to the synthesis of Pd octahedra with controlled edge lengths from cubes.[209] Using HCl/O_2 as the oxidative etchant and TEG as a reducing agent, Pd atoms were first removed from the corners of the cube due to the capping of {100} facets by Br^- ions. The resultant Pd(II) ions were then reduced and deposited back onto the cube, but preferentially on {100} facets considering their higher surface energy than {111}, leading to the formation of octahedral products (Figure 13A,B). Besides, the conventional seed-mediated growth can also be conducted in one step through the use of dual reductants with different reducing power.[212] In a typical protocol, a strong reductant (e.g., AA and ethanol) was used to control the reduction and nucleation steps to generate single-crystal seeds, while a weak reductant such as CA only worked in growth step for the conversion of the unreacted precursor and stabilization of the {111} facets. This one-pot, dual-reductant method provides an effective and time-saving route to the synthesis of Pd octahedra with high purity, and this strategy can also be potentially extended to other metals.

In contrast to other basic shapes such as cube and octahedron, tetrahedron is rarely explored for Pd. By leveraging Pd cuboctahedra as seeds, Pd nanocrystals with a tetrahedral shape could be synthesized by adding $Pd(acac)_2$ into a mixture of tetraethylene glycol (TTEG) and PVP (Figure 13C,D).[210] Interestingly, when replacing $Pd(acac)_2$ with Na_2PdCl_4, octahedral nanocrystals were obtained. The weak coordination of acac to Pd^{2+} led to a fast reduction rate of $Pd(acac)_2$ and the growth of nanocrystals into a kinetically favored tetrahedral shape. In comparison, the slow reduction of Na_2PdCl_4 induced by the strong binding of Cl^- to Pd^{2+} could maintain the precursor at a relatively high concentration and ensure the thermodynamically controlled growth of Pd into an octahedral shape. In another example, Pd tetrahedra were produced in one step by reducing $Pd(acac)_2$ with DMF in the presence of PVP and $Fe(acac)_2$, and the relatively fast reduction rate was also considered as the main reason for the formation of tetrahedra.[223]

4.1.2.4. Silver. As we discussed previously, Ag cubes could be synthesized within 6 min through a 1,5-pentanediol-based polyol process by introducing $CuCl_2$.[176] Interestingly, when the synthesis was extended to 2 h at a constant supply of precursor, the Ag nanocrystals gradually transformed from cubes to truncated cubes, cuboctahedra, truncated octahedra, and finally octahedra. This shape transformation was attributed to the relatively low concentration of PVP in the solution. As the Ag nanocrystals grew larger, the amount of PVP in the reaction mixture became inadequate to fully cover the Ag{100} facets, leading to the formation of octahedron as the final product.

Seed-mediated growth has also been employed for the preparation of Ag octahedra. In one report, cubic Ag nanocrystals were used as the seeds for further growth in a DMF solution to produce Ag octahedra with an average edge length of 170 nm.[213] However, nanocrystals with such large size could hardly be applied to industrial catalytic applications. To this end, smaller Ag octahedra with sizes tunable in the range of 20−72 nm were synthesized using uniform cubic or quasi-spherical Ag nanocrystals as the seeds.[214] The addition of citrate as an effective capping agent toward Ag{111} facets greatly contributed to the formation of Ag octahedra that were compact in size, together with sharp corners, sharp edges, and smooth side faces.[215]

In the case of tetrahedra, their lower degree of symmetry has brought some difficulties to the synthesis involving seed-mediated growth. The formation of Ag tetrahedra was first discovered as a byproduct in the EG-based polyol synthesis of Ag cubes.[175] It was found that when introducing NaCl into the reaction, a mixture of Ag cubes and truncated tetrahedra were formed at the same time. Higher yield of Ag tetrahedra was achieved in a later study, where Ag seeds were first produced by reducing $AgNO_3$ with $NaBH_4$ in an aqueous solution containing tartrate, followed by the irradiation with a sodium lamp for 9 h.[225] Afterward, PVP and citrate were introduced into the seed suspension under irradiation for another 20 h. The success of this synthesis could be attributed to the introduction of tartrate and citrate for promoting the formation of nuclei in the shape of truncated tetrahedra and facilitating their growth into tetrahedra, respectively. In another example, $AgNO_3$ was reduced in DMF in the presence of PVP.[224] When the molar ratio of PVP to $AgNO_3$ was set to 10, Ag tetrahedra were produced with a purity of 70%.

4.1.2.5. Platinum. Compared to cubes, it is neither easy nor straightforward to synthesize Pt octahedra due to the difficulty in finding the proper capping and reducing agents. The addition of Ag^+ ions was first reported to help produce Pt octahedra in high yields.[187] It was proposed that Ag atoms would preferentially passivate Pt{100} facets. The deposited Ag was then replaced by Pt through galvanic replacement, facilitating the growth of Pt along ⟨100⟩ directions. Later on, several other methods were developed for Pt octahedra (Figure 13E), including the addition of metal carbonyl, where the metal atoms and CO generated from decomposition served as the shape-directing agent and reductant, respectively.[35,191] By employing glucose as a reducing agent and cetyltrimethylammonium bromide (CTAB) or CTAC as a capping agent, Pt octahedra in high purity were obtained during the reduction of a Pt(IV) precursor.[34] Interestingly, by tuning the amount of glucose and reaction time, Pt nanocrystals in the shape of cuboctahedron, cube, and concave cube could also be produced, revealing the generality of this protocol. When glucose was used at a relatively low concentration, the surface diffusion rate of Pt atoms overwhelmed the deposition rate and the thermodynamically favored octahedron was obtained due to the lower surface energy of {111} facets. By increasing the amount of glucose, the faster deposition rate relative to that of diffusion, together with the preferential growth from corners and edges, resulted in the formation of concave cubes. The use of a fixed reaction system eliminated the influence of surface contamination, making it more accurate to compare the catalytic performance of nanocrystals bounded by different facets.

Decreasing the size of nanocrystals is an effective strategy to optimize their mass-specific activities by increasing the specific surface area. Recently, a modified protocol was reported for the synthesis of Pt octahedra with sizes below 10 nm.[216] The method involved a simple reaction system, where Na_2PtCl_6 was mixed with PVP in an aqueous solution and heated at 90 °C for 48 h. Here PVP served as both a stabilizer and a mild reducing agent due to its hydroxyl end groups. Pseudospherical, single-crystal seeds were observed at the early stage of a synthesis, which further evolved into octahedra for the expression of the thermodynamically favored {111} facets.

Recently, the utilization of citrate ions further decreased the size of Pt octahedra down to 7 nm.[217] Combined with seed-mediated growth, Pt octahedra were synthesized with tunable sizes ranging from 7−18 nm. In a typical protocol, Pt seeds were first prepared by reducing H_2PtCl_6 with $NaBH_4$ in the presence of CA and sodium citrate. The seeds were then mixed with additional H_2PtCl_6, AA, and sodium citrate, and reacted at 105 °C to enable their growth into an octahedral shape. Previous DFT simulations have demonstrated that citrate ions in an aqueous solution could adsorb onto the Pt(111) surface with three dehydrogenated carboxylic groups in a bidentate configuration, enabling the passivation of {111} facets on Pt octahedra.[144] It was shown that other parameters such as the moderate reaction temperature and the resultant low rate of reduction also played an important role in promoting the formation of an octahedral shape.[217]

In the case of Pt tetrahedra, the first report was based on a synthetic protocol similar to that for cubes, where K_2PtCl_4 was reduced by H_2 gas in the presence of sodium polyacrylate.[182,183] Compared to cubes, a higher concentration of sodium polyacrylate was needed for tetrahedra in order to stabilize the Pt{111} facets. A similar trend was also observed when the capping agent was switched to PVP, and Pt tetrahedra were found to prevail over cubes at a higher concentration of PVP.[226] Besides, inspired by biomolecules that can specifically recognize a chosen surface, a peptide in the sequence of Ac−Ser−Ser−Phe−Pro−Gln−Pro−Asn−$CONH_2$ (termed S7) was used as a capping agent for the production of Pt tetrahedra.[141] The formation of the tetrahedral shape could be attributed to the favorable interaction between the peptide and the atoms on {111} facets. However, the uniformity and purity of the tetrahedral samples still need to be improved.

4.1.2.6. Gold. As reported in one EG-based synthesis of Au octahedra, poly(diallyldimethylammonium) chloride (PDDA), a cationic surfactant, was effective in stabilizing Au{111} facets.[219] The size of the octahedra could be tailored in the range of 20−320 nm by introducing an acid or base into the reaction solution to control the reduction rate of $HAuCl_4$, and the yield could reach as high as 95%. Interestingly, although the presence of PDDA was essential to the production of Au octahedra, changes to their concentration did not pose an impact on the purity of the product. It was observed that Au octahedra could be produced in high yield within a broad range of PDDA concentration (5−125 mM). Based on the results from a set of characterizations, the authors suggested that PDDA formed a stable pair with $AuCl_4^-$ precursor and decreased the reduction rate, which was one possible reason for the formation of Au octahedra. In addition to the polyol route, Au octahedra were also synthesized in an aqueous system with the assistance of CTAB.[220] It was reported that Au octahedra as small as 52.3 nm could be obtained with AA serving as a reducing agent, CTAB as a shape-directing agent, and H_2O_2 as a reaction promoter under sonication at 40 °C. Here, the H_2O_2 acted as an activator to prompt the release of electrons from AA and thus the reduction of $HAuCl_4$.

Besides one-pot synthesis, Au octahedra could also come from seed-mediated growth. Using Au spheres as seeds, the shape evolution of the Au nanocrystals to cubes, cuboctahedra, and finally octahedra with different sizes was observed in a growth solution containing PVP and $HAuCl_4$, as the amount of Au(III) precursor was increased.[196,197] Even Au nanocrystals with an anisotropic shape, such as rods, could serve as seeds to produce octahedra through a reshaping process conducted under sonication in the presence of PVP.[218]

As discussed in section 4.1.1, Au cubes could be synthesized by reducing $HAuCl_4$ with EG in the presence of PVP and $AgNO_3$.[32] This protocol was also used to produce Au tetrahedra by simply eliminating the addition of $AgNO_3$ while varying the concentrations of $HAuCl_4$ and PVP. The formation of tetrahedra was attributed to the capping effect of PVP toward Au{111} facets. The seed-mediated growth could also be applied to the synthesis of Au tetrahedra. Starting from Au spherical nanocrystals, tetrahedra were produced by inducing unsymmetrical growth through the careful manipulation of the reaction kinetics (Figure 13F).[227] In particular, the slow addition of precursor solution and the use of CTAB and CTAC at appropriate concentrations are crucial to the formation of Au tetrahedra in high purity.

4.1.3. Rhombic Dodecahedra.

A RDD is covered by 12 congruent rhombic side faces terminated in {110} facets. Compared with cube and octahedron, there are much fewer reports on the synthesis of RDD, mainly due to the high surface energy of {110} facets and the lack of capping agents for this type of facet. To the best of our knowledge, there are only reports on the synthesis of Pd and Au nanocrystals taking this unique shape, despite the enigma about the growth mechanism. Figure 14 shows scanning electron microscopy (SEM) and TEM images of several typical examples of Au nanocrystals in the shape of RDD.

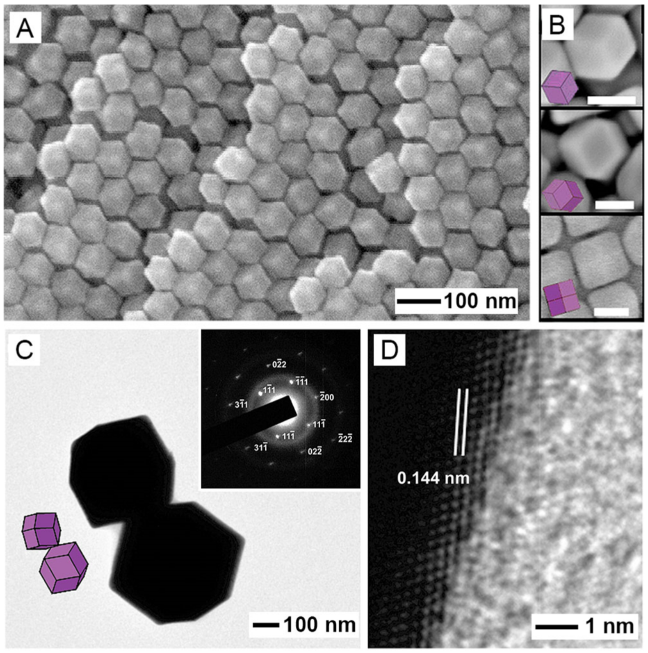

Figure 14. (A) SEM image of an ordered assembly of Au RDD. (B) SEM images and the corresponding models of Au RDD viewed from different orientations (scale bars: 50 nm). (C) TEM image of Au RDD. The insets show models of two RDD and the selected area electron diffraction (SAED) pattern, which can be indexed to the diffraction spots along the [011] zone axis. (D) High-resolution TEM image of a Au RDD showing the exposed {110} planes with a *d*-spacing of 0.144 nm. (A) Reprinted with permission from ref 229. Copyright 2009 American Chemical Society. (B) Modified with permission from ref 230. Copyright 2011 American Chemical Society. (C and D) Modified with permission from ref 231. Copyright 2009 American Chemical Society.

4.1.3.1. Palladium. To synthesize Pd RDD, the choice of a proper capping agent and reaction temperature is of great significance. In one synthesis, Pd cubes were used as seeds and Pd atoms reduced from H_2PdCl_4 were deposited onto them in the presence of CTAB and KI.[165,228] A medium concentration of KI and a relatively high temperature were necessary for the generation of RDD, and it was believed that the growth mechanism was closely related to a synergistic capping effect arising from CTAB and I^- ions. Additionally, Pd RDD could also be produced through the reduction of Na_2PdCl_4 in an aqueous solution containing PVP and glucose, with no additional capping agent added.[384] A further investigation is needed in order to elucidate the formation mechanism of RDD enclosed by {110} facets.[385]

4.1.3.2. Gold. Gold RDD could be obtained from both seed-mediated growth and one-pot synthesis. For example, using single-crystal Au seeds capped by cetylpyridinium chloride (CPC), Au RDD were obtained after growth in a solution containing $HAuCl_4$, AA, and CPC (Figure 14A).[229] The generation of RDD could be ascribed to both the selective stabilization of {110} facets by CPC and the well-regulated growth kinetics. It was suggested that a lower concentration of CPC and a higher concentration of AA favored the production of RDD because $AuCl_4^-$ tended to be reduced on {111} facets, resulting in the disappearance of {111} facets and formation of {110} facets. In contrast, when a high concentration of CPC and a low concentration of AA were used, Au octahedra were obtained due to the stronger capping of CPC on {111} than {110} facets. In another seeded growth method, RDD were synthesized with the assistance of CTAC and a low concentration of Ag^+ ions to stabilize the {110} facets (Figure 14B).[230] The final product contained a mixture of RDD and bipyramids, both enclosed by {110} facets. It was proposed that Ag^+ ions played a critical role during the synthesis because Ag could deposit on these {110} facets through underpotential deposition (UPD), preventing the further growth of Au atoms on these facets for the generation of nanocrystals enclosed by {110} facets.

Besides the seed-mediated growth, several other studies also suggested that Au RDD could be obtained through one-pot synthesis. An early report claimed that Au RDD could be obtained in a one-pot synthesis without the involvement of additional surfactant (Figure 14C,D).[231] The reaction mixture only contained $HAuCl_4$ as the precursor and DMF as both the reductant and solvent. In a typical synthesis, the mixture of the two chemicals were heated in oven at 90−95 °C for 15 h, followed by centrifugation to collect the solid product. The Au RDD possessed sharp corners and edges, with an average edge length of about 200 nm. Since the reducing power of DMF is dependent on temperature, the choice of a proper reaction temperature could facilitate the formation of this unique structure. In this case, the formation of Au RDD was attributed to a kinetically controlled reduction process at a relatively low temperature which resulted in a slow rate of crystal growth. Although the authors claimed that no additional capping agent was added into the reaction mixture, they did not rule out the possibility that the shape formation of RDD could be contributed by the stabilization effect from DMF or its oxidation products.

4.1.4. Plates and Sheets.

As a two-dimensional (2-D) structure, a plate is characterized by a much greater area for the basal planes relative to that of the side faces. When the thickness of a plate is reduced to several atomic layers, the 2-D structure is often referred to as a sheet. Most of the reported plates and sheets contain planar defects parallel to their basal planes (see section 4.2.4). However, there are a few exceptions that feature a single-crystal structure. The absence of planar defects can be largely attributed to the following two factors: (i) the ultrathin thickness (e.g., only a few atomic layers) that prevents the inclusion of planar defects and (ii) the use of seed-mediated growth and the involvement of single-crystal seeds. Figure 15 shows TEM images of some typical examples of noble-metal nanocrystals with a plate- or sheet-like shape while featuring a single-crystal structure.

4.1.4.1. Rhodium. Compared with other noble metals, there are more reports on the synthesis of Rh sheets with a single-crystal structure. The sheets typically take irregular shapes, rather than the triangular or hexagonal shapes commonly observed for plates made of fcc metals. In one study, it was reported that Rh sheets could be synthesized in the shape of rhomboids under the confinement of CO (Figure 15A).[232] The sheets took a single-crystal structure, together with basal planes terminated in {111} facets. Their average edge length could be increased up to 1 μm by increasing the pressure of CO. According to the atomic-resolution TEM image recorded from the side face of a sheet, the atoms took a regular

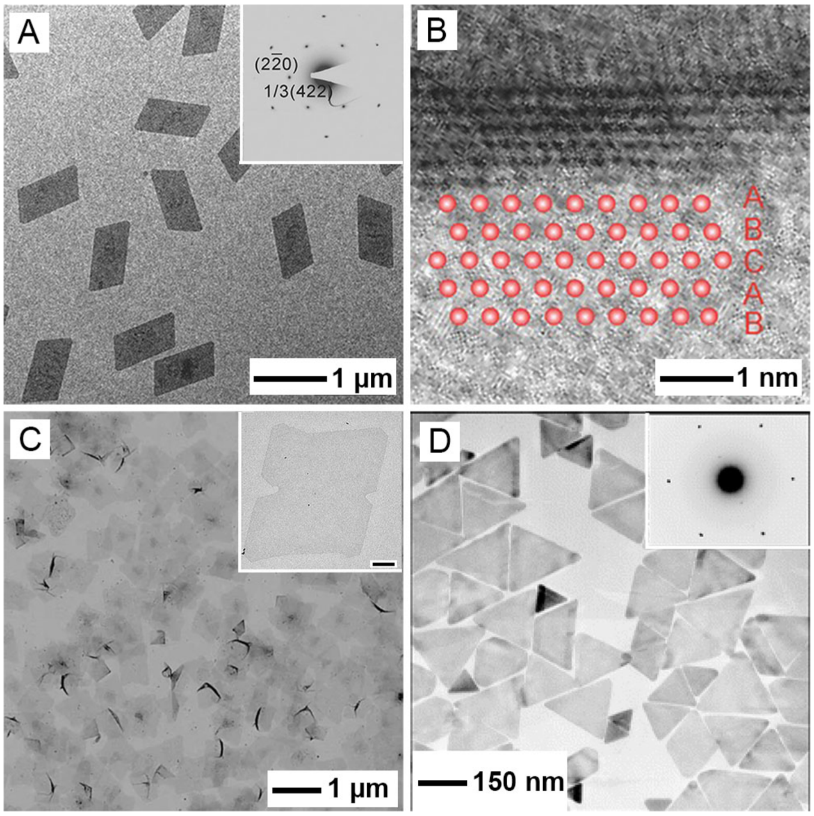

Figure 15. (A) TEM image of the single-crystal Rh sheets with the SAED pattern shown in the inset. (B) High-resolution TEM image of the cross-section of a Rh sheet, showing ABCAB stacking sequence along the [111] direction. (C) TEM image of Rh sheets with the thickness being reduced to one atomic layer. The inset shows the TEM image of a single sheet at higher magnification (scale bar: 100 nm). (D) TEM image of Au triangular plates, with the SAED pattern shown in the inset, confirming that the plates had a single-crystal structure, with the top and bottom faces enclosed by {111} facets. (A and B) Reprinted with permission from ref 232. Copyright 2015 Wiley-VCH. (C) Reprinted with permission from ref 233. Copyright 2014 Nature Publishing Group. (D) Reprinted with permission from ref 235. Copyright 2005 American Chemical Society.

arrangement without showing any disorder (Figure 15B). It is worth pointing out that although the 1/3{422} reflection spots were observed in the SAED pattern, their presence was attributed to the thin thickness of the sheet preventing the extinction to occur. With the assistance of PVP as a stabilizer, the thickness of Rh sheets could be further reduced down to one atomic layer (Figure 15C).[233] The shape of the final product also became more uniform, typically appearing as rhomboids with several notches at the edges. The single-atomic-layer thickness not only exposes all of the atoms on the surface but also changes the bonding strength among the atoms, giving rise to enhancement in catalytic activity (see section 6.3).

4.1.4.2. Gold. One compelling example demonstrating the synthesis of single-crystal Au plates was based on seed-mediated growth. In one report, triangular plates could be grown from the Au seeds prepared by reducing $HAuCl_4$ with $NaBH_4$ in the presence of trisodium citrate (Figure 15D).[235] The growth step led to the formation of plates with an average edge length of 144 nm. Employing the as-obtained plates as seeds, Au plates with edge lengths up to 300 nm were also obtained with the addition of more Au(III) precursor.[234] The single-crystal nature of the plates was verified by electron diffraction, with the basal planes and side faces indexed as {111} and {211} facets, respectively.

4.1.5. Conclusion. The formation of single-crystal nanocrystals with well-defined shapes, such as cubes, octahedra, and RDD, typically requires the following conditions: (i) the presence of oxidative etching for eliminating the formation of seeds with twin defects and stacking faults; (ii) fast reduction kinetics for generating single-crystal seeds, and this can be achieved by manipulating reaction temperature and the concentration/chemical activity of the precursor and reductant; and (iii) introduction of a capping agent to selectively passivate a certain type of facet to promote its exposure on the surface. Both the amount and strength of the capping agent play a critical role in directing the shape evolution process.

4.2. Nanocrystals with Planar Defects

Both twin plane and stacking fault are planar defects commonly observed in crystals made of an fcc metal. A twin plane refers to a plane across which the atoms are arranged in a mirror image of each other. On the other hand, stacking fault represents a short-range disruption in the ideal stacking sequence in a crystal lattice. The formation of these defects usually starts in the stage of seed formation, during which the nuclei evolve into seeds featuring single-crystal, singly twinned, multiply twinned, or lined with stacking faults, respectively. Subsequently, these seeds grow into nanocrystals with specific shapes and thus surface structures. The formation of different types of defects has a strong correlation with the reduction kinetics,[69] which will be emphasized in the following sections. Our presentation is based on the type of defect, following the order of singly twinned, multiply twinned, and stacking fault-lined.

4.2.1. Bipyramids and Beams Containing a Single Twin Plane. A bipyramid can be regarded as a base-to-base integration of two pyramids through the inclusion of a twin plane that passes through the center of the bipyramid. Similarly, a one-dimensional (1-D) nanostructure with a single twin plane running along the longitudinal axis is referred to as a beam (Figure 16A). The synthesis of such nanocrystals can be achieved either through a one-pot method or using seed-mediated growth. It is worth noting that in seed-mediated growth, the number of planar defects in bipyramids could be more than one depending on the exact defect structure of the seeds. Here we only focus on the synthesis of bipyramids and beams possessing a single twin plane and those characterized with multiple twin planes will be discussed in section 4.2.5. Figure 16B−E shows TEM images of some typical examples of noble-metal nanocrystals featuring a bipyramidal or beam-like shape.

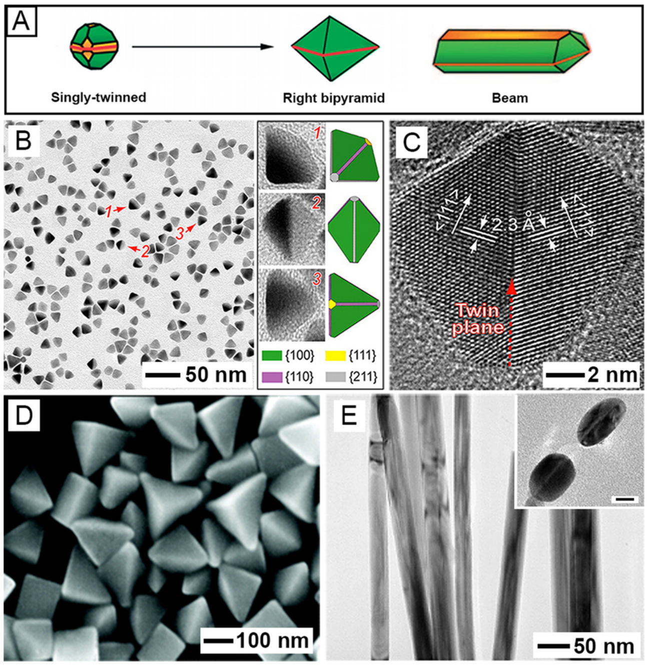

Figure 16. (A) Schematic illustrating the formation of RBP and beam from seeds with a single twin plane. (B) TEM image of Pd RBPs and models of RBPs in three common orientations. (C) High-resolution TEM image of a Pd RBP showing a twin plane in the structure. (D) SEM image of Ag RBPs. (E) TEM image of Ag beams, with the inset showing its cross section with the presence of a twin plane parallel to the basal plane. The scale bar in the inset is 20 nm. (A) Modified with permission from ref 28 and 385. Copyrights 2009 and 2007 Wiley-VCH, respectively. (B and C) Modified with permission from ref 71. Copyright 2013 American Chemical Society. (D) Reprinted with permission from ref 116. Copyright 2006 American Chemical Society. (E) Reprinted with permission from ref 239. Copyright 2006 American Chemical Society.

4.2.1.1. Palladium. Most Pd bipyramids exist in the form of RBP, which is a special case of the bipyramidal system. In a RBP, two trigonal pyramids are joined base-to-base in a mirror image, with all of the side faces being right isosceles triangles terminated in {100} facets. Compared with a cube that has the same edge length and is also enclosed by {100} facets, a RBP shows a 33% greater surface-to-volume ratio, making it a favorable structure for catalysis. In a typical synthesis of Pd RBPs, Na_2PdCl_4 was reduced by EG in the presence of PVP and NaI, with the latter serving as both an oxidative etchant and a capping agent (Figure 16B,C).[71] A moderate oxidative etching was necessary for the production of singly twinned nanocrystals. A stronger level of oxidative etching induced by a high concentration of NaI or oxygen atmosphere resulted in the dominance of single-crystal products, while a weaker level caused by decreasing the concentration of I^- or purging the solution with Ar gas led to the survival of multiply twinned particles.[237]

Another bipyramidal structure similar to RBP but with side faces covered by {111} facets is known as bitetrahedron. Up until now, there is only one report on the synthesis of Pd bitetrahedra with truncated vertices.[236] The typical synthesis involved the reduction of K_2PdCl_4 in EG with the assistance of PVP and $RuCl_3$. The atomic percentage of Ru in the final products was negligible (0.6%), making them suitable to be considered as monometallic Pd nanocrystals. The six side faces and other two located at the top and bottom were all confirmed to be {111} facets, and a single twin plane was located at the center, illustrating that the shape of the products could be regarded as two truncated tetrahedra joining together face-to-face.

4.2.1.2. Silver. In the polyol synthesis of Ag cubes, RBPs were often observed as a byproduct, albeit it was a challenging task to significantly improve the yield.[171,179] By replacing NaCl with NaBr in the EG-based process for the synthesis of Ag cubes, it was demonstrated that Ag RBPs could be prepared at a yield of 80% (Figure 16D).[116] Similar to the preparation of Pd RBPs, the Br^- ions played a critical role in the formation of Ag RBPs because of their moderate oxidative etching power. The multiply twinned seeds formed in the early stage of a synthesis were more susceptible to oxidative etching and thus would be preferentially etched away, while the singly twinned seeds were retained for the formation of RBPs. In contrast, when Cl^- ions with a stronger oxidative etching power were used for the synthesis, all of the twinned seeds would be etched away, leading to the generation of single-crystal products.

Silver beams could be produced by slightly modifying the polyol process developed for the synthesis of Ag RBPs (Figure 16E).[239] By doubling the concentrations of $AgNO_3$ and PVP while lowering the reaction temperature, the singly twinned seeds formed in the initial stage would adopt an anisotropic growth mode under slow reduction kinetics, generating nanoscale beams instead of RBPs. The length of the as-obtained Ag beams could reach up to 30 μm, with widths ranging in 17−70 nm and a width-to-thickness ratio of 1.4.

4.2.1.3. Platinum. Similar to the synthetic method developed for Pt tetrahedra in section 4.1.2, peptides were also employed to synthesize Pt bipyramids covered by either {100} or {111} facets. It was reported that BP7A (Ac-Thr-Leu-His-Val-Ser-Ser-Tyr-$CONH_2$), a Pt-binding peptide, could induce the formation of singly twinned seeds and stabilize them in an aqueous solution at room temperature.[238] During the following step, by introducing T7 (Ac-Thr-Leu-Thr-Thr-Leu-Thr-Asn-$CONH_2$) and S7 (Ac-Ser-Ser-Phe-Pro-Glu-Pro-Asp-$CONH_2$) as the capping agents in the seed-mediated growth, Pt bipyramids enclosed by {100} and {111} facets, respectively, were obtained.

4.2.1.4. Gold. Using the same protocol developed for the synthesis of Au RDD (see section 4.1.3), {110}-covered Au bipyramids were produced.[230] The as-obtained bipyramid was consisted of two irregular tetrahedra enclosed by {110} facets, and the two tetrahedra joined together through their {111} basal planes. The single twin plane was well resolved under high-resolution TEM. Even though the product was a mixture of twinned bipyramids and single-crystal RDD, the purity could be improved by filtration due to their large difference in size. Further analysis on the seeds suggested that both singly twinned and single-crystal seeds were formed in the initial stage of a synthesis, which then evolved into bipyramids and RDD, respectively.

4.2.2. Decahedra and Icosahedra. These two shapes share a lot of similar features in terms of surface structure, including the exposure of {111} facets on the surface and the presence of 5-fold twinning and tensile strain (Figures 17A and 18A).[60,61] Recent studies involving both experimental and computational methods showed that the presence of twin boundaries and tensile strains on the surface could greatly improve the catalytic activity of the metal nanocrystals toward some reactions.[386,387] To this end, understanding the growth mechanisms for these two structures can help us design more active catalysts in a rational way. Figures 17 and 18 show TEM and SEM images of some typical examples of noble-metal nanocrystals featuring decahedral and icosahedral shapes, respectively.

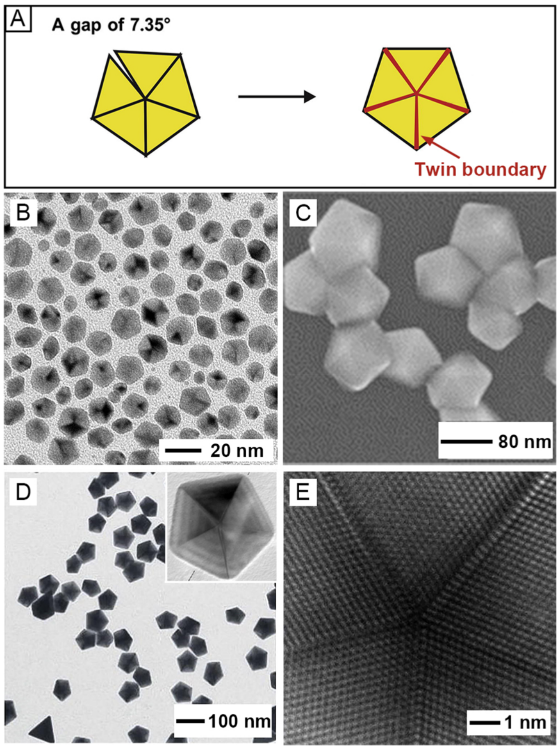

Figure 17. (A) Schematic showing a decahedron assembled from five single-crystal, tetrahedral units. A gap of 7.35° was left behind, causing disorder in the twin boundaries and a tensile strain on each side face. (B) TEM image of Pd decahedra. (C) SEM image of Ag decahedra. (D) TEM image of Au decahedra, with inset showing an individual nanocrystal at higher magnification. (E) High-resolution TEM image recorded from the center of a Au decahedron, clearly showing the five twin boundaries in the structure. (A) Modified with permission from ref 61. Copyright 2019 Elsevier. (B) Reprinted with permission from ref 242. Copyright 2014 American Chemical Society. (C) Reprinted with permission from ref 224. Copyright 2006 Elsevier. (D and E) Reprinted with permission from ref 102. Copyright 2006 Wiley-VCH.

4.2.2.1. Copper. Different from other noble metals, it remains a major challenge to synthesize Cu nanocrystals with a penta-twinned structure because of the high susceptibility of Cu to oxidation, which makes it easier for oxygen to dissolve the twinned Cu seeds formed in the nucleation step.[389] To our knowledge, no regular Cu decahedra or icosahedra has been reported so far. A recent report described the successful synthesis of Cu decahedra with a star-like shape and characterized by 5-fold twinning.[240] In a typical synthesis, Cu(acac)$_2$ was reduced with AA in the presence of OAm. To attain the twinned structure, a slow growth rate was desired, which was achieved using a weak reducing agent and a relatively low temperature of 130 °C. Before heating, the solution was sonicated for a few minutes to remove the O$_2$ trapped in the solvent. Further characterizations revealed that the nanocrystals had a penta-twinned structure with the angles between two adjacent twin boundaries measured to be 71.5−72.5°, consistent with those in a decahedron. Tensile strains were observed for surface atoms near the edge of the decahedron, as well as the twin boundaries, while compressed strains were observed at the center. The tensile strains played an important role in increasing the binding of CO intermediates, contributing to a high selectivity for C$_{2+}$ products during the electrochemical reduction of CO$_2$ (see section 7.6).

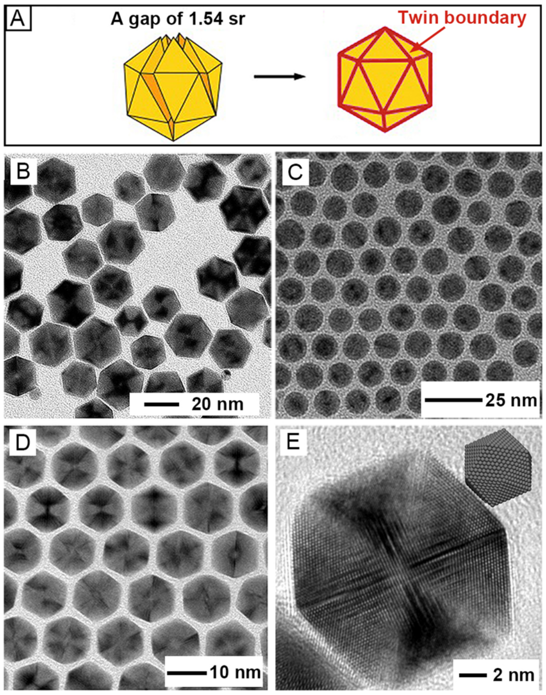

Figure 18. (A) Schematic of an icosahedron, which can be dissected as an assembly of 20 densely packed single-crystal, tetrahedral units. Again, a gap of 1.54 steradians (sr) results in disorder in the twin boundary and a tensile strain on each side face. (B and C) TEM images of Pd and Ag icosahedra, respectively. (D) TEM and (E) high-resolution TEM images of Pt icosahedra, with the inset showing the corresponding atomic model of the nanocrystal. (A) Modified with permission from ref 388. Copyright 2015 Wiley-VCH. (B) Reprinted with permission from ref 242. Copyright 2014 American Chemical Society. (C) Reprinted with permission from ref 250. Copyright 2018 Wiley-VCH. (D and E) Reprinted with permission from ref 253. Copyright 2013 American Chemical Society.

4.2.2.2. Rhodium. Similar to other noble metals, the key requirements for the formation of decahedral Rh nanocrystals are the elimination of oxidative etching and appropriate reduction kinetics. An early report demonstrated the synthesis of Rh starfish-like nanocrystals using a chloride-free precursor to avoid oxidative etching.[390] Although the exposed facets were not well-defined, the 5-fold twinning was clearly resolved from TEM images. Inspired by this work, a recent study reported the successful synthesis of Rh decahedra with a regular shape and sharp corners.[241] By leveraging TTEG as both a solvent and a mild reducing agent and $Rh(acac)_3$ as the precursor, the reduction rate could be well regulated while the twinned nanocrystals could be protected from etching. It was suggested that a moderate reduction rate was important for the formation of Rh decahedra. A faster reduction rate would result in the formation of single-crystal structures while a slower rate favored the formation of Rh icosahedra. Moreover, the use of PVP with a relatively low molecular weight (10 kDa) and at a high concentration contributed to the uniformity of the Rh decahedra.

The Rh icosahedra were first observed in an early study that was systematically investigating the influence of different types of polyols and metal precursors on the shapes of Rh nanocrystals.[104] It was proposed that the anionic ligand of the metal precursor largely determined the morphology of Rh nanocrystals while the solvent posed an effect on the uniformity. In the case of Rh icosahedra, the synthesis relied on the use of rhodium(II) trifluoroacetate dimer, $Rh_2(TFA)_4$, as a precursor, and EG as the solvent. The resultant Rh icosahedra had an average size of 4−5 nm. It is difficult to synthesize Rh icosahedra in larger sizes, which could be mainly attributed to the increased strain associated with enlarged icosahedra. Rh icosahedra with larger size up to 12 nm were obtained in a most recent study that used $Rh(acac)_3$ as a precursor, PVP as a reducing agent and colloidal stabilizer, and benzyl alcohol as a solvent.[249] Similarly, the reduction rate has to be controlled by varying the coordination ligand in Rh(III) precursor, as well as the molecular weight of PVP, to achieve the optimal kinetics for the generation of icosahedra.

4.2.2.3. Palladium. Due to the sharing of a number of features, decahedra and icosahedra usually appear in the same batch of synthesis for Pd nanocrystals. Therefore, finely tuning the reduction kinetics has become a key factor in obtaining each multiply twinned nanocrystal in high purity.[242] The typical synthesis of Pd decahedra involved the injection of Na_2PdCl_4 into a mixture of Na_2SO_4, PVP, and DEG. It was found that Na_2SO_4 could speed up the reduction of Pd(II) precursor by enhancing the reducing power of DEG, and a relatively faster reduction rate favored the formation of decahedral seeds (Figure 17B). By substituting Na_2SO_4 with HCl, which reduced the pH of the reaction solution and increased the difficulty of reducing $PdCl_4^{2-}$ complex, the resultant slow reduction kinetics led to the generation of Pd icosahedra (Figure 18B).

4.2.2.4. Silver. Although decahedral seeds were commonly observed in the synthesis of Ag nanocrystals, only a few studies reported the generation of Ag decahedra, probably due to the tendency for these seeds to further grow into rods or wires with a pentagonal cross section.[273,281] Using the DMF reduction route previously discussed in section 4.1.2 for the synthesis of Ag tetrahedra, in which $AgNO_3$ was reduced in DMF in the presence of PVP, decahedra could be produced with a purity of 70% when the molar ratio of PVP to $AgNO_3$ was set to 1:1 (Figure 17C).[224] It was proposed that the Ag decahedron was assembled from five tetrahedral units in a step-by-step fashion. However, based on detailed TEM and SEM analyses of the products, it was later demonstrated that the Ag decahedron was formed through the stepwise growth of tetrahedral units on specific facets, instead of the assembly of tetrahedral units formed separately.[244]

In the case of Ag icosahedra, most of the reported protocols were based on the organic-phase synthesis. In an early report, Ag icosahedra with diameters of 11 and 14 nm were produced through the decomposition of CF_3COOAg in *o*-dichlorobenzene (ODCB) or isoamyl ether in the presence of OAm.[177] However, the products turned out to be a mixture of icosahedra and decahedra. The protocol was later refined to produce uniform icosahedra with tunable sizes by adjusting the molar ratio between the Ag(I) precursor and the reducing agent, reaction time, and temperature (Figure 18C).[250] Another modified polyol method was also developed to synthesize Ag icosahedra in high purity, in which $AgNO_3$ was reduced in a mixture of 1,2-hexadecanediol, 4-*tert*-butyl toluene, and OAm.[391] Although notable size variations were observed in the as-obtained icosahedra, the size distribution could be narrowed after digestive ripening post treatment. Similarly, it was reported that the reduction of $AgNO_3$ in OAm, which acted as both the solvent and reductant, under N_2 atmosphere at an elevated temperature resulted in the formation of Ag icosahedra.[251]

4.2.2.5. Platinum. For the synthesis of Pt decahedra and icosahedra, slow reduction kinetics plays a key role in generating multitwinned seeds at the beginning of a synthesis. To our knowledge, until now there is only one report on Pt decahedra, in which icosahedra were also produced by simply changing the type of Pt(II) precursor.[245] In a typical protocol, Pt(II) complexes in the form of Magnus' green salt (MGS, $[Pt(NH_3)_4][PtCl_4]$) and methylamine-substituted Magnus' green salt (MSMGS, $[Pt(CH_3NH_2)_4][PtCl_4]$) were reduced by OAm to generate Pt decahedra and icosahedra, respectively. The insolubility of the Pt(II) precursor in OAm resulted in the formation of a solid−liquid interface and an extremely low concentration of Pt(II) species in the solution. This greatly slowed down the reduction of Pt(II) precursor so that 1 week was needed to complete the reaction, leading to the generation of multitwinned seeds for their growth into decahedral or icosahedral nanocrystals.

In addition to the method involving solid−liquid-interface-mediated reduction, Pt icosahedra can also be synthesized in other ways. In one example, $Pt(acac)_2$ was mixed with dodecylamine (DDA), OA, diphenyl ether (DPE), and $Y(acac)_3$, followed by heating under a CO atmosphere.[253] The protection from oxidative etching by CO, which helped preserve the multitwinned seeds, and the synergistic effect from CO, $Y(acac)_3$, and long-chain amines both contributed to the formation of icosahedral nanocrystals in high yields (Figure 18D,E). A similar method involving the reduction of $Pt(acac)_2$ by $Mn_2(CO)_{10}$ was also reported, and a purity approaching 98% was achieved for Pt icosahedra after a purification process.[35] In another example, a simple and fast synthesis of Pt icosahedra was reported by reducing $Pt(acac)_2$ in TTEG, with PVP serving as a stabilizer.[252] The slow reduction of the Pt(II) precursor caused by the mild reducing power of TTEG contributed to the formation of a multiply twinned structure. By tuning the amount of the Pt(II) precursor or introducing additional AA, icosahedral nanocrystals with size varying from 7−25 nm were obtained.

4.2.2.6. Gold. The synthesis of Au decahedra was first reported in 2006 by modifying a protocol previously developed to prepare Ag nanocrystals,[392−394] in which $HAuCl_4$ was reduced by DMF in the presence of small Au nanoparticles that served as seeds (Figure 17D,E).[102] Ultrasonication was key to the growth of Au nanoparticles into uniform decahedra in a high yield because of the noticeably elevated temperature. Afterward, the same group demonstrated that truncated decahedra could be obtained when the seeds were replaced with penta-twinned Au rods.[247] In another report, by introducing foreign Cu(II) ions into the growth solution, the Au seeds could grow into rods, cuboids, and finally decahedra as the concentration of Cu(II) ions was increased.[246] It was proposed that the Cu(II) ions could selectively retard the growth rate of the {111} facets and thus direct the shape evolution. Besides the seeded growth, the synthesis of Au decahedra could also be achieved through a one-pot polyol route, in which $HAuCl_4$ was reduced by DEG with PVP serving as a stabilizer.[254] Importantly, the concentration of PVP should be high enough (up to 360 equiv of the Au(III) precursor) to protect the multiply twinned seeds from oxidative etching, giving rise to the formation of decahedra.

In the case of Au icosahedra, the synthesis was achieved by slightly modifying the protocols for Au tetrahedra and decahedra.[32] As discussed in section 4.1.2, when the synthesis of Au tetrahedra was conducted using a polyol method, Au icosahedra could also be obtained by simply reducing the concentration of the Au(III) precursor to 80% of that used for tetrahedra.[32] The decrease in precursor concentration and thus the reduction rate contributed to the formation of the multiply twinned icosahedra. In another example, it was found that Au icosahedra were produced when following the protocol developed for the synthesis of decahedra, except that the concentration of PVP was significantly reduced, suggesting that icosahedra were more stable at a lower concentration of PVP.[254] Gold icosahedra with a size of 18 nm were also synthesized in high yield through an aqueous route, in which $HAuCl_4$ was reduced with *N*-vinylpyrrolidone (NVP), a precursor to an effective reductant and stabilizer.[395] Furthermore, synthetic protocols based on hydrothermal method[255] and decomposition of Au(I) halides[103] have been reported.

4.2.3. Penta-Twinned Rods and Wires.

Similar to decahedra and icosahedra, penta-twinned rods and wires also contain multiple twin defects. The rods and wires have a pentagonal cross-section, with the two ends covered by ten {111} and the five side faces terminated in {100}.[42] The easiest way to distinguish these 1-D structures with their single-crystal counterparts is to resolve their cross-section. Single-crystal rods and wires usually have a rectangular or octagonal cross section, while their penta-twinned counterparts typically have a pentagonal cross section.[295] Because the focus of this review article is on the surface structures of metal nanocrystals, here we only present a discussion on the methods and principles for shape control, rather than on their aspect ratios and fascinating optical properties. Figure 19 shows TEM images of some typical examples of penta-twinned rods and wires made of various noble metals.

4.2.3.1. Copper. Penta-twinned wire is one of the most commonly observed morphologies among Cu nanocrystals, not only as the targeted product but also as a byproduct of most syntheses. Generally speaking, a relatively low reduction rate of the Cu(II) precursor and the presence of capping agent(s) capable of blocking {100} facets are required for the synthesis of Cu wires. It was reported that, by using HDA as a capping agent and glucose as a reducing agent, Cu wires with a high purity and a diameter below 20 nm could be produced (Figure 19B).[262] Removal of O_2 was regarded as an important factor in producing the ultrathin wires as it contributed to the generation of a large number of penta-twinned seeds in the initial stage of a synthesis while protecting the ends of the wires from being oxidized and blocked by O_2.[262] When the temperature was reduced and the concentration of glucose was doubled, tadpole-like Cu wires with a penta-twinned structure were obtained.[153] The high concentration of reductant led to the generation and consumption of a large number of Cu atoms at the beginning of the synthesis, forming decahedral seeds with a relatively large size. As the synthesis proceeded, the reduction rate dropped with the decreasing amount of glucose, resulting in the formation of tapered rods and wires with "tails".

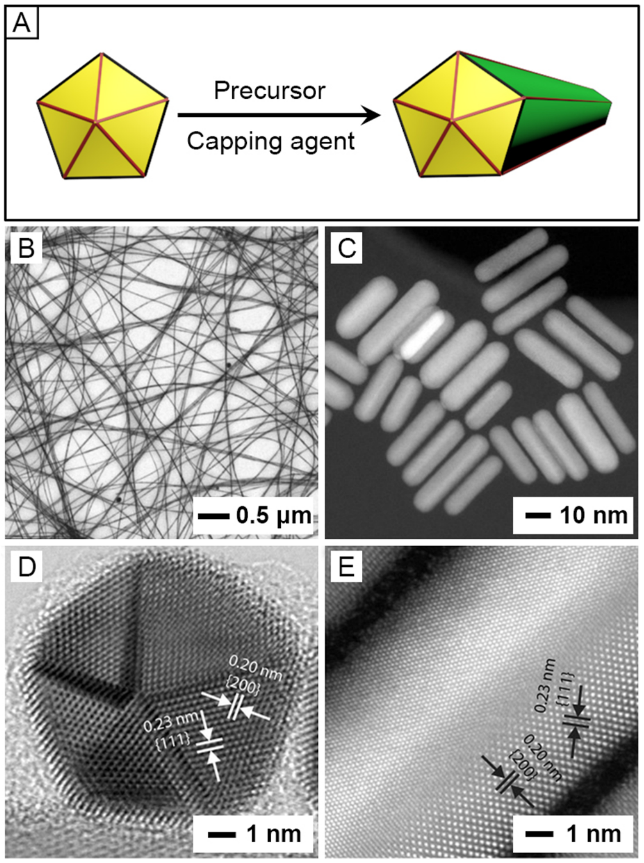

Figure 19. (A) Schematic illustration showing the formation of a penta-twinned rod and then wire from a decahedral seed. (B) TEM image of Cu wires with a diameter below 20 nm. (C) HAADF-STEM image of Pd rods. (D) High-resolution TEM image taken from one of the ends of a Pd rod along the ⟨110⟩ direction. (E) High-resolution TEM image captured from the edge of a middle portion of a Pd rod. (B) Reprinted with permission from ref 262. Copyright 2017 Wiley-VCH. (C–E) Reprinted with permission from ref 267. Copyright 2015 Wiley-VCH.

The presence of HDA also played an important role in the evolution of Cu wires, and its role was usually discussed in the context of selective binding to Cu{100} facets for the formation of nanocrystals enclosed by these facets. However, this assumption was challenged in recent years and it was proposed that the disruption of HDA layer on {111} facets by Cl^- ions was the main reason responsible for the selective passivation of {100} facets.[263] When fixing the amount of HDA and increasing the concentration of Cl^-, Cu nanocrystals with shapes varying from cube and cuboctahedron, wire, and finally a javelin shape were obtained. The authors conducted single-crystal electrochemical measurements and demonstrated that by increasing the amount of Cl^-, the HDA layer would be increasingly disrupted on none of the surfaces, the (111) surface only, and both (100) and (111) surfaces. This led to the deposition of Cu atoms with no preference on both surfaces, preferentially on (111) surface, and on both (111) and (100) surfaces, respectively. Besides, based on DFT calculations, the binding of HDA to Cu(100) surface was just slightly stronger (0.12 eV) than (111) surface, making it unclear whether the difference was adequate to drive the preferential exposure of {100} facets on Cu nanocrystals without the assistance of Cl^-. Contradictory to traditional viewpoints, more experimental and simulation evidence is still required to further prove the roles played by HDA and halide ions in the synthesis of Cu nanocrystals encased by {100} facets.

Seed-mediated growth was also explored for the synthesis of penta-twinned wires of Cu. Specifically, $Cu(NO_3)_2$ was reduced by hydrazine in an aqueous solution containing NaOH and ethylenediamine (EDA).[256,258,396] Large polycrystalline Cu nanoparticles were generated first, from which wires were grown. Electrochemical measurements with single-crystal substrates revealed that, instead of selectively capping Cu{100} facets, EDA promoted the growth of wires by keeping Cu{111} facets free from oxidation in the initial stage of the synthesis. With {100} facets covered by oxides, the newly formed Cu atoms would prefer to deposit onto {111} facets at the two ends, enabling the elongation of wires.

Copper wires could also be synthesized at high temperatures using OAm as a solvent, which served as a coordination ligand for Cu(I) or Cu(II) ions and a capping agent for Cu{100} facets at the meantime.[257,259] In one example, Cu wires with an average diameter of 17.5 nm were produced by reducing $CuCl_2$ with tris(trimethylsilyl)silane.[259] The mild reducing power of tris(trimethylsilyl)silane afforded sufficiently slow reduction kinetics for Cu, which was favorable for the generation of multiply twinned decahedral seeds. In the presence of OAm, the seeds subsequently grew into wires with {100} facets as the side faces.

Uniquely, benzoin, which is commonly used as a photoinitiator in polymerization, can also be used for the synthesis of Cu wires with well-defined facets.[260] Under inert atmosphere and heating, benzoin decomposed into radicals that could donate electrons to Cu(II) ions. With OAm serving as a solvent and a surfactant, Cu{100} facets were protected by amine groups, leading to the formation of wires. The reactivity of the radicals could be tuned through the modification of the aromatic rings with different groups. Specifically, modifying with electron donating groups would promote the reducing power of the radicals, while electron withdrawing groups would suppress the reduction. This controllable reactivity gave the organic radicals great potential as a reducing agent in the synthesis of metal nanocrystals.

4.2.3.2. Palladium. The formation of decahedral seeds represents a necessary step in the synthesis of penta-twinned rods and wires. One strategy is to use high-purity Pd decahedra as seeds, onto which Pd atoms were deposited along the <110> directions in the presence of NaI (Figure 19C–E).[267] By tuning the reaction time or the amount of Pd(II) precursor, Pd rods with different aspect ratios were obtained. A modified, one-pot protocol for synthesizing Pd wires involved the controlled reduction of Na_2PdCl_4 by DEG and AA in the presence of NaI and HCl.[147] The formation of PdI_4^{2-} complexes and the weakened reducing power of AA in an acidic solution both contributed to the generation of Pd decahedral seeds, which then grew into wires in the presence of I^-. Considering the high energy of twinned seeds and their susceptibility to oxidative etching, small organic molecules (e.g., acetonitrile, acetone, 1,4-dioxane, 1,3,5-trioxane; ethanol, and 2-propanol) could be used to attract the halide ions via electrostatic interactions, thus adjusting the etching strength of the O_2/halide pair and protecting the Pd decahedral seeds.[237] Methods involving hydrothermal conditions[265] or the introduction of a trace amount of Ag(I) or Cu(II) ions[264,266] were also developed for the synthesis of rods in high quality. It should be mentioned that the role of metal ions in directing the growth of rods is yet to be elucidated.

4.2.3.3. Silver. Among the various 1-D nanostructures, Ag wire is one of the most extensively studied morphologies because it holds great potential in a variety of applications such as touchscreen and flexible electronics.[397] Polyol synthesis has been the most successful and versatile route to the production of Ag wires with well-controlled sizes. The early studies focused on a two-step, seed-mediated method, using either Pt or Ag as the seeds.[270,290] In the original report, the seeds were formed through the reduction of $PtCl_2$ or $AgNO_3$ with EG, followed by the dropwise addition of $AgNO_3$ and PVP solutions for the anisotropic growth. The as-obtained wires had uniform diameters in the range of 30 to 40 nm, together with lengths up to 50 μm. By varying the experimental parameters, including concentration of seeds, reaction temperature, and the ratio of $AgNO_3$ to PVP, the aspect ratio of the Ag wires could be controlled to reach as high as 1000. By controlling the rate at which the precursor was introduced into the reaction, these aforementioned two-step protocols were later simplified to a self-seeding process, in which Ag atoms nucleated to generate the seeds in situ, followed by their anisotropic growth.[269] It was later revealed that decahedral seeds were involved in the synthesis, and PVP played a critical role in the generation of Ag wires due to its stronger binding toward the {100} over {111} of Ag.[271] The preferential deposition of Ag atoms to the twin boundaries of decahedral seeds resulted in the uniaxial elongation and thus the formation of penta-twinned rods and then wires.

According to the mechanism proposed for the generation of Ag wires, both protection of the decahedral seeds from oxidative etching and passivation of Ag{100} are vital to the synthesis of Ag wires. As such, additives have been introduced into the reaction solutions for the optimization of product quality. For example, Br^- and Cl^- ions were introduced into the synthesis, together with PVP with a high molecular weight, for the selective passivation of the Ag{100}, restraining the growth along the lateral direction while preventing aggregation.[272−274] Moreover, the Br^- and Cl^- ions could react with Ag^+ to form largely insoluble AgBr and AgCl compounds. These insoluble compounds could release Ag^+ ions at a very slow rate, resulting in slow reduction kinetics which was essential to avoid homogeneous nucleation. By employing both PVP with a high molecular weight of 1300 kDa and Br^- ions as capping agents for {100} facets, as well as slow introduction of Ag(I) precursor, sub-20 nm Ag wires could be produced with an aspect ratio over 1000 and high purity greater than 85%.[273] However, as mentioned previously, the introduction of halide ions could possibly eliminate the formation of multiply twinned decahedral seeds due to oxidative etching. To this end, Fe(II) or Fe(III) species were introduced into the synthesis, which mainly existed in the Fe(II) form under polyol reduction and could thus remove O_2 to preserve the multiply twinned seeds for their growth to wires.[277] In another example, Cu(I) or Cu(II) chloride were employed as the oxygen scavenger.[280] Besides these inorganic additives, a recent study reported that benzoin could be introduced into the polyol process as a precursor to strongly reductive radicals, decreasing the reaction temperature and leading to the production of Ag wires with average diameter as small as 13 nm and aspect ratios up to 3000.[281]

In addition to the polyol process, a variety of methods were also reported to prepare Ag wires through an aqueous route,[268,275,278] a solvothermal route,[285,286,288] or a polyol route with the assistance of microwave.[276,279,282] In one example, aqueous $AgNO_3$ was reduced by sodium citrate at 100 °C in the presence of NaOH, generating Ag wires with lengths up to 12 μm in a seedless and surfactant-free fashion.[275] In another example, a hydrothermal method was developed to synthesize Ag wires with diameters thinner than 15 nm, in which glucose was used as a reducing agent with the assistance of tetrabutylammonium dichlorobromide (TBA2CB) salt and PVP.[287] The solvothermal method based on EG or ethanol also led to the successful preparation of Ag wires in high yields and with a small diameter or a high aspect ratio.[285,286,288] Based on the conventional polyol method, heating the reaction solution with microwave irradiation demonstrated the ability to produce Ag wires rapidly within a few minutes.[279]

With regard to Ag rods, protocols based on both seed-mediated growth and one-pot synthesis have been successfully developed. In one example, Ag decahedra were employed as seeds for the growth, with citrate as a reducing agent, to produce penta-twinned rods.[283] The width of the as-obtained rods depended on the size of the decahedral seeds, and the length could be tuned in the range of 50 nm to 2 μm by controlling the amount of Ag(I) precursor added into the growth solution. Penta-twinned rods could also be synthesized through a plasmon-mediated method, in which an aqueous solution containing Ag decahedral seeds, $AgNO_3$, and trisodium citrate, was irradiated using a light source with wavelengths in the range of 600−750 nm.[284] Importantly, the wavelength of the light could be tuned to control the aspect ratio of the rods, with longer wavelengths favoring higher aspect ratios. In addition, a template-free, seedless aqueous route was reported to produce Ag rods through the reduction of $AgNO_3$ by trisodium citrate with the assistance of sodium dodecyl sulfonate (SDSN) as a capping agent.[289]

4.2.3.4. Gold. Different from Ag, more attention was paid to the synthesis of Au rods instead of wires due to their vast applications in the field of plasmonics and biomedical engineering.[294] Among various protocols, seed-mediated growth has attracted much interest in the past two decades due to the versatility and simplicity in controlling the aspect-ratio of the final products.[42,296] The synthesis of penta-twinned Au rod typically relies on two factors: (i) the formation of penta-twinned seeds at the initial stage and (ii) the careful control of anisotropic growth to develop {100} as the side faces. To generate seeds with a penta-twinned structure, citrate or PVP was typically applied as a stabilizing agent to facilitate the formation of decahedral seeds.[254,291,292] When citrate was replaced with CTAB, single-crystal seeds were obtained.[398] However, CTAB was necessary in inducing the anisotropic growth of decahedral seeds into Au rods during the growth stage. Recently, the growth process of a single Au rod was observed using liquid-cell TEM.[293] When decahedral nanocrystals were introduced as seeds, it was found that the involvement of CTAB could allow the anisotropic growth of seed into a penta-twinned rod. The addition of Au atoms started at the reentrant grooves on the decahedral seed, followed by the formation of Au{100} facets along one direction under the capping effect of CTAB. In the absence of CTAB, the decahedral seeds would only turn into truncated decahedra.

4.2.4. Plates and Sheets Lined with Planar Defects.

Most plates and sheets can be categorized as a 2-D structure lined with one or more planar defects parallel to the basal faces. The planar defect could be either a twin plane or a stacking fault, depending on the metal and the synthetic protocol. The plates synthesized from noble metals in an fcc structure typically take a triangular or hexagonal shape, with the two basal planes being covered by {111} facets. In this section, we only discuss plates and sheets lined with planar defects, together with well-identified basal planes. The planar defects can either be directly observed under high-resolution TEM from the side of a plate/sheet or indirectly confirmed by the presence of 1/3(422) reflection in the SAED pattern.[399] As discussed in section 4.1.4, however, the ultrathin thickness of some single-crystal sheets can also result in the presence of 1/3(422) spots. Unless we have direct evidence from atomic-resolution TEM images showing the exact packing of atoms on the side face of a plate, we categorize all of the samples with 1/3(422) reflection into plates or sheets lined with planar defects. Figure 20 shows TEM images of some typical examples of such plates and sheets made of various noble metals.

4.2.4.1. Copper. For the synthesis of Cu plates, different precursors, capping agents, and solvents have been explored, with the purpose of slowing the reduction kinetics. For example, by adding a small amount of I_2 into the aqueous solution containing $CuCl_2$, HDA, and glucose, Cu plates with triangular, truncated triangular, and hexagonal shapes were obtained and their edge lengths varied from 1−12 μm.[300] From the high-resolution TEM, the basal planes of the plate were demonstrated to be {111} facets, covered by a thin layer of oxides. The preferential adsorption of I^-, which was generated from disproportionation or reduction of I_2, on Cu{111} facets was believed to be the essential factor contributing to the formation of plates, and the adsorption of I^- on Cu surface was confirmed by X-ray photoelectron spectroscopy (XPS). Change of the I^- source to PbI_2 or methylammonium iodide still led to the formation of Cu plates.

Other methods of synthesizing Cu plates include the use of hydrazine as a reducing agent and the involvement of a relatively low temperature. Specifically, by reducing $Cu(OAc)_2$ with hydrazine at 60 °C in the presence of PVP and DMF, Cu plates with a hexagonal shape, an average diameter of 48.2 nm, and a thickness of 19.5 nm were produced.[298] The use of DMF as a solvent, which prevented Cu from oxidation, and the presence of hydrazine as a reductant, made it unnecessary to keep the synthesis under an inert atmosphere. Though not discussed in literature, the formation of plates might arise from the low reduction rate of Cu(II) precursor and the possible capping effect of DMF. In another report on the synthesis of

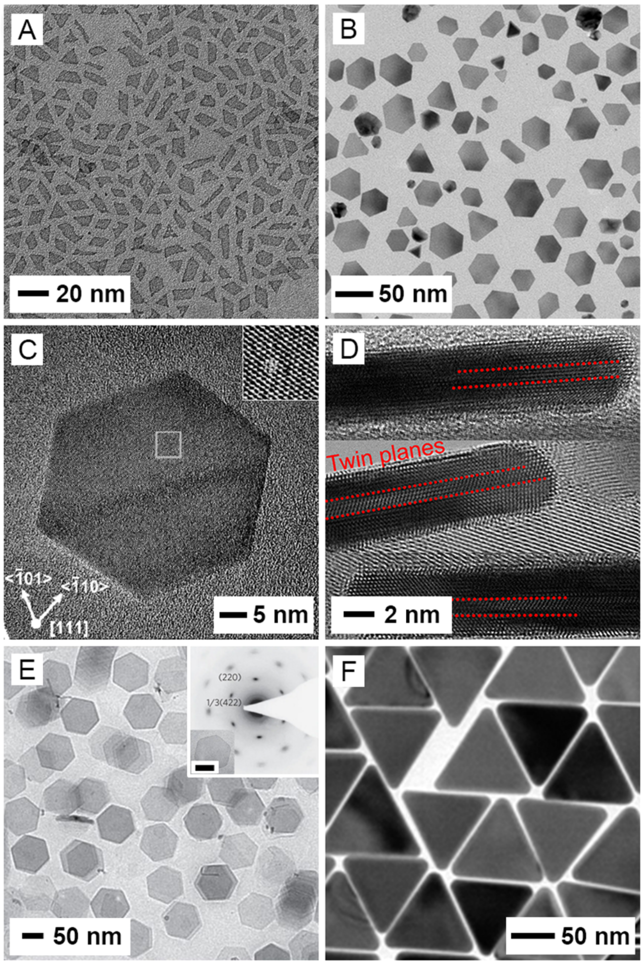

Figure 20. (A) TEM image of the top view of Rh sheets. (B) TEM image of hexagonal Pd plates. (C) High-resolution TEM image taken from the top surface of a Pd plate with an orientation along its [111]-zone axis. The inset shows a magnified view of the boxed region in panel C. (D) High-resolution TEM images taken from the side of Pd plates. The twin planes are marked by red dashed lines. (E) TEM image of Pd sheets, with the insets showing the TEM image and SAED pattern of a single sheet. (F) TEM image of triangular Au plates. (A) Reprinted with permission from ref 302. Copyright 2010 American Chemical Society. (B and D) Reprinted with permission from ref 400. Copyright 2019 Wiley-VCH. (C) Reprinted with permission from ref 306. Copyright 2018 Royal Society of Chemistry. (E) Reprinted with permission from ref 307. Copyright 2011 Nature Publishing Group. (F) Reprinted with permission from ref 319. Copyright 2014 American Chemical Society.

Cu plates, hydrazine was used as reductant in a copper(II) bis(2-ethylhexyl) sulfosuccinate (Cu(AOT)$_2$)/NaAOT/water/isooctane reverse micellar system.[297] Multiple twin planes and stacking faults were observed on the side faces of the plate, leading to the formation of alternating troughs and ridges. The authors proposed that the troughs (reentrant intersections) served as the nucleation sites for preferential deposition of Cu atoms, resulting in the formation of a 2-D structure through a mechanism similar to that for Pt tripods (see section 4.3.2). Additionally, Cu plates could be synthesized by reducing a Cu(II)-tartrate complex with NaH$_2$PO$_2$, a mild reductant, in the presence of PVP without the protection of an inert gas.[299] PVP was supposed to passivate the {111} facets of Cu, enabling the formation of a plate-like shape with basal planes covered by {111}.

4.2.4.2. Ruthenium. Compared to other noble metals, there were fewer reports on the synthesis of Ru plates with well-defined surface structures. In one example, a hydrothermal method was employed to synthesize Ru plates by reducing RuCl$_3$ with HCHO in the presence of PVP.[301] By varying the amount of Ru(III) precursor and PVP, ultrathin Ru plates with triangular or irregular shapes were obtained, whose basal planes were covered by Ru{0001} facets. Compared with other low-index facets, {0001} has the lowest surface energy and is thus favored thermodynamically, contributing to the anisotropic growth of Ru into plates because the total surface energy could be minimized through the maximization of Ru{0001} facets. Characterization using high-resolution TEM and X-ray diffraction (XRD) indicated the existence of defects in the triangular plates. For irregular plates, no conclusion could be drawn due to the limitation of image resolution.

4.2.4.3. Rhodium. Unlike other noble metals such as Pd, Au, and Ag, most of the reported synthetic strategies for Rh 2-D structures involved ultrathin sheets in a single-crystal structure (see section 4.1.4),[232,233] Only a few of them showed the evidence of planar defects. The earliest synthesis of Rh sheets could be traced back to 2010.[302] It was reported that ultrathin Rh sheets could be obtained through kinetic control under a low reaction temperature. In a typical synthesis, rhodium carbonyl chloride dimer, [Rh(CO)$_2$Cl]$_2$, was dissolved in OAm at room temperature. The reaction mixture was held at 50 °C for 10 days without stirring. The final product took the shape of a mixture of triangles, rhomboid, and trapezoid, with all the corners taking the angle of either 60° or 120° (Figure 20A). High-resolution TEMs revealed that the average thickness of the sheets was around 1.3 nm, with the top and bottom faces being terminated in {111} facets. The observed 1/3{422} crystal planes indicated the existence of stacking faults or twin planes in the sheets, which is commonly observed in plates composed of fcc metals.[399] In another example, by simply mixing RhCl$_3$ with ODA, followed by solvothermal treatment, triangular Rh sheets with a hyperbranched structure were generated, and the hierarchical ordering could be tuned by intentionally introducing *tert*-butylamine (TBA) into the synthesis.[303] The SAED pattern verified that the top and basal planes of the hyperbranched plates were terminated in {111} facets. Remarkably, the weak 1/3(422) diffraction spots in the SAED pattern, which are normally forbidden for a perfect fcc lattice, confirmed the existence of planar defects in the sheet.

4.2.4.4. Palladium. In terms of Pd plates, a slow reduction rate is often required in order to get the 2-D structure. In one example, Pd triangular plates with a purity of 70% were obtained by reducing Na$_2$PdCl$_4$ in an EG solution in the presence of PVP, HCl, and FeCl$_3$.[304] When doubling the amount of FeCl$_3$, Pd plates with a hexagonal shape were obtained. The top and bottom faces of the plates were both bounded by {111} facets. The introduction of two etchants, Fe(III) and O$_2$/Cl$^-$ pair, substantially slowed the reduction rate of Pd(II) precursor, leading to the formation of kinetically favored plates. A modified protocol for synthesizing Pd plates in higher purity involved the leverage of PVP as a dual functional reductant and stabilizer.[305] The reaction was conducted in an aqueous solution at a relatively low temperature. The slow reduction rate induced by the mild reducing power of the hydroxyl end groups of PVP contributed mainly to the kinetically controlled synthesis of Pd plates. Hydroxylamine (NH$_2$OH), a mild reducing agent, could also be used to synthesize Pd plates, with CA serving as a capping agent (Figure 20B−D).[306] The planar defects lined parallel to the basal faces were resolved through high-resolution TEM (Figure 20D). According to time-elapsed experiments, it was proposed that these defects were already formed in the nucleation stage. This protocol was quite robust as Pd plates could be obtained regardless of the acidity, temperature, and reaction atmosphere. The synthesis was also extended to a continuous flow reactor, scaling up the production of Pd plates without losing the quality.

The thickness of Pd plates can be further reduced down to a few atomic layers for the production of sheets. These ultrathin structures exhibit a significantly enlarged surface-to-volume ratio for unique physical and chemical properties. The most popular protocol for synthesizing Pd sheets involved the use of CO.[307] The strong adsorption of CO molecules on the {111} basal planes prevented the growth of Pd atoms along the ⟨111⟩ directions, enabling the formation of sheets with a thickness thinner than 10 atomic layers (Figure 20E). The appearance of the 1/3{422} reflections indicated the existence of planar defects in the sheets.

4.2.4.5. Silver. The detailed mechanism for the synthesis of Ag plates has not been completely unveiled for now. However, it is generally accepted that the anisotropic growth originates from the lower surface energy of basal planes due to the preferential binding of capping agent[311] or the higher energy of the side faces due to the presence of planar defects.[401] Both seed-mediated growth and one-pot approach have been applied to the synthesis of Ag plates, with the former focusing on the structure of seeds and capping agent, while the latter paying more attention to the control of reduction kinetics.

One of the early reports on the synthesis of Ag plates with well-defined shapes and sharp corners involved the refluxing of an aqueous dispersion of spherical colloids of Ag with an average diameter of 3.5 nm.[346] The refluxing process facilitated the growth of plate-like seeds by sacrificing Ag spheres through Ostwald ripening. The plates all carried a triangular shape with an average edge length of around 100 nm. Although the presence of planar defects was not directly mentioned in the report, the presence of normally forbidden 1/3{422} spots in the diffraction pattern confirmed that the lattice in the plate was not arranged in a perfect fashion. Several mechanisms accounting for the shape evolution of Ag plates have been proposed, including the capping effect from CTAB, CA, and citrate ions.[308,310,311] Under controlled experimental conditions, it was observed that the addition of citrate ions could promote the lateral growth of Ag plate while the involvement of PVP only increased the thickness of the plate-like seeds, making the products deviated from a 2-D structure.[311] However, the capping effect could not fully explain the growth of plates in an anisotropic way. The formation mechanism was further explored in a later report, where the surface structure of the Ag seed was analyzed under high-resolution TEM.[312] The result suggested that the defects were formed during the seed formation stage, the high surface energy of which would then direct the deposition of atoms along lateral directions.

On the other hand, the one-pot synthesis mainly focused on controlling the reduction kinetics of the Ag(I) precursor. As mentioned in section 3.2, slowing down the reduction rate is critical to the generation of stacking faults and thus the formation of Ag plates, which could be achieved by using a reductant with moderate reducing power[305,309] or adding coordinating ligands to form complexes with Ag(I) precursor.[313−315] For example, PVP terminated with hydroxyl groups could serve as a mild reducing agent to achieve the kinetically controlled synthesis of Ag triangular plates.[309,402] Moreover, the introduction of polyacrylamide (PAM)[313,315] or ethylenediaminetetraacetic acid (EDTA)[314] into the reduction of $AgNO_3$ could effectively slow down the reduction kinetics by forming complexes with Ag^+ ions, resulting in the formation of plates.

4.2.4.6. Gold. Similar to the case of Ag, seed-mediated growth and one-pot synthesis could both be employed to produce Au plates. A large number of protocols have been developed for the syntheses of Au plates with different sizes and shapes, and the key point was to slow down the reduction of Au(III) precursor for the generation of seeds with stacking faults. Typical methods include the use of a reductant with appropriate reducing power. For example, some organic compounds such as lemongrass extract[316] and bovine serum albumin[318] were found to be well-suited reductants for the synthesis of Au plates. Similar to the synthesis of Ag plates, PVP could serve as both a stabilizer and a reductant with mild reducing power, and be used to generate Au plates with an average edge length of 800 nm.[305] Decreasing the reduction rate could also be achieved by conducting the synthesis at room temperature,[317] reducing the concentration of reductant,[305] or introducing halide ions (Figure 20F).[319]

4.2.5. Twinned Cubes and Bipyramids Bearing Multiple Planar Defects.

Different from a normal cube characterized by a cubic shape and single-crystal structure, a twinned cube can be defined as a cube containing multiple planar defects. Similarly, bipyramids could also possess more than one planar defect. Figure 21 shows TEM images of some typical examples of such twinned nanocrystals made of various noble metals. The synthesis of such unique structures is typically achieved through seed-mediated growth, where the planar defects of the seeds can also be extended to the surface of the final product. The growth mechanisms for these two structures are related.

4.2.5.1. Copper. There are very few reports on the synthesis of Cu bipyramids, although they were often observed as byproducts in the synthesis of other types of Cu nanocrystals.[403,404] The challenge of producing Cu bipyramids in high purity mainly lies in the susceptibility of Cu to oxidative etching and the difficulty in controlling the reduction rate of the precursor. To overcome this problem, seeds bearing twin defects were introduced to facilitate the formation of Cu nanocrystals with twinned structures.[320] In the synthesis of Cu RBPs, a trace amount of Pd was introduced to induce the formation of twinned seeds lined with multiple planar defects (Figure 21B,C). According to the standard reduction potential (0.91 and 0.34 V for Pd^{2+}/Pd and Cu^{2+}/Cu pairs, respectively, vs standard hydrogen electrode, SHE), Pd(II) ions would be first reduced to Pd atoms, generating seeds for the subsequent deposition of Cu atoms. The amount of Pd contained in the final product was too low to affect the surface and bulk properties, as confirmed by energy-dispersive X-ray (EDX) mapping and XRD. As such, the nanocrystals could be considered as nearly monometallic Cu RBPs. By varying the amount of Pd(II) precursor, the size of the RBPs could be tuned between 38−67 nm, and this dependence also proved the role of Pd seeds. Upon coordination with HDA molecules, the reduction of Pd(II) and Cu(II) precursors was greatly slowed down, leading to the formation of twinned seeds. From

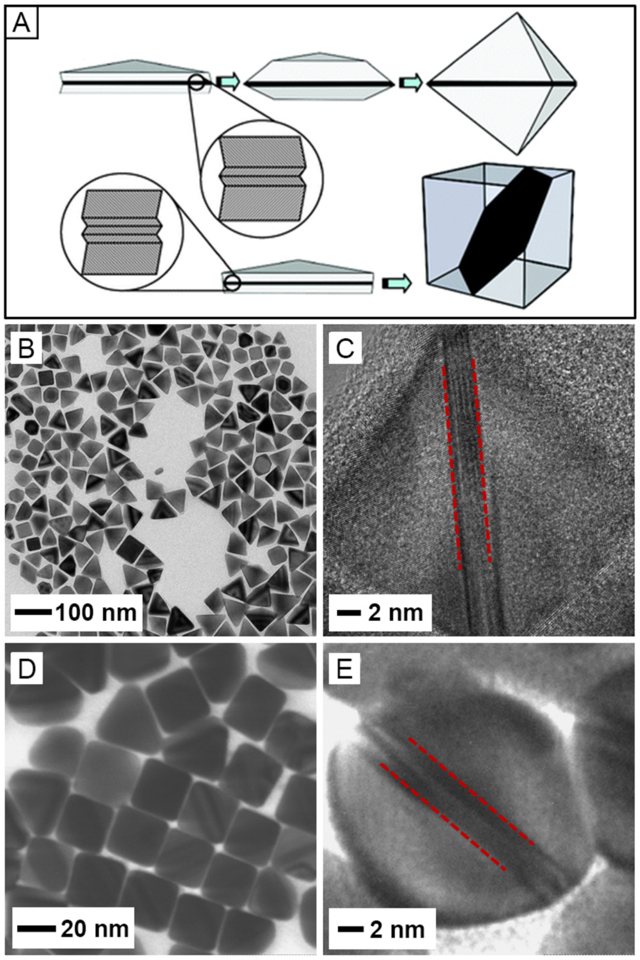

Figure 21. (A) Schematic illustration showing the formation mechanism of twinned RBP and cube. It was proposed that seeds with an odd number of twin defects would grow into RBPs, while those with an even number of twin defects would evolve into cubes. (B) TEM image of the Cu RBPs lined with planar defects. (C) High-resolution TEM image of an individual Cu RBP. (D) TEM image of Ag twinned cubes grown from Ag plates. (E) High-resolution TEM image showing the planar defects in a Ag twinned cube. The defects in panels C and E are marked by red dash lines. (A, D, and E) Modified with permission from ref 321. Copyright 2008 Royal Society of Chemistry. (B and C) Reprinted with permission from ref 320. Copyright 2018 American Chemical Society.

high-resolution TEM, multiple planar defects were observed in a single RBP(Figure 21C), illustrating that the product was not the commonly observed bipyramidal structure bearing a single twin defect.

4.2.5.2. Silver. Silver RBPs with multiple twin defects could be generated using seeds taking different morphologies, from plates[321] to irregular nanoparticles.[322] An early report proposed that the number of planar defects in the seed would affect the morphology of final product from seed-mediated growth.[321] The study observed the generation of RBPs and twinned cubes from Ag plates in an aqueous solution containing $AgNO_3$, PVP, and citrate ions (Figure 21D,E). It was suggested that Ag plates with an odd number of twin defects would transform into RBPs while those with an even number of twin defects evolved into twinned cubes. At that time, this was just an assumption proposed based on the experimental observation. Later, this assumption was verified by another study that used a plasmon-mediated method to prepare Ag RBPs, in which an aqueous solution containing $AgNO_3$, sodium citrate, bis(*p*-sulfonatophenyl) phenylphosphine dihydrate dipotassium (BSPP) salt, and NaOH was irradiated with a halogen lamp.[322] Multiple stacking faults and twin defects were observed from the atomic-resolution TEM of a Ag seed. The odd number of defects in the seed was in consistency with the RBP shape of the final product. Atomic-resolution TEM image of the RBP also clearly showed an odd number of planar defects at the bisecting region. The mechanism hidden behind was that only odd number of twin planes allowed a crystal to evolve into two halves in mirror symmetry. With even number of twin planes, the mirror effect would cancel out and twinned cubes would prevail.

4.2.5.3. Gold. Most of the protocols reported for the synthesis of Au bipyramids with multiple planar defects were based on seed-mediated growth.[248] It was first reported that Au bipyramids could be synthesized with a yield of 30% with the assistance of Ag(I) ions by employing CTAB as a stabilizer and penta-twinned particles as seeds.[292] The bipyramids preserved the penta-twinned structure from the seeds during growth, with highly stepped Au{11*n*} ($n \approx 7$) facets exposed on the surface. Furthermore, the protocol was modified by switching to citrate-stabilized seeds and changing the surfactant to cetyltriethylammonium bromide (CTEAB)[323] and cetyltributylammonium bromide (CTBAB),[324] improving the yield of Au bipyramids to 37% and 50−60%, respectively. The increased yield could probably be ascribed to the stronger binding of the surfactants to the surface of bipyramids as their head groups became larger. It should be mentioned that the presence of Ag(I) ions is critical to all the successful syntheses of bipyramids. One possible explanation is that the UPD of Ag on the Au seeds slowed down the growth and stabilized the highly stepped surface of bipyramids with high energy.[292]

It is noteworthy that the penta-twinned structure of Au bipyramids was challenged by another group later using electron tomography coupled with high-resolution TEM to characterize the Au bipyramids.[325] It was found that the nanocrystals had an irregular 6-fold twinning structure enclosed by highly stepped {151} facets. The 6-fold symmetry was supported by a later study, in which the micelle formed by CTAC and salicylate anions was employed as a template for the synthesis.[405] To resolve if the Au bipyramids contained 5 or 6-fold twinning or both types coexisted, it is necessary to apply advanced characterization tools for a more comprehensive understanding of the structural features of Au bipyramids.

4.2.6. Conclusion. Different from the synthesis of single-crystal nanocrystals, generating those with twin defects and/or stacking faults typically requires slow reduction kinetics, which can be achieved through the utilization of a less-reactive precursor, a milder reducing agent, and a lower temperature. The elimination of O_2 to prevent oxidative etching is also critical in some cases. In general, a precise control over the reaction kinetics to obtain nanocrystals with well-defined surface defects and in high purity still remains a challenge. Many reports have shown that nanocrystals in different shapes could be produced under similar experimental conditions, severely compromising the yield of the target product. Alternatively, nanocrystals with twin defects could also be synthesized via seed-mediated growth through the use of seeds possessing well-defined twin structures. The surface defects on the seed can be extended to the lattice deposited on it, making the synthesis more reliable and controllable.

4.3. Nanocrystals Enclosed by High-Index Facets

Nanocrystals enclosed by high-index facets are typically correlated with unique polyhedral profiles, including concave, convex, and/or branched structures, with a high density of under-coordinated atoms on the surface. The models of some typical concave and convex structures are shown in Figure 22A. The high specific surface area and surface energy make these nanocrystals particularly attractive in catalysis, but they also pose a grand challenge in their syntheses. Typically, the formation of such nanocrystals calls for collective manipulation of the reduction kinetics, surface diffusion, and surface capping.[39,59] Here we only focus on those shapes with well-defined facets or defects so their surface structures can be clearly correlated with catalytic properties.

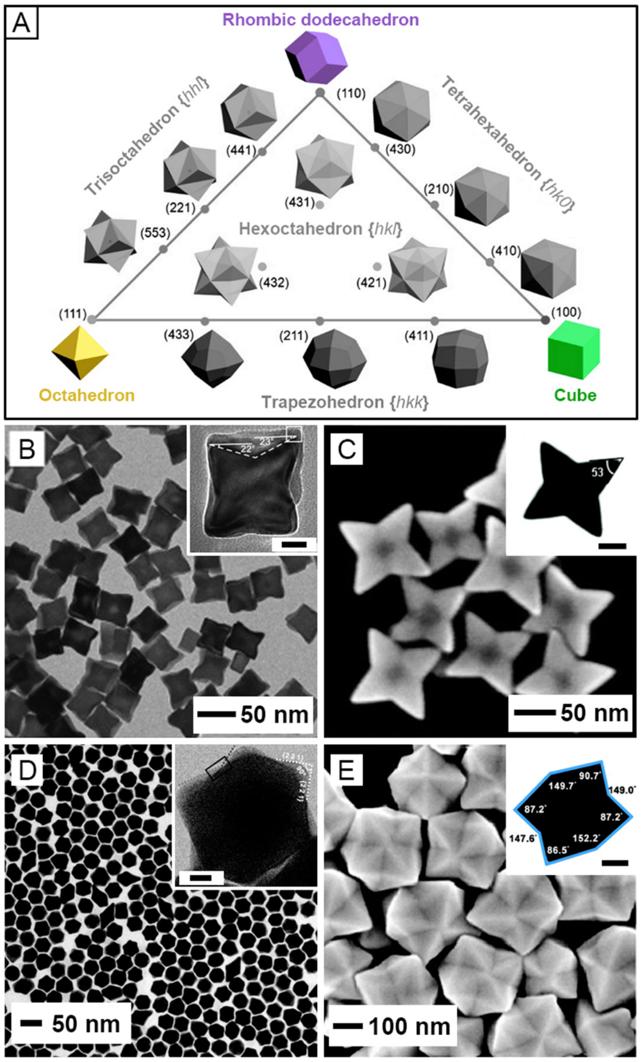

Figure 22. (A) Diagram showing fcc-metal polyhedra enclosed by different facets. (B) TEM image of Pd concave cubes covered by {730} facets. The inset shows the high-resolution TEM image of an individual concave cube (scale bar: 10 nm). (C) SEM image of Pt concave nanocrystals. The inset shows the TEM image of an individual nanocrystal oriented along [100] direction (scale bar: 20 nm). (D) TEM image of Au TOHs. The inset shows the high-resolution TEM image of an individual TOH oriented along [110] direction (scale bar: 5 nm). (E) SEM image of Au HOHs. The inset shows the TEM image of an individual Au HOH viewed along the [110] direction (scale bar: 100 nm). (A) Modified with permission from ref 406. Copyright 2010 American Chemical Society. (B) Reprinted with permission from ref 327. Copyright 2011 Wiley-VCH. (C) Reprinted with permission from ref 64. Copyright 2011 American Chemical Society. (D) Reprinted with permission from ref 336. Copyright 2018 Royal Society of Chemistry. (E) Reprinted with permission from ref 337. Copyright 2012 American Chemical Society.

4.3.1. Concave Polyhedra. A concave structure refers to a surface curving inward for the generation of a negative curvature.[59] Notable examples of concave structures include trisoctahedron (TOH) in $\{hhl\}$ facets ($h > l > 0$), hexoctahedron (HOH) in $\{hkl\}$ facets ($h > k > l > 0$), and a variety of concave shapes derived from regular polyhedra such as concave cube (also named octapod in some cases) and concave octahedron. They can be obtained through both seed-mediated growth and one-pot synthesis. In the seed-mediated growth, site-selected deposition of metal atoms on the seed is a key requirement for generating a concave shape, which can be achieved by either selectively blocking or activating particular sites on the surface of a seed. On the other hand, the formation mechanism is more difficult to understand in one-pot synthesis and it is also harder to control the surface structure. In both cases, manipulating atom deposition and surface diffusion rates is of paramount importance. Figure 22B−E shows TEM and SEM images of some typical examples of concave polyhedral nanocrystals whose surfaces are terminated in high-index facets.

4.3.1.1. Palladium. A fast deposition rate that overwhelms the surface diffusion rate is necessary for generating concave structures in seed-mediated growth. In a typical example, by depositing Pd atoms onto Pd cubic seeds in the presence of PVP and KBr, Pd concave cubes were obtained (Figure 22B).[327] Based on the atomic-resolution imaging and measurement of projection angles, the eight edge-on faces were indexed as {730} planes, which could be regarded as a combination of {100} terraces and {110} steps. The Br^- ions could coordinate to Pd(II) ions to form a $PdBr_4^{2-}$ complex, retarding the reduction of Pd(II). To this end, fast reduction of Pd(II) precursor could be achieved by leveraging a low concentration of KBr or a high concentration of reductant, and the deposition of Pd atoms would be faster than their diffusion to side faces, leading to the formation of concave cubes. Similar protocols such as selective activation of corners/edges via oxidative etching[329] and autocatalytic growth from single-crystal seeds[330] have also been employed to produce Pd concave cubes in high quality. In addition to cubes, concave structures including tetrahedra,[326] trigonal bipyramids,[326] decahedra,[118] and icosahedra[118] have all been reported as well. However, unlike the concave cubes with well-identified facets, the high-index facets on other concave structures still require further characterizations to assign the surface structures.

Compared to seed-mediated growth, it was harder to precisely control the surface structure of concave cubes using one-pot method due to the random nucleation and growth pattern typical of this process. By reducing H_2PdCl_4 with AA in the presence of CTAC and CTAB, Pd concave cubes were achieved with surfaces covered by high-index facets such as {730} and {310}, together with different degrees of concavity.[328] Combining the characterization results from time-elapsed UV−vis spectra and TEM images, it was proposed that the Pd(II) precursor formed complexes with CTA^+ at the beginning of a synthesis. The complexes were then reduced to generate nanocrystals of about 30 nm in size,

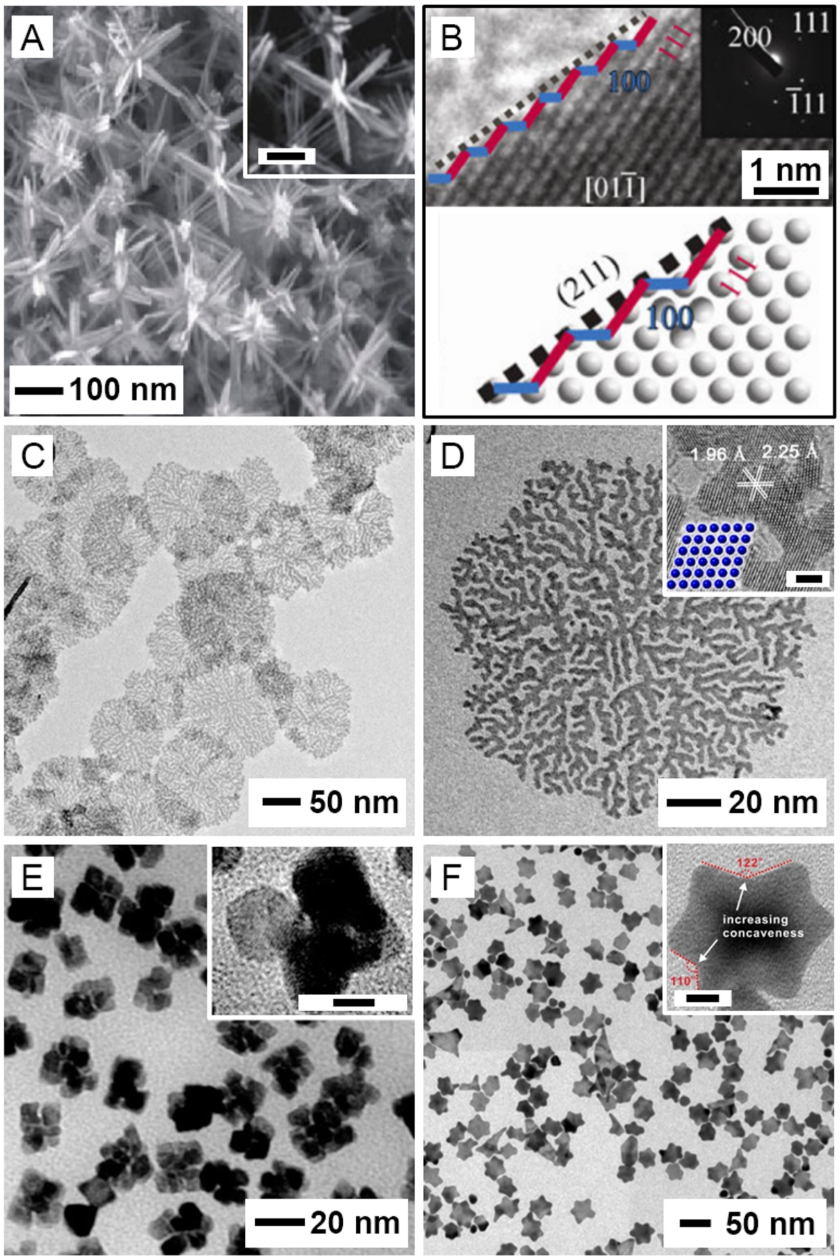

Figure 23. (A) SEM image of Pt multipods enclosed by {211} facets. The inset shows a high-magnification SEM image of an individual multipod (scale bar: 50 nm). (B) High-resolution TEM image, SAED pattern, and atomic model of a branch projected along the [011] direction, showing the {211} packing of atoms. (C) TEM image of 2-D Pt dendrites. (D) TEM image of an individual dendrite with a high-resolution TEM image in the inset showing the {110} facets for basal planes (scale bar: 2 nm). (E) TEM image of multioctahedral Pt nanocrystals. The inset shows a magnified image of an individual nanocrystal (scale bar: 5 nm). (F) TEM image of Au hexagonal stars. The inset shows a magnified image of an individual Au star (scale bar: 10 nm). The projected dihedral angle is marked by red dashed lines. (A and B) Reprinted with permission from ref 47. Copyright 2012 Springer Nature. (C and D) Reprinted with permission from ref 339. Copyright 2019 American Chemical Society. (E) Reprinted with permission from ref 340. Copyright 2008 American Chemical Society. (F) Reprinted with permission from ref 341. Copyright 2019 American Chemical Society.

together with the presence of interstices. As the reaction continued, the interstices were gradually filled with Pd atoms and cubes with a shallow concave structure were formed. The authors proposed that the addition of CTAB and CTAC into the reaction mixture contributed to the formation of $[PdBr_4(CTA)_2]$ and $[PdCl_4(CTA)_2]$ complexes, which played a significant role in decreasing the reduction rate, therefore kinetically affecting the shape of the final products.

4.3.1.2. Platinum. Similar to Pd, concave cube is the most commonly observed shape in concave Pt nanocrystals. The production of Pt concave cubes relies on careful manipulation of the reduction kinetics. The reduction should be fast enough at the initial stage to generate single-crystal seeds and then slowed down to facilitate the overgrowth of atoms on the corners and edges. Excess amount of Pt atoms in the solution and the suppression of surface diffusion are two other key factors critical to the success of a synthesis.[34,331] For example, using a high concentration of glucose to reduce Na_2PtCl_6 in the presence of CTAB and OAm, Pt cubes were generated at the early stage, followed by the deposition of Pt atoms onto corners/edges for the generation of a concave shape.[34] In another example, an aqueous $NaBH_4$ solution and a mixture of K_2PtCl_4, KBr, and $Na_2H_2P_2O_7$ were injected simultaneously into water held at 95 °C to generate Pt concave cubes.[62] The surface of the nanocrystals was confirmed to be dominated by {720} facets, along with some other high-index facets such as {510}, {830}, and {310}, by measuring the angles between the exposed facets and {100} facets of an ideal cube. The slow growth rate enabled by titration of precursor and reducing agent, together with the block of {100} facets by Br^- ions, was considered major contributors to the formation of a concave structure. Hydrothermal synthesis was also applied to produce Pt concave cubes, where an aqueous solution of H_2PtCl_6, PVP, and glycine was sealed in an autoclave and heated at 200 °C.[332] High-index {*hk*0} facets were observed on the surface of the products. The glycine played a dual role during the synthesis, serving as a coreductant apart from PVP and a capping agent. The synergistic effect of the amino and carboxyl groups favored the formation of a concave structure.

Concave nanocrystals of Pt covered by high-index facets have also been synthesized using a solvothermal method. For example, Pt concave polyhedra with a shape like octapod were prepared by reducing H_2PtCl_6 at 160 °C in an autoclave with PVP serving as a stabilizer, methylamine as a capping agent, and DMF as a solvent.[64] Confirmed by microscopy imaging, the products were essentially composed of eight trigonal pyramidal arms and covered by 24 identical {411} facets (Figure 22C). The presence of amine, which helped stabilize the low-coordinated Pt sites, was considered the main reason for generating {411} facets, and the substitution of methylamine by other amines could also yield Pt concave structures. Likewise, Pt concave nanocrystals covered by {411} facets were synthesized by reducing $Pt(acac)_2$ in 1-octylamine with the addition of HCHO.[47] In this case, the CO generated from the decomposition of HCHO was proposed to stabilize {411} facets due to its adsorption on the {100} terraces.

4.3.1.3. Gold. It is easier to control the exposed facets on Au nanocrystals because of its overall lower surface energy compared to other noble metals.[407] In an early report, Au concave cubes covered by 24 {720} high-index facets were obtained through the growth of CTAC-stabilized Au seeds.[334] At that time, the formation mechanism still remained enigmatic and the authors proposed that the unique shape was generated under a combination effect from Ag^+ and Cl^- involved in the reaction. Besides concave cubes, other concave structures were also obtained by manipulating the reaction kinetics, with notable examples including Au TOH. The TOH can be regarded as a shape generated by pulling out the centers of eight triangular faces of an octahedron. The first wet-chemical method reported for Au TOHs was based on the reduction of aqueous $HAuCl_4$ with AA in the presence of CTAC.[333] The Au TOHs had an average size between 100−200 nm, with 24 high-index facets such as {221}. Later, the protocol was optimized to achieve a size control for the Au TOHs in the range of 60−255 nm by adding tiny Au seeds or the as-obtained TOH to initiate seeded growth.[335] In another example, by employing EDTA-chelated Au^{3+} as a precursor, Au TOHs with sizes in the range of 20−80 nm, together with a dihedral angle of 142° were synthesized, owing to the slow reduction rate and the ability of CTA^+ to stabilize the high-index facets (Figure 22D).[336] Structural characterization revealed that the exposed faces were terminated in a mix of {*hhl*} facets such as {11 11 7}, {331}, and {221}. By carefully adjusting the reaction kinetics, more complicated shapes such as Au HOH bounded by 48 triangular {321} facets have also been obtained, with an average size of 200 nm (Figure 22E).[337] The success of this synthesis relied on the fast reduction induced by a high concentration of AA, as well as an elevated reaction temperature. The involvement of CTAC as a surfactant also contributed to the formation of HOH.

4.3.2. Multipods. Multipods represent another type of concave structure. Compared with a concave polyhedron, a multipod is typically characterized by a more negative surface curvature and a higher diversity in terms of shape, morphology, or surface structure. The dimensions of the branches can be reduced down to the length scale of a typical industrial catalyst (<5 nm), making multipods attractive for catalytic applications. Similar to the conventional nanoparticles, the surface of a multipod is usually enclosed by grain boundaries, undercoordinated atoms, and a mix of different types of facets, making it difficult to elucidate the structure−property relationship. Here we only focus on multipods with well-defined surface structures. Figure 23 shows SEM and TEM images of some typical examples comprised of different noble metals.

4.3.2.1. Platinum. The use of capping agents is one of the approaches that could help define the surface structures of multipods in a systematic way. For example, when 1-octylamine was employed as the solvent and capping agent, Pt multipods dominated by {211} side faces were produced (Figure 23A,B).[47] It was proposed that the amine groups preferentially adsorbed on the monatomic step edges consisting of {111} terraces and {100} steps, resulting in the creation of {211} facets. The multipods with high-index facets and a large surface area exhibited superior catalytic activity in the electrochemical ethanol oxidation reaction (EOR) compared to either commercial Pt/C catalyst or Pt cubes covered by low-index {100} facets.

In addition to the 3-D multipods, 2-D ultrathin Pt dendrite with a single-crystal structure and sheet-like morphology was also reported (Figure 23C,D).[339] The dendrites had a thickness of around 2.3 nm and were enclosed by {110} facets for the top and bottom planes and {111} facets for the side faces. The amphiphilic surfactant, $C_{22}H_{45}-N^+(CH_3)_2CH_2COOH(Br^-)$, played the most important role in this synthesis by acting as both the structure-directing template and the capping agent. The nanoconfined lamellar structure formed through the coassembly of $C_{22}H_{45}-N^+(CH_3)_2CH_2COOH$ and H_2PtCl_6, together with the selective binding of the surfactants to {110} facets, facilitated the in-plane epitaxial growth of Pt nanocrystals along ⟨111⟩ directions, leading to the formation of ultrathin Pt dendrites with a 2-D morphology. The protocol could also be extended to other noble metals, including Pd and Au dendrites.

There is another interesting type of structure unique to Pt nanocrystals, which can be regarded as a combination of multiple identical shapes such as cube or octahedron. For example, multioctahedral Pt nanocrystals with several interconnected arms in a quasi-octahedral shape were reported (Figure 23E).[340] The product was confirmed to be single-crystalline, and most of the exposed facets were {111} although there was truncation at corners to introduce high-index facets. In a typical synthesis, H_2PtCl_6 was reduced by PVP in an aqueous solution containing a trace amount of $FeCl_3$. The Fe(III) species helped control the concentration of Pt atoms at a low level, promoting the overgrowth of Pt seeds along the

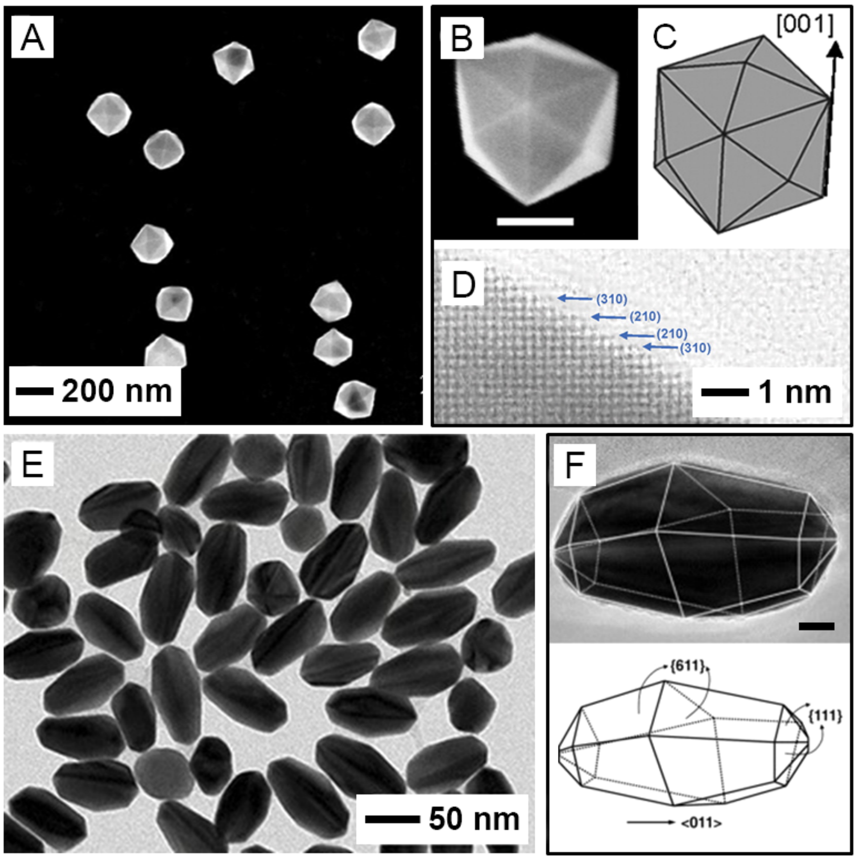

Figure 24. (A) SEM image of Pt THH. (B) High-magnification SEM image of an individual Pt THH (scale bar: 100 nm). (C) Geometrical model of an ideal THH. (D) High-resolution TEM image of a Pt THH, revealing surface atomic steps made of {210} and {310} subfacets. (E) TEM image of Au rice. (F) TEM image and the corresponding model of a Au rice (scale bar: 10 nm). (A–D) Modified with permission from ref 342. Copyright 2007 AAAS. (E and F) Reprinted with permission from ref 344. Copyright 2011 Wiley-VCH.

corners for the formation of multiarmed nanocrystals. Besides, Pt multicubes were also synthesized in the presence of Ni^{2+} ions, and their surface was mostly bounded by {100} facets, together with a small portion of high-index facets at the junctions between adjacent cubes.[338] The existence of Ni^{2+} ions and their UPD onto Pt could alter the surface energies of different Pt facets substantially, leading to the formation of cubic arms enclosed mainly by {100} facets. The Ni atoms would then be replaced by Pt atoms through galvanic replacement and removed from the surface.

4.3.2.2. Gold. Although Au typically features an fcc lattice, Au nanoscale hexagonal stars with an unconventional hexagonal close-packed (hcp) atomic arrangement at tips could be obtained using fcc-Au spheres as the seeds (Figure 23E).[341] In a typical synthesis, a Au(III)-EDTA complex was employed as a precursor, together with the use of 2-phospho-L-ascorbic acid trisodium salt (Asc-2P), an unusual reductant capable of maneuvering the reaction kinetics, to facilitate the formation of hcp-Au hexagonal stars from fcc-Au seeds. The existence of both fcc and hcp phases in the Au hexagonal stars was confirmed by XRD and high-resolution TEM. At the tip of the star, hcp high-index facet $(\bar{2}112)$ could be resolved in atomic resolution.

4.3.3. Convex Polyhedra. Typical convex structures with high-index facets on the surface include tetrahexahedron (THH) terminated in $\{hk0\}$ $(h > k > 0)$ facets and trapezohedron (TPH) covered by $\{hkk\}$ $(h > k > 0)$ facets. Compared to concave structures, the convex structures are more thermodynamically favorable due to their relatively lower surface-to-volume ratio. Therefore, when used as catalysts, they more likely show enhanced stability under the reaction conditions.[39] Figure 24 shows SEM and TEM images of some typical examples of convex polyhedral nanocrystals whose surface is terminated in high-index facets.

4.3.3.1. Platinum. The first report on the synthesis of Pt THH involved an electrochemical method that treated Pt polycrystalline nanoparticles with a square wave potential (Figure 24A–D).[342] A THH has 24 faces that can be obtained from a cube by "pulling out" the centers of the six square faces. The high-index facets exposed on the surface were determined to be {730}, as confirmed by high-resolution TEM. The {730} facet can be regarded as a periodic combination of two {210} facets and one {310} facet, which could be further divided into a combination of low-index {100} and {110} facets (Figure 24D). Despite the well-defined morphology, it was impractical to scale up the synthesis based on such an electrochemical treatment. As an alternative approach, a recent report described a method for synthesizing Pt THH through dealloying.[63] In their report, Pt THH was produced by heating a solid metal precursor in a tube containing a foreign metal such as Sb, Bi, Tb, or Te as the shape-directing agent, followed by evaporation of the foreign metal at a higher temperature. This new method was not only more suitable for scale-up production, but also offered a promising approach to converting the poorly shaped Pt catalysts to the THH shape.

4.3.3.2. Gold. In the case of Au, the successful syntheses of both TPH and THH have been reported in literature. A TPH can be viewed as a convex shape sharing the features between a cube and an octahedron. In a typical synthesis of Au TPH, dimethyl sulfoxide (DMSO) was reported to play a critical role in stabilizing the {311} facets exposed on the surface and thus shape evolution into Au TPH.[345] DFT calculations and scanning tunneling microscopy study revealed that both the oxygen and sulfur atoms in DMSO could simultaneously bind to the Au(311) surface in a "two center bonding" mode, facilitating the stabilization of the surface atoms with a lower CN. Similarly, Au THH could be obtained with the prudent choice of surfactants involved in the reaction. It was reported that mixing CTAB with didodecyldimethylammonium bromide (DDAB) at a certain ratio was crucial to the formation of THH.[343]

Besides the aforementioned shapes, Au rice with the surface covered by 10 {611} facets and two ends enclosed by 10 {111} facets were prepared by using Au(I)-TEG complex as a precursor to Au (Figure 24E,F).[344] It was proposed that the addition of Ag(I) ions played a significant role in directing the shape evolution. A monolayer of Ag atoms could be selectively deposited on the {100} facets of the penta-twinned seeds formed initially in the synthesis, suppressing the growth of these facets and promoting the formation of Au rice.

4.3.4. Conclusion. A precise control over the reaction kinetics is the most important factor in the colloidal synthesis of nanocrystals covered by high-index facets. The reduction rate has to be fast enough to allow site-selected deposition of atoms but not too fast to induce irregular surface structures and multiple nucleation events. To this end, it is easier to control the surface structure using seed-mediated growth than one-pot synthesis. Although numerous reports have been published on the successful synthesis of nanocrystals enclosed by high-index facets, there are still a few challenges remained to be addressed: (i) the roles played by a capping agent or surfactant in the generation of high-index facets are still elusive; (ii) the size of the majority of nanocrystals covered by high-index facets are too large (typically, >100 nm) to be applied to industrial catalytic processes; and (iii) the stability of these nanocrystals still needs to be systematically evaluated.

4.4. Other Nanocrystals with Well-Defined Surface Structures

4.4.1. Belts. A belt can be regarded as an elongated and flattened bar in a single-crystal structure. However, different from a cube or bar, the surface of a belt can be terminated in a mix of low-index and high-index facets. Most belts reported in literature preferentially grow along the ⟨110⟩ direction, with the top and bottom faces terminated in {111} facets, while the side faces are covered by {211} high-index facets.[347,349,350] There are also a few reports on the belts possessing stacking faults along the growth direction.[408] In general, although the belts may possess well-defined surface structures, it is difficult to classify all of them into a single category.

4.4.1.1. Silver. The earliest report on the wet-chemical synthesis of Ag belts was achieved by simply refluxing an aqueous suspension of colloidal Ag nanoparticles that were formed through the reduction of $AgNO_3$ by $NaBH_4$ in the presence of PVP and sodium citrate.[346] The formation of Ag belts was attributed to the assembly of small triangular plates derived from the nanoparticles, as driven by the strong dipole−dipole interaction between adjacent plates. The SAED pattern and the lattice spacing measured from high-resolution TEM suggested that the belt had a single-crystal structure, with a growth direction along [101]. However, the yield of belts in this report was only 5%. The synthesis was later improved by leveraging a low-temperature aqueous synthesis in which $AgNO_3$ was reduced with AA in the presence of poly(acrylic acid) (PAA) at 4 °C.[347] Belts with a high yield close to 100% and length longer than 10 μm were produced. The SAED pattern of a single belt indicated that the growth direction was along the [110] direction, while the top and side faces were terminated in {111} and {211} facets, respectively.

4.4.1.2. Gold. The surface structures and growth mechanisms of Au belts were similar to those reported for Ag belts. In one report, single-crystal Au belts were prepared by reducing $HAuCl_4$ with AA in the presence of a binary surfactant mixture made of CTAB and SDSN (Figure 25A−C).[349] When the reaction temperature was set to 4 and 27 °C, belts grown along ⟨110⟩ and ⟨211⟩ directions were obtained, respectively. In both cases, the top faces were still covered by {111} facets. However, the side faces of the belt growing along ⟨110⟩ and ⟨211⟩ directions turned out to be {211} and {110} facets, respectively. A unique type of Au belt growing along ⟨111⟩ direction was also achieved through a sonochemical approach.[348] The authors proposed that the belts were formed through oriented attachment from small Au nanoparticles. The

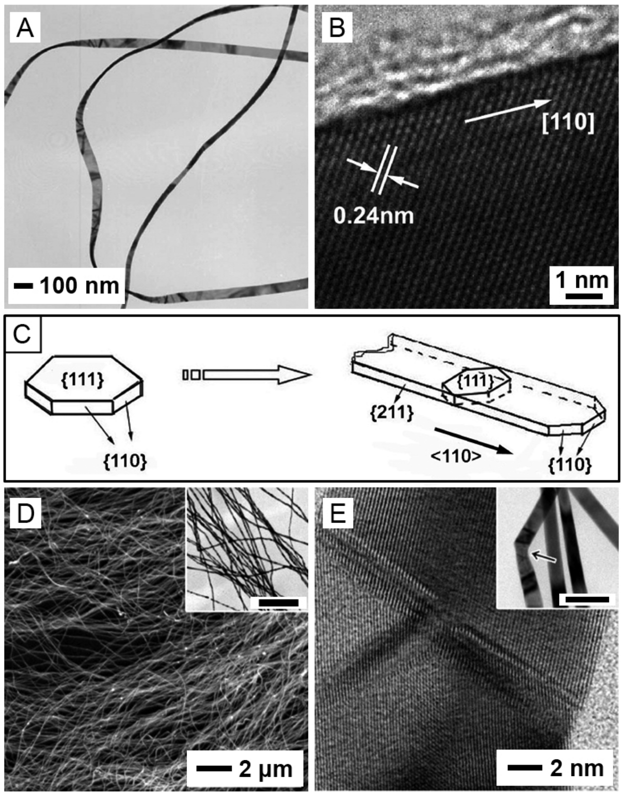

Figure 25. (A) TEM and (B) high-resolution TEM images of Au belts. (C) Schematic illustration showing the growth of a Au belt along the ⟨110⟩ direction. (D) SEM and TEM (inset) images of Au wavy wires. The scale bar in the inset is 500 nm. (E) High-resolution TEM image of the wavy wire marked by an arrow in the inset (scale bar: 50 nm). (A−C) Reprinted with permission from ref 349. Copyright 2008 American Chemical Society. (D and E) Reprinted with permission from ref 353. Copyright 2012 American Chemical Society.

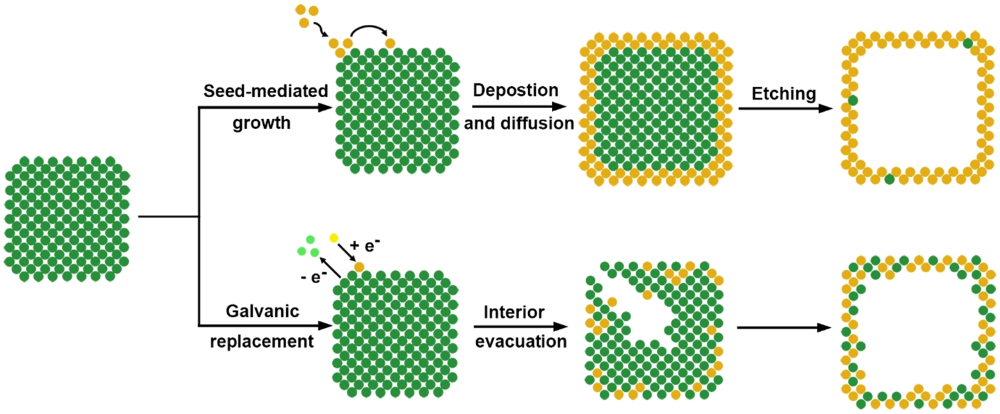

Figure 26. Schematic illustration of seed-mediated growth and galvanic replacement for the generation of core−shell and hollow metal nanocrystals. The 2-D atomic models correspond to the cross-section of a cubic seed at different stages into the reaction. Preformed nanocrystals with a well-defined shape serve as the template in both processes in an effort to replicate the atomic arrangement and control the surface structure of the product.

Au nanoparticles melted during the attachment process and finally merged together to form a belt. There are a variety of possible factors that could cause the contrast in the Au belt observed under TEM, including bending, grain boundaries, and change in the thickness. In this work, based on the electron diffraction pattern, the authors claimed that the product was single crystal.

4.4.2. Wavy Wires. Wavy wires are unique due to the presence of a large number of grain boundaries on their surface. They are usually formed through oriented attachment of small nanoparticles and take a worm-like morphology. Some typical examples of wavy wires with surface containing a high density of grain boundaries will be discussed.

4.4.2.1. Iridium. It is still a grand challenge to synthesize Ir nanocrystals with well-defined shapes and morphologies, which could be primarily ascribed to the difficulty in growing Ir nanocrystals to large sizes.[409] Wavy wires is one of the few samples that can be produced to present well-defined surface structures for Ir nanocrystals. In a typical protocol, H_2IrCl_6 was reduced by $NaBH_4$ in the presence of CTAB, generating ultrathin, wavy wires with a diameter around 1.7 nm.[351] From high-resolution TEM, {111} and {200} were identified as the major facets exposed on the surface of the wires. It was proposed that the attachment of the thermodynamically unstable, small Ir nanoparticles formed in the early stage of a synthesis contributed to the formation of the wavy wires, and the junctions between adjacent nanoparticles induced the formation of grain boundaries and twin defects.

4.4.2.2. Gold. Oriented attachment has also been applied to the synthesis of Au wires. Because of the low stacking fault energy of Au,[37] defects were commonly observed in the wavy wires. In an early study, Au wavy wires were synthesized through the attachment of small single-crystal Au nanoparticles capped by OAm.[352] It was suggested that the nanoparticles could attach to each other in a perfectly matched orientation or a misoriented fashion, giving single-crystal and defect-lined wires, respectively. It was proposed that the amine group in OAm had a stronger binding to the high-index facets on Au nanoparticles compared to low-index facets and the coverage was lower on {111} than {100}.[410] Therefore, it was easier to have the OAm on Au{111} facets partially removed than from other types of facets. The preferential removal of OAm from the {111} facets of Au nanoparticles induced the particle fusion along this direction for the generation of wires. Similarly, wavy wires were directly obtained by reducing $HAuCl_4$ with AA in the presence of CTAB as a result of oriented attachment, followed by cold welding, surface diffusion, and additional growth (Figure 25D,E).[353]

5. CORE−SHELL AND HOLLOW NANOCRYSTALS

As discussed in section 4, it remains a major challenge to achieve shape- or facet-controlled synthesis for some noble metals as limited by their intrinsic properties and/or the lack of proper capping agents. To this end, replicating the atomic arrangement on existing metal nanocrystals through seed-mediated growth or template-engaged galvanic replacement offers a viable approach for presenting these noble metals in well-defined and controllable surface structures. In some cases, it is also feasible to transfer the crystal structure (or phase) from the underlying nanocrystal to the metal deposited on its surface. Figure 26 shows a side-by-side comparison of these two different methods. Both of them involve the use of preformed nanocrystals as a template to dictate and control the surface structure of the final products. To a certain extent, the galvanic replacement route can be considered as a natural integration of both the seed-mediated deposition and selective etching processes.

This section covers examples of both core−shell and hollow nanocrystals fabricated using the surface-replicating approach. Although the major focus of this review is on monometallic systems, the nanocrystals with a bimetallic, core−shell structure offers an alternative for those metals that are still limited by our synthetic capabilities in terms of shape control. For the core−shell system, one can tune the shell thickness to either nullify or leverage the impacts from the metal in the core. For example, when the shell is more than six atomic layers in thickness, the ligand and geometric effects arising from the metal in the core can be largely neglected.[37,411,412] Regarding the synthesis of core−shell nanocrystals, the core metal should be judiciously selected to ensure that it shares similar identities, including lattice constant and electronegativity, with the shell metal. During the synthesis, it is critical to ensure adequate surface diffusion relative to atom deposition so that the adatoms will adopt a layer-by-layer rather than island growth mode. As a result, a smooth surface

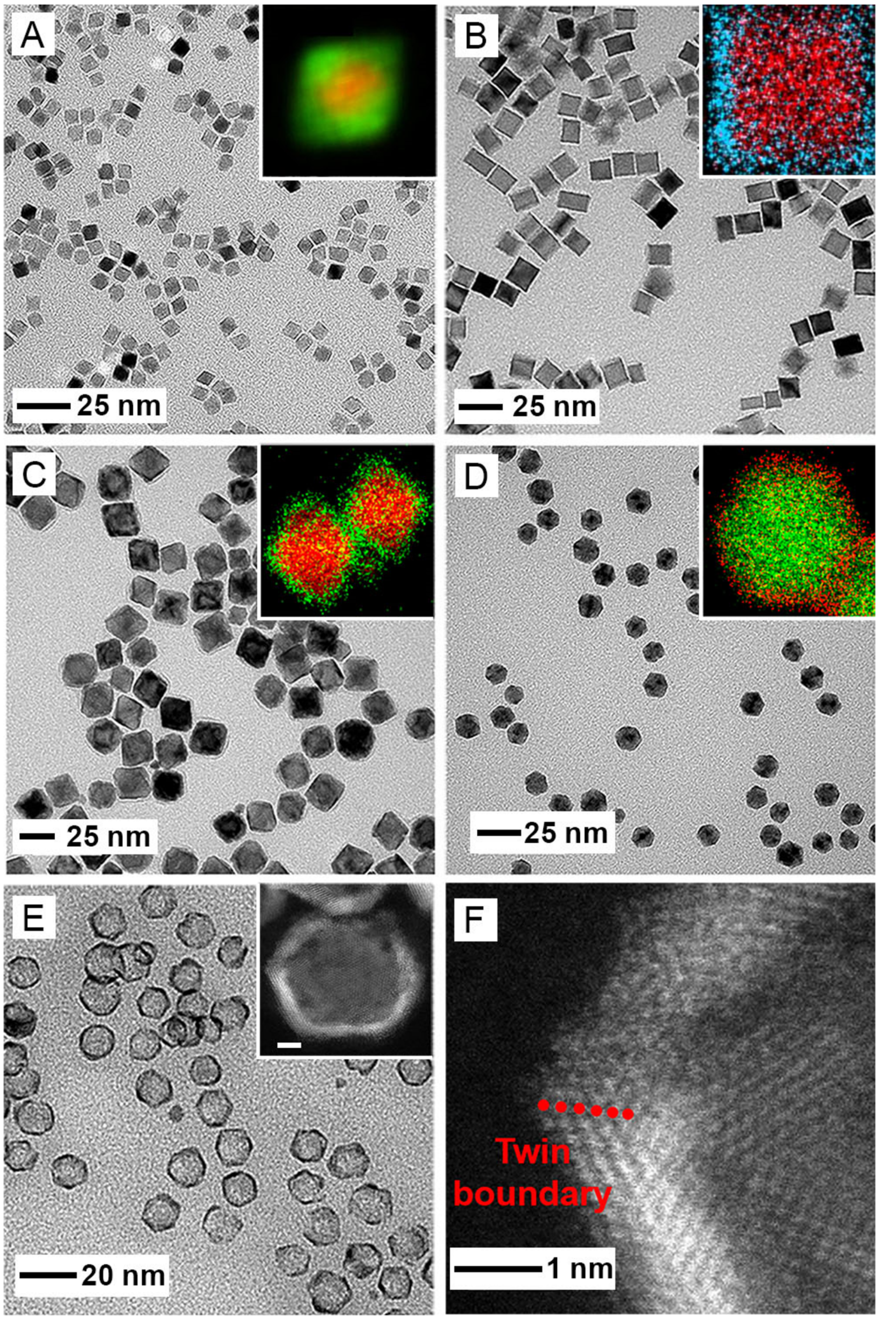

Figure 27. (A–D) TEM images of (A) Rh@Ru core–shell octahedra and Pd@Ru core–shell nanocrystals with (B) cubic, (C) octahedral, and (D) icosahedral shapes, respectively. The insets show the corresponding EDX mapping of an individual nanocrystal. (E and F) TEM and HAADF-STEM image of Ru icosahedral cages, indicating the twin boundary preserved in the Ru cage. The scale bar in the inset of panel E is 2 nm. (A) Reprinted with permission from ref 95. Copyright 2019 American Chemical Society. (B) Reprinted with permission from ref 354. Copyright 2016 American Chemical Society. (C) Reprinted with permission from ref 355. Copyright 2017 American Chemical Society. (D–F) Reprinted with permission from ref 356. Copyright 2018 American Chemical Society.

will be formed to faithfully replicate the atomic structure on the underlying seed.

When the shell is more resistant toward oxidative etching than the core, it will be feasible to selectively remove the core for the fabrication of a novel class of nanocrystals known as cages. The success in the extraction of the core lies in the formation of atom-wide channels through interdiffusion between the core and shell atoms during the synthesis or codeposition of the atoms when the shell is generated.[413] By optimizing the etching conditions, the facet or surface structure on the shell can be well preserved. The as-obtained cages are characterized by a hollow interior, ultrathin and porous walls, as well as a well-defined surface structure. The porous walls of a cage allow the reaction species to easily access the atoms on the inner surface. When combined with an ultrathin thickness for the walls, one can substantially increase the utilization efficiency of atoms. In the meantime, the well-defined facets offer the capability to optimize the active sites for a variety of reactions.

In addition to the two-step method that involves seed-mediated growth and selective etching, another effective strategy for fabricating hollow metal nanocrystals is based on template-engaged galvanic replacement. This approach leverages the spontaneous reduction of metal ions at the expense of the template.[413] In principle, the only requirement for galvanic replacement is that the reduction potential of the template metal is lower than that of the metal to be deposited. The power of galvanic replacement in engineering the properties of nanocrystals can be understood from three major aspects.[413,414] First, the elemental composition of the final product can be tuned by reacting the template with different amounts of the metal precursor. Second, the final product typically possesses porous walls, whose thickness can be readily controlled by varying the amount of the precursor added into the reaction mixture. Third, since the newly formed atoms are deposited on the surface of the template, the final product typically takes a surface structure closely resembling that of the original template. In this section, we focus on the synthesis of bimetallic core−shell nanocrystals with controlled surface structures and the hollow nanocrystals derived from them. We also showcase the leverage of other strategies such as galvanic replacement and self-etching for the production of hollow metal nanocrystals with well-defined surface structures. The presentation follows the order of atomic number.

5.1. Ruthenium

In contrast to all other noble metals that feature an fcc structure, bulk Ru crystallizes in an hcp phase. The intrinsic hcp phase and low reduction potential, as well as the high cohesive and surface energies, make it a difficult task to fabricate Ru nanocrystals with well-defined shapes via the conventional one-pot synthesis. A viable solution to this issue is to introduce a template into the synthesis. The presence of a template not only results in a lower nucleation barrier but also makes it possible to create a well-defined surface structure on the final product. One compelling example can be found in the hydrothermal synthesis of Rh@Ru core−shell octahedra by templating with 4.5 nm Rh cubes (Figure 27A).[95] The use of 4.5 nm of Rh cubes as the seeds was critical to the successful synthesis in multiple aspects: (i) Rh shares similar physicochemical properties with Ru, including lattice constant and electronegativity, promoting epitaxial growth of Ru; (ii) Rh is stable under hydrothermal conditions and can be retained throughout the growth process; and (iii) Rh cubes can be prepared as small as 4.5 nm, advantageous for achieving adequate surface diffusion of Ru atoms relative to deposition. During the synthesis, the nanocrystals gradually evolved from cubes to truncated cubes, cuboctahedra, and truncated octahedra. Eventually, Rh@Ru octahedra with well-defined {111} facets were obtained. Interestingly, the arrangement of the deposited Ru atoms followed an fcc structure rather than the hcp of bulk Ru. Despite this accomplishment, the synthesis of Ru-based nanocrystals featuring other surface structures is yet to be explored.

In a set of parallel studies, Pd nanocrystals were extensively exploited as the templates for Ru deposition. Although the lattice mismatch between Pd and Ru is slightly greater than that between Rh and Ru (1.8% vs 0.5%), the use of Pd seeds offers many advantages. First, there are a number of well-established protocols for the synthesis of Pd nanocrystals featuring controlled sizes, shapes, and internal structures.[200] Second, compared with Ru, Pd is much more susceptible to oxidative etching, making it easier to produce Ru hollow nanocrystals through selective etching of the Pd in the core. In contrast to the one-shot synthesis involving Rh seeds, the Ru(III) precursor had to be titrated into the growth solution containing Pd seeds using a programmable syringe pump. As such, the generation rate and thus deposition rate of Ru atoms could be manipulated to ensure layer-by-layer growth. With Pd cubes of 10 nm in size, for example, Pd@Ru core−shell cubes with Ru shell thickness controlled up to six atomic layers have been successfully synthesized (Figure 27B).[354] Significantly, the Ru atoms in the shells faithfully replicated both the {100} facets and fcc packing of the underlying Pd template.

When Pd octahedra were utilized as the template, self-nucleation would become a major issue because of the lower surface energy of Pd{111} facets relative to the {100} counterparts.[355] This issue was mitigated by adding KBr to manipulate the reduction kinetics of Ru(III) ions so that the concentration of the Ru atoms was reduced to a level favorable for heterogeneous nucleation while avoiding homogeneous nucleation. As a result, the deposited Ru atoms preferentially diffused to the side faces of the Pd octahedral seeds in a layer-by-layer manner rather than piling up at the edges and corners, giving rise to the formation of Pd@Ru core−shell octahedra (Figure 27C). The core−shell octahedra displayed well-controlled {111} facets, together with a Ru shell of five atomic layers in thickness. Simply by varying the size of Pd octahedral seeds, the dimension of the Pd@Ru core−shell octahedra could be readily tuned in the range of 12−26 nm. Again, the Ru atoms in the core−shell octahedra were crystallized in an fcc structure rather than the hcp phase intrinsic to bulk Ru.[355] Although both fcc-{111} and hcp-{0001} facets were composed of close-packed atoms, the Ru atoms preferred to follow the fcc-{111} rather than hcp-{0001} stacking in order to lower the total surface energy by maintaining a smooth surface at the edges of the fcc template. Otherwise, the formation of a large number of low-coordination atoms at the edges would substantially increase the total surface energy of the nanocrystals.

In addition to the single-crystal facets, twin structures are also attractive for various reactions owing to the existence of plenty of highly active sites and induced surface strains.[415,416] In the context of metal deposition, the twin boundaries are most favorable sites for Ru deposition due to their highest surface energy. The strong interaction between the defect site and a Ru atom also impedes its diffusion to other areas on the surface. Nevertheless, preferential surface diffusion over atom deposition could still be achieved when switching from octahedral to icosahedral template while keeping other reaction conditions unchanged. By following a layer-by-layer growth mode, the deposited Ru atoms faithfully replicated both the {111} facets and twin boundaries on the Pd icosahedral template, in addition to the fcc structure (Figure 27D−F).[356] Similarly, Pd@Ru core−shell plates with tunable thicknesses were also attained using a hydrothermal approach, in which the Ru shell was characterized by stacking faults and {111} facets, as well as an fcc structure.[417]

By subjecting the Pd@Ru core−shell nanocrystals to wet-chemical etching for the selective removal of the Pd in the core, Ru cages were obtained. A selective etchant for oxidizing Pd was based on the Fe^{3+}/Fe^{2+} pair. To facilitate the removal of Pd from the core, Br^- ions were added to increase the difference in standard reduction potentials between the etchant (Fe^{3+}/Fe^{2+}, 0.77 V) and Pd through ligand exchange ($PdCl_4^{2-}/Pd$ = 0.59 V, $PdBr_4^{2-}/Pd$ = 0.49 V).[418] Under optimal conditions, both the surface structure and the unconventional fcc phase could be transferred to the resultant

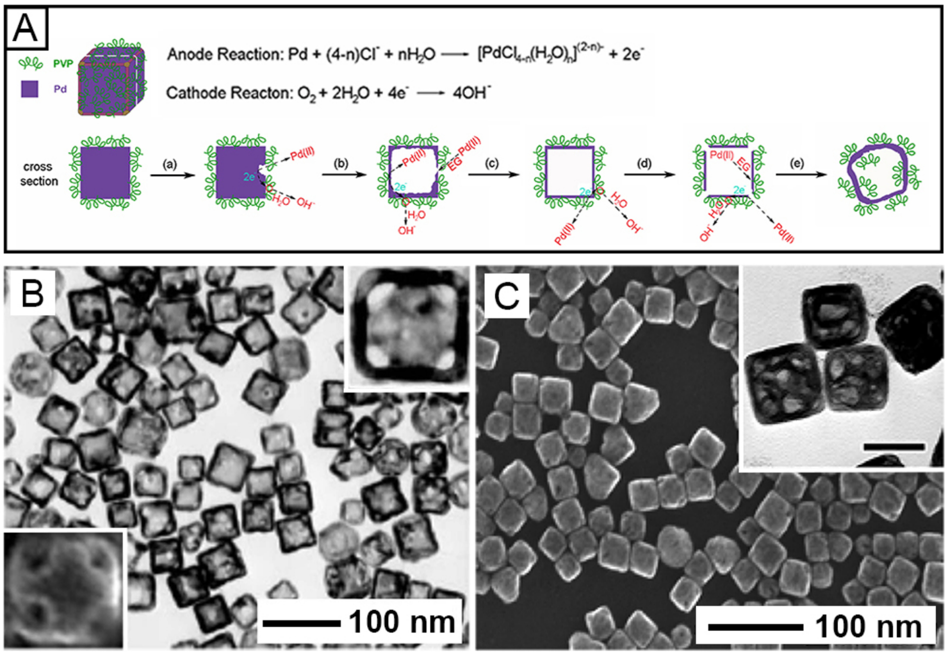

Figure 28. (A) Schematic illustrating the synthesis of Pd hollow nanocrystals by corrosive etching. The presence of a Cl^-/O_2 pair promotes the self-etching of Pd cubes, resulting in the formation of Pd cubic boxes and then cages. (B) TEM image of Pd cubic cages synthesized by corrosive etching with well-defined openings at the corners. The insets show TEM and SEM images of an individual cage at higher magnification. (C) SEM image of Pd−Ag cubic cages obtained through a galvanic replacement route. The inset shows a TEM image of the cages (scale bar: 50 nm). (A and B) Modified with permission from ref 360. Copyright 2005 Wiley-VCH. (C) Reprinted with permission from ref 361. Copyright 2005 American Chemical Society.

Ru cages. Using this approach, Ru{100}, Ru{111}, and Ru{111} plus twin boundaries were all retained in the corresponding cubic, octahedral, and icosahedral cages, respectively.[354−356] The three types of cages featured a hollow interior and ultrathin, porous walls of 5−6 atomic layers in thickness. Both features are instrumental to maximizing the utilization efficiency of Ru atoms and thus boosting the mass-specific activity of the catalyst. After selective etching, only a small portion of the Pd atoms (<12.5 wt %) were left behind in the cages whereas the proportion of Ru contents was greater than 87.5 wt %, confirming the dominance of Ru.

Apart from seed-mediated growth followed by selective etching, galvanic replacement is another effective route to the fabrication of Ru-based cages. However, it has been a long-lasting challenge to control the shape of Ru-based hollow nanocrystals through galvanic replacement. The predicament can be ascribed to the unfavorable thermodynamics between Ru(III) ions and the template metals featuring controllable shapes, such as Pd and Pt. To address this issue, our group reported a facile synthesis of Pd−Ru cages via I^--assisted galvanic replacement.[357] The success of this synthesis depended on the addition of I^- ions into the reaction to enforce ligand exchange with Pd(II) ions for the formation of PdI_4^{2-} ions, a precursor with a reduction potential as low as 0.18 V. As such, the difference in reduction potential between the Pd template (PdI_4^{2-}/Pd, 0.18 V) and Ru(III) ions (Ru^{3+}/Ru, 0.39 V) became thermodynamically capable of activating the galvanic replacement reaction, giving rise to the production of Pd−Ru alloy cages. The as-synthesized cages possessed a hollow interior, ultrathin walls of 2.5 nm in thickness, and a cubic shape. Additionally, Ru atoms in the cages were crystallized in an fcc lattice. The size of the cages could be readily tuned in the range of 6−18 nm by using Pd seeds with different sizes. Although the protocol could be applied to Pd octahedral, decahedral, and icosahedral templates for the generation of cages, their shapes, however, were significantly deviated from the templates owing to the strong binding of I^- ions to the {100} facets and suboptimal reduction kinetics.

5.2. Rhodium

Although Rh has been synthesized as nanocrystals with a variety of shapes, some samples, for example, octahedral nanocrystals, showed a poorly defined shape and/or a rough surface, thus limiting the exploration of their facet-dependent properties.[207] To this end, seed-mediated growth offers an effective strategy for controlling the surface structure of Rh nanocrystals by templating with the preformed seeds with desired attributes.[419] Relative to other fcc metals including Ag, Au, Pd, and Pt, the synthesis of Rh-based core−shell nanocrystals has been a challenging task. The difficulty can be rationalized from the following aspects: (i) the energy barrier to heterogeneous nucleation of Rh is not significantly reduced as compared with that to homogeneous nucleation[419] and (ii) the bond energy of Rh−Rh (236 kJ mol^{-1}) is much greater than those of Ag, Au, and Pd, leading to a higher energy barrier to the diffusion of Rh adatoms for the formation of a smooth surface. To address the issue, a facile template-directed method was developed for the synthesis of Pd@Rh core−shell octahedra, by which the deposited Rh atoms faithfully replicated the octahedral shape of the underlying seeds.[419] To mitigate the homogeneous nucleation issue of Rh atoms on the Pd{111} facets, a mild reductant, TTEG, was used to retard the reduction rate of the Ru(III) precursor and meanwhile, an elevated temperature was used to promote surface diffusion. Additionally, the use of Pd octahedral seeds with an edge length as short as 6.4 nm was also critical to achieve layer-by-layer growth for the Rh atoms. When switched to Pd octahedra with enlarged sizes of 18 and 37 nm, the deposited Rh atoms followed an island growth mode. The Rh shell in the as-obtained Pd@Rh core−shell octahedra displayed well-defined {111} facets when the shell thickness was controlled at roughly 0.5 nm, corresponding to two atomic layers.

Despite the accomplishments in controlling the surface structure of Rh nanocrystals, the ever-increasing price and extremely low abundance in the Earth's crust create an obstacle to the large-scale use of Rh. One effective solution to this predicament relies on the synthesis of Rh hollow nanocrystals with well-controlled surface structures. To this end, a hydrothermal method was developed for the one-pot synthesis of Pd@Rh core−shell cubes, in which Br^- ions were added to help create {100} facets on the final product.[358] When subjected to an etchant based on the I^-/O_2 pair, the Pd core could be selectively removed while the {100} facets were transferred into the resultant Rh cages. The as-synthesized cages had an average edge length of 14.4 nm and a wall thickness of about 4 nm. To further reduce the wall thickness while still maintaining the surface structure, the one-pot synthesis was modified by introducing I^- ions as an additive.[359] In addition to the role as a capping agent for the expression of {100} facets, the presence of I^- ions also helped retard the reduction of both Pd(II) and Rh(III) precursors. The argument was confirmed by the formation of Pd@Rh core−shell cubes with a greater size relative to those prepared using Br^- ions (33.0 vs 14.4 nm). After selective removal of the Pd core, Rh cubic cages with well-defined {100} facets and a wall thickness of 2 nm were attained.

5.3. Palladium

Different from other noble metals, there are a large number of protocols available for the shape-controlled synthesis of Pd nanocrystals.[71,132,139,147,166,242,243,306] However, almost all of the reported nanocrystals feature a solid interior. When used as catalysts, only the surface atoms are accessible to the reaction species, while all of the atoms in the bulk are more or less wasted, drastically compromising the mass-specific activity. One effective strategy for mitigating this issue relies on the synthesis of Pd hollow nanocrystals with well-defined surface structures, by which the utilization efficiency of atoms is substantially enhanced while the benefits stemming from the controlled shape are still kept. In one report, a corrosion-based method was developed for the facile synthesis of Pd cages (Figure 28A,B).[360] The formation of such hollow nanocrystals involved three major stages: (i) the Pd(II) precursor was reduced to generate Pd cubes with truncation at the corners; (ii) the self-templating and self-etching of the Pd cubes, together with the deposition of Pd atoms formed via reduction, giving rise to the formation of boxes; (iii) further etching led to the formation of holes at the corners, turning the boxes into cages. Both the boxes and cages were characterized by a hollow interior, a cubic shape, well-defined {100} facets, and thin walls, except for the presence of holes on the surface of cages. The components key to this synthesis included the Cl^- ions (from Na_2PdCl_4) and a small amount of H_2O for O_2 dissolution, facilitating the formation of a Cl^-/O_2 pair to promote the self-etching process. The involvement of excess PVP in the synthesis was another critical parameter, which could effectively cover the {100} facets of each Pd cube and make the outer faces less active than the newly formed surface. Once a pit was formed at a specific site on the surface of a Pd cube, further corrosion would preferentially take place inside the pit, eventually leading to the formation of a hollow structure.

Another effective strategy for producing Pd-based hollow nanocrystals involves the use of galvanic replacement. By templating with 50 nm Ag cubes, Pd−Ag cubic cages were successfully synthesized (Figure 28C).[361] The success of this synthesis relied on the favorable thermodynamics between the Ag template (Ag^+/AgCl, 0.20 V) and Pd(II) ions ($PdCl_4^{2-}$/Pd, 0.59 V). During the synthesis, white AgCl precipitates was observed, validating the involvement of AgCl in the galvanic replacement reaction. The as-obtained Pd−Ag cages were able to duplicate the attributes of the Ag template, showing a cubic shape and well-defined {100} facets, except for the increase of edge length to 63 nm. Based on elemental analysis, the Pd/Ag ratio in the cages was found to be 2:3, suggesting an alloy structure.

5.4. Iridium

Similar to the case of Rh, it is also a challenging task to fabricate Ir-based core−shell nanocrystals owing to the even higher bond energy (361 kJ mol^{-1}).[420] As a consequence, the Ir atoms tend to follow an island growth mode for the generation of tiny nanoparticles.[409,421] In an effort to obtain core−shell nanocrystals, one has to accelerate surface diffusion relative to the deposition of Ir atoms. To this end, a polyol method was developed for the synthesis of Pd@Ir core−shell cubic and octahedral nanocrystals by templating with Pd seeds featuring cubic and octahedral shapes, respectively (Figure 29).[409] During the conformal deposition, the Ir shell was able to faithfully replicate the surface structure of the underlying Pd template when its size was only 6 nm while the Ir thickness was controlled below four atomic layers. The successful production of Pd@Ir nanocrystals with well-defined surface structures relied on the optimization of a set of reaction parameters, including a slow injection rate for the Ir(III) precursor, a small size for the Pd template, and an elevated reaction temperature.[409] The injection rate of the Ir(III) precursor was strongly associated with the reduction rate and thus affecting the deposition rate of Ir atoms. When the Ir(III) precursor was added at a faster pace, the deposition of Ir atoms would be switched from layer-by-layer to island growth mode, leading to the formation of a rough surface. The size of the template determined the distance that the Ir adatoms had to diffuse across in order to cover the entire surface, with a smaller size more favorable for generating the core−shell nanocrystals. A notable difference was observed when the size of the Pd cubes was increased from 6 to 18 nm. In the latter case, plenty of Ir small islands were formed on the template, in addition to free-standing Ir nanoparticles generated through homogeneous nucleation. The reaction temperature was another parameter vital to the formation of a smooth shell as it strongly affected both the deposition and diffusion rates of Ir atoms. When the reaction temperature was lowered, the Ir adatoms would not have sufficient kinetic energy for diffusion, generating small islands on the template.

The reaction parameters of the above protocol were also optimized by increasing the amount of the Pd cubes, reducing the concentration of the reductant, and decreasing the injection rate of the Ir(III) precursor to achieve layer-by-layer growth on Pd cubes as large as 18 nm in edge length.[422] All those modifications collectively contributed to a slow reduction rate for the Ir(III) precursor, decreasing the

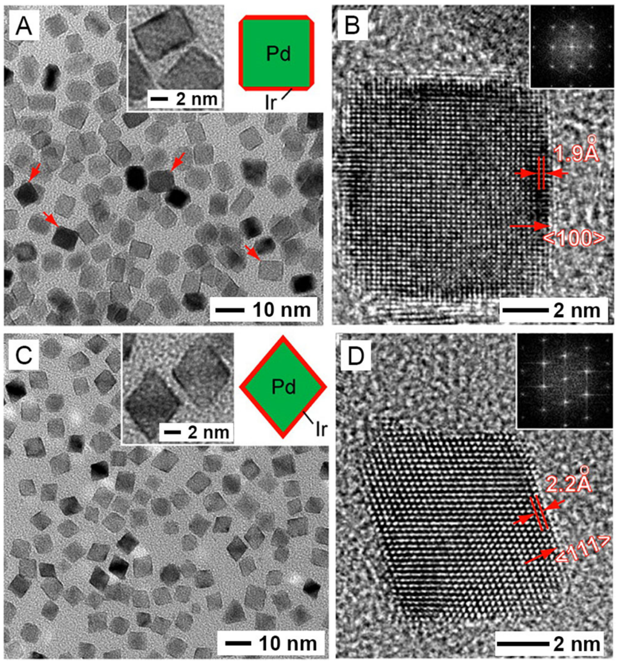

Figure 29. (A) TEM image of Pd@Ir core−shell cubes. (B) High-resolution TEM image of an individual Pd@Ir cube along the [100] zone axis, clearly demonstrating that the core−shell cube was bounded by Ir{100} facets. The inset shows the corresponding Fourier transform pattern. (C and D) TEM and high-resolution TEM images of Pd@Ir core−shell octahedra enclosed by Ir{111} facets. The insets in panels A and C show the TEM images at higher magnification and 2-D schematic models of the core−shell nanocrystals. Reprinted with permission from ref 409. Copyright 2014 American Chemical Society.

deposition rate of the Ir atoms. Given that surface diffusion (i.e., reaction temperature) was kept the same, the deposited Ir atoms would have enough time to diffuse across the entire surface of an 18 nm Pd cube rather than accumulated at the corners and edges, leading to the generation of Pd@Ir core−shell cubes with well-defined {100} facets. After deposition, the average edge length of the cubes was increased to 19.2 nm, suggesting the effective deposition of Ir shells. Notably, the thickness of the Ir shell in the core−shell cubes was only about three atomic layers, thinner than the case of 6 nm Pd cubes. The reduced shell thickness could be attributed to the suppressed reduction rate of the Ir(III) precursor in the modified protocol and thus a lower conversion to Ir atoms. In this case, the thin Ir shell (i.e., 3.2 atomic layers) made it more challenging to fabricate Ir cages by selectively removing the Pd core without breaking the shell.

A modification was made to the protocol for the growth of a thicker Ir shell on the 18 nm Pd cubes.[362] The success of the new protocol relied on the deceleration of the deposition rate of Ir atoms in multiple ways: (i) diluting the Ir(III) precursor by eight times while doubling the total amount of the precursor; (ii) decreasing the injection rate of the Ir(III) precursor by two times; (iii) reducing the concentration of the reductant by 2.5 times; and (iv) introducing a large amount of KBr into the synthesis, an additive known for promoting layer-by-layer growth for Pt atoms.[362] The Ir shell thickness could be increased to 1.1 nm, corresponding to about six atomic layers. After subjecting the core−shell cubes to an etching solution containing $FeCl_3$, KBr, and HCl, Ir cages were obtained. The cages had an edge length of 19.7 nm and were enclosed by well-defined {100} facets. The percentage of Ir content was as high as 88.9 wt %, confirming the dominance by Ir in the cages.

5.5. Platinum

As an intriguing catalytic material, Pt has found widespread use in heterogeneous catalysis. Its extremely low abundance and high price, however, set obstacles to the commercialization of many technologies based on Pt catalysts, such as fuel cells. To mitigate this issue, one strategy is to deposit a few atomic layers of Pt atoms on a template for the generation of core−shell nanocrystals, followed by selective removal of the core for the production of Pt hollow nanocrystals.[363−365,423] Under the right conditions, the surface structure can be faithfully transferred from the template to the core−shell nanocrystal and further to the hollow nanocrystals.[38] Among various metals, Pd is the best candidate for serving as a template because it shares similar physicochemical identities with Pt in terms of lattice constant (only 0.77% lattice mismatch) and electronegativity, in addition to many well-established protocols for the synthesis of Pd nanocrystals with controlled sizes, facets, and twin structures. Using 18 nm Pd cubes as template, $Pd@Pt_{nL}$ (n denotes the number of atomic layers) core−shell cubes could be achieved by titrating the solution of a Pt(IV) precursor into a suspension of Pd cubes in EG at a slow rate while holding the system at 200 °C.[371] The Pt shell faithfully replicated the {100} facets of the underlying Pd cubes and its thickness could be tuned from one to six atomic layers by varying the amount of the Pt(IV) precursor (Figure 30).

A similar approach was also successfully extended to Pd octahedral nanocrystals. In contrast to the {100} facets on cubes, the {111} facets on octahedra have a greater packing density of atoms and a lower surface energy. As a consequence, homogeneous nucleation became a major challenge when applying the same protocol for the synthesis of $Pd@Pt_{nL}$ core−shell cubes to the octahedral system. To mitigate this issue, a diluted Pt(IV) precursor solution and a reduced titration rate were used to ensure a layer-by-layer growth mode for the Pt atoms on 19 nm Pd octahedra, giving rise to the formation of $Pd@Pt_{nL}$ core−shell octahedra.[424] The Pt shell in the core−shell nanocrystal also strictly replicated the surface structure of the underlying Pd octahedron, whose surface was dominated by {111} facets, together with a small fraction of {100} facets due to the slight truncation at corners.

Nanocrystals with multiple twin defects are highly desired for catalytic application owing to the abundance of highly active atoms on the twin boundaries and the surface strain on side faces. When multiply twinned Pd nanocrystals were employed as template, the twin boundaries were more favorable sites for the initial deposition of Pt atoms due to their high surface free energy.[61,62] When conducting the synthesis at 200 °C, the Pt atoms initially deposited on the vertices of the icosahedron can diffuse along the twin boundaries and further to the side faces, enabling a layer-by-layer growth mode.[416] The resultant Pd@Pt core−shell icosahedra featured a conformal and uniform shell, well-defined {111} facets, and twin boundaries, as well as tunable shell thicknesses of 0.7−4.5 atomic layers (Figure 31). The deposition behavior of Pt atoms on Pd decahedral template was completely different from the case of icosahedral template even under the same condition.[364] On a decahedron, there exists two types of vertices, with the type-A intersected by two

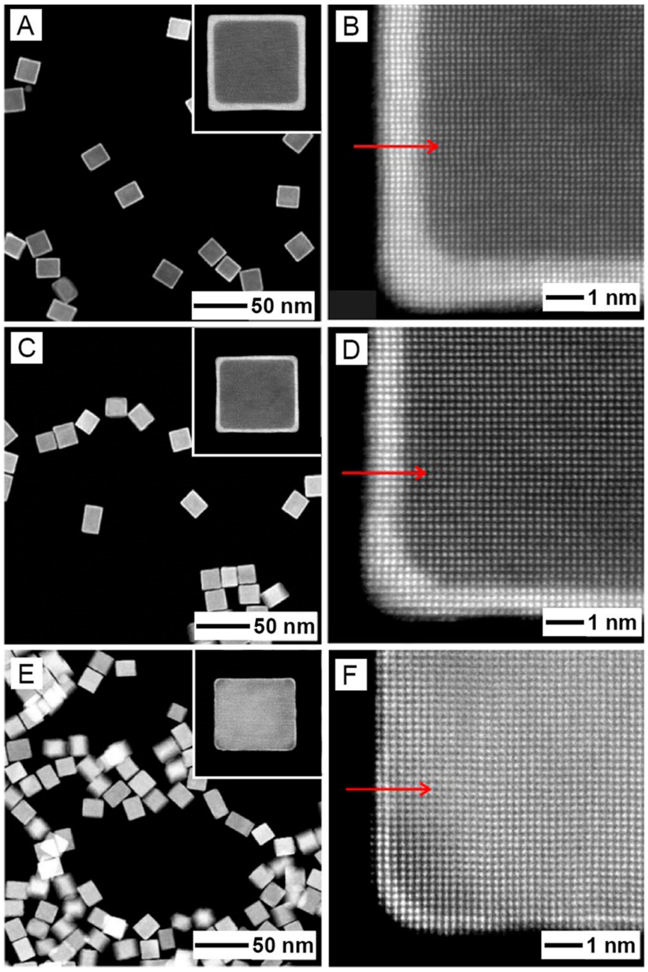

Figure 30. Low-magnification and atomic-resolution HAADF-STEM images of (A and B) Pd@Pt$_{6L}$, (C and D) Pd@Pt$_{4L}$, and (E and F) Pd@Pt$_{1L}$ core−shell cubes, respectively, showing the well-defined surface of the Pt shell and the different numbers of Pt atomic layers along the red arrows. The insets show HAADF-STEM images of individual core−shell cubes at a higher magnification. Reprinted with permission from ref 371. Copyright 2014 American Chemical Society.

single-crystal edges and two twin boundaries and type-B intersected by five twin boundaries. The atoms at type-A vertices had a lower CN (4 vs 5) and higher tensile strain than those at type-*B* vertices,[60,61] making the former more favorable sites for Pt deposition and accumulation. In the presence of surface diffusion, the Pt adatoms on the type-*A* vertices would more preferentially diffuse to the edges and twin boundaries rather than to the side faces owing to the lower CN and higher surface energies of the former sites, resulting in the formation of concave side faces.

Palladium nanocrystals with other types of twin structures and/or facets, including penta-twinned wires and plates, could also be leveraged as templates to direct the deposition of Pt atoms for expanding the diversity of surface structure.[147,423,425] With regard to the penta-twinned Pd wires, a uniform Pt sheath could still be generated for the formation of Pd@Pt core−sheath wires.[147] As for Pd plates, at a slow injection rate for the Pt(IV) precursor and an elevated temperature, the Pt adatoms were able to diffuse from the defect sites to the basal planes for the generation of a smooth shell and thus Pd@Pt core−shell plates.[423] For the polyol-based system at 200 °C, the Pd plate was conformally coated with a more or less uniform Pt shell due to the use of a high reaction temperature. When switched to a water-based system at 80 °C, Pt shell could still be formed but with a greater thickness on the side faces than on the basal planes.

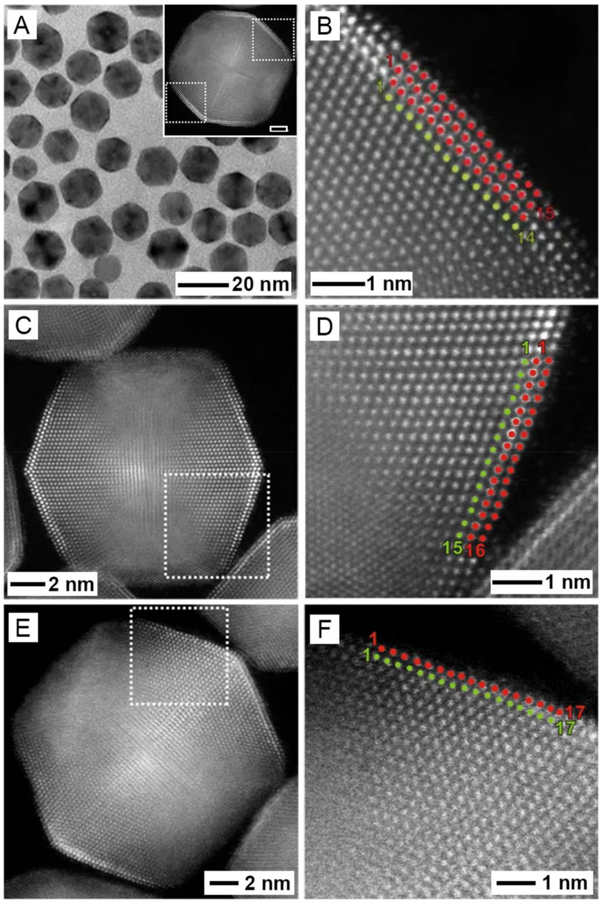

Figure 31. (A) TEM image of Pd@Pt$_{2.7L}$ core−shell icosahedra. The inset shows the HAADF-STEM image of an individual Pd@Pt$_{2.7L}$ icosahedron (scale bar: 2 nm). (B) Atomic-resolution HAADF-STEM image taken from the edge of a Pd@Pt$_{2.7L}$ icosahedron, revealing the detailed surface structure of the core−shell nanocrystal (green dots: Pd atoms; red dots: Pt atoms). (C−F) Atomic-resolution HAADF-STEM images of (C and D) Pd@Pt$_{2L}$ and (E and F) Pd@Pt$_{0.7L}$ icosahedra, respectively, showing the different numbers of Pt atomic layers on the Pd seeds. Reprinted with permission from ref 416. Copyright 2015 Nature Publishing Group.

When subjected to an etchant, the Pd core could be selectively removed from the Pd@Pt$_{nL}$ nanocrystals for the production of Pt cages with well-defined surface structures, including the specific type of facet and twin boundaries (Figure 32). To facilitate the etching of Pd in the core, a small amount of the Pd(II) precursor could be added into the Pt(IV) precursor solution (at a molar ratio of 1:99) to intentionally create more Pd channels in the shell through codeposition. A typical etching solution contained $FeCl_3$, HCl, KBr, and PVP, and their concentrations need to be individually optimized when applying to core−shell nanocrystals with different shapes.[363] Owing to a greater packing density of the {111} facets relative to {100} facets, the etching solution used for the generation of Pt octahedral cages needed to be more concentrated than what was used for the generation of cubic cages. In this case, an increased concentration of $FeCl_3$ and HCl, together with an elongation of the etching time, were

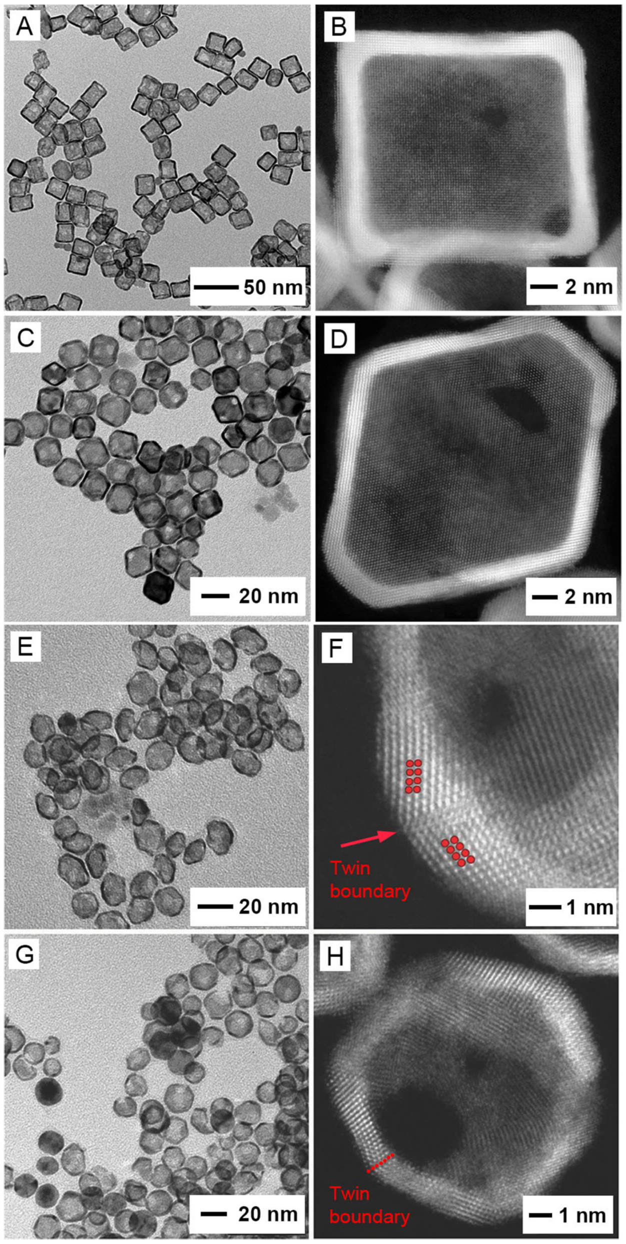

Figure 32. TEM and atomic-resolution HAADF-STEM images of Pt-based cages with (A and B) cubic, (C and D) octahedral, (E and F) decahedral, and (G and H) icosahedral shapes, respectively, demonstrating their well-defined surface structures. (A–D) Reprinted with permission from ref 363. Copyright 2015 AAAS. (E and F) Modified with permission from ref 364. Copyright 2015 American Chemical Society. (G and H) Modified with permission from ref 365. Copyright 2016 American Chemical Society.

required to provide sufficient etching power for the formation of Pt octahedral cages.[363] After Pd etching, the Pt cages showed a well-preserved shape of the original core–shell nanocrystals, with the surface covered by well-defined facets. The weight percentage of Pt contents could be as high as 91%, suggesting the dominance of Pt in the cages. Typically, the wall of the Pt cages was thicker than the Pt shell of the core–shell nanocrystals due to the inclusion of some remaining Pd atoms and the presence of vacancies. For example, starting from the Pd@$Pt_{4.5L}$ core–shell icosahedra, Pt icosahedral cages with a wall thickness of about six atomic layers were obtained.[365] Their surface was characterized by well-defined {111} facets and twin boundaries, in addition to some small holes.

Compared with the approach involving core–shell nanocrystals and selective removal of the core, galvanic replacement offers a simpler route to the fabrication of hollow nanocrystals and can be completed within a short period of time.[413] However, different from the products obtained from the two-step method, the hollow nanocrystals prepared using galvanic replacement typically feature an alloy composition. Additionally, since galvanic replacement involves the random removal of template atoms and deposition of Pt atoms, it is not easy for the deposited Pt atoms to faithfully replicate the shape or surface structure of the template. As a result, the as-synthesized hollow nanocrystals often showed a rough surface and reduced crystallinity.[413] A recent study reported a facile route to the synthesis of Pt–Ag cages with a smooth surface using 15.8 nm Ag cubes as the sacrificial template.[426] The success of this synthesis relied on the use of a syringe pump to titrate the Pt(II) precursor into a suspension containing Ag cubes, so that galvanic replacement could be manipulated at an appropriate rate favorable for the formation of a smooth surface. Additionally, the reaction temperature also had to be finely controlled, which not only determined surface diffusion but also affected the rate of galvanic replacement.[426] After reaction, the as-obtained Pt–Ag cages were characterized by an edge length of 18 nm and a wall thickness of about 3 nm, as well as well-defined {100} facets. Apart from Ag cubes, other types of templates such as Ag wires[427] and Se wires[428] have also been employed for the production of Pt nanotubes through galvanic replacement. However, their surfaces were poorly defined, primarily owing to the lack of a precise control over the galvanic replacement rate (i.e., the deposition rate of Pt atoms) and surface diffusion.

5.6. Gold

Owing to the high reduction potential of Au (Au^{3+}/Au, 1.50 V), galvanic replacement becomes a major issue when the surface-replicating method is extended to the fabrication of M@Au (M denotes a metal other than Au) core–shell nanocrystals.[370,429] To address this challenge, a faster parallel reduction reaction was introduced in an attempt to compete with and thereby suppress the galvanic replacement between a Au(III) precursor and the template (Figure 33A–C).[370] The concept was initially demonstrated using a strong reductant such as AA, together with the use of an alkaline pH of 11.2 to further enhance its reduction power. From 38-nm Ag cubes, Ag@Au core–shell cubes encased by well-defined {100} facets were successfully synthesized. Due to the involvement of an alkaline pH, Ag_2O patches were formed at the corners. By simply increasing the volume of the Au(III) precursor, the thickness of the Au wall could be tuned up to 1.3 nm (or about six atomic layers). The core–shell cubes were then treated with a weak acid to dissolve the Ag_2O patches at the corners, paving the way for the dissolution of Ag from the core. When mixed with aqueous H_2O_2 to selectively remove the Ag in the core, the Ag@Au_{6L} core–shell cubes were transformed into Au boxes with small openings at the corners (Figure 33C). Their side faces were covered by {100} facets.[370]

In addition to the {100}-enclosed Au cubic cages, Au cuboctahedral cages with controlled openings at {111} or {100} facets could also be produced (Figure 33D,E).[429] The synthesis started from the selective deposition of Au atoms on Ag cuboctahedral nanocrystals of 47.2 nm in edge length, as

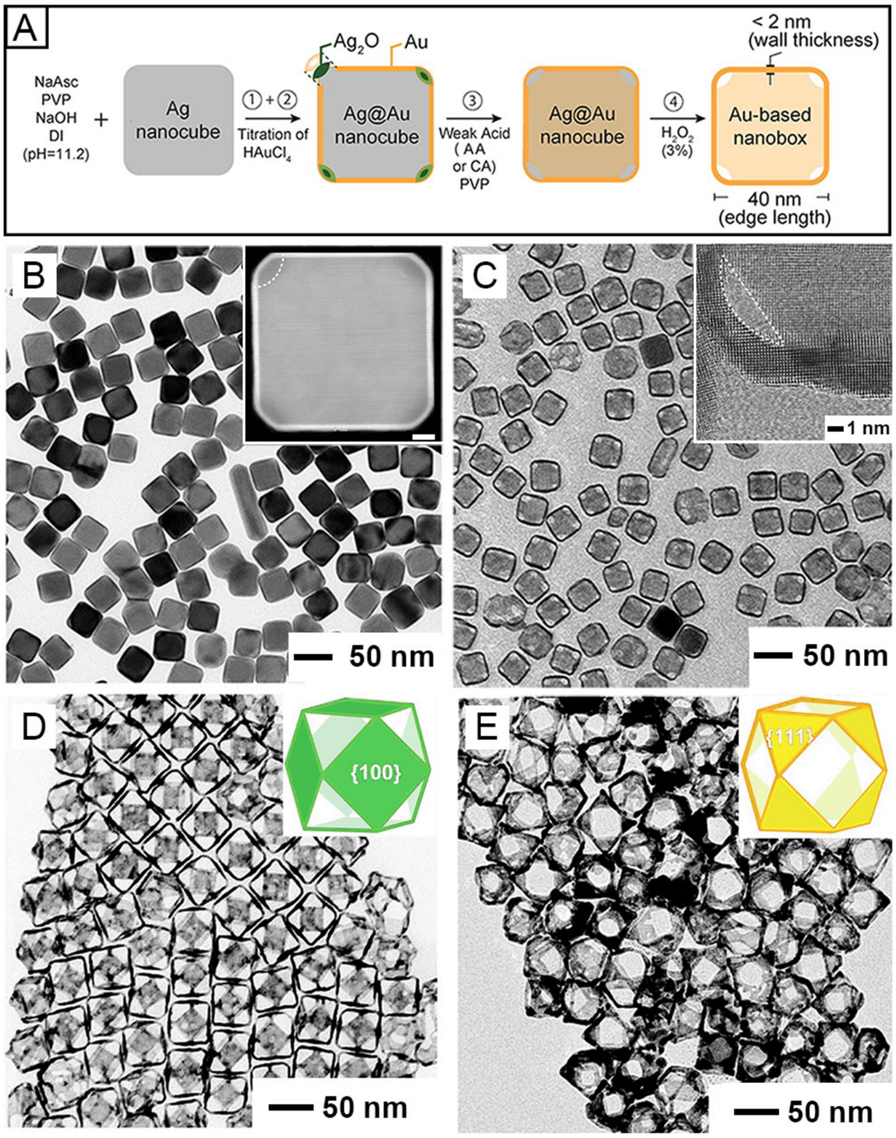

Figure 33. (A) Schematic illustrating the formation of a Ag@Au core−shell cube, followed by its transformation into a Au-based box. (B) TEM image of Ag@Au$_{6L}$ core−shell cubes. The inset shows the HAADF-STEM image of an individual cube (scale bar: 5 nm). (C) TEM image of the Au-based boxes obtained by removing the Ag in the core. The inset shows an atomic-resolution TEM image recorded from the corner of a Au box. (D and E) TEM images of the Au cuboctahedral cages with controlled openings at (D) {111} and (E) {100} facets, respectively. The insets show the corresponding models of the cuboctahedral cages. (A−C) Reprinted with permission from ref 370. Copyright 2016 American Chemical Society. (D and E) Modified with permission from ref 429. Copyright 2020 Royal Society of Chemistry.

enabled by the use of different capping agents. When PVP was used as a capping agent toward Ag{100} facets, the oxidation of Ag through galvanic replacement would be initiated from the {111} facets and the resultant Ag$^+$ ions would react with OH$^-$ for the formation of Ag$_2$O on the {111} facets. As a consequence, the deposition of Au atoms would be confined to the {100} facets, giving rise to the formation of Ag@Au core−shell cuboctahedra with their {111} facets free of Au. In contrast, when Cl$^-$ ions served as a capping agent toward the Ag{100} facets, they would facilitate the oxidation of Ag from the {100} facets by undergoing ligand exchange with Ag$^+$ ions to produce soluble AgCl$_2{}^-$ ions. As a result, the Au atoms, together with a small amount of Ag atoms formed via chemical reduction, were selectively deposited on the {111} facets, leading to the production of Ag@Au core−shell cuboctahedra with their {100} facets free of Au. By selectively dissolving the Ag core using H$_2$O$_2$, the Ag@Au core−shell cuboctahedra were converted into Au cuboctahedral boxes with controlled openings at the {111} and {100} facets, respectively. Although a cuboctahedron is supposed to be enclosed by a mix of {100} and {111} facets, the surface of the as-obtained Au cuboctahedral cages was exclusively covered by either {100} or {111} facets.

In addition to the approach involving core−shell nanocrystals and selective etching, Au-based hollow nanocrystals with well-defined surface structures could also be obtained in one step through galvanic replacement (Figure 34A).[369] Among various noble metals, Ag is an excellent candidate for engaging the galvanic replacement reaction with a Au(III) or Au(I) precursor owing to their similar lattice constant and electronegativity, in addition to the favorable thermodynamics. For a typical synthesis, one can simply titrate an aqueous solution of HAuCl$_4$ into a suspension of Ag nanocrystals in water at a controlled temperature. When Ag cubes with sharp corners

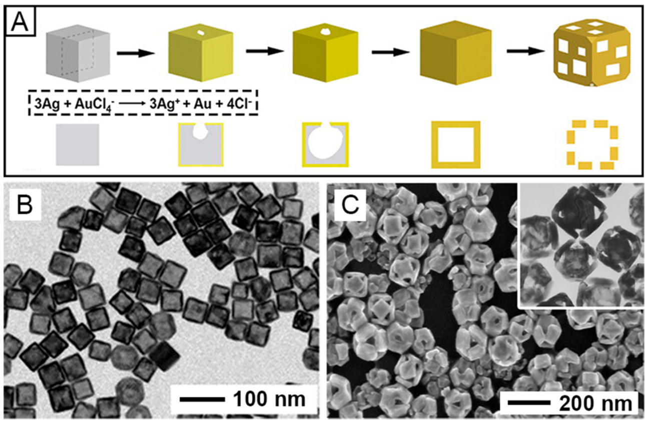

Figure 34. (A) Schematic illustration of the major morphological and structural changes during the galvanic replacement reaction between a sharp Ag cube and a Au(III) precursor. The cross-sectional views correspond to the plane along the dashed lines. (B) TEM image of Au−Ag alloy cubic cages. (C) SEM image of Au−Ag cubic cages with well-defined pores at all corners, with inset showing the TEM image of the cages. (A) Modified with permission from ref 369. Copyright 2010 Elsevier. (B) Reprinted with permission from ref 431. Copyright 2010 Wiley-VCH. (C) Reprinted with permission from ref 376. Copyright 2006 American Chemical Society.

were used, the as-obtained Au−Ag alloy cages showed a well-defined cubic shape (Figure 34B).[370] Using Ag cubes with different edge lengths, the size of the Au−Ag cages could be readily tuned in the range of tens to hundreds of nanometers.[367,368,430] Additionally, the wall thickness and porosity of the cages could be controlled by further treating the sample with an etchant based on $Fe(NO_3)_3$ or NH_4OH to dealloy Ag from the walls of the cages.[366]

When Ag cubes with slight truncation at corners were used, Au−Ag cages with well-defined openings at the corners were obtained (Figure 34C).[376] The success of this synthesis relied on the pretreatment of Ag cubes in EG containing HCl and PVP for slightly truncating the corners. Given the selective binding of PVP toward Ag{100} facets, galvanic replacement preferentially started from the corners of the truncated Ag cubes, while confining the codeposition of Au and Ag atoms to the side faces. As a result, Au−Ag cubic cages with well-defined openings at all corners were obtained as one of the intermediate structures. As the reaction proceeded, surface reconstruction took place, during which the {111} facets were gradually enlarged. Since the openings were located on the {111} facets, they were enlarged accordingly. The enlargement of the {111} facets and the opening size would be terminated when the cages evolved into a cuboctahedral shape. At this point, the cages were characterized by well-defined and enlarged pores on the {111} facets, in sharp contrast to the small pores on the initial cubic cages. Apart from the cubes and truncated cubes, octahedral nanocrystals could also serve as a sacrificial template. By titrating the Au(III) precursor at an appropriate rate into the solution containing Ag octahedra at 90 °C, Au−Ag cages featuring an octahedral shape and well-controlled {111} facets were obtained.[214]

5.7. Conclusion

The surface-replicating method offers an alternative approach to controlling the surface structure of noble-metal nanocrystals, especially for Ru and Ir that are still difficult to achieve shape-controlled synthesis. The key factor in achieving a faithful replication through epitaxial deposition is to generate a conformal shell by ensuring adequate surface diffusion over atom deposition. To this end, the deposition rate of the shell atoms has to be optimized, which may vary significantly when dealing with templates made of different metals and/or covered by different types of surface structures. More significantly, the core−shell nanocrystals prepared using the template-directed method could serve as precursors to the production of hollow nanocrystals with well-defined and controllable surface structures. Additionally, galvanic replacement has also been demonstrated with great simplicity and capability in producing hollow nanocrystals in one step without compromising the control over surface structure. As the two major limitations, galvanic replacement can only occur between metals with favorable difference in reduction potentials and the products are typically made of alloys rather than a pure element. At this moment, the capabilities of these two routes to hollow metal nanocrystals are still limited by a number of factors, including the lack of templates with the desired attributes, the difficulty in precisely controlling the reaction kinetics, the involvement of oxidative etching, and related side reactions. Future endeavors should be focused on mechanistic understanding for the achievement of a tighter control over all the steps involved.

6. APPLICATIONS IN HETEROGENEOUS CATALYSIS

Heterogeneous catalysis has a long history of several hundred years, and it has found use in many industrial processes that are typically driven by thermal energy and hence involve the use of elevated temperatures and pressures. Notable examples include water−gas shift reaction, methanol synthesis, and ammonia production. As determined by their intrinsic properties, different noble metals would fit specific applications. When the reaction is structure-sensitive, one can enhance the activity and/or selectivity of a catalyst based on noble-metal nanocrystals by engineering their surface structure. The surface structure is collectively determined by a variety of factors, including the type of facet, type of defect, particle size, and crystal structure. Here we only highlight the most important factor(s) for each noble metal in the context of its target reactions, in the order of increasing atomic number. For each metal, at least one catalytic reaction is chosen to illustrate the correlation between the catalytic performance and surface structure.

6.1. Copper

Metallic Cu is commercially used as the catalysts for methanol synthesis[4,5,432] and water−gas shift reaction,[433−435] both of which are of great technological and societal significance. Besides, it is also used as catalysts for the conversion of esters to alcohols and selective hydrogenation of oils.[436] The excellent performance of Cu in various catalytic reactions, along with its high abundance in the Earth's crust, makes its nanocrystals of particular interest for fundamental studies, including elucidation of structure−property relationship and understanding of surface reconstruction under the reaction environment.

6.1.1. Methanol Synthesis. The global production of methanol reached 110 million metric tons in 2018. The demand for this chemical has shown significant growth in the past ten years and is expected to keep increasing in the future.[437] The major uses of methanol are in the context of fuel production, organic synthesis, and antifreezing.[438−441] Currently, the majority of methanol is produced worldwide from the syngas (a mixture of CO, CO_2, and H_2) on a Cu-based catalyst,[1] with ZnO and Al_2O_3 serving as the support and promoter, respectively:

$$CO_2 + 3H_2 \leftrightharpoons CH_3OH + H_2O \tag{6}$$

The following two exothermic reactions are also involved in this process:

$$CO + 2H_2 \leftrightharpoons CH_3OH \tag{7}$$

$$CO_2 + H_2 \leftrightharpoons CO + H_2O \tag{8}$$

The Cu-based catalyst for methanol synthesis has been widely used for about half a century. Nonetheless, the nature of the catalytic active sites on the surface remained enigmatic until recently. A study involving the use of both experiments and DFT simulations suggested that surface steps and twin boundaries were required to make the catalyst active.[5] For the industrially used Cu catalyst, twin boundaries and disordered overlayers were observed under aberration-corrected high-resolution TEM (Figure 35A,B). When pure Cu sample with neither surface distortion nor support was applied instead, the catalyst was rather inactive, indicating that surface steps were necessary to ensure the high performance of Cu catalyst in methanol synthesis (Figure 35C,D). Combined with DFT calculations, it was found that the high-index {211} facets or stepped sites created by stacking faults on the catalyst were most effective in lowering the adsorption energy barrier of the reaction. On the other hand, it was found that the reaction intermediate binds to the defect-free Cu(111) surface too weakly to have the reaction activated. In the future, one should pay close attention to these structural features when designing catalysts based on Cu nanocrystals for this reaction. More importantly, it is critical to find ways for preserving these features during the catalytic process. It is also worth pointing out that the ZnO support plays an important role in creating the active sites albeit it is beyond the scope of this article.

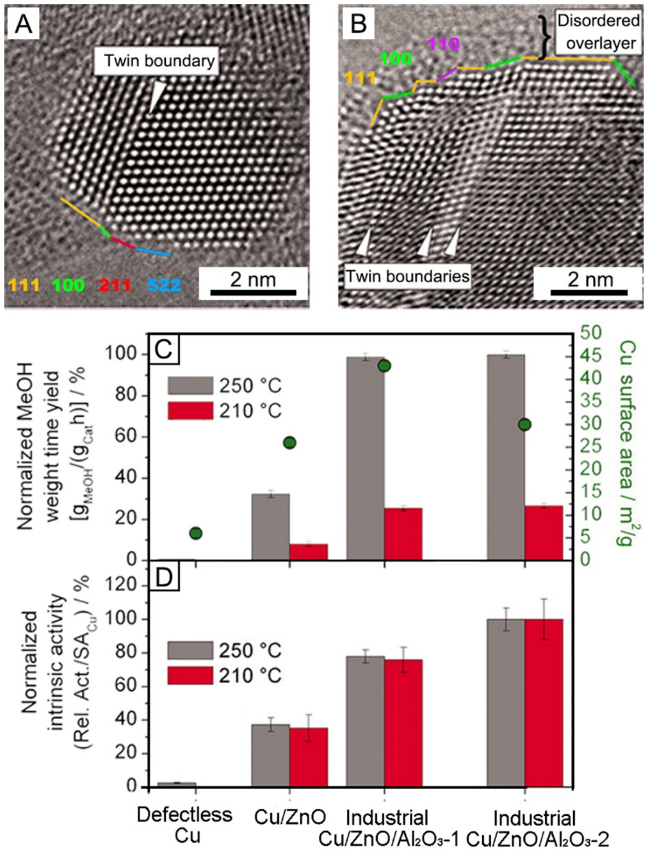

Figure 35. Catalysts based upon Cu for methanol synthesis. (A and B) Aberration-corrected high-resolution TEM images of Cu nanoparticles prepared using a conventional method by precipitating zincian malachite, indicating that the surface was rich in defects. (C) Mass-specific activities and Cu surface areas of different catalysts used for methanol synthesis (P = 60 bar, normalized to the most active sample). (D) Area-specific activities of Cu catalysts (normalized to the most active sample). Modified with permission from ref 5. Copyright 2012 AAAS.

6.1.2. Water–Gas Shift Reaction.

Water–gas shift reaction is typically involved as a side reaction in many industrial processes, including methanol synthesis, Fischer–Tropsch (FT) synthesis, and steam reforming. Besides, it is also an important reaction capable of producing hydrogen gas from CO and H_2O:

$$CO + H_2O \leftrightharpoons CO_2 + H_2 \tag{9}$$

The produced H_2 can be further used for other industrial processes such as ammonia synthesis. The low-temperature water–gas shift reaction is also essential to the development of solid oxide fuel cells.[442] So far, Cu is the most widely used catalyst for low-temperature water–gas shift reaction due to its low price, high CO conversion, and high H_2 yield.[443] The structure–property relationship of the Cu catalyst has been investigated through both experimental and computational approaches.[434,435] In one study, Cu microcrystals with well-defined shapes and high purity were explored as model catalysts to investigate the facet-dependent catalytic activity in water–gas shift reaction at a temperature up to 548 K.[435] The results indicated that Cu cubes covered by {100} facets had the highest activity among all of the catalysts, including Cu RDD terminated in {110} facets. For Cu octahedra enclosed by {111} facets, they were found to be completely inactive toward the reaction. From both experimental characterizations and theoretical calculations, the active sites were identified to be Cu–Cu suboxide (Cu_xO, $x \geq 10$) interface. It was suggested that all elementary steps of the reaction could proceed smoothly on Cu–Cu_xO interface of Cu(100) surface while the Cu–Cu_xO interface of Cu(111) was poisoned by the accumulation of formate intermediate. Although the shapes of the microcrystals were uniform and well-suited for investigating the facet dependence of water–gas shift reaction, they hardly belong to the "nano" regime because of their relatively large size around 1 μm. Catalytic particles with such a large size will likely suffer from a low mass-specific activity. Nevertheless, this study offers an insightful guideline for the rational design of catalysts based on Cu nanocrystals toward water–gas shift reaction.

In summary, there is still a gap between the shape-controlled synthesis of Cu nanocrystals and their implementation in industrial catalysis. As discussed in section 4, it remains a challenge to control both the shape and size of Cu nanocrystals. In order to have a tight control over the shape and thus surface structure of Cu nanocrystals, their sizes are usually kept above 20 nm, much larger than the nanoparticles used in commercial Cu catalysts. Besides, the effect arising from the support also plays a pivotal role in determining the activity and selectivity of a Cu catalyst. Despite these barriers imposed by the synthetic capabilities, both computational and experimental studies have established that the surface structures of Cu nanocrystals can have a major impact on their catalytic performance.

6.2. Ruthenium

Ruthenium is considered a minor component among the noble metals. The annual production of Ru is only on the scale of tens of metric tons,[444] while Pd and Pt can reach up to hundreds of tons, and Au is even as much as several thousand tons. Nevertheless, the excellent performance of Ru in various catalytic processes and its ability to crystallize in both hcp and fcc phases have brought up significant attention to this metal in recent years.[445] In the context of industrial applications, Ru mostly shines as the catalysts for FT synthesis,[446,447] ammonia production,[6,8,448] and CO oxidation reaction.[449,450]

6.2.1. Fischer–Tropsch Synthesis. Fischer–Tropsch synthesis refers to a set of chemical reactions for converting a mixture of CO and H_2 into liquid hydrocarbons, and the general reaction can be written as

$$n\mathrm{CO} + (2n + 1)\mathrm{H}_2 \rightarrow \mathrm{C}_n\mathrm{H}_{2n+2} + n\mathrm{H}_2\mathrm{O} \tag{10}$$

The FT process has a major impact on the energy industry all over the world. The products from this process have become a major alternative fuel because of the low cost for transportation and the capability of FT synthesis to convert stranded gases into useful chemicals. Among all the catalysts for FT synthesis, Ru works at the lowest temperature and gives hydrocarbons with the highest molecular weight.[451] Unlike Cu, whose catalytic performance is strongly related to the support, it has been reported that Ru can perform well in FT synthesis as a pure metal without involving any support.[452]

Due to the limitation in terms of synthetic capability for Ru-based nanocrystals, most of the studies were conducted to investigate the effect of size and crystal structure on the activity in FT synthesis. Compared with the size effect,[447] the impacts of crystal structure on both the activity and selectivity have been studied more thoroughly and systematically.[446,447,450] Changing the crystal structure will alter the arrangement of atoms in a lattice, naturally creating new surface structures on the nanocrystals. For example, the atom arrangements on fcc{100} facets are different from that on hcp{1000} facets, and therefore might exhibit different surface properties in catalytic reactions. A recent study demonstrated that fcc-Ru outperformed its traditional hcp counterpart in FT synthesis.[446] The experimental results indicated that the density of active sites on the fcc-Ru catalyst was 2 orders of magnitude higher than that of the catalyst based on hcp-Ru. This trend was further validated by a computational study, in which fcc-Ru was found to present more open facets capable of lowering the energy barrier of the reaction than hcp-Ru.[446] Remarkably, the 6.8 nm fcc-Ru nanocrystals showed a mass-specific activity three times as high as that of 1.9 nm hcp-Ru nanocrystals at 433 K. Moreover, the selectivity toward the desired C_{5+} product was as high as 81.3% for fcc-Ru, while it was only 66.7% for hcp-Ru.

6.2.2. CO Oxidation and Ammonia Production. The size and structure dependences were also investigated for other reactions that rely on the use of Ru as catalysts, including CO oxidation and ammonia synthesis.[6,453] By manipulating the reaction kinetics, one could obtain Ru nanocrystals in either an fcc or hcp phase.[449] The reduction kinetics are typically controlled through the utilization of different metal precursors and/or solvents. The Ru nanocrystals synthesized from $Ru(acac)_3$ and TEG were crystallized in the fcc phase, while those from $RuCl_3$ and EG would crystallize in the hcp phase. It was proposed that if the metal precursor could be dissolved in the solvent as a neutral molecule, the products would take the fcc phase. On the other hand, if the precursor was dissolved in the solvent to take an ionic form, the products tended to be in the hcp phase. The surface structures could be well-resolved in high-resolution TEM images (Figure 36A,B). When applied to CO oxidation, the temperature for 50% conversion (T_{50}) of CO to CO_2 increased with particle size for hcp-Ru nanocrystals, whereas the T_{50} took an opposite trend for fcc-Ru nanocrystals (Figure 36C). The difference in crystal structure and the presence of twin boundaries in fcc-Ru nanocrystals naturally alter the arrangement of atoms on the surface and thereby give different catalytic activities toward CO oxidation.[449]

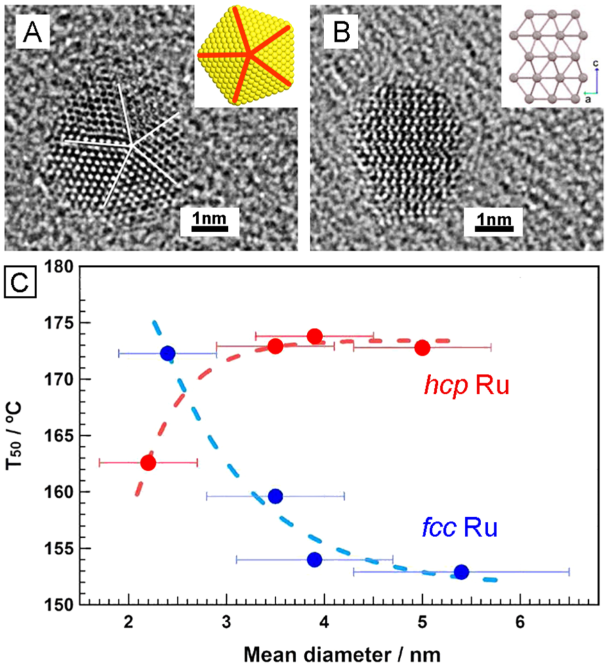

Figure 36. Catalysts based upon Ru for CO oxidation. (A and B) High-resolution TEM images of Ru nanoparticles in (A) fcc and (B) hcp crystal structures, respectively. The insets show atomic models of the corresponding atomic arrangements of the products. (C) Size dependence of the T_{50} values for fcc-(blue) and hcp- (red) Ru nanocrystals. (A–C) Modified with permission from ref 449. Copyright 2013 American Chemical Society. Inset in (A) is modified with permission from ref 76. Copyright 2019 IOP Publishing.

The poor control in terms of shape represents a major drawback for the Ru nanocrystals used in the aforementioned study. In an effort to obtain fcc-Ru nanocrystals with well-defined facets, a surface-replicating method was developed by leveraging Pd nanocrystals with well-controlled shapes as seeds for overgrowth (section 5.1). It was reported that Pd@Ru core–shell nanocrystals and Ru-based cages in the fcc phase, including those covered by {111} and {100} facets, could be readily synthesized using this method.[354−356] The well-defined facets, unique crystal structure, and high specific surface area associated with fcc-Ru cages offered some immediate advantages for catalytic applications. According to DFT calculations, both the fcc-Ru(111) and fcc-Ru(100) surfaces

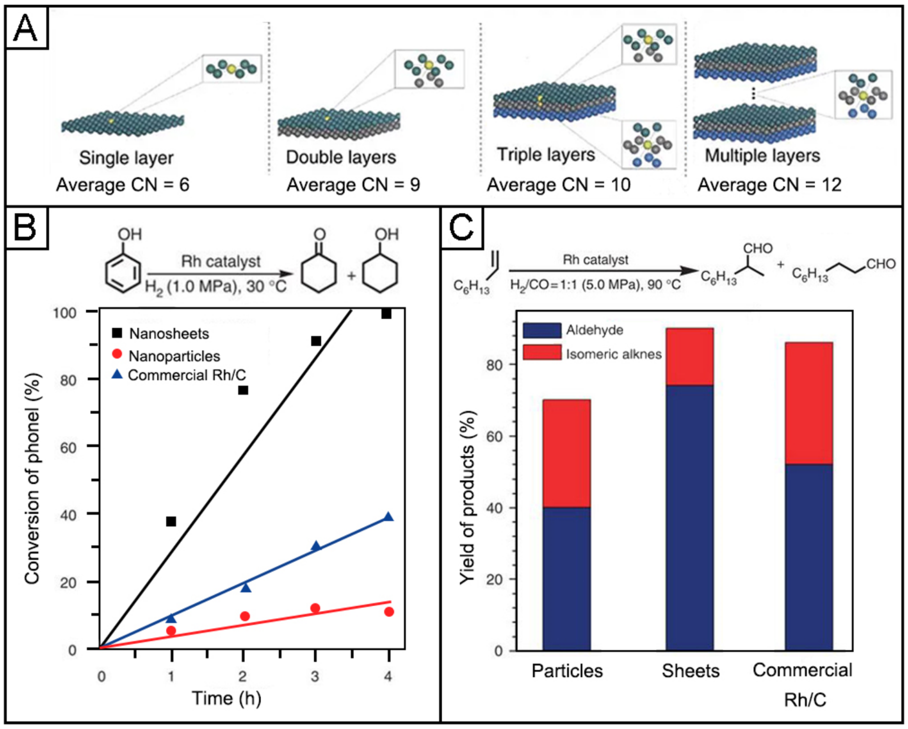

Figure 37. Catalysts based upon Rh for hydrogenation and hydroformylation. (A) Schematic illustration of the coordination states of Rh sheets with different thicknesses. (B and C) Comparison of the catalytic performance of PVP-capped Rh sheets, PVP-capped Rh particles, and commercial Rh/C, toward (B) hydrogenation of phenol and (C) hydroformylation of 1-octene, respectively. Modified with permission from ref 233. Copyright 2014 Nature Publishing Group.

exhibited lower activation energies for N_2 dissociation when benchmarked against that of the hcp-Ru (0001) surface.[354,355] The simulation result suggested that fcc-Ru is potentially capable of improving the efficiency of ammonia synthesis. However, as discussed in section 5.1, the synthesis of hollow nanocrystals can hardly avoid the process of alloying. The incorporation of Pd atoms might also affect the catalytic performance of the Ru-based cages,[355] which should be taken into consideration when evaluating their catalytic properties.

Up until now, there are very few reports on the shape-dependent catalytic performance of Ru-based nanocrystals, mainly because of the limitation in synthetic capability. One of the studies compared the activities of Ru nanocrystals with different shapes toward CO methanation.[301] Using a hydrothermal method, Ru spherical nanoparticles, triangular plates, irregular plates, and capped columns were synthesized in autoclaves and then used to catalyze the methanation reaction. However, since this reaction is structure-insensitive,[454,455] the observed changes to the activity has to be attributed to the variation in specific surface area rather than crystal facets or surface defects. Despite this, the reported Ru nanocrystals with well-defined facets and identified surface defects can possibly be applied to other reactions that are sensitive to these surface features. Considering the lower price of Ru relative to those of Au, Pt, and Pd, developing Ru-based nanocrystals with well-defined surface structures hold a promising future in the field of heterogeneous catalysis.

6.3. Rhodium

As the most expensive noble metal, Rh is very good at catalyzing a variety of industrial reactions, including hydrogenation and hydroformylation.[233,456] It is also an important component in the three-way catalytic converters for reducing the harmful NO_x in the automobile exhaust.[15] Several strategies have been developed for improving the activity and selectivity of Rh-based catalysts by carefully controlling the surface structure. Shape control, and thereby facet engineering, is the most effective approach to enhancing their performance in structure-sensitive reactions. An early report indicated that Rh tetrahedra with an average size of 5 nm had an activity 5.8 times as high as that of the spherical counterpart toward the hydrogenation of anthracene,[221] suggesting that Rh{111} facets were favorable for this reaction. Moreover, the Rh tetrahedral nanocrystals also exhibited perfect selectivity in hydrogenating only one side ring of anthracene. However, the authors did not offer explanation for the enhancement in activity and selectivity unique to Rh tetrahedral nanocrystals. Later, another group synthesized Rh sheets with a thickness down to one atomic layer and further explored them as catalysts for hydrogenation and hydroformylation.[233] The δ-bonding framework constructed from metallic d_{z^2}-s hybrid orbitals, along with the presence of PVP, contributed to their stability and therefore enhanced their performance in the catalytic reaction. In particular, the sheets of one atomic layer in thickness not only enabled the maximum exposure of metal atoms to the catalytic environment but also changed the coordination state of the Rh atoms and the surface electronic structure of the metal. In a monolayer sheet, the Rh atom situated in {111} facet only had a CN of 6, whereas those on the surface of a sheet with multiple layers would have a higher CN of 9 (Figure 37A). The unique surface structure of the monolayer sheets gave them higher activity and selectivity toward both phenol hydrogenation and hydroformylation of 1-octene (Figure 37B,C). To exclude the possible effect from PVP, a capping agent involved in the synthesis of sheets, on the catalytic performance, three catalysts including PVP-capped Rh

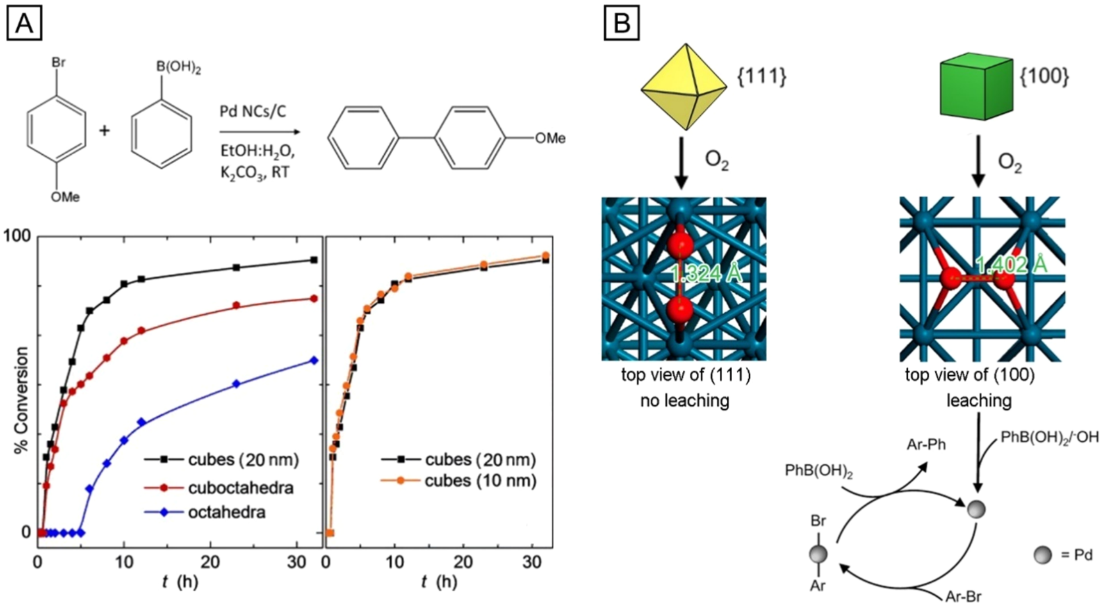

Figure 38. Catalysts based upon Pd for cross-coupling reaction. (A) Comparison of catalytic activities of Pd nanocrystals with different shapes and sizes toward the Suzuki-Miyaura reaction. (B) Schematic illustration of the O_2-promoted leaching mechanism for Pd nanocrystals with different shapes. (A) Modified with permission from ref 462. Copyright 2014 Wiley-VCH. (B) Modified with permission from refs 462 and 463. Copyrights 2014 Wiley-VCH and 2013 American Chemical Society, respectively.

monolayer sheets, PVP-capped Rh nanoparticles, and commercial Rh/C catalyst were tested and compared. It was observed that the PVP-capped Rh monolayer sheets outperformed the PVP-capped Rh nanoparticles in both reactions, indicating the key role played by the surface structure rather than PVP in catalyzing the reactions.

6.4. Palladium

Palladium is highly active toward many catalytic reactions, including C−C coupling,[9,457] selective hydrogenation,[457] and some oxidation reactions.[10] However, its largest end use is no doubt in the realm of catalytic converters. Such a use accounts for almost 60% of the annual consumption of Pd.[458] The demand from automotive catalysis has kept pushing up the price of Pd since the end of 2018. Therefore, there is a strong desire to maximize their performance by optimizing the surface structure of Pd-based catalysts. Compared with other noble metals, it is easier to engineer the surface structure of Pd nanocrystals owing to the availability of various reliable methods developed over the past two decades. At the current stage of development, both the shape and size of Pd nanocrystals can be readily controlled by changing the experimental conditions. As a result, their shape-dependent catalytic performances have been extensively and systematically examined.

6.4.1. Selective Hydrogenation. It is well documented that selective hydrogenation over Pd nanocrystals is structure-sensitive. One study compared the activity and selectivity of different Pd nanocrystals toward alkynol hydrogenation.[459] The authors compared the selectivity of Pd catalysts based on cubic, octahedral, and cuboctahedral nanocrystals toward the hydrogenation of 2-methyl-3-butyn-2-ol (MBY). These nanocrystals were enclosed by {100}, {111}, and a mix of {100} and {111}, respectively. When the conversion of the reactant was 50%, the selectivity toward 2-methyl-3-buten-2-ol (MBE) was independent of both the size and shape of the nanocrystals. However, as the conversion increased to 90%, a significant change in the selectivity was observed. The results indicated that the catalysts had two different active sites, corresponding to atoms situated on the side faces and edges. Semihydrogenation of MBY to MBE likely occurred on the side faces, regardless of {100} or {111}. On the other hand, the edges would favor the overhydrogenation of MBY to 2-methylbutan-2-ol (MBA). This site-dependent selectivity was believed to originate from the difference in CN for the surface atoms. The higher ratio of edge sites with lower CNs on cuboctahedral nanocrystals made them most effective in overhydrogenating the reactant, which was not a favored process.

The CN-dependent catalytic performance was also observed in another system involving the hydrogenation of acetylene.[460] Two types of Pd catalysts were compared, including twisted wires and cuboctahedral nanocrystals. High-resolution TEM images revealed that the twisted wires were also consisted of primary cuboctahedral units. Therefore, the major difference that distinguishes the wires from cuboctahedral nanocrystals should arise from the presence of grain boundaries at the interfaces between adjacent cuboctahedral units, which tended to have lower CNs than those on the faces. As a result, the twisted wires gave a higher conversion of acetylene while supporting a poorer selectivity toward ethylene. In general, atoms with low CNs are not favorable in selective hydrogenation reaction because they are too active and tend to overhydrogenate the reactant.

The variation in the shape of a nanocrystal not only alters the coordination environment of surface atoms but also changes their sensitivity toward surface reconstruction. As shown in a study, the different types of facets exposed on Pd nanocrystals had different degrees of propensity toward the formation of palladium carbide during the hydrogenation of acetylene.[461] From in situ XRD, the {100} facets formed $PdC_{0.13}$ at a rate six times as fast as that of {111} facets. DFT calculations ascribed this trend to a stronger interaction between acetylene and Pd(100), leading to C−C bond scission and thus the formation of carbide.

6.4.2. Suzuki Coupling Reaction. Suzuki coupling reaction is a key step in the production of many organic compounds and drug molecules.[9] The general scheme of Suzuki coupling is shown below. By coupling organoboron compounds (R_1-BY_2) with a halide (R_2-X), a C−C single bond can be formed in the presence of Pd as a catalyst:

$$R_1 - BY_2 + R_2 - X \rightarrow R_1 - R_2 \qquad (11)$$

Early studies on the synthesis of Pd nanocrystals for the Suzuki coupling reaction focused on the control of shape for maximizing the proportion of surface atoms with low CNs.[327] It was reported that Pd concave cubes exhibited a turnover frequency (TOF) 3.5 times as high as that of the normal cubes toward Suzuki coupling. The authors attributed the high activity to the {730} high-index facets exposed on the surface of the concave cubes. However, a later report suggested that the shape-dependent activity of Pd nanocrystals in Suzuki coupling came from the leaching susceptibility of different crystal facets.[462] Instead of the Pd atoms on surface, the catalytic active species were found to be soluble metal ions derived from the leaching of palladium oxide and the reaction proceeded via a homogeneous pathway. It was observed that the conversion of a Suzuki coupling reaction was dependent on the shape of the nanocrystals, but not on the size, with cubic nanocrystals possessing a better performance than the octahedral counterpart (Figure 38A). As shown in Figure 38B, it is easier for the surface atoms on cubes with lower CNs to get oxidized and dissolved, giving a higher catalytic activity. The leaching effect on the catalytic performance of Pd concave cubes was also supported by a study involving TEM analysis.[65] Using Pd concave cubes covered by the same {730} facets as a catalyst, small Pd clusters were observed from high-resolution TEM after the catalytic reaction, indicating the involvement of leaching mechanism.

In summary, Pd nanocrystals have been applied to a range of structure-sensitive reactions and the focus has been placed on shape control and thereby variation in terms of surface structure. Although the major impact arising from shape control can be ascribed to the change in coordination environment for the atoms, surface reconstruction can also take place and play a pivotal role under the reaction condition. Therefore, it is crucial to uncover the fundamental mechanism of a reaction in order to develop the most effective catalyst.

6.5. Silver

Compared with Pd, Pt, and Au, Ag offers an immediate advantage for being a much cheaper metal. In practice, Ag is a catalytic material key to many manufacturing processes such as hydrogenation of unsaturated aldehydes,[464,465] partial oxidation of methanol to formaldehyde,[466] and oxidative coupling of methane to ethylene and ethane.[467] Most importantly, Ag is a crucial catalyst toward ethylene epoxidation for the production of ethylene oxide (EO), a chemical that is produced annually on a scale of 26 million metric tons in 2018.[12]

6.5.1. Ethylene Epoxidation. As an important raw material, EO can be further processed into plastics, polyester, and glycols.[12,468] Millions of ounces of Ag are used each year in industry for the production of EO because of its capability to selectively oxidize ethylene into EO while preventing the overoxidation into CO_2 and H_2O:

$$2C_2H_4 + O_2 \rightarrow 2C_2H_4O \qquad (12)$$

$$2C_2H_4O + 5O_2 \rightarrow 4CO_2 + 4H_2O \qquad (13)$$

The origin of the selectivity is determined by the intrinsic material property of Ag, which allows for the generation of weakly bonded electrophilic oxygen while inactivating the C−H bond in ethylene.[469] As a matter of fact, small Ag nanocrystals are too active toward the oxidation reaction and they tend to completely oxidize ethylene to the undesired CO_2 and H_2O. Many early studies have already investigated the size effect of supported Ag nanoparticles on ethylene epoxidation.[470] Their results suggested that large sizes (>20 nm) were more suitable for ethylene epoxidation and the selectivity kept increasing as the size was increased.[471] However, the structure-sensitivity of Ag toward ethylene epoxidation could hardly be claimed by that time, mainly due to the poorly defined surface structure of the Ag nanoparticles.

Thanks to the synthetic capabilities developed over the past two decades, the structure-sensitive nature of ethylene epoxidation was confirmed by a combination of experimental and computational studies.[472] It was reported that penta-twinned Ag wires, covered by {100} facets on the side surface, were highly selective toward EO relative to conventional Ag nanoparticles. According to DFT calculations, the transformation of the surface oxametallacycle intermediate to EO was more favorable on Ag(100) than on Ag(111). Later, the same group further investigated the effects of both size and shape by comparing Ag cubes, wires, and conventional particles with different sizes.[81] The results showed the selectivity toward EO decreased in the order of cubes > wires > irregular particles. For nanocrystals with the same shape, larger particles offered better selectivity, in agreement with the previous conclusion (Figure 39). It was proposed that the under-coordinated atoms on the surface were responsible for the diminished selectivity since wires had a larger proportion of atoms with low CNs on the surface relative to cubes, as caused by the twin boundary, and the decrease in particle size also increased the proportion of atoms located at vertices and edges. However, the mass-specific activity of the catalyst will be compromised as the size is increased. If decreasing under-coordinated atoms is key to increasing the selectivity, sharpening the corners,[174] as well as optimizing the size of Ag cubes,[379] will improve the overall activity and selectivity of a Ag-based catalyst.

6.5.2. Selective Hydrogenation of Aldehyde. Another important catalytic application for Ag is in selective hydrogenation of α,β-unsaturated aldehyde to unsaturated alcohols. The unsaturated alcohols (allylic alcohols) are extensively used to produce fine chemicals required for perfumes, pharmaceuticals, and flavoring compounds.[465] Conventional hydrogenation catalysts based on Pd, Pt, and Cu tend to hydrogenate the C═C first to produce saturated aldehyde, and further transform the product into a saturated alcohol. In contrast, Ag has the unique capability to hydrogenate C═O bond first without destroying C═C, making it an ideal catalyst for the target reaction.[473]

Both experimental and computational studies have been carried out on Ag-based catalysts to understand the structure−property relationship. One study investigated the correlation between the size of the Ag nanoparticles and their selectivity toward unsaturated alcohols.[464] With the assistance of high-resolution TEM, it was possible to resolve the surface structure of the Ag nanoparticles with different sizes. The results showed that larger nanoparticles were mostly covered by {111} and

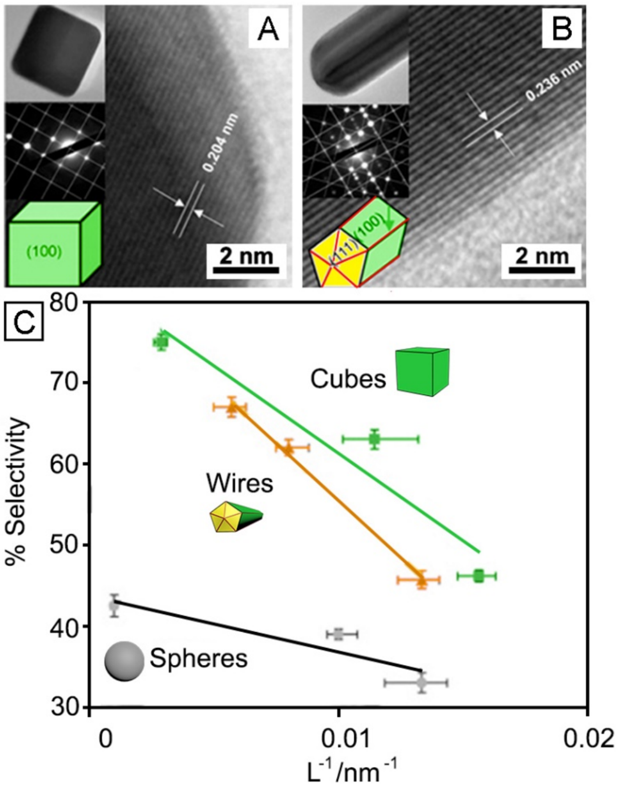

Figure 39. Catalysts based upon Ag for the ethylene epoxidation reaction. (A and B) High-resolution TEM images illustrating the surface structures of a Ag cube and Ag wire, respectively. Insets from top to bottom: TEM images of the nanocrystals at a low magnification; SAED patterns used for zone axis identification; models. (C) Selectivity toward EO as a function of L^{-1} for cubes, wires, and spheres of three different sizes, where L^{-1} stands for the inverse characteristic length. Modified with permission from ref 81. Copyright 2010 Wiley-VCH.

exhibited higher selectivity toward C═O hydrogenation. In comparison, smaller Ag nanoparticles having a higher ratio of high-index facets on the surface showed lower selectivity for the reaction. Although the nanoparticles available at that time were of poor quality in both shape and size, their results seem to be convincing enough to elucidate the correlation between the surface structure of nanoparticles and the catalytic performance.

Apart from the arrangement of atoms, the surface reconstruction caused by oxidation could also induce a change to the selectivity. It was observed through experiments that both the activity and selectivity of the catalysts could be enhanced in acrolein hydrogenation by oxidizing Ag/SiO_2 catalyst with O_2, followed by a reductive preconditioning prior to activity test.[474] Although XPS confirmed that oxygen did not remain on the surface after the reductive preconditioning, it was suggested that the oxygen dissolved into the subsurface of the catalyst could create electropositive sites on the surface. These sites could facilitate the H_2 and change the adsorption geometry of acrolein, enhancing the activity and selectivity toward allyl alcohol. This proposed mechanism was verified by DFT calculations involving Ag(111) surface in the presence of subsurface oxygen.[465] These oxygen atoms located at the subsurface could upshift the *d*-band center of the Ag atoms, affecting their ability to dissociate the adsorbed hydrogen.

The above two examples have shown that for structure-sensitive reactions, decreasing the size might not always be the best option for improving the performance of a catalyst. Moreover, since Ag is highly sensitive toward oxidation or sulfurization, the involvement of oxygen or sulfur atoms may alter the surface properties. The recent progress in DFT calculations and in situ spectroscopy methods might eventually allow people to rationally design Ag-based catalysts toward various applications.

6.6. Iridium

The major catalytic applications of metallic Ir are hydrogenation reactions involving olefin, arene, and ketone.[351,475−478] As discussed in sections 4.4.2 and 5.4, it is extremely difficult to control the shape and thus facets of Ir nanocrystals. Nevertheless, there are still a few reports on the possible correlation between the catalytic performance of Ir nanocrystals and their surface structures.

Combining experiments and DFT simulations, one study investigated the facet dependence of Ir nanocrystals toward the hydrogenation of *o*-chloronitrobenzene.[351] The authors compared Ir nanoparticles mainly covered by {111} and Ir wavy wires terminated in both {200} and {111}. Both catalysts showed excellent selectivity toward chloroaniline, the desired product that is of high industrial value. However, the wavy wires exhibited a higher conversion (>90%) than that of the Ir nanoparticles (<80%). From DFT calculations, the energy barrier to H_2 dissociation was found to be lower on {200} than on {111}, giving Ir wavy wires a higher activity toward the reaction. However, the simulation work did not take into consideration the existence of grain boundaries in the wavy wires, despite that the defects were clearly observed on the high-resolution TEM images.

As discussed in section 5.4, replicating the surface of a template offers an effective way to scrutinize the structure−property relationship for metals limited by our synthetic capability. To this end, Pd@Ir nanoscale cubes, cuboctahedra, and octahedra were synthesized and tested as catalysts toward the decomposition of hydrazine at room temperature.[409] Iridium nanoparticles have been found to be efficient in catalyzing hydrazine decomposition for the generation of H_2. The well-defined core−shell structure obtained in this report further enabled the studies on the structure−property relationships of Ir nanocrystals in this reaction. The Pd@Ir cubes terminated in {100} performed the best among the three candidates, giving the highest selectivity, followed by the Pd@Ir cuboctahedra encased by a mix of {100} and {111}, while Pd@Ir octahedra covered by {111} gave the lowest selectivity. As a control, Pd nanocrystals were also tested but they were essentially inactive for the decomposition reaction. The authors attributed the higher activity of Ir{100} to its unique atom arrangement on the surface, which might be favorable in facilitating the elementary steps for hydrazine decomposition. This assumption still needs to be verified by computational studies. Although hydrazine decomposition is not a major application of Ir-based catalysts, the observed facet-dependence and the trend might be extendible to other catalytic reactions.

6.7. Platinum

Platinum has been applied as a catalyst since the early 19th century, when Pt powders were used to catalyze the ignition of hydrogen.[479] Currently, the most commonly used form of Pt catalyst is Pt black, fine powders of the metal with an average size below 10 nm. Similar to Pd, the largest end use of Pt is in catalytic converters due to its excellent performance in oxidizing CO and NO_x.[15] Besides, Pt is also a good catalyst toward selective hydrogenation and isomerization.[480]

6.7.1. Selective Hydrogenation.

The selective hydrogenation on Pt-based catalysts has been extensively explored using single-crystal substrates since the end of the last century.[481−484] The conclusions obtained from these studies make hydrogenation an ideal reaction to probe the shape-dependent activity of Pt nanocrystals. A study reported in 2007 investigated the selectivity of Pt nanocrystals toward benzene hydrogenation.[192] The authors synthesized Pt nanoscale cubes and cuboctahedra covered by TTAB using a solution-phase method. The selectivity was found to be highly dependent on the shape of the Pt nanocrystals. Specifically, Pt cubes covered by {100} only yielded cyclohexane, while Pt cuboctahedra covered by a mix of {100} and {111} resulted in the production of both cyclohexane and cyclohexene (Figure 40).

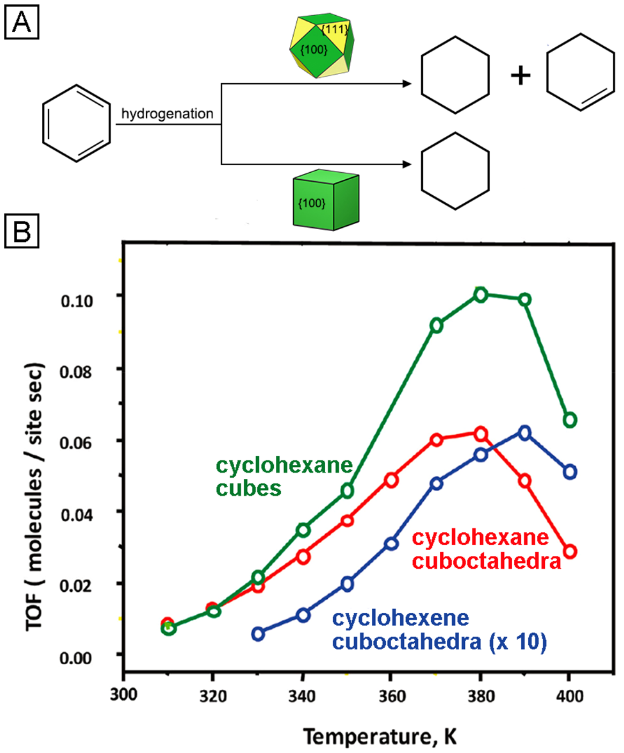

Figure 40. Catalyst based upon Pt cubes and cuboctahedra for benzene hydrogenation. (A) Schematic illustration of the facet-dependent selectivity of Pt nanocrystals in benzene hydrogenation. Cuboctahedra produced both cyclohexane and cyclohexene while cubes only generated cyclohexane. (B) Turnover rates of cyclohexane and cyclohexene on the cubic and cuboctahedral nanocrystals under 10 Torr C_6H_6, 100 Torr H_2, and 650 Torr Ar. Modified with permission from ref 192. Copyright 2007 American Chemical Society.

This result was in agreement with the data from previous studies involving single-crystal substrates.[485,486] However, the activation energy for the nanocrystals was much lower than that of a single-crystal surface, giving Pt nanocrystals higher turnover rates for the same reaction. The lower activation energy was attributed to the change in electronic structure for the Pt surface when the size of the crystal was reduced down to the nanoscale. Similar experiments were also carried out for the hydrogenation of ethylene and pyrrole.[487] The authors examined the effects of both size and shape on these reactions for Pt nanoscale cubes and particles. For pyrrole hydrogenation, Pt cubes gave a higher selectivity toward *n*-butylamine relative to the nanoparticles. Interestingly, ethylene hydrogenation was independent of the shape or size of the catalysts, and the activity was comparable to that obtained from single-crystal substrates, suggesting that it is a structure-insensitive reaction.

6.7.2. Isomerization.

Isomerization refers to the transformation of one molecule to another with the same atoms but in different configurations. It is another reaction toward which Pt nanocrystals show shape-dependent catalytic performance. In one report, Pt nanoscale tetrahedra and cubes were used as the catalysts to test the structure-sensitivity of olefin isomerization.[479] This reaction is used in the industry to convert a *trans*-olefin to the thermodynamically less favorable *cis*-isomer. The selectivity of the reaction was derived from the relative rates for trans-to-cis conversion and cis-to-trans conversion. For Pt cubes enclosed by {100}, the rates for the forward and backward transformations were comparable, regardless of the temperature used for the calcination of the catalysts. For Pt tetrahedra terminated in {111}, however, the trans-to-cis conversion was in dominance, and the dominance became more significant as the calcination temperature was increased. The same group also analyzed the mechanism for the extra stability of *cis*-olefin on hydrogen-saturated Pt(111) surface through DFT calculations.[488] It was found that the less extent of surface reconstruction for Pt(111) surface was favorable for the adsorption of cis-isomer. The flat (111) surface had the ability to adsorb the cis-isomer with minimal degree of atom rearrangement. For other types of surfaces with more open structures, adsorption of the stable molecule (i.e., trans-isomer) was in dominance.

Over the past two decades, the research on shape-controlled Pt nanocrystals has shifted from heterogeneous catalysis to electrocatalysis due to the excellent performance of Pt in fuel cell reactions. Only a few studies were reported on the use of Pt nanocrystals as heterogeneous catalysts over the past five years. As a result, here we are only able to offer a few representative, but not up-to-date, examples to illustrate the structure−property relationships.

6.8. Gold

Gold is typically considered an inert metal that can hardly participate in any chemical reaction. By the early 1970s, people started to observe that Au could act as a catalyst to speed up the oxidation of graphite.[489] However, the real revolutionary discovery was not made until 1987 by Haruta and co-workers. They demonstrated that Au could become a very active catalyst toward CO oxidation at a temperature much lower than room temperature when the size of Au nanoparticles decreased below 6 nm.[490] Because of the fascinating size-dependent surface property of Au, considerable effort has been made to investigate both the reaction mechanisms and practical applications of Au-based catalysts.[80,82,85,491]

6.8.1. Water−Gas Shift Reaction.

As discussed in section 6.1.2, Cu has been mostly used as the catalysts for water−gas shift reaction. However, the $Cu/ZnO/Al_2O_3$ catalyst currently used in industrial applications suffers from high susceptibility to sulfur and chloride poisoning and pyrophoricity. Moreover, the catalyst also requires complex activation steps prior to use.[1] To this end, Au was proposed as an alternative catalyst for low-temperature water−gas shift reaction. Currently, Au/CeO_2 has been reported as the best catalyst for this specific reaction.[442] However, the catalytic performance was found to be mainly dependent on the surface properties of the support, rather than those of Au.[492] Considering the high cost of Au, it might be difficult to commercialize the Au-based catalyst on an industrial scale.

6.8.2. CO Oxidation. As mentioned in section 2.4, the size of Au-based catalysts has to be kept below 6 nm in order to effectively catalyze the oxidization of CO at room temperature. However, the synthetic capabilities developed so far still fail to control the shape or facets of Au nanocrystals at such small sizes. In the case of Au, the surface structure−property relationship can only be explored when the size of the nanocrystals is large enough (>20 nm) for attaining shape control. Inspired by the low CNs of surface atoms on nanocrystals covered by high-index facets, a study in 2011 reported the synthesis of Au rice with a size around 50 nm and covered by {611} high-index facets.[344] When evaluated for CO oxidation, the temperature for activating the catalyst and the temperature for reaching 100% conversion were both lower for Au rice relative to the conventional Au nanoparticles of 50 nm in diameter (Figure 41). This study demonstrated that Au atoms with low CNs were highly active toward CO oxidation. In the future, synthesizing Au nanocrystals with high-index facets and compact sizes might hold the promise to further enhance the catalytic performance of Au-based catalyst.

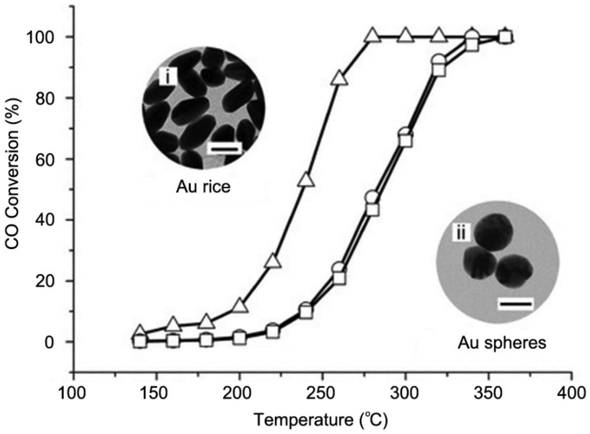

Figure 41. CO conversion as a function of the reaction temperature for Au rice and Au spheres. The scale bars are 50 nm. Three catalysts were compared: Au rice capped by PVP (Δ), Au spheres capped by citrate (○), and Au spheres capped by PVP (□). Reprinted with permission from ref 344. Copyright 2010 Wiley-VCH.

The shape-dependent catalytic properties have also been investigated for other reactions such as 4-nitrophenol reduction.[493,494] Although these reactions are not as important as those mentioned above in terms of industrial value, they can serve as model systems for investigating the dependence of catalytic performance on the surface structure of Au-based catalysts.

In summary, the activity of Au-based catalysts is mainly determined by the particle size and catalyst support. Although Au nanocrystals can be synthesized in various shapes and high purity, their large size and high unit price will present a barrier to large-scale commercialization.

6.9. Summary

We have discussed the most-important industrial reactions related to each noble metal. In general, the surface structure of a catalyst is determined by a number of factors, including shape, facet, size, defect, and crystal structure. For each metal, the most prominent factor can vary depending on the target reaction. The shape-dependent performance can only be understood without ambiguity when the synthetic capabilities allow the nanocrystals to be produced with well-defined shapes and relatively large sizes (>10 nm), whereas the size effect is most distinguishable when the size drops below 10 nm. So far, it remains a major challenge to generate nanocrystals with well-defined surface structures while keeping their sizes well below 10 nm.

It should be emphasized that the above strategies only apply to catalytic reactions that are structure-sensitive. For structure-insensitive reactions such as ethylene hydrogenation,[495] decreasing the size of the catalyst will be directly beneficial to the mass-specific activity, while no change in area-specific activity or selectivity should be observed.

7. APPLICATIONS IN ELECTROCATALYSIS

Electrocatalysis refers to the acceleration of a redox reaction occurring on the surface of an electrode through the introduction of a catalyst.[496] Noble-metal nanocrystals are effective catalysts toward a wide variety of electrochemical reactions, including those essential to the operation of energy-conversion devices such as fuel cells and metal-air batteries.[497,498] It is well-established that the activity of an electrocatalyst strongly depends on its interaction with the intermediate involved in the rate-determining step, as illustrated by the Sabatier principle (see section 2).[496] In this section, we highlight the importance of surface engineering in optimizing the activity of noble-metal nanocrystals toward a broad range of electrocatalytic reactions.

7.1. Oxygen Reduction Reaction (ORR)

ORR refers to the electrochemical reaction in which O_2 is reduced to H_2O. It is a cathodic reaction key to the operation of PEMFCs or metal-air batteries.[499] PEMFCs are considered one of the most attractive sources of energy owing to the zero emission (with H_2O as the only byproduct) and the ability to power a broad range of electronic devices, automobiles, and stationary systems.[496,500,501] Despite the obvious advantages, the sluggish kinetics of ORR requires the deposition of an effective catalyst on the cathode in order to draw a current density adequate to drive the device. DFT has been leveraged to calculate the ORR activities for a variety of transition metals and the results indicate that the activity is strongly correlated with the binding energy of atomic oxygen, an intermediate arising from the dissociation of O_2.[502] As shown by the volcano plot in Figure 42A, Pt is located at nearly the top, suggesting its use as an effective catalyst toward ORR. Despite the excellent performance, this precious metal is plagued by its extreme scarcity and ever-increasing price as both factors limit its cost-effective and sustainable use in large-scale commercialization. One solution to this predicament is to engineer the surface structure of the Pt nanocrystals as the arrangement of surface atoms strongly affects the electronic structure of a catalyst and thus its interaction with the rate-limiting intermediate. As revealed for single-crystal electrodes through ultraviolet photoemission spectroscopy (UPS), the positions of the *d*-band center of Pt(100), Pt(111), and Pt(110) surfaces were

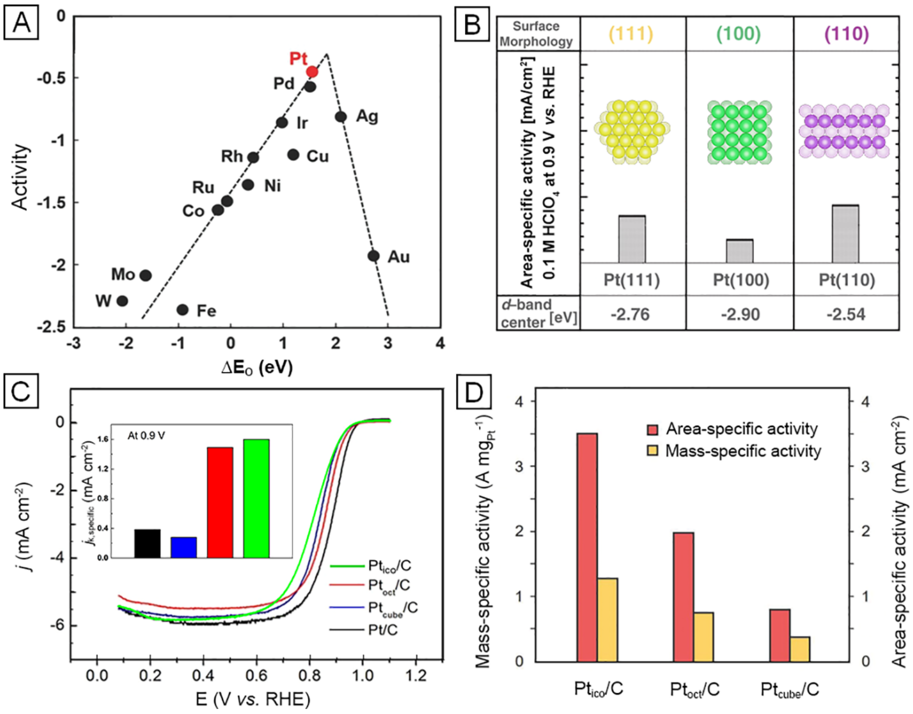

Figure 42. Catalysts based upon Pt for ORR. (A) Volcano plot showing the activities of different metals toward ORR as a function of the oxygen binding energy. (B) Area-specific activities for different types of Pt single-crystal electrodes measured at 0.9 V (vs reversible hydrogen electrode, RHE). The position of *d*-band center obtained using UPS is also listed for each surface. (C) ORR polarization curves of Pt_{ico}/C, Pt_{oct}/C, Pt_{cube}/C, and commercial Pt/C catalysts in an O_2-saturated 0.1 M $HClO_4$ solution. The inset shows the area-specific activities of the four catalysts at 0.9 V. (D) Comparison of the area- and mass-specific activities measured at 0.9 V toward ORR for the Pt-based icosahedral, octahedral, and cubic cages. (A) Reprinted with permission from ref 502. Copyright 2004 American Chemical Society. (B) Modified with permission from ref 503. Copyright 2007 AAAS. (C) Modified with permission from refs 253, 216, and 252. Copyrights 2013 American Chemical Society, 2017 and Wiley-VCH, respectively. (D) Modified with permission from ref 414. Copyright 2018 Wiley-VCH.

located at −2.90, −2.76, and −2.54 eV (Figure 42B), respectively. The difference in *d*-band center strongly affected the interactions between oxygenated species and various Pt surfaces and thereby their ORR activities.[503] When performed in an electrolyte solution based on $HClO_4$, the catalytic activities of various Pt surfaces toward ORR were found to follow the order of (100) ≪ (111) < (110).[27] A later study based on DFT calculations suggested that the binding of O to the Pt(100) surface is stronger than that to the Pt(111) surface, which limits the removal of the oxygenated species and gives a compromised ORR performance.[503] In conjunction with the change in electronic structure, the reaction intermediates and thus reaction pathways of ORR on various types of Pt surfaces may also differ significantly, as demonstrated by a recent study involving in situ Raman spectroscopy analysis.[504] It was shown that, under the acidic condition, the pathway of ORR on Pt(111) occurred via the formation of HO_2*, whereas both Pt(110) and Pt(100) surfaces involved the generation of OH*. These results collectively suggested the critical role of surface structure in determining the electronic structure and reaction pathway for the optimization of catalytic performance.

Inspired by the results from single-crystal electrodes, tremendous efforts have been made in the synthesis of Pt nanocrystals with surface structures beneficial to ORR.[414,505−508] To this end, Pt nanocrystals have been synthesized with cubic, octahedral, and icosahedral shapes, respectively, to present {100}, {111}, and {111} plus twin boundaries, on the surface.[216,252,253] When evaluated as catalysts toward ORR in aqueous $HClO_4$, the cubic nanocrystals exhibited an area-specific activity 1.4 times lower than that of the commercial Pt/C catalyst whereas the octahedral nanocrystals displayed a 3.9-fold enhancement, in agreement with the results from single-crystal electrodes (Figure 42C). With regard to the icosahedral nanocrystals enclosed by a combination of {111} and twin boundaries, their area-specific activity was 4.2 times as high as that of the commercial Pt/C.[252] The further enhancement in area-specific activity relative to the octahedral counterpart could be attributed to the presence of twin boundaries on the surface of an icosahedral nanocrystal for the induction of tensile strains on the side faces and thus enhancement in ORR activity (see section 2.3). Apart from the nanocrystals covered by low-index facets and twin boundaries, those encased by high-index facets have also been explored for ORR. As reported in one study, Pt concave cubes enclosed by {720} high-index facets were 5.7 times as active (normalized to ECSA) as the commercial Pt/C in catalyzing ORR.[34]

Despite the enhancement in area-specific activity arising from the unique surface structure, it should be pointed out that the mass-specific activities, a parameter most important in determining the commercial relevance, of catalysts based on various types of Pt polyhedral nanocrystals only showed a slight increase or even decrease when benchmarked against commercial Pt/C.[216,252,253] This trend can be mainly attributed to the large sizes of the polyhedral nanocrystals and thus the unavailability of most atoms in the bulk to the reactants. To address this issue, one can switch from the conventional solid nanocrystals to their hollow counterparts, a new class of materials known as cages (see section

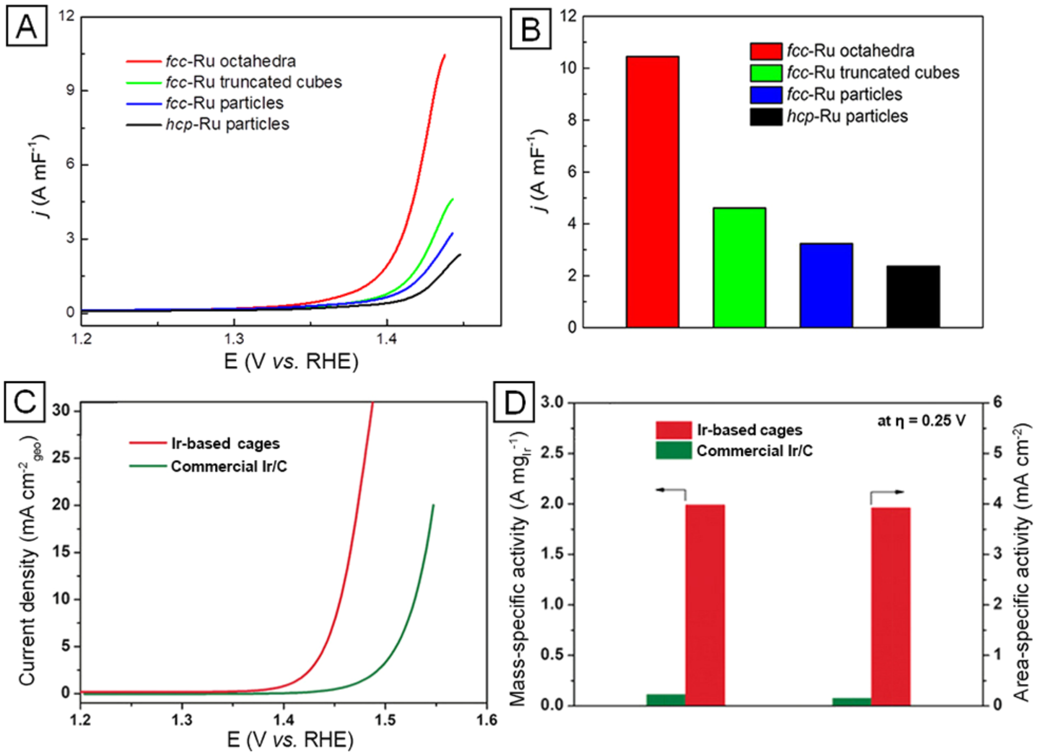

Figure 43. Catalysts based upon Ru and Ir for OER. (A) OER polarization curves of different Ru catalysts in a 0.05 M H_2SO_4 solution. The current density was normalized to the double-layer capacitance of the catalyst. (B) Area-specific activities of different Ru catalysts. (C) OER polarization curves recorded from the Ir-based cubic cages and commercial Ir/C catalyst in a 0.1 M $HClO_4$ solution. (D) Mass- and area-specific activities of different Ir catalysts. (A and B) Modified with permission from ref 95. Copyright 2019 American Chemical Society. (C and D) Modified with permission from ref 362. Copyright 2019 Wiley-VCH.

5).[40,414,509,510] The presence of small holes on the surface of cages allows the access of atoms on the inner surfaces by the reactants, while the ORR activity can still be augmented by optimizing the surface structure.[363−365] A good example can be found in Pt cubic cages, whose area- and mass-specific activities were 3.2 and 2.7 times, respectively, greater than those of commercial Pt/C(Figure 42D).[414] In comparison, Pt solid cubes of similar dimensions only gave area- and mass-specific activities of 0.7 and 0.2 times, respectively, as high as those of commercial Pt/C.[216,363] When switched to Pt octahedral cages encased by well-defined {111} facets, the area- and mass-specific activities were enhanced by 7.9 and 5.4 folds, respectively, relative to commercial Pt/C.[363] For Pt icosahedral cages whose surface is covered by 20 {111} facets, and more importantly, 30 twin boundaries, their area-specific activity was about 10 times as high as that of commercial Pt/C while the mass-specific activity exhibited a 6.7-fold enhancement, confirming the positive role of twin boundaries and surface strains in further boosting the catalytic activity.[365,511]

Besides the impressive activities, the cage-based catalysts also showed enhancement in durability, as confirmed by the results from the accelerated durability test (ADT).[363−365] After 5,000 cycles of ADT, the mass-specific activities of the Pt cubic and octahedral cages only dropped by 18 and 22%, respectively, relative to their initial values. A more drastic drop of 40% in terms of mass-specific activity was observed for the icosahedral cages after the same number of cycles. Despite the decrease in performance during ADT, the mass-specific activities of the cubic, octahedral, and icosahedral cages after 5,000 cycles were still 2.2, 4.2, and 4.0 times as high as that of the pristine Pt/C catalyst. When the ADT was extended to 10,000 cycles, the mass-specific activities of the cubic and octahedral cages further dropped to 68 and 64%, respectively, of the initial values. However, the cubic and octahedral cages still displayed 1.8- and 3.4-fold enhancements, respectively, in terms of mass-specific activity relative to the value of the pristine commercial Pt/C. The improvement in durability can be attributed to the increase in interaction between the catalytic particles and carbon support because of the much larger size of Pt cages relative to the Pt solid particles in Pt/C (20 nm vs 3 nm).

7.2. Oxygen Evolution Reaction (OER)

Water splitting has received tremendous interest owing to its ability to generate O_2 and H_2 in a clean and renewable way.[512] As the anodic half-reaction, OER (also known as water oxidation reaction) has also found use in other applications related to energy storage and conversion.[512,513] The first report on OER appeared in 1789, but its commercial use nowadays is still impeded by the slow kinetics. According to DFT calculations, Ru is an optimal element for the OER catalyst.[514] However, the extremely low abundance in the Earth's crust and the high price tag of Ru place a severe limit on the large-scale use of this precious metal. This issue can be mitigated by engineering both the bulk and surface structures of Ru nanocrystals.[445] Recently, Ru nanocrystals with well-defined facets and in the metastable fcc phase were prepared and further evaluated as catalysts toward OER (Figure 43A,B). Regarding the phase dependence, fcc-Ru showed a 1.4-fold enhancement and 0.009 V drop in terms of area-specific activity and overpotential at 10 mA cm^{-2}, respectively, relative to the hcp counterpart.[95] More significantly, when the fcc-Ru

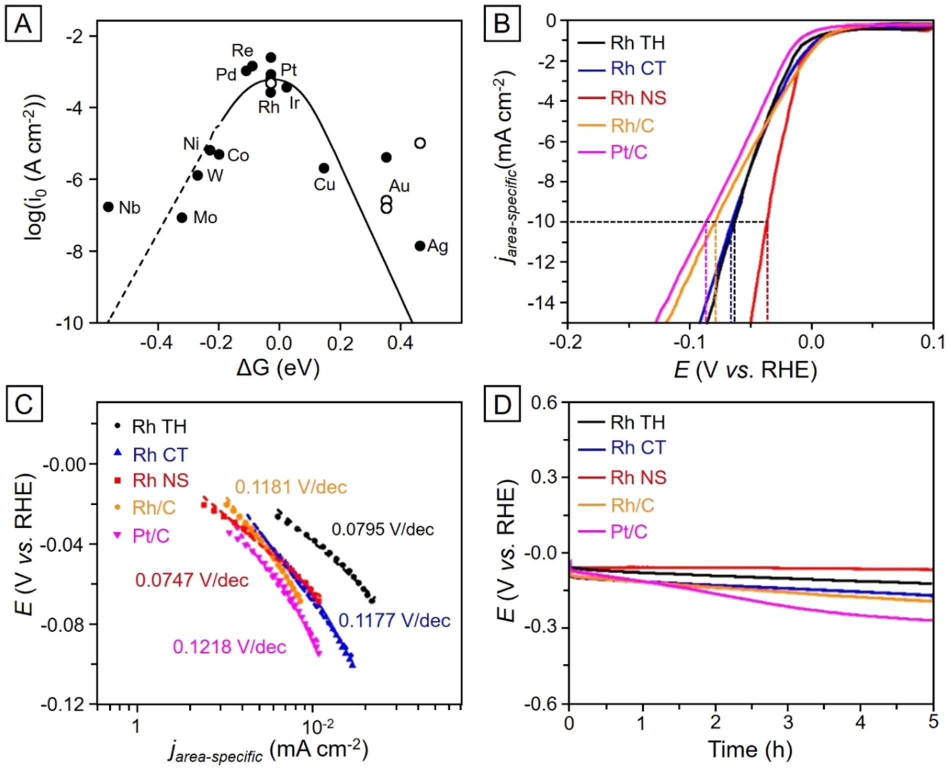

Figure 44. Catalysts based upon Rh for HER. (A) Volcano plot showing the exchange current density of different metals toward HER as a function of the free energy of H adsorption at 0 V vs normal hydrogen electrode (NHE). The metals on the left side of the volcano have high H coverage (1 monolayer) and those on the right side have low H coverage (0.25 monolayer). The dashed line indicates that the metals that bind H stronger than 0.2 eV/H usually form oxides at U = 0 V. The open circles are data from {111} facets whereas the filled circles are from polycrystalline surfaces. (B) HER polarization curves and (C) the corresponding Tafel plots of different Rh catalysts benchmarked against Pt/C in a 0.1 M KOH solution. (D) Chronopotentiometry curves of the catalysts at a constant current density of 5 mA cm^{-2}. TH, CT, and NS in panels (B−D) stand for tetrahedra, concave tetrahedra, and sheets, respectively. (A) Reprinted with permission from ref 529. Copyright 2010 American Chemical Society. (B−D) Reprinted with permission from ref 222. Copyright 2017 American Chemical Society.

nanocrystals were fabricated with an octahedral shape to present well-defined {111} facets, the area-specific activity was 3.3 times as high as that of the irregular fcc-Ru nanoparticles, suggesting the positive role of shape engineering in boosting the catalytic activity. The fcc-Ru octahedral nanocrystals also showed an overpotential of 0.029 V lower than that of the irregular fcc-Ru nanoparticles, confirming the superiority of {111} facets in catalyzing OER. The fcc-Ru truncated cubes were also evaluated as a catalyst toward OER. Their performance was enhanced relative to the irregular fcc-Ru nanoparticles but was inferior to the octahedral counterparts. Since truncated cubes are enclosed by a mix of {111} and {100} facets whereas octahedra are bound by {111} facets, it could be concluded that the fcc-Ru{111} facets were more active than fcc-Ru{100} facets in catalyzing OER. Despite the superior performance of the fcc-Ru{111} facets, the mechanism is yet to be elucidated. The facet-dependent activity can be rationalized by examining the adsorption of reactant and product molecules on the surfaces of fcc- and hcp-Ru, as well as their derived oxides, in addition to the effect arising from the Ru−RuO_x interface.[95,515,516] As discussed in sections 4 and 5, the synthesis of Ru nanocrystals has been limited to a few shapes. In the future, more endeavors should be devoted to engineering both the bulk and surface structures of Ru nanocrystals, pushing their catalytic performance to new limits.

Aside from Ru, Ir is also promising for OER.[496] Although the activity of Ir is slightly lower than that of Ru, the impressive stability makes Ir an intriguing catalyst for OER.[515,517] Again, the ever-increasing price of Ir has to be taken into consideration when applying this scarce metal to commercial use. To utilize this metal cost-effectively, reducing the particle size has been a commonly used strategy.[518] As an alternative, a recent study reported that the Ir catalyst can be presented as a 3-D assembly of ultrathin sheets to greatly enhance both the activity and stability toward OER.[519] When benchmarked against the irregular Ir nanoparticles, the overpotential at a current density of 10 mA cm^{-2} for the assembly of Ir sheets indicated drops of about 0.02 and 0.036 V in 0.1 and 1 M KOH solutions, respectively, demonstrating its superior activity in catalyzing OER. Moreover, the corresponding Tafel slopes of the sheet assembly were 0.0079 and 0.0074 V dec^{-1}, respectively, lower than that of Ir nanoparticles, confirming the role of a well-defined surface structure on the sheets in accelerating the reaction kinetics.

Although water splitting in an alkaline electrolyte has been well-developed, the high ohmic loss and low current density have impeded its further use. Alternatively, water splitting in an acidic electrolyte has received increasing interest in recent years owing to the high electrolytic efficiency.[520] When tested as a catalyst in an acidic medium, the assembly of Ir sheets could still maintain the enhanced performance toward OER.[519] The overpotentials at a current density of 10 mA cm^{-2} were 0.02 and 0.018 V in 0.1 and 0.5 M $HClO_4$ solutions, respectively, lower than those of Ir nanoparticles. In particular, by switching from irregular nanoparticles to the assembly composed of well-defined sheets, the area-specific activity was increased by 5.2 times when tested in 0.1 M aqueous $HClO_4$. The durability of the Ir catalysts was also evaluated by subjecting them to ADT at a constant current density of 2.5 mA cm^{-2}. After 8 h of ADT, more than 0.05 V increase in overpotential was observed for Ir nanoparticles in both 0.1 and 0.5 M $HClO_4$ solutions. In contrast, the overpotentials for the assembly of Ir sheets showed an increases of less than 0.02 V, suggesting improvement in terms of stability. Despite the strong performance for the assembly of Ir sheets, there was essentially no discussion on the mechanism responsible for the enhanced activity and stability. Further study is needed in order to elucidate this unique structure−property relationship.

Compared with solid nanocrystals, cages offer some immediate advantages for catalysis, such as optimization of the active sites by engineering the shape or surface structure while substantially increasing atom utilization efficiency.[40] A recent report demonstrated the synthesis of Ir-based cages featuring well-defined {100} facets and ultrathin walls of 1.1 nm in thickness.[362] When evaluated as a catalyst toward OER in 0.1 M $HClO_4$, the cages required an overpotential 0.074 V lower than that of commercial Ir/C catalyst, to reach a current density of 10 mA cm^{-2} (Figure 43C). When compared with the assembly of Ir sheets,[519] the overpotential at 10 mA cm^{-2} for the cages showed a drop of 0.049 V, confirming the role of well-defined {100} facets and cage structure in further improving the performance. When benchmarked against commercial Ir/C catalyst at an overpotential of 0.25 V, the {100} facets on the Ir cages were demonstrated to be 26.2 times more active than the poorly defined surface on the irregular nanoparticles (Figure 43D). Additionally, the mass-specific activity of the cages exhibited 18.1-fold enhancement relative to that of commercial Ir/C catalyst, which also significantly outperformed other catalysts reported in literature. The durability was evaluated by subjecting the catalysts to ADT through electrochemical cycling the catalyst in the potential range of 1.2−1.6 V at a rate of 0.1 V s^{-1}. After 500 cycles of ADT, the overpotential at 10 mA cm^{-2} for the cages showed essentially no change while the Ir/C catalyst exhibited a notable increase of 0.008 V. Especially, after 5,000 cycles of ADT, the cages only showed 41% loss in mass-specific activity, in contrast to a dramatic drop of 88% for the Ir/C catalyst. Relative to the Ir/C before and after durability test, the cages offered 10.6- and 90.3-fold enhancement, respectively, in terms of mass-specific activity.

7.3. Hydrogen Evolution Reaction (HER)

As the cathodic half-reaction in water splitting, HER has received extensive attention given that the generated H_2 can provide fuels for an array of clean-energy devices, such as fuel cells.[521−523] The sluggish kinetics of HER, however, tends to give a high overpotential, making it an energy-consuming process. Platinum has been identified as one of the most efficient catalyst in HER, with fast reaction kinetics and a negligible overpotential in an acidic medium, allowing its applications in proton exchange membrane electrolysis (Figure 44A). However, their activities can drop by 2 orders of magnitude when switching to an alkaline electrolyte such as seawater.[524,525] This sharp decrease in activity is mainly caused by the involvement of additional water-dissociation steps, as well as the weaker binding energy between metal surface and water relative to hydronium.[526] To this end, it is advantageous to switch to highly active electrocatalysts for HER in alkaline media. Rhodium has been identified as one of the promising candidates since its activity in an alkaline medium only dropped by 1 order of magnitude relative to the acidic system.[527−529] To further improve the performance, Rh nanocrystals with well-controlled shapes were fabricated and tested. In this case, the small dimensions of the nanocrystals can substantially increase the atom utilization efficiency while the well-defined surface structures are instrumental in optimizing the active sites toward HER. A recent study reported the synthesis of Rh tetrahedral nanocrystals, concave tetrahedral nanocrystals, and sheets, and further evaluated them as catalysts toward HER.[222] Figure 44B,C, shows the HER polarization curves and the corresponding Tafel plots of various catalysts in 0.1 M KOH, with the Rh nanocrystals featuring well-defined shapes all displaying better performance than commercial Rh/C catalyst. In particular, the overpotentials at a current density of 10 mA cm^{-2} for Rh tetrahedral and concave tetrahedral nanocrystals were 0.016 and 0.014 V, respectively, much lower than that of the Rh/C. Interestingly, for the Rh sheets, the overpotential indicated a significant drop of 0.043 V relative to the Rh/C catalyst. Moreover, the Tafel slopes of Rh tetrahedra, concave tetrahedra, and sheets were 0.0795, 0.1177, and 0.0747 V dec^{-1}, respectively, much lower than that of the commercial Rh/C (0.1181 V dec^{-1}), validating the effectiveness of surface engineering in enhancing the catalytic performance (Figure 44C).

In addition to the impressive activity, the Rh nanocrystals featuring well-controlled shapes also exhibited substantial improvement in durability (Figure 44D), when tested by subjecting the various catalysts to controlled-current electrolysis at a current density of 5 mA cm^{-2}.[222] After 5 h of electrolysis, the Rh/C catalyst showed a drastic increase in overpotential to 0.193 V, whereas those of the Rh tetrahedral and concave tetrahedral nanocrystals were only increased to 0.122 and 0.168 V, respectively. Significantly, the Rh sheets after electrolysis test displayed a very minor rise in overpotential to 0.065 V, much lower than that of the Rh/C catalyst (0.193 V). When switching the concentration of KOH electrolyte from 0.1 to 1 M, the Rh nanocrystals with controlled shapes still showed promising HER activities than the commercial Rh/C catalyst. Particularly, the Rh sheets greatly outperformed the Rh/C catalyst in terms of overpotential at a current density of 10 mA cm^{-2}, catalytic activities, and durability. Collectively, these results demonstrated the crucial function of shape engineering in improving the catalytic properties of Rh-based catalysts toward HER.

7.4. Alcohol Oxidation Reaction (AOR)

Direct alcohol fuel cells (DAFCs) can be used to power portable devices and transportation vehicles.[530,531] Compared with H_2-based fuel cells, DAFCs are advantageous in terms of easy storage, transportation, and refueling of the fuels, in addition to their higher volumetric energy densities. However, the anodic half-reaction, AOR, is kinetically sluggish and needs to be substantially improved through the assistance of a catalyst. The most effective catalyst is based upon Pd, whose activity shows a strong dependence on the surface structure.[228,530,532] In one study, Pd nanocrystals with cubic, rhombic dodecahedral, and octahedral shapes for the presentation of {100}, {110}, and {111} facets, respectively, have been evaluated as catalysts for a systematic investigation of their facet-dependent performance toward the electro-oxidation of both ethanol and EG in an alkaline medium

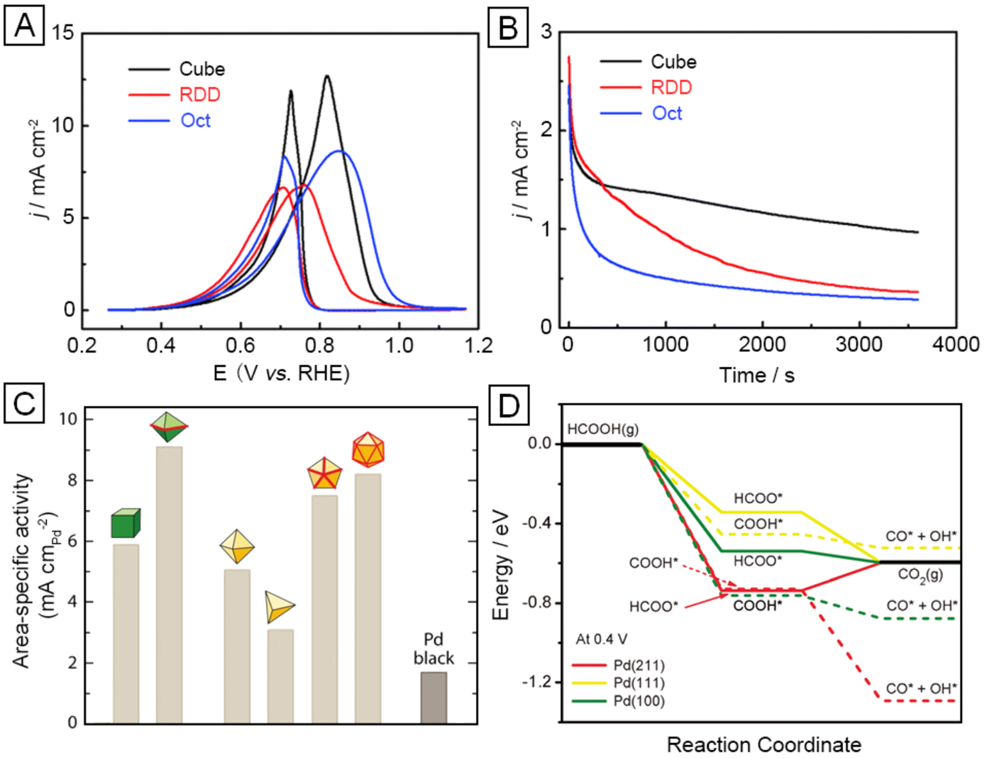

Figure 45. Catalysts based upon Pd for AOR and FAO. (A) CVs and (B) chronoamperometric curves at 0.67 V recorded from Pd cubes, RDD, and octahedra in a mixture of 1.0 M NaOH and 1.0 M ethanol toward EOR. (C) Area-specific activities toward FAO for Pd single-crystal and twinned catalysts enclosed by {100} or {111} facets at 0.4 V (vs RHE). (D) DFT-calculated thermochemical potential energy surfaces for FAO at 0.4 V (vs RHE) through HCOO-mediated (solid lines) and COOH-mediated (dashed lines) pathways on (211) (red), (111) (yellow), and (100) (green) surfaces of Pd. The reaction stoichiometry is balanced with H$^+$ and e$^-$. (A and B) Reprinted with permission from ref 228. Copyright 2018 Royal Society of Chemistry. (C) Reprinted with permission from ref 45 and ref 388. Copyrights 2016 Annual Reviews and 2015 Wiley-VCH, respectively. (D) Reprinted with permission from ref 388. Copyright 2015 Wiley-VCH.

(Figure 45A).[228] In the case of EOR, Pd cubes exhibited the greatest area-specific activity, which was 1.9 and 1.5 times greater than those of their rhombic dodecahedral and octahedral counterparts. Based on DFT calculations, the superior performance of Pd{100} facets could be attributed to both the lowest energy barrier to the dehydrogenation of ethanol among the three types of facets and the favorable oxidation of intermediates such as $CH_3C^*{=}O$ and CO.[533−535] Different from the trend in area-specific activity, the onset potential of the Pd nanocrystals followed the order of {110} < {100} < {111}. The authors claimed that this trend could be ascribed to the lowest potential for OH^- chemisorption on {110} facets, which served as an essential reactant in oxidizing carbonaceous intermediates including $CH_3C^*{=}O$, CO, and CH_x. However, the lower mobility of surface species on the {110} stepped facet, as compared to those on flat {111} and {100} facets, tended to compromise the overall oxidation reaction and resulted in a low activity for Pd RDD.

The durability of these Pd-based catalysts was also examined through chronoamperometric measurement at 0.67 V for 1 h (Figure 45B).[357,533,536] In particular, the area-specific activity of the Pd cubic nanocrystals showed 59% decay from the initial value, whereas those of the rhombic dodecahedral and octahedral nanocrystals dropped by 82 and 87%, respectively. According to the results from CO stripping measurement and DFT calculations, Pd{100} facets were more resistant to the accumulation of both CO and intermediates such as acetate species relative to {110} and {111} facets. As a result, more active sites remained accessible on {100} than on {110} and {111} during the long-term operation, giving rise to the great enhancement in durability for the {100}-enclosed Pd cubes.

With regard to the electro-oxidation of EG, the performance of Pd nanocrystals was also found to be sensitive to the surface structure. Similar to the case of EOR, the {100} facets on Pd cubes were catalytically more active than both {110} and {111} facets toward ethylene glycol oxidation reaction (EGOR).[537] However, the onset potentials of Pd catalysts for EGOR indicated a positive shift of roughly 0.2 V relative to the case of EOR, which could be attributed to higher CO coverage resulting from enhanced C−C bond cleavage of EG than the case of ethanol. Additionally, Pd{110} facets showed enhanced area-specific activity than {111} facets toward EGOR, which was opposite to the trend for EOR. In analogy to the role played by the intermediate $CH_3C^*{=}O$ in EOR, the authors argued that the trend in EGOR could be explained by the difference in interaction between the pivotal intermediate $HO{-}CH_2C^*{=}O$ and various Pd surfaces.[538] When subjected to a durability test at 0.82 V for 1 h, the oxidation current of Pd RDD was found to decay at a larger magnitude than those of cubic and octahedral nanocrystals after 100 s, suggesting the enhancement in stability for {100} and {111} facets relative to {110} facets during long-term operation.

7.5. Formic Acid Oxidation (FAO)

Direct formic acid fuel cells (DFAFCs) have received considerable attention owing to their lower crossover flux and toxicity relative to the devices based on methanol.[539−541] As the anodic half-reaction, FAO can proceed through both direct and indirect pathways, with CO_2 and CO generated as

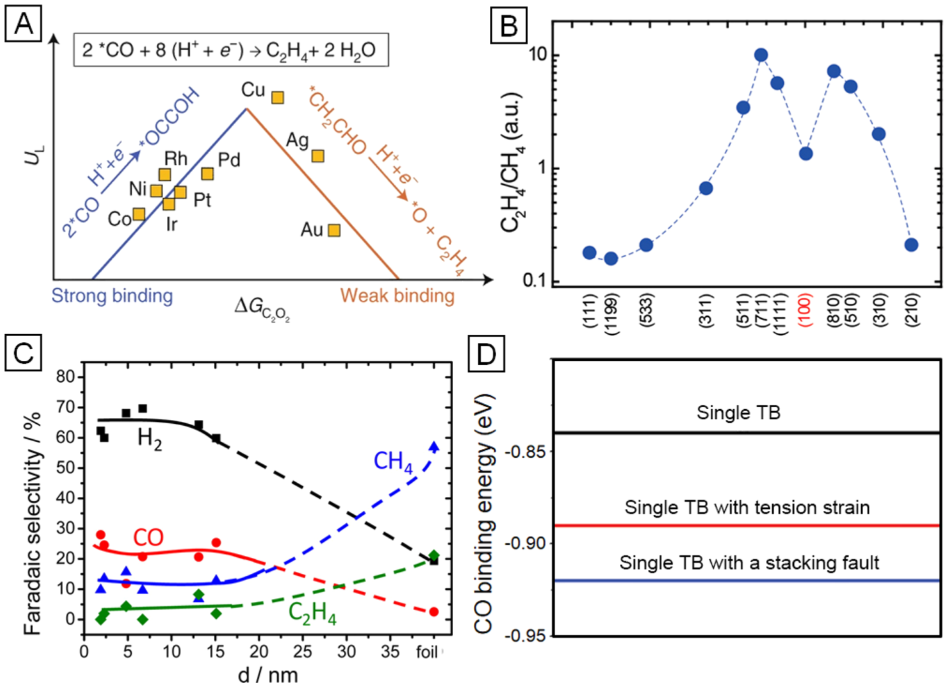

Figure 46. Catalysts based upon Cu for CO_2RR. (A) Volcano plot showing the limiting potential for C_2H_4 production from CO as a function of $^*C_2O_2$ binding energy on the (100) facets of different transition metals. (B) Variation in the ratio of C_2H_4 to CH_4 in terms of current efficiency on different types of Cu surfaces. (C) Faradaic selectivity of reaction products during CO_2RR on Cu nanoparticles with different sizes. The measurements were conducted in a 0.1 M $KHCO_3$ solution at −1.1 V (vs RHE). (D) DFT-calculated CO binding energies for various defect structures on Cu(111) surface, with the most stable one achieved by the single twin boundary (TB) combined with a stacking fault. (A) Reprinted with permission from ref 554. Copyright 2019 Nature Publishing Group. (B) Reprinted with permission from ref 17. Copyright 2019 American Chemical Society. (C) Reprinted with permission from ref 553. Copyright 2014 American Chemical Society. (D) Modified with permission from ref 240. Copyright 2018 Wiley-VCH.

the products, respectively. Compared with other metals, Pd-based catalysts are known for their capability to promote the direct pathway and thus mitigate the poisoning effect caused by the CO adsorption on the catalyst.[542] As the most promising catalyst toward FAO, the activities of Pd nanocrystals have been reported to show a strong correlation with the surface structure.[71,132,388,543] One study systematically examined the FAO activities of Pd nanocrystals enclosed by a variety of facets, twin boundaries, and their combinations under identical experimental conditions.[388] As shown in Figure 45C, essentially all of the Pd nanocrystals with well-defined shapes showed enhancement in area-specific activity relative to commercial Pd black. Specifically, Pd cubes enclosed by well-defined {100} facets showed a 2-fold enhancement relative to their tetrahedral counterpart, suggesting that {100} facets were more catalytically active than {111} facets in catalyzing FAO.[544] Although covered by the same {111} facets, it is interesting to note that Pd octahedra showed a higher area-specific activity than Pd tetrahedra, confirming the importance of shape control rather than facet engineering.

In addition to the facets on single-crystal particles, it was demonstrated that twin boundaries and surface strains could be introduced to further boost the activity.[388] For example, despite the enhanced activity of {100} over {111}, Pd decahedra covered by {111} facets but with additional twin boundaries outperformed the cubic counterpart in terms of area-specific activity. When Pd icosahedra with an even larger number of twin boundaries on the surface were employed as the catalyst, further enhancement in area-specific activity was observed. Significantly, owing to a combination of both the {100} facets and twin defects, Pd RBPs were found to exhibit the greatest area-specific activity among all the Pd nanocrystals that have been tested.

To rationalize the experimental observations, DFT calculations were conducted to derive the reaction intermediates on various catalytic surfaces.[388] Figure 45D shows the calculated potential energy surface for FAO at 0.4 V (vs RHE) through the carboxyl (COOH*)-mediated and formate (HCOO*)-mediated pathways, respectively. It was found that both COOH* and HCOO* species had lower energies on Pd(100) relative to Pd(111), giving rise to a superior activity toward FAO. In terms of twin boundaries, which can be modeled as Pd(211) surface, both COOH* and HCOO* species were isoenergetic. Although the energies of the two intermediates on Pd(211) were not the lowest among the various types of Pd surfaces, the relative stability of HCOO* over COOH* on the twin boundaries drove the reaction flux and selectivity toward the HCOO*-mediated pathway rather than the COOH*-mediated pathway dominated by Pd(111) and Pd(100) surfaces. As such, the CO poisoning stemming from the decomposition of COOH* could be effectively mitigated on the twin boundaries, leading to substantial enhancement in activity.

7.6. Carbon Dioxide Reduction Reaction (CO_2RR)

As a harmful greenhouse gas, excessive emission of CO_2 has caused major environmental concerns. Electrochemically reducing CO_2 to valuable fuels is a promising approach to decreasing the net emission of CO_2 while completing the carbon cycle.[545] Compared with the commonly produced small molecules (e.g., CO and formate), further reduced products such as multicarbon oxygenates and hydrocarbons have received more attention due to their higher energy densities, a wider scope of application, and the corresponding higher values and larger markets.[545] During the reduction process, the chemically stable CO_2 will be first reduced to CO on the surface of a catalyst. The CO intermediate then undergoes further reduction, hydrogenation, as well as C−C coupling to generate hydrocarbons and multicarbon products (e.g., CH_4, C_2H_4, and ethanol). The adsorbed CO can also be released from the surface for the production of CO. As documented by many reports, the selectivity toward a specific product is highly sensitive to the surface structure of the catalyst, in addition to other parameters such as size, composition, support, and electrolyte.[546]

Nanocrystals made of Cu, Ag, Pd, Au, and Sn have all been explored as catalysts toward CO_2RR. Different from other metals that typically generate CO and CH_4 as the major products, Cu is able to produce significant amounts of oxygenates and hydrocarbons such as ethylene (Figure 46A). The catalysts based on Cu nanocrystals, however, tend to suffer from the following drawbacks: (i) poor selectivity as a variety of products such as CO, CH_4, formate, ethylene, ethanol, and *n*-propanol can all be generated; (ii) high overpotentials because the highest selectivity toward multicarbon products is often achieved at a potential more negative than −1.0 V (vs RHE); and (iii) poor stability as the original shape of the Cu nanocrystals can hardly be maintained during CO_2RR, making it difficult to keep the selectivity and activity. Engineering the surface structure of Cu nanocrystals holds great promise in achieving purer products at a reduced overpotential. According to the results from both experimental and computational studies (Figure 46B), the {100} and {111} facets on Cu nanocrystals favored the formation of ethylene and methane, respectively.[547−549] The formation of ethylene involved the dimerization of CO molecules to generate $C_2O_2^-$ intermediates, followed by their protonation. The square arrangement of Cu atoms on {100} facets presented an optimal geometry for the adsorption of $C_2O_2^-$ dimers while the negative charges on the adsorbed dimers could cause additional stabilization through solvation.[550,551] In a recent study involving cubic and octahedral nanocrystals with similar sizes, the FE of ethylene for the cubes was found to be much higher than that for the octahedra, with the former approaching 34% at −1.15 V while the latter was only 19%.[159] This study also validated the computational result in that the {100} facets preferred the formation of ethylene, as well as the significance in controlling the shape of Cu nanocrystals.[552]

The size of the Cu nanocrystals also plays an important role in determining their catalytic performance. Decreasing the size would lead to an increase in the mass-specific activity, but the change in surface structure could impact the selectivity and, in most cases, was detrimental to CO_2RR. It was reported that a dramatic increase in both activity and selectivity toward H_2 and CO was observed when the Cu nanoparticles were reduced to a size below 5 nm (Figure 46C).[553] At the same time, the selectivity toward hydrocarbons such as methane and ethylene was substantially suppressed. Based on DFT calculations, this trend could be attributed to the higher proportion of low-coordination atoms (CN < 8, starting as low as CN = 5) on smaller nanoparticles. These atoms imposed strong chemisorption to CO and H, limiting their movement on the Cu surface and thus their coupling for the generation of hydrocarbons. On the other hand, the strong adsorption of H accelerated the rate-determining step of HER (the Volmer reaction, $H^+ + e^- + * \rightarrow H_{ad}$, * represents the free Cu surface sites), greatly facilitating the generation of H_2 while suppressing the reduction of CO_2.[553] A similar trend was also observed in the case of Cu cubes,[156] where a higher proportion of H_2 was obtained at a smaller particle size.

Planar defects, including twin boundaries and stacking faults, also enhance the selectivity toward C_{2+} products by affecting the adsorption of CO intermediate. For Cu star decahedra, the presence of twin boundaries and tensile strain, together with the stacking faults induced by a stress release mechanism, led to an upshift for the *d*-band center of the surface atoms and thus an increased binding energy between the catalyst and CO molecules.[240] The higher density of CO on the Cu surface improved the selectivity toward ethylene for the achievement of the highest FE approaching 52.4%. The influence of planar defects was further confirmed by DFT calculations, where three types of atomic models containing twin boundaries were compared (Figure 46D).[240] A CO binding energy of −0.92 eV was obtained for {111} facets with a single twin boundary and a stacking fault, which was 0.08 eV stronger than the single twin boundary alone, revealing the importance of planar defects in enhancing the CO coverage density and thus C_{2+} selectivity.

By introducing a certain number of steps into the surface of a nanocrystal, high-index facets can be generated and, in most cases, improve the selectivity toward C_{2+} products due to the enrichment of under-coordinated sites and thus the enhanced adsorption of CO molecules.[547] In one study, highly defective, prism-shaped Cu nanocrystals showed a 4-fold greater current density for ethylene production relative to a planar Cu foil.[555] Through CV measurements, an intense reduction peak was observed between −0.25 and 0 V for the prism-based catalyst, which was previously assigned to the voltammetric feature of the defect sites. In the presence of surface defects, the C_1 intermediates could be effectively stabilized and their high coverage density greatly promoted the generation of C_{2+} products. However, different from the twin defects that could be maintained after long-term electrolysis,[240] the steps and kinks on the Cu surface could hardly be stabilized during CO_2RR and the contribution of surface defects to the enhancement of C_{2+} production was questionable. For example, a decrease in the FE of ethylene from 57% to below 40% was observed for Cu dendrites after 150 min of electrolysis, and this could be assigned to the structural degradation.[556] After long-time electrolysis, the needle shape of dendrites was hardly retained and the high-index facets containing low-coordinated sites, which were responsible for the high selectivity toward ethylene, were also lost, leading to a decrease in the production of C_{2+} species. Whether the high-index facets could be stabilized for continuously contributing to the high selectivity in CO_2RR is still under debate, and more attention and efforts should be directed to the design and stabilization of Cu nanocrystals enclosed by active high-index facets.[556,557]

Apart from surface reconstruction, it is also challenging to prevent the shape degradation of Cu nanocrystals. As revealed in a recent report, when Cu cubes of different sizes were used as catalysts, Cu nanoclusters surrounding the catalysts were observed after 1 h of electrolysis, together with sintering of the cubes when the reaction time was further extended.[558] Since the stability test was conducted at −1.1 V, a potential below the oxidation potential of Cu, the possible dissolution and then redeposition of Cu atoms could be ruled out. Clusters with high surface energies were not favored by thermodynamics either. According to DFT calculations, the adsorption of H and CO on Cu surface and the subsequent change to surface energies of different facets were the main factors that contributed to the degradation of the cubic shape. Under negative potentials, nanocrystals enclosed by {111}, {110}, and high-index facets capable of stabilizing H and CO intermediates were preferred. Thus, pinholes were generated on the surface of cubes, and clusters would appear around the cubes. Interestingly, when lower overpotentials (e.g., −0.7 and −0.3 V) were applied, the cubic shape was essentially preserved and no aggregation of the nanocrystals was observed either, indicating the importance of decreasing the overpotential of CO_2RR for Cu-based catalysts.[558] Besides lowering the overpotential, other methods such as covering the nanocrystals with graphene or surface oxides[559] and in situ generation of nanocrystals with well-defined facets[261] have also been applied to improve the stability of Cu nanocrystals. Maintaining the shape and thus facet structure of a Cu-based catalyst at relatively high overpotentials plays a key role in retaining its high selectivity toward a specific product.

7.7. Other Electrochemical Reactions

In addition to the representative electrocatalytic reactions highlighted above, there are many emerging applications where engineering the surface structure of noble-metal nanocrystals also offers an avenue to enhance the performance. For example, electrochemical nitrogen reduction reaction (NRR) has received ever increasing attention as it can potentially lead to cost-effective and sustainable production of NH_3 for use as a fertilizer and a carbon-free energy carrier.[560] In consideration of the large (941 kJ mol^{-1}) bond energy of the N≡N triple bond, metal nanocrystals made of Au, Ru, and Mo have recently been investigated as NRR catalysts. Their structure−property relationships have also been explored to a certain extent. For example, Au rods with two ends covered by {730} high-index facets were found to be highly active at −0.2 V (vs RHE), with yields as high as 1.648 and 0.102 $\mu g\ h^{-1}\ cm^{-2}$ for NH_3 and N_2H_4, respectively.[561] Such performance was even comparable to that for N_2 fixation under high temperatures and high pressures. The stepped, unsaturated facets were proposed to play a vital role in facilitating the cleavage of N≡N bonds for the chemisorption of N atoms on the Au surface, followed by their reduction to NH_3 and N_2H_4.

As the anodic half-reaction of a hydrogen-based fuel cell, hydrogen oxidation reaction (HOR) converts H_2 molecules to protons. Because of its rapid kinetics in an acidic medium, this reaction has attracted limited attention from the research community.[562] Among various metal catalysts, Pt is most active toward HOR in terms of both exchange current density and mass-specific activity, and the activity is highly sensitive to the surface structure.[562,563] In one study involving HOR under acidic condition, specific current densities were measured for Pt nanoparticles with sizes varying in the range of 2−15 nm, and the smallest particle showed the greatest activity.[564] The authors attributed this result to the higher activity of undercoordinated atoms situated at edges and vertices than those on the side faces. They also predicted that nanoparticles enriched in edges and/or vertices would show improved performance toward HOR. When switching to an alkaline medium, however, the HOR kinetics will be slowed down drastically and an effective catalyst is of great necessity in order to accelerate the reaction. According to the measurements involving single-crystal substrates, Pt(110) was more active toward HOR than both Pt(100) and Pt(111) in alkaline media, and the trend could be ascribed to a higher coverage density of the underpotentially deposited hydrogen (H_{UPD}) on Pt(110).[565,566] Due to the lack of extensive experimental and/or computational studies, it is difficult to discuss the electrochemical reactions presented in this section in detail. More endeavors should be devoted to the shape- or facet-dependence of these electrocatalytic reactions.

8. OUTLOOKS

In this review article, we have discussed how to engineer the shape and thus surface structure of monometallic nanocrystals for enhancing their performance in heterogeneous catalysis. In general, the performance of a catalyst based on noble-metal nanocrystals is dependent on a number of factors other than the shape, including catalyst support, capping agent, as well as the introduction of other metals to form a bi- or multimetallic system. When moving into practice, how to preserve the shape of a nanocrystal and how to scale up a colloidal synthesis without losing quality control also need to be taken into consideration. Having a good understanding of these additional factors also plays a vital role in rationally developing the most effective catalyst toward a specific reaction. In this section, we offer a brief discussion on each one of these subjects, with an aim to provide the readers with a broader perspective regarding the use of shape-controlled nanocrystals in catalytic applications.

8.1. Removal of Surface Contaminants

Unlike the conventional single-crystal substrates, the surface of nanocrystals prepared using colloidal synthesis can be complicated due to their inherent heterogeneity caused by vertices and edges, as well as the adsorption of capping agents, stabilizers, solvents, and many other known or unknown chemical species. For capping agents, including inorganic ions, organic polymers, and biomolecules, they are indispensable for shape-controlled syntheses owning to their capability to selectively bind to specific types of facets.[106,107] Despite their immediate advantages in directing the shape evolution process, capping agents can significantly alter the surface of a metal nanocrystal by changing the coordination environment of atoms and blocking the active sites. In order to take full advantage of the structure−property relationship discussed in this article, it is necessary to remove the capping agents for the creation of a clean surface. Same is true for other types of surface contaminants. To this end, it is important to have a good understanding of the interaction between a contaminant species and the surface of a nanocrystal. Typically, the interaction can be either physisorption or chemisorption in nature.[567,568] Physisorption is driven by intermolecular interactions such as van der Waals force, whereas chemisorption involves charge transfer and bond formation. Depending on the mechanism of adsorption, one can rely on the use of different methods to effectively remove the surface contaminants.

Washing with a proper solvent during centrifugation, a routine procedure involved in almost all colloidal syntheses of nanocrystals, is the simplest way to remove the surface contaminants that are weakly attached to the surface. As demonstrated in one study, the poly(vinyl alcohol) (PVA) on Au nanocrystals could be simply removed by washing with solvent during centrifugation at a low temperature.[569] Compared with other methods that were carried under harsh conditions, including UVO treatment,[149,150] plasma etching,[71] and thermal annealing,[151,570] washing could avoid possible shape deformation to the nanocrystals. As expected, the washing process only works for the systems involving physically adsorbed contaminants.

As for chemisorbed species, such as halide ions on metal surface,[143,571,572] the removal of capping agents mainly relies on weakening the bonding strength. One report suggested that the Br^- adsorbed on the surface of Pd cubes could be removed when the sample was heated in EG at 100 °C, together with the addition of CA and PVP as a reducing agent and a colloidal stabilizer, respectively.[571] The reducing power from CA could convert the partially oxidized Pd surface back to Pd(0) to facilitate the detachment of Br^- ions. The high temperature involved in the post treatment would help break the bond between Pd and Br^- ions. Another study reported that the Pd cubes treated with TBA would give a clean surface without PVP and Br^-.[151] The removal of Br^- and PVP was verified by XPS and IR spectroscopy analysis (Figure 47A,B). The CV curves of the cleaned cubes exhibited strong peaks corresponding to hydrogen adsorption/desorption on Pd{100}, while none of these peaks was observed for the as-prepared Pd cubes because their surface was covered by various chemical species. They also observed that heating the Pd cubes at 200 °C in an O_2 atmosphere could only remove the Br^- and PVP partially, and was not adequate in obtaining a clean surface (Figure 47C). It was claimed that the PVP was naturally removed by TBA since polar compounds were soluble in polar solvents, while the removal of Br^- was attributed to its capability of forming a salt with the amine compound. Despite the experimental evidence, the mechanism seems to be questionable as PVP could not be efficiently removed by washing with ethanol, which is also a polar solvent.

For nanocrystals applied to electrocatalysis, potential holding offers another nondestructive method for cleaning the surface of metal nanocrystals. As shown in one study, holding the electrode potential in the hydrogen evolution region for 1 min was adequate to remove both the halide ions and PVP adsorbed on the surface of Pd cubes.[573] It was suggested that the hydrogen generated during the potential holding resulted in lattice expansion for Pd cubes, weakening the bonding strength between Br^- ions and metal atoms. This nondestructive method has attracted much attention recently and was applied to a number of electrochemical studies.[574,575] It is worth pointing out that the capping agent may also be beneficial to the catalytic activity in some cases, similar to an activity promoter or a selectivity modifier.[576,577] However, there are very limited reports on such dual-functional species capable of directing the evolution of shape during a synthesis while promoting the catalytic activity during an application.

8.2. Shape Instability

Stability is of great importance in determining the long-term use of a catalyst. In terms of shape instability (see section 2.6), it can be induced through either a physical transformation such as sintering[23] or a chemical process such as leaching.[578] Nanocrystals with controlled shapes are susceptible to deformation because of their intrinsically high specific surface area and high surface energy. When nanocrystals undergo changes in size, shape, and/or surface structure, their catalytic activity and selectivity will be altered accordingly.[579]

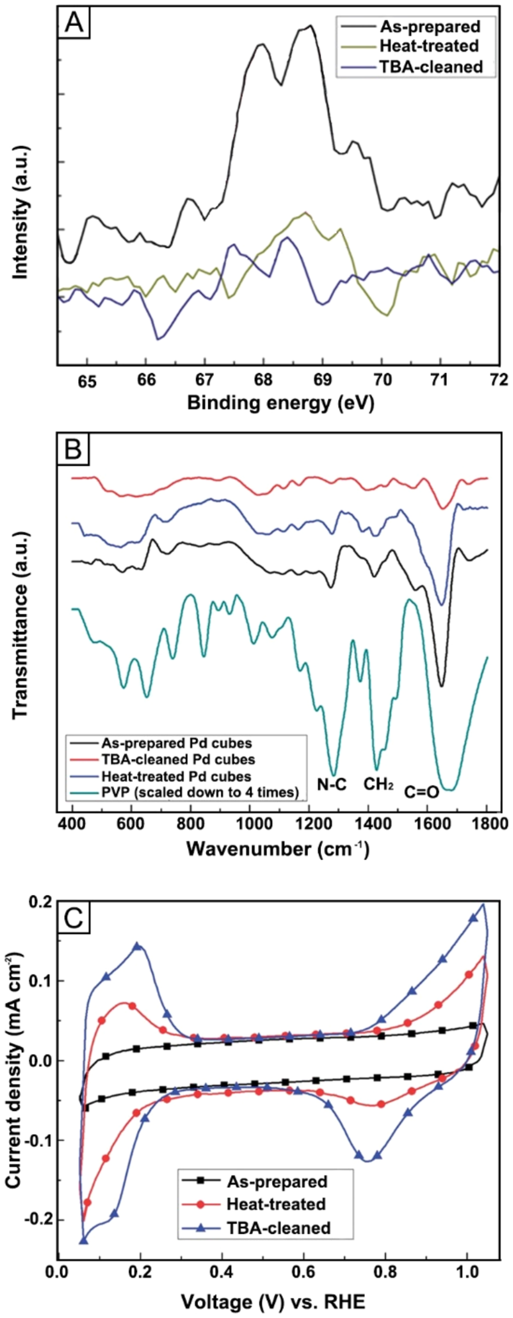

Figure 47. Removal of surface contaminants. (A) Br 3d XPS spectra, (B) Fourier-transform infrared spectroscopy (FTIR) spectra, and (C) CV curves of carbon-supported Pd cubes treated under different conditions. Reprinted with permission from ref 151. Copyright 2013 Royal Society of Chemistry.

As for the physical transformation, elevation in temperature is the most common stress that will induce changes to the shape or morphology of nanocrystals.[95,580−583] As discussed in section 2.6, the overall higher surface energy makes most shape-controlled nanocrystals vulnerable to intraparticle sintering. The driving force is to reduce the total surface energy by transforming the shape to the thermodynamically stable shape defined by the Wulff construction. The thermal stability of different nanocrystals can vary significantly depending on their composition, crystal structure, and shape. For example, a simulation study analyzed the structural and thermal stabilities of Pt nanocrystals enclosed by different high-index facets.[584] It was found that the general shape stability complied with the order in TOH < THH < TPH, with a high dependence on the size and specific surface area of the nanocrystals.

Except for the physical parameters such as temperature and pressure, chemical reactions can also induce changes to the shape of metal nanocrystals. Typical examples include leaching,[65] surface poisoning,[585] and chemical transformation (e.g., the formation of metal hydride, oxide, or carbide).[435,461,586] One report suggested that Pd nanoparticles could go through a "refaceting process" in N_2 atmosphere at an elevated temperature.[587] Figure 48 shows the time-elapsed TEM images of a Pd sphere that evolved into a truncated cuboid under 1 bar N_2 at 200 °C. Similar to the mechanism of a capping agent, the interaction between N_2 gas molecule and Pd surface is facet-dependent. The strong interaction between N_2 and Pd{110} stabilized these facets and thus transformed the nanoparticles to possess a specific geometric shape, that is, faceting. This report indicated that even N_2, an inert gas, could cause changes to the shape of a nanocrystal. Therefore, for chemical reactions involving a gas as the reactant/product, the possible change in shape induced by the gas should be taken into consideration as the metal nanocrystals might have different catalytic performance under different gas environments as a result of the refaceting process.

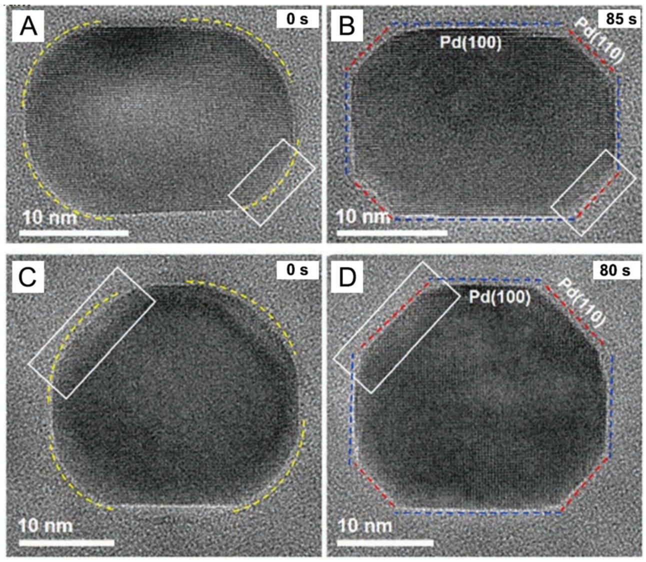

Figure 48. Time-elapsed TEM images of two different Pd nanoparticles under 1 bar N_2 at 200 °C. The nanoparticles with round corners were transformed into truncated cuboids encased by a mix of {100} and {110} facets. Reprinted with permission from ref 587. Copyright 2018 Royal Society of Chemistry.

Covering the surface of nanocrystals with a "protective layer" is the most commonly used strategy for improving their shape stability. The use of a proper ligand can enhance the colloidal stability, thermal stability, and even the chemical stability of nanocrystals. However, as discussed in section 8.1, the binding of ligand to the surface can also block the active sites and even change the surface structure and electronic structure of the nanocrystals. Up until now, there are only a few cases showing that the catalytic activity/selectivity will not be affected by the presence of a stabilizing ligand. One notable example involves the use of graphene to protect Cu wires.[559] Bare Cu wires were shown to have good selectivity toward methane in CO_2RR, but they suffered from poor shape stability. By wrapping the wires with a layer of graphene, both the morphology and the high selectivity of the catalyst could be preserved. The ability to maintain stability and activity of nanocrystals requires a good understanding of the mechanisms for both the target reaction and the shape deformation process.

8.3. Introduction of Catalyst Support

In practical use, metal nanocrystals are typically loaded on another material that can provide physical support, and a pathway for electron transport in the case of electrocatalysis. The support can also help fix the nanocrystals and prevent them from aggregation or sintering. However, the two steps involved in the preparation of a catalyst, including colloidal synthesis of nanocrystals and their dispersion on a support, will inevitably introduce additional costs. The performance of the catalyst will be severely tarnished if the nanocrystals are not uniformly distributed across the support. Moreover, the capping agent, stabilizer, and other chemical species usually involved in a colloidal synthesis tend to adsorb on the nanocrystals, greatly limiting the accessibility of the active sites and thus downgrading the catalytic activity. To this end, a method was demonstrated for the in situ growth of well-dispersed PtNi and PtNiCo octahedral nanocrystals on various types of carbon materials in the absence of any capping agent (Figure 49A–C).[588] These nanocrystals exhibited superior performance toward ORR because of the improvement in surface cleanness and a better interface with the support associated with the in situ growth method. An electrochemical method was also reported for the in situ growth of Pt nanocrystals covered by high-index facets on a carbon support, in which insoluble Cs_2PtCl_6 dispersed on carbon black was subjected to a square-wave potential cycling.[589] In principle, these methods should be extendible to other systems.

Additionally, it was reported that the support could modify the electronic structure of the catalyst and even introduce a synergistic effect between the catalyst and support to significantly enhance the catalytic activity and durability.[591−593] For example, when Au nanocrystals were supported on a reducible transition metal oxide (e.g., Fe_2O_3 or TiO_2) capable of providing reactive oxygen, they exhibited enhanced activity toward CO oxidation by up to one magnitude than the control sample on an "inert" support.[591] In another example, $Ti_{0.7}Mo_{0.3}O_2$ nanostructures were employed as a novel support for Pt nanocrystals, and they could modify the electronic structure of the surface Pt atoms and thus enhance their catalytic activity by 7 and 2.6 times toward ORR when compared with those of commercial Pt/C and PtCo/C catalysts, respectively (Figure 49D).[590] Moreover, due to the strong interaction between Pt nanocrystals and $Ti_{0.7}Mo_{0.3}O_2$ support, the catalyst exhibited extremely high stability during potential cycling (Figure 49E). Along the same line, considerable efforts have been made in searching for the optimal support materials for various catalysts. Taking ORR as an example, both carbon materials, such as reduced graphene oxide[594,595]and carbon nanotubes,[596] and novel noncarbon materials like titanium nickel binary nitride[597] and tin-doped indium oxide nanoparticles[598] have all been identified as effective supports for Pt electrocatalysts. There is a strong interest in developing advanced supports featuring beneficial interactions with the catalytic nanocrystals while providing strong resistance to sintering.

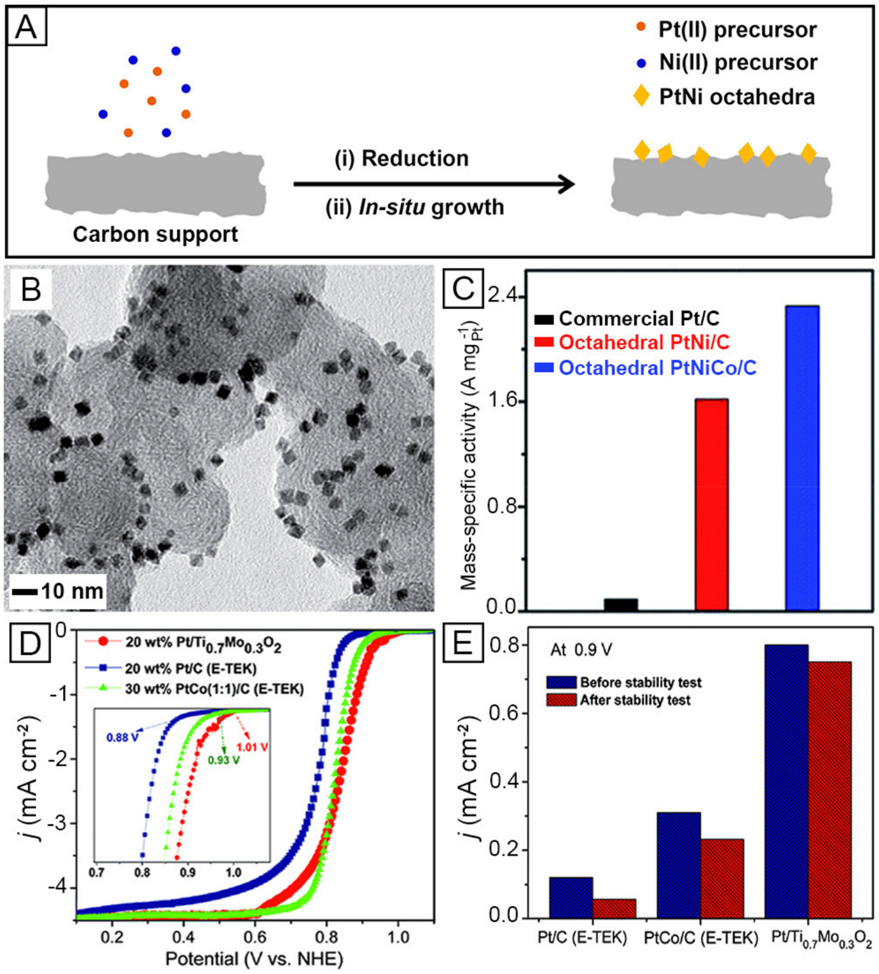

Figure 49. (A) Schematic illustration of in situ growth of highly dispersed PtNi octahedra on a carbon support without the involvement of a capping agent. (B) TEM image of octahedral PtNi/C catalyst. (C) Comparison of the mass-specific activities of the Pt/C, octahedral PtNi/C, and octahedral PtNiCo/C catalysts toward ORR at 0.9 V vs RHE. (D) Polarization curves showing the ORR current of Pt/$Ti_{0.7}Mo_{0.3}O_2$ catalyst and commercial Pt/C (E-TEK) and PtCo/C (E-TEK) catalysts. (E) Stability test of Pt/$Ti_{0.7}Mo_{0.3}O_2$ and the commercial catalysts before and after 5,000 potential cycles. (B and C) Modified with permission from ref 588. Copyright 2014 Royal Society of Chemistry. (D and E) Modified with permission from ref 590. Copyright 2011 American Chemical Society.

8.4. Mass Production without Compromising the Quality

Although significant progress has been made in controlling the colloidal synthesis of noble-metal nanocrystals with well-defined surface structures for various catalytic reactions, it remains a grand challenge to scale up their production for industrial applications without compromising the product quality. So far, the protocols reported in literature are mainly based on the use of small batch reactors, with throughputs far below the demands from industrial applications. For example, it takes almost 3 h to just produce 0.02 g of Pd cubes in a typical vial without considering complicated post treatments,[166] whereas a typical three-way catalytic converter for a compact passenger vehicle requires 1−2 g of the Pd catalyst.[15] Therefore, it is of great importance to bridge the gap between lab-scale production and commercial demand by scaling up the synthesis. To this end, it seems to be straightforward to simply conduct the synthesis in an enlarged reactor by slightly modifying the experimental protocol. Unfortunately, the product quality would be significantly marred by the thermal and compositional inhomogeneity arising from a large reaction volume.[599] The uncertainty about the product quality may also result in the production of a large amount of waste, which is economically and environmentally unfavorable.

Instead of increasing the volume of the reaction solution and the size of the reactor, one can achieve mass production without compromising the product quality by conducting the synthesis in a continuous flow of droplet reactor.[600] With the introduction of two immiscible liquid/gas into a channel, a train of uniform droplets can be generated and used as discrete reactors for conducting a synthesis of nanocrystals (Figure 50A). The throughput can be readily increased by running the synthesis continuously because of the linear correlation between the volume of production and the duration of a synthesis. Benefiting from the fast rates of heat and mass transfer in the small droplets, the nucleation and growth of nanocrystals can be kept essentially the same as in a conventional batch reactor, ensuring a tight control over the size and shape of the products. In one demonstration, it was reported that Pd and Au nanocrystals with various sizes and shapes could be continuously produced at a throughput of 1−10 g per hour using droplet reactors of milliliter in size.[601] The fluidic system was also extended to seed-mediated growth for

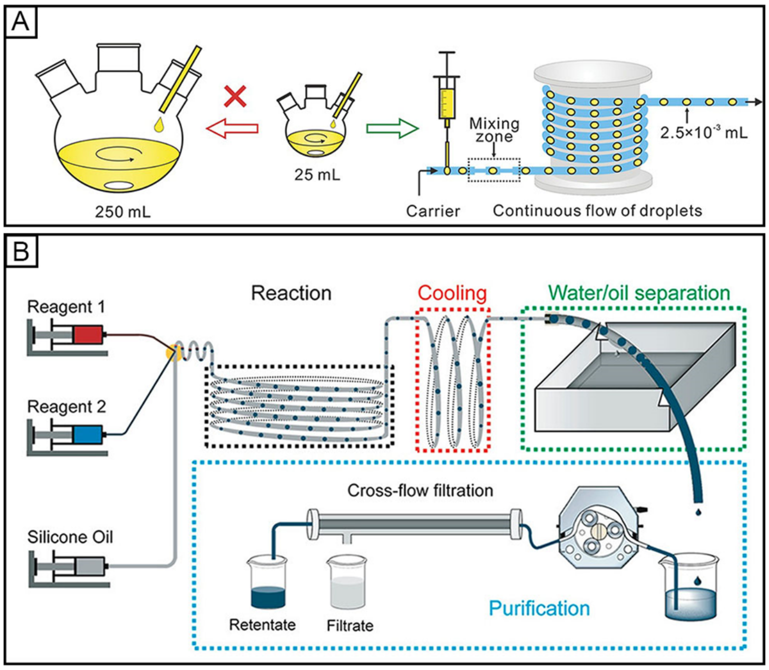

Figure 50. Schematic illustrations of (A) an approach for scaling up the synthesis of noble-metal nanocrystals by switching to a continuous flow of droplet reactor and (B) a droplet reactor system containing online separation and filtration units, which has the capability of automation for mass production of noble-metal nanocrystals. (A) Reprinted with permission from ref 599. Copyright 2014 Wiley-VCH. (B) Reprinted with permission from ref 602. Copyright 2018 American Chemical Society.

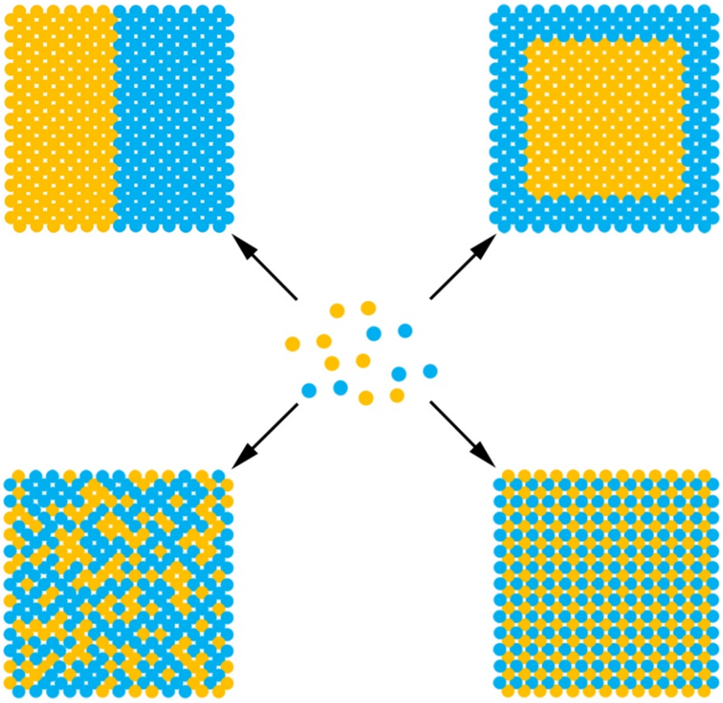

Figure 51. Diversity in the atomic arrangement of a bimetallic nanocrystal, including Janus (upper left), core−shell (upper right), alloy (lower left), and intermetallic (lower right) structures.

the production of Pd−M (M = Au, Pd, and Ag) bimetallic nanocrystals, with Pd cubes serving as the seeds.

Since the throughput of droplet reactors is still limited by post-treatment procedures such as centrifugation, a new system was developed for automated operation by introducing units for online separation and filtration (Figure 50B).[602] The new system was able to automatically separate the aqueous phase containing the products from the silicon oil that served as a spacer between the droplets, as well as purify and concentrate the products. This new system holds great promise for the continuous, automated, and scalable production of colloidal nanocrystals with well-controlled sizes and shapes. In addition to a droplet-based system, the synthesis can also be directly conducted in a continuous flow without losing quality control, at least, for several metals and some shapes.[603−606] By running multiple devices in parallel, it is feasible to produce the nanocrystals on a hundred-gram scale per day. With an ability to mass-produce the noble-metal nanocrystals without compromising the quality, this new platform holds great promise for moving them from academic studies to industrial applications.

8.5. Extension to Bi- and Multi-Metallic Systems

Incorporation of a second metal or even more metals into the shape-controlled nanocrystals can greatly expand their diversity in terms of surface composition (Figure 51). In addition, the spatial ordering and atomic distribution can also be leveraged as additional handles to significantly enhance their performance in a catalytic reaction.[37] Taking bimetallic nanocrystals as an example, the inclusion of a second metal can result in, at least, ensemble, ligand, and/or geometric effects. For the ensemble effect, the functionality of an alloy ensemble will change as a function of the surface composition.[607,608] In other words, a certain number and type of atoms can be combined to suit a specific chemical reaction. The ligand effect refers to the change in electronic structure and catalytic activity of the atoms because of the charge transfer between two different types of atoms.[609,610] The charge redistribution can lead to a shift in the *d*-band center, affecting the adsorption energies of the reactants, intermediates, and products. Geometric effect is defined as the spatial arrangement of surface atoms that is affected by the size, shape, and strain of a bimetallic nanocrystal.[611] In the context of catalysis, these three effects could work independently or synergistically to augment the catalytic performance of a heterogeneous catalyst.

There are a number of reports on the synthesis of bi- or multimetallic, alloyed nanocrystals with well-defined and controllable surface structures.[36−38,128,413,612]Such nanocrystals have also been exploited to study the three effects mentioned above. However, the interactions between different types of metal atoms are inherently complicated and are yet to be fully understood. Despite the numerous reports on the successful synthesis in terms of shape control for bi- and multimetallic nanocrystals, some of the fundamental mechanisms that dictate the shape evolution remain elusive. It has also been a challenging task to even resolve the exact atomic composition and spatial distribution of atoms on the surface of a bimetallic nanocrystal, not mentioning the highly dynamic nature of such a surface.[37,38,128,413] Further developments in electron microscopy and surface spectroscopy are needed for the resolution of these fundamental issues.[48] Of course, computational simulations are also expected to make a major contribution to such an endeavor.[613,614]

AUTHOR INFORMATION

Corresponding Author

Younan Xia − *The Wallace H. Coulter Department of Biomedical Engineering, Georgia Institute of Technology and Emory University, Atlanta, Georgia 30332, United States; School of Chemistry and Biochemistry and School of Chemical and Biomolecular Engineering, Georgia Institute of Technology, Atlanta, Georgia 30332, United States;* orcid.org/0000-0003-2431-7048; Email: younan.xia@bme.gatech.edu

Authors

Yifeng Shi − *School of Chemical and Biomolecular Engineering, Georgia Institute of Technology, Atlanta, Georgia 30332, United States*

Zhiheng Lyu − *School of Chemistry and Biochemistry, Georgia Institute of Technology, Atlanta, Georgia 30332, United States;* orcid.org/0000-0002-1343-4057

Ming Zhao − *School of Chemistry and Biochemistry, Georgia Institute of Technology, Atlanta, Georgia 30332, United States;* orcid.org/0000-0003-0127-1470

Ruhui Chen − *School of Chemistry and Biochemistry, Georgia Institute of Technology, Atlanta, Georgia 30332, United States*

Quynh N. Nguyen − *Department of Chemistry, Agnes Scott College, Decatur, Georgia 30030, United States*

Complete contact information is available at:
https://pubs.acs.org/10.1021/acs.chemrev.0c00454

Author Contributions

Y.S., Z.L., M.Z., and R.C. contributed equally to the preparation of this review article. Y.S., Z.L., M.Z., and R.C. wrote this Review. Y.X. helped define the scope and structure of this review article while both Q.N.N. and Y.X. were involved in editing the manuscript.

Notes

The authors declare no competing financial interest.

Biographies

Yifeng Shi received her B.S. in Chemical Engineering in 2017 from Sichuan University, China. She is pursuing her Ph.D. in Chemical and Biomolecular Engineering at the Georgia Institute of Technology under the supervision of Prof. Xia. Her research interest includes shape-controlled synthesis of metal nanocrystals for heterogeneous catalysis and related applications.

Zhiheng Lyu received her B.S. in Chemistry from the University of Science and Technology of China in 2016, where she worked on noble-metal nanocrystals for photocatalysis. She is pursuing her Ph.D. degree in Chemistry and Biochemistry at the Georgia Institute of Technology under the supervision of Prof. Xia. Her research interest includes shape-controlled synthesis of metal nanocrystals and their utilization for energy-related applications.

Ming Zhao received his B.S. in Materials Science and Engineering and M.S. in Materials Physics and Chemistry in 2012 and 2015, respectively, both from Nanjing University, China. His M.S. thesis work was focused on the durability test of proton-exchange membrane fuel cells. From 2015 to 2019, he was working on the synthesis of nanomaterials for energy-related applications as a Ph.D. student in the Xia group at the Georgia Institute of Technology. Since 2019, he has been exploring the single-molecule catalysis as a postdoctoral fellow at Cornell University.

Ruhui Chen received her B.E. in Macromolecular Materials and Engineering from University of Science and Technology of China in 2017, where she studied metal−organic framework nanostructures as a theranostic agent for cancer therapy. She is pursuing her Ph.D. in Chemistry and Biochemistry at the Georgia Institute of Technology under the supervision of Prof. Xia. Her research focuses on the development of new methods for controlling the synthesis of nanostructured materials.

Quynh N. Nguyen received her B.S. in Chemistry from Agnes Scott College in 2020. As a Research Experiences for Undergraduates (REU) awardee, she worked in the Xia group and conducted research related to the growth mechanism of anisotropic nanostructures. She is pursuing her Ph.D. degree in Chemistry and Biochemistry at the Georgia Institute of Technology under the supervision of Prof. Xia starting in the fall of 2020. Her research interest includes the shape-controlled synthesis of metal nanocrystals for catalysis and energy-related applications.

Younan Xia received his Ph.D. in Physical Chemistry from Harvard University in 1996 (with Whitesides). He started as an Assistant Professor of Chemistry at the University of Washington, Seattle in 1997 and then joined the Department of Biomedical Engineering at Washington University in St. Louis in 2007 as the James M. McKelvey Professor. Since 2012, he has held the position of Brock Family Chair and GRA Eminent Scholar in Nanomedicine at the Georgia Institute of Technology. He served as an Associate Editor of Nano Letters from 2002–2019.

ACKNOWLEDGMENTS

This work was supported in part by the NSF (DMR-1215034, DMR-1505400, CHE-1505441, and CHE-1804970) and startup funds from the Georgia Institute of Technology.

ABBREVIATIONS

1-D = one-dimensional
2-D = two-dimensional
3-D = three-dimensional
AA = ascorbic acid
ac = acetate
acac = acetylacetonate
ADT = accelerated durability test
AOR = alcohol oxidation reaction
$Cu(AOT)_2$ = copper(II) bis(2-ethylhexyl) sulfosuccinate
Asc-2P = 2-phospho-L-ascorbic acid trisodium salt
BSPP = phenylphosphine dihydrate dipotassium salt
CA = citric acid
CN = coordination number
CO_2RR = carbon dioxide reduction reaction
CPC = cetylpyridinium chloride
CTAB = cetyltrimethylammonium bromide
CTAC = cetyltrimethylammonium chloride
CTBAB = cetyltributylammonium bromide
CTEAB = cetyltriethylammonium bromide
CV = cyclic voltammetry
DAFC = direct alcohol fuel cell
DDA = dodecylamine
DDAB = didodecyldimethylammonium bromide
DEG = diethylene glycol
DFAFC = direct formic acid fuel cell
DFT = density functional theory
DMF = dimethylformamide
DMSO = dimethyl sulfoxide
DPE = diphenyl ether
ECSA = electrochemically active surface area
EDA = ethylenediamine
EDTA = ethylenediaminetetraacetic acid
EDX = energy-dispersive X-ray
EG = ethylene glycol
EGOR = ethylene glycol oxidation reaction
EO = ethylene oxide
EOR = ethanol oxidation reaction
FAO = formic acid oxidation
fcc = face-centered cubic
FE = faradaic efficiency
FT = Fischer–Tropsch
FTIR = Fourier-transform infrared spectroscopy
HAADF = high-angle annular dark-field
hcp = hexagonal close-packed
HDA = hexadecylamine
HER = hydrogen evolution reaction
HOH = hexoctahedron
HOR = hydrogen oxidation reaction
H_{UPD} = underpotentially deposited hydrogen
ICP-MS = inductively-coupled plasma mass spectrometry
IR = infrared
MBA = 2-methylbutan-2-ol
MBE = 2-methyl-3-buten-2-ol
MBY = 2-methyl-3-butyn-2-ol
MD = molecular dynamics
MGS = Magnus' green salt
MSMGS = methylamine substituted Magnus' green salt
NHE = normal hydrogen electrode
NMR = nuclear magnetic resonance
NRR = nitrogen reduction reaction
NVP = *N*-vinylpyrrolidone
OA = oleic acid
OAm = oleylamine
ODA = octadecylamine
ODCB = *o*-dichlorobenzene
OER = oxygen evolution reaction
ORR = oxygen reduction reaction
PAA = poly(acrylic acid)
PAM = polyacrylamide
PDDA = poly(diallyldimethylammonium) chloride
PEG = poly(ethylene glycol)
PEMFC = proton-exchange membrane fuel cell
PGM = platinum group metal
PVA = poly(vinyl alcohol)
PVP = poly(vinylpyrrolidone)
RBP = right bipyramid
RDD = rhombic dodecahedron
RHE = reversible hydrogen electrode
SAED = selected area electron diffraction
SCE = saturated calomel electrode
SDSN = sodium dodecylsulfonate
SEM = scanning electron microscopy
SERS = surface-enhanced Raman scattering
SHE = standard hydrogen electrode
STEM = scanning transmission electron microscopy
T_{50} = temperature for 50% conversion
TBA = *tert*-butylamine
TBA2CB = tetrabutylammonium dichlorobromide
TEG = triethylene glycol
TEM = transmission electron microscopy
THH = tetrahexahedron
TOF = turnover frequency
TOH = trisoctahedron
TOP = trioctylphosphine
TOPO = trioctylphosphine oxide
TPH = trapezohedron
TTAB = tetradecyltrimethylammonium bromide
TTEG = tetraethylene glycol
UPD = underpotential deposition
UPS = ultraviolet photoemission spectroscopy
UVO = UV-ozone
UV–vis = ultraviolet–visible
XAFS = X-ray absorption fine structure

XAS = X-ray absorption spectroscopy
XPS = X-ray photoelectron spectroscopy
XRD = X-ray diffraction

REFERENCES

(1) Thomas, J. M.; Thomas, W. J. *Principles and Practice of Heterogeneous Catalysis*; Wiley-VCH: Weinheim, Germany, 2015.

(2) Liu, L.; Corma, A. Metal Catalysts for Heterogeneous Catalysis: From Single Atoms to Nanoclusters and Nanoparticles. *Chem. Rev.* **2018**, *118*, 4981−5079.

(3) Herman, R.; Klier, K.; Simmons, G.; Finn, B.; Bulko, J. B.; Kobylinski, T. Catalytic Synthesis of Methanol from COH_2: I. Phase Composition, Electronic Properties, and Activities of the Cu/ZnO/M_2O_3 Catalysts. *J. Catal.* **1979**, *56*, 407−429.

(4) Grabow, L. C.; Mavrikakis, M. Mechanism of Methanol Synthesis on Cu through CO_2 and CO Hydrogenation. *ACS Catal.* **2011**, *1*, 365−384.

(5) Behrens, M.; Studt, F.; Kasatkin, I.; Kuhl, S.; Havecker, M.; Abild-Pedersen, F.; Zander, S.; Girgsdies, F.; Kurr, P.; Kniep, B. L.; et al. The Active Site of Methanol Synthesis over Cu/ZnO/Al_2O_3 Industrial Catalysts. *Science* **2012**, *336*, 893−897.

(6) Jacobsen, C. J. H.; Dahl, S.; Hansen, P. L.; Törnqvist, E.; Jensen, L.; Topsøe, H.; Prip, D. V.; Møenshaug, P. B.; Chorkendorff, I. Structure Sensitivity of Supported Ruthenium Catalysts for Ammonia Synthesis. *J. Mol. Catal. A: Chem.* **2000**, *163*, 19−26.

(7) Miyazaki, A.; Balint, I.; Aika, K.-i.; Nakano, Y. Preparation of Ru Nanoparticles Supported on γ-Al_2O_3 and Its Novel Catalytic Activity for Ammonia Synthesis. *J. Catal.* **2001**, *204*, 364−371.

(8) Honkala, K.; Hellman, A.; Remediakis, I. N.; Logadottir, A.; Carlsson, A.; Dahl, S.; Christensen, C. H.; Norskov, J. K. Ammonia Synthesis from First-Principles Calculations. *Science* **2005**, *307*, 555−558.

(9) Johansson Seechurn, C. C. C.; Kitching, M. O.; Colacot, T. J.; Snieckus, V. Palladium-Catalyzed Cross-Coupling: A Historical Contextual Perspective to the 2010 Nobel Prize. *Angew. Chem., Int. Ed.* **2012**, *51*, 5062−5085.

(10) Mandal, S.; Roy, D.; Chaudhari, R. V.; Sastry, M. Pt and Pd Nanoparticles Immobilized on Amine-Functionalized Zeolite: Excellent Catalysts for Hydrogenation and Heck Reactions. *Chem. Mater.* **2004**, *16*, 3714−3724.

(11) Campbell, C. T.; Paffett, M. T. Model Studies of Ethylene Epoxidation Catalyzed by the Ag(110) Surface. *Surf. Sci.* **1984**, *139*, 396−416.

(12) Pu, T.; Tian, H.; Ford, M. E.; Rangarajan, S.; Wachs, I. E. Overview of Selective Oxidation of Ethylene to Ethylene Oxide by Ag Catalysts. *ACS Catal.* **2019**, *9*, 10727−10750.

(13) Lin, S. D.; Vannice, M. A. Hydrogenation of Aromatic Hydrocarbons over Supported Pt Catalysts.I. Benzene Hydrogenation. *J. Catal.* **1993**, *143*, 539−553.

(14) Bariås, O. A.; Holmen, A.; Blekkan, E. A. Propane Dehydrogenation over Supported Pt and Pt−Sn Catalysts: Catalyst Preparation, Characterization, and Activity Measurements. *J. Catal.* **1996**, *158*, 1−12.

(15) Tollefson, J. Worth Its Weight in Platinum. *Nature* **2007**, *450*, 334−335.

(16) Zhao, Z.; Chen, C.; Liu, Z.; Huang, J.; Wu, M.; Liu, H.; Li, Y.; Huang, Y. Pt-Based Nanocrystal for Electrocatalytic Oxygen Reduction. *Adv. Mater.* **2019**, *31*, 1808115.

(17) Nitopi, S.; Bertheussen, E.; Scott, S. B.; Liu, X.; Engstfeld, A. K.; Horch, S.; Seger, B.; Stephens, I. E. L.; Chan, K.; Hahn, C.; et al. Progress and Perspectives of Electrochemical CO_2 Reduction on Copper in Aqueous Electrolyte. *Chem. Rev.* **2019**, *119*, 7610−7672.

(18) Munnik, P.; de Jongh, P. E.; de Jong, K. P. Recent Developments in the Synthesis of Supported Catalysts. *Chem. Rev.* **2015**, *115*, 6687−6718.

(19) Somorjai, G. A.; Park, J. Y. Molecular Factors of Catalytic Selectivity. *Angew. Chem., Int. Ed.* **2008**, *47*, 9212−9228.

(20) Pozio, A.; De Francesco, M.; Cemmi, A.; Cardellini, F.; Giorgi, L. Comparison of High Surface Pt/C Catalysts by Cyclic Voltammetry. *J. Power Sources* **2002**, *105*, 13−19.

(21) Gontard, L. C.; Chang, L. Y.; Hetherington, C. J.; Kirkland, A. I.; Ozkaya, D.; Dunin-Borkowski, R. E. Aberration-Corrected Imaging of Active Sites on Industrial Catalyst Nanoparticles. *Angew. Chem., Int. Ed.* **2007**, *46*, 3683−3685.

(22) Parthasarathy, P.; Virkar, A. V. Electrochemical Ostwald Ripening of Pt and Ag Catalysts Supported on Carbon. *J. Power Sources* **2013**, *234*, 82−90.

(23) Dai, Y.; Lu, P.; Cao, Z.; Campbell, C. T.; Xia, Y. The Physical Chemistry and Materials Science behind Sinter-Resistant Catalysts. *Chem. Soc. Rev.* **2018**, *47*, 4314−4331.

(24) Spencer, N. D.; Schoonmaker, R. C.; Somorjai, G. A. Structure Sensitivity in the Iron Single-Crystal Catalysed Synthesis of Ammonia. *Nature* **1981**, *294*, 643−644.

(25) McCabe, R. W.; Schmidt, L. D. Binding States of CO on Single Crystal Planes of Pt. *Surf. Sci.* **1977**, *66*, 101−124.

(26) Furuya, N.; Koide, S. Hydrogen Adsorption on Platinum Single-Crystal Surfaces. *Surf. Sci.* **1989**, *220*, 18−28.

(27) Marković, N. M.; Adžić, R. R.; Cahan, B. D.; Yeager, E. B. Structural Effects in Electrocatalysis: Oxygen Reduction on Platinum Low Index Single-Crystal Surfaces in Perchloric Acid Solutions. *J. Electroanal. Chem.* **1994**, *377*, 249−259.

(28) Xia, Y.; Xiong, Y.; Lim, B.; Skrabalak, S. E. Shape-Controlled Synthesis of Metal Nanocrystals: Simple Chemistry Meets Complex Physics? *Angew. Chem., Int. Ed.* **2009**, *48*, 60−103.

(29) An, K.; Somorjai, G. A. Size and Shape Control of Metal Nanoparticles for Reaction Selectivity in Catalysis. *ChemCatChem* **2012**, *4*, 1512−1524.

(30) Cao, Y. C.; Jin, R.; Mirkin, C. A. Nanoparticles with Raman Spectroscopic Fingerprints for DNA and RNA Detection. *Science* **2002**, *297*, 1536−1540.

(31) Sun, Y.; Xia, Y. Shape-Controlled Synthesis of Gold and Silver Nanoparticles. *Science* **2002**, *298*, 2176−2179.

(32) Kim, F.; Connor, S.; Song, H.; Kuykendall, T.; Yang, P. Platonic Gold Nanocrystals. *Angew. Chem., Int. Ed.* **2004**, *43*, 3673−3677.

(33) Liz-Marzán, L. M. Nanometals: Formation and Color. *Mater. Today* **2004**, *7*, 26−31.

(34) Qian, J.; Shen, M.; Zhou, S.; Lee, C.-T.; Zhao, M.; Lyu, Z.; Hood, Z. D.; Vara, M.; Gilroy, K. D.; Wang, K.; et al. Synthesis of Pt Nanocrystals with Different Shapes Using the Same Protocol to Optimize Their Catalytic Activity toward Oxygen Reduction. *Mater. Today* **2018**, *21*, 834−844.

(35) Kang, Y.; Pyo, J. B.; Ye, X.; Diaz, R. E.; Gordon, T. R.; Stach, E. A.; Murray, C. B. Shape-Controlled Synthesis of Pt Nanocrystals: The Role of Metal Carbonyls. *ACS Nano* **2013**, *7*, 645−653.

(36) Liu, X.; Wang, D.; Li, Y. Synthesis and Catalytic Properties of Bimetallic Nanomaterials with Various Architectures. *Nano Today* **2012**, *7*, 448−466.

(37) Gilroy, K. D.; Ruditskiy, A.; Peng, H. C.; Qin, D.; Xia, Y. Bimetallic Nanocrystals: Syntheses, Properties, and Applications. *Chem. Rev.* **2016**, *116*, 10414−10472.

(38) Gilroy, K. D.; Yang, X.; Xie, S.; Zhao, M.; Qin, D.; Xia, Y. Shape-Controlled Synthesis of Colloidal Metal Nanocrystals by Replicating the Surface Atomic Structure on the Seed. *Adv. Mater.* **2018**, *30*, 1706312.

(39) Quan, Z.; Wang, Y.; Fang, J. High-Index Faceted Noble Metal Nanocrystals. *Acc. Chem. Res.* **2013**, *46*, 191−202.

(40) Xia, Y.; Yang, X. Toward Cost-Effective and Sustainable Use of Precious Metals in Heterogeneous Catalysts. *Acc. Chem. Res.* **2017**, *50*, 450−454.

(41) Chen, Y.; Fan, Z.; Zhang, Z.; Niu, W.; Li, C.; Yang, N.; Chen, B.; Zhang, H. Two-Dimensional Metal Nanomaterials: Synthesis, Properties, and Applications. *Chem. Rev.* **2018**, *118*, 6409−6455.

(42) Huo, D.; Kim, M. J.; Lyu, Z.; Shi, Y.; Wiley, B. J.; Xia, Y. One-Dimensional Metal Nanostructures: From Colloidal Syntheses to Applications. *Chem. Rev.* **2019**, *119*, 8972−9073.

(43) Xie, S.; Choi, S.-I.; Xia, X.; Xia, Y. Catalysis on Faceted Noble-Metal Nanocrystals: Both Shape and Size Matter. *Curr. Opin. Chem. Eng.* **2013**, *2*, 142−150.

(44) Ruditskiy, A.; Choi, S.-I.; Peng, H.-C.; Xia, Y. Shape-Controlled Metal Nanocrystals for Catalytic Applications. *MRS Bull.* **2014**, *39*, 727−737.

(45) Ruditskiy, A.; Peng, H. C.; Xia, Y. Shape-Controlled Metal Nanocrystals for Heterogeneous Catalysis. *Annu. Rev. Chem. Biomol. Eng.* **2016**, *7*, 327−348.

(46) Cao, S.; Tao, F.; Tang, Y.; Li, Y.; Yu, J. Size- and Shape-Dependent Catalytic Performances of Oxidation and Reduction Reactions on Nanocatalysts. *Chem. Soc. Rev.* **2016**, *45*, 4747−4765.

(47) Zhang, L.; Chen, D.; Jiang, Z.; Zhang, J.; Xie, S.; Kuang, Q.; Xie, Z.; Zheng, L. Facile Syntheses and Enhanced Electrocatalytic Activities of Pt Nanocrystals with *{hkk}* High-Index Surfaces. *Nano Res.* **2012**, *5*, 181−189.

(48) Ding, K.; Cullen, D. A.; Zhang, L.; Cao, Z.; Roy, A. D.; Ivanov, I. N.; Cao, D. A General Synthesis Approach for Supported Bimetallic Nanoparticles via Surface Inorganometallic Chemistry. *Science* **2018**, *362*, 560−564.

(49) Shi, S.; Qin, D. Bifunctional Metal Nanocrystals for Catalyzing and Reporting on Chemical Reactions. *Angew. Chem., Int. Ed.* **2020**, *59*, 3782−3792.

(50) Che, M. Nobel Prize in Chemistry 1912 to Sabatier: Organic Chemistry or Catalysis? *Catal. Today* **2013**, *218*, 162−171.

(51) Medford, A. J.; Vojvodic, A.; Hummelshøj, J. S.; Voss, J.; Abild-Pedersen, F.; Studt, F.; Bligaard, T.; Nilsson, A.; Nørskov, J. K. From the Sabatier Principle to a Predictive Theory of Transition-Metal Heterogeneous Catalysis. *J. Catal.* **2015**, *328*, 36−42.

(52) Ruban, A.; Hammer, B.; Stoltze, P.; Skriver, H. L.; Nørskov, J. K. Surface Electronic Structure and Reactivity of Transition and Noble Metals. *J. Mol. Catal. A: Chem.* **1997**, *115*, 421−429.

(53) Mavrikakis, M.; Hammer, B.; Nørskov, J. K. Effect of Strain on the Reactivity of Metal Surfaces. *Phys. Rev. Lett.* **1998**, *81*, 2819−2822.

(54) Nilsson, A.; Pettersson, L. G. M.; Hammer, B.; Bligaard, T.; Christensen, C. H.; Nørskov, J. K. The Electronic Structure Effect in Heterogeneous Catalysis. *Catal. Lett.* **2005**, *100*, 111−114.

(55) Kibler, L. A.; El-Aziz, A. M.; Hoyer, R.; Kolb, D. M. Tuning Reaction Rates by Lateral Strain in a Palladium Monolayer. *Angew. Chem., Int. Ed.* **2005**, *44*, 2080−2084.

(56) Xia, Z.; Guo, S. Strain Engineering of Metal-Based Nanomaterials for Energy Electrocatalysis. *Chem. Soc. Rev.* **2019**, *48*, 3265−3278.

(57) Rootsaert, W. J. M.; Sachtler, W. M. H. Interaction of Formic Acid Vapour with Tungsten. *Z. Phys. Chem.* **1960**, *26*, 16−26.

(58) Liu, P.; Qin, R.; Fu, G.; Zheng, N. Surface Coordination Chemistry of Metal Nanomaterials. *J. Am. Chem. Soc.* **2017**, *139*, 2122−2131.

(59) Zhang, H.; Jin, M.; Xia, Y. Noble-metal Nanocrystals with Concave Surfaces: Synthesis and Applications. *Angew. Chem., Int. Ed.* **2012**, *51*, 7656−7673.

(60) Wang, H.; Zhou, S.; Gilroy, K. D.; Cai, Z.; Xia, Y. Icosahedral Nanocrystals of Noble Metals: Synthesis and Applications. *Nano Today* **2017**, *15*, 121−144.

(61) Zhou, S.; Zhao, M.; Yang, T.-H.; Xia, Y. Decahedral Nanocrystals of Noble Metals: Synthesis, Characterization, and Applications. *Mater. Today* **2019**, *22*, 108−131.

(62) Yu, T.; Kim, D. Y.; Zhang, H.; Xia, Y. Platinum Concave Nanocubes with High-Index Facets and Their Enhanced Activity for Oxygen Reduction Reaction. *Angew. Chem., Int. Ed.* **2011**, *50*, 2773−2777.

(63) Huang, L.; Liu, M.; Lin, H.; Xu, Y.; Wu, J.; Dravid, V. P.; Wolverton, C.; Mirkin, C. A. Shape Regulation of High-Index Facet Nanoparticles by Dealloying. *Science* **2019**, *365*, 1159−1163.

(64) Huang, X.; Zhao, Z.; Fan, J.; Tan, Y.; Zheng, N. Amine-Assisted Synthesis of Concave Polyhedral Platinum Nanocrystals Having {411} High-Index Facets. *J. Am. Chem. Soc.* **2011**, *133*, 4718−4721.

(65) Collins, G.; Schmidt, M.; O'Dwyer, C.; McGlacken, G.; Holmes, J. D. Enhanced Catalytic Activity of High-Index Faceted Palladium Nanoparticles in Suzuki−Miyaura Coupling Due to Efficient Leaching Mechanism. *ACS Catal.* **2014**, *4*, 3105−3111.

(66) Calle-Vallejo, F.; Tymoczko, J.; Colic, V.; Vu, Q. H.; Pohl, M. D.; Morgenstern, K.; Loffreda, D.; Sautet, P.; Schuhmann, W.; Bandarenka, A. S. Finding Optimal Surface Sites on Heterogeneous Catalysts by Counting Nearest Neighbors. *Science* **2015**, *350*, 185−189.

(67) Calle-Vallejo, F.; Pohl, M. D.; Reinisch, D.; Loffreda, D.; Sautet, P.; Bandarenka, A. S. Why Conclusions from Platinum Model Surfaces Do Not Necessarily Lead to Enhanced Nanoparticle Catalysts for the Oxygen Reduction Reaction. *Chem. Sci.* **2017**, *8*, 2283−2289.

(68) Kumar, D.; Idapalapati, S.; Wang, W.; Narasimalu, S. Effect of Surface Mechanical Treatments on the Microstructure-Property-Performance of Engineering Alloys. *Materials* **2019**, *12*, 2503.

(69) Wang, Y.; Peng, H. C.; Liu, J.; Huang, C. Z.; Xia, Y. Use of Reduction Rate as a Quantitative Knob for Controlling the Twin Structure and Shape of Palladium Nanocrystals. *Nano Lett.* **2015**, *15*, 1445−1450.

(70) Gilroy, K. D.; Peng, H. C.; Yang, X.; Ruditskiy, A.; Xia, Y. Symmetry Breaking During Nanocrystal Growth. *Chem. Commun.* **2017**, *53*, 4530−4541.

(71) Xia, X.; Choi, S.-I.; Herron, J. A.; Lu, N.; Scaranto, J.; Peng, H.-C.; Wang, J.; Mavrikakis, M.; Kim, M. J.; Xia, Y. Facile Synthesis of Palladium Right Bipyramids and Their Use as Seeds for Overgrowth and as Catalysts for Formic Acid Oxidation. *J. Am. Chem. Soc.* **2013**, *135*, 15706−15709.

(72) Wu, J.; Li, P.; Pan, Y.-T.; Warren, S.; Yin, X.; Yang, H. Surface Lattice-Engineered Bimetallic Nanoparticles and Their Catalytic Properties. *Chem. Soc. Rev.* **2012**, *41*, 8066−8074.

(73) Luo, M.; Guo, S. Strain-Controlled Electrocatalysis on Multimetallic Nanomaterials. *Nat. Rev. Mater.* **2017**, *2*, 17059.

(74) Huang, H.; Jia, H.; Liu, Z.; Gao, P.; Zhao, J.; Luo, Z.; Yang, J.; Zeng, J. Understanding of Strain Effects in the Electrochemical Reduction of CO_2: Using Pd Nanostructures as an Ideal Platform. *Angew. Chem., Int. Ed.* **2017**, *56*, 3594−3598.

(75) Barnard, A. S.; Young, N. P.; Kirkland, A. I.; van Huis, M. A.; Xu, H. Nanogold: A Quantitative Phase Map. *ACS Nano* **2009**, *3*, 1431−1436.

(76) Palomares-Báez, J. P.; Montejano-Carrizales, J. M.; Guisbiers, G.; José-Yacamán, M.; Rodríguez-López, J. L. The Decmon: A New Nanoparticle Shape Along the Truncation Path from the Icosahedron to the Decahedron. *Nanotechnology* **2019**, *30*, 425701.

(77) Wang, L.; Zeng, Z.; Gao, W.; Maxson, T.; Raciti, D.; Giroux, M.; Pan, X.; Wang, C.; Greeley, J. Tunable Intrinsic Strain in Two-Dimensional Transition Metal Electrocatalysts. *Science* **2019**, *363*, 870−874.

(78) Valden, M.; Lai, X.; Goodman, D. W. Onset of Catalytic Activity of Gold Clusters on Titania with the Appearance of Nonmetallic Properties. *Science* **1998**, *281*, 1647−1650.

(79) Wu, J. C.; Harriott, P. The Effect of Crystallite Size on the Activity and Selectivity of Silver Catalysts. *J. Catal.* **1975**, *39*, 395−402.

(80) Overbury, S. H.; Schwartz, V.; Mullins, D. R.; Yan, W.; Dai, S. Evaluation of the Au Size Effect: CO Oxidation Catalyzed by Au/TiO_2. *J. Catal.* **2006**, *241*, 56−65.

(81) Christopher, P.; Linic, S. Shape- and Size-Specific Chemistry of Ag Nanostructures in Catalytic Ethylene Epoxidation. *ChemCatChem* **2010**, *2*, 78−83.

(82) Chen, S.; Luo, L.; Jiang, Z.; Huang, W. Size-Dependent Reaction Pathways of Low-Temperature CO Oxidation on Au/CeO_2 Catalysts. *ACS Catal.* **2015**, *5*, 1653−1662.

(83) Campbell, C. T. The Energetics of Supported Metal Nanoparticles: Relationships to Sintering Rates and Catalytic Activity. *Acc. Chem. Res.* **2013**, *46*, 1712−1719.

(84) Cleveland, C. L.; Landman, U.; Schaaff, T. G.; Shafigullin, M. N.; Stephens, P. W.; Whetten, R. L. Structural Evolution of Smaller Gold Nanocrystals: The Truncated Decahedral Motif. *Phys. Rev. Lett.* **1997**, *79*, 1873−1876.

(85) Bokhimi, X.; Zanella, R.; Morales, A. Au/Rutile Catalysts: Effect of Support Dimensions on the Gold Crystallite Size and the Catalytic Activity for CO Oxidation. *J. Phys. Chem. C* **2007**, *111*, 15210−15216.

(86) Rahm, J. M.; Erhart, P. Beyond Magic Numbers: Atomic Scale Equilibrium Nanoparticle Shapes for Any Size. *Nano Lett.* **2017**, *17*, 5775−5781.

(87) Williams, D. B.; Carter, C. B. *Transmission Electron Microscopy: A Textbook for Materials Science*; Springer US: New York, 2009.

(88) Bradshaw, A. M.; Hoffmann, F. M. The Chemisorption of Carbon Monoxide on Palladium Single Crystal Surfaces: IR Spectroscopic Evidence for Localised Site Adsorption. *Surf. Sci.* **1978**, *72*, 513−535.

(89) Szanyi, J.; Kuhn, W. K.; Goodman, D. W. CO Adsorption on Pd(111) and Pd(100): Low and High Pressure Correlations. *J. Vac. Sci. Technol., A* **1993**, *11*, 1969−1974.

(90) Lamberti, C.; Zecchina, A.; Groppo, E.; Bordiga, S. Probing the Surfaces of Heterogeneous Catalysts by *in situ* IR Spectroscopy. *Chem. Soc. Rev.* **2010**, *39*, 4951−5001.

(91) Wu, M.; Vartanian, A. M.; Chong, G.; Pandiakumar, A. K.; Hamers, R. J.; Hernandez, R.; Murphy, C. J. Solution NMR Analysis of Ligand Environment in Quaternary Ammonium-Terminated Self-Assembled Monolayers on Gold Nanoparticles: The Effect of Surface Curvature and Ligand Structure. *J. Am. Chem. Soc.* **2019**, *141*, 4316−4327.

(92) De, M.; You, C.-C.; Srivastava, S.; Rotello, V. M. Biomimetic Interactions of Proteins with Functionalized Nanoparticles: A Thermodynamic Study. *J. Am. Chem. Soc.* **2007**, *129*, 10747−10753.

(93) Wulff, G. Zur Frage der Geschwindigkeit des Wachstums und der Auflosung der Kristall Achen. *Z. Kristallogr. - Cryst. Mater.* **1901**, *34*, 449−530.

(94) Barmparis, G. D.; Lodziana, Z.; Lopez, N.; Remediakis, I. N. Nanoparticle Shapes by Using Wulff Constructions and First-Principles Calculations. *Beilstein J. Nanotechnol.* **2015**, *6*, 361−368.

(95) Zhao, M.; Chen, Z.; Lyu, Z.; Hood, Z. D.; Xie, M.; Vara, M.; Chi, M.; Xia, Y. Ru Octahedral Nanocrystals with a Face-Centered Cubic Structure, {111} Facets, Thermal Stability up to 400 °C, and Enhanced Catalytic Activity. *J. Am. Chem. Soc.* **2019**, *141*, 7028−7036.

(96) Wang, L.; Wang, L.; Meng, X.; Xiao, F. S. New Strategies for the Preparation of Sinter-Resistant Metal-Nanoparticle-Based Catalysts. *Adv. Mater.* **2019**, *31*, 1901905.

(97) Hansen, T. W.; DeLaRiva, A. T.; Challa, S. R.; Datye, A. K. Sintering of Catalytic Nanoparticles: Particle Migration or Ostwald Ripening? *Acc. Chem. Res.* **2013**, *46*, 1720−1730.

(98) Baletto, F.; Rapallo, A.; Rossi, G.; Ferrando, R. Dynamical Effects in the Formation of Magic Cluster Structures. *Phys. Rev. B: Condens. Matter Mater. Phys.* **2004**, *69*, 235421.

(99) Song, M.; Zhou, G.; Lu, N.; Lee, J.; Nakouzi, E.; Wang, H.; Li, D. Oriented attachment Induces Fivefold Twins by Forming and Decomposing High-Energy Grain Boundaries. *Science* **2020**, *367*, 40−45.

(100) Thanh, N. T.; Maclean, N.; Mahiddine, S. Mechanisms of Nucleation and Growth of Nanoparticles in Solution. *Chem. Rev.* **2014**, *114*, 7610−7630.

(101) Rodrigues, T. S.; Zhao, M.; Yang, T. H.; Gilroy, K. D.; da Silva, A. G. M.; Camargo, P. H. C.; Xia, Y. Synthesis of Colloidal Metal Nanocrystals: A Comprehensive Review on the Reductants. *Chem. - Eur. J.* **2018**, *24*, 16944−16963.

(102) Sánchez-Iglesias, A.; Pastoriza-Santos, I.; Pérez-Juste, J.; Rodríguez-González, B.; García de Abajo, F. J.; Liz-Marzán, L. M. Synthesis and Optical Properties of Gold Nanodecahedra with Size Control. *Adv. Mater.* **2006**, *18*, 2529−2534.

(103) Lu, X.; Tuan, H.-Y.; Korgel, B. A.; Xia, Y. Facile Synthesis of Gold Nanoparticles with Narrow Size Distribution by Using AuCl or AuBr as the Precursor. *Chem. - Eur. J.* **2008**, *14*, 1584−1591.

(104) Biacchi, A. J.; Schaak, R. E. The Solvent Matters: Kinetic versus Thermodynamic Shape Control in the Polyol Synthesis of Rhodium Nanoparticles. *ACS Nano* **2011**, *5*, 8089−8099.

(105) Arrhenius, S. Über die Dissociationswärme und den Einfluss der Temperatur auf den Dissociationsgrad der Elektrolyte. *Z. Phys. Chem.* **1889**, *4*, 96−116.

(106) Niu, Z.; Li, Y. Removal and Utilization of Capping Agents in Nanocatalysis. *Chem. Mater.* **2014**, *26*, 72−83.

(107) Yang, T. H.; Shi, Y.; Janssen, A.; Xia, Y. Surface Capping Agents and Their Roles in Shape-Controlled Synthesis of Colloidal Metal Nanocrystals. *Angew. Chem., Int. Ed.* **2020**, DOI: 10.1002/anie.201911135.

(108) LaMer, V. K.; Dinegar, R. H. Theory, Production and Mechanism of Formation of Monodispersed Hydrosols. *J. Am. Chem. Soc.* **1950**, *72*, 4847−4854.

(109) Vekilov, P. G. The Two-Step Mechanism of Nucleation of Crystals in Solution. *Nanoscale* **2010**, *2*, 2346−2357.

(110) Loh, N. D.; Sen, S.; Bosman, M.; Tan, S. F.; Zhong, J.; Nijhuis, C. A.; Kral, P.; Matsudaira, P.; Mirsaidov, U. Multistep Nucleation of Nanocrystals in Aqueous Solution. *Nat. Chem.* **2017**, *9*, 77−82.

(111) Yao, T.; Sun, Z.; Li, Y.; Pan, Z.; Wei, H.; Xie, Y.; Nomura, M.; Niwa, Y.; Yan, W.; Wu, Z.; et al. Insights into Initial Kinetic Nucleation of Gold Nanocrystals. *J. Am. Chem. Soc.* **2010**, *132*, 7696−7701.

(112) Woehl, T. J.; Evans, J. E.; Arslan, I.; Ristenpart, W. D.; Browning, N. D. Direct in situ Determination of the Mechanisms Controlling Nanoparticle Nucleation and Growth. *ACS Nano* **2012**, *6*, 8599−8610.

(113) Zhou, M.; Wang, H.; Vara, M.; Hood, Z. D.; Luo, M.; Yang, T. H.; Bao, S.; Chi, M.; Xiao, P.; Zhang, Y.; et al. Quantitative Analysis of the Reduction Kinetics Responsible for the One-Pot Synthesis of Pd-Pt Bimetallic Nanocrystals with Different Structures. *J. Am. Chem. Soc.* **2016**, *138*, 12263−12270.

(114) Zheng, Y.; Zeng, J.; Ruditskiy, A.; Liu, M.; Xia, Y. Oxidative Etching and Its Role in Manipulating the Nucleation and Growth of Noble-Metal Nanocrystals. *Chem. Mater.* **2014**, *26*, 22−33.

(115) Long, R.; Zhou, S.; Wiley, B. J.; Xiong, Y. Oxidative Etching for Controlled Synthesis of Metal Nanocrystals: Atomic Addition and Subtraction. *Chem. Soc. Rev.* **2014**, *43*, 6288−6310.

(116) Wiley, B. J.; Xiong, Y.; Li, Z.-Y.; Yin, Y.; Xia, Y. Right Bipyramids of Silver: A New Shape Derived from Single Twinned Seeds. *Nano Lett.* **2006**, *6*, 765−768.

(117) Yang, T. H.; Peng, H. C.; Zhou, S.; Lee, C. T.; Bao, S.; Lee, Y. H.; Wu, J. M.; Xia, Y. Toward a Quantitative Understanding of the Reduction Pathways of a Salt Precursor in the Synthesis of Metal Nanocrystals. *Nano Lett.* **2017**, *17*, 334−340.

(118) Yang, T. H.; Zhou, S.; Gilroy, K. D.; Figueroa-Cosme, L.; Lee, Y. H.; Wu, J. M.; Xia, Y. Autocatalytic Surface Reduction and Its Role in Controlling Seed-Mediated Growth of Colloidal Metal Nanocrystals. *Proc. Natl. Acad. Sci. U. S. A.* **2017**, *114*, 13619−13624.

(119) Mostafavi, M.; Marignier, J. L.; Amblard, J.; Belloni, J. Nucleation Dynamics of Silver Aggregates Simulation of Photographic Development Processes. *Int. J. Radiat. Appl. Instrum. C Radiat. Phys. Chem.* **1989**, *34*, 605−617.

(120) Watzky, M. A.; Finke, R. G. Transition Metal Nanocluster Formation Kinetic and Mechanistic Studies. A New Mechanism When Hydrogen Is the Reductant: Slow, Continuous Nucleation and Fast Autocatalytic Surface Growth. *J. Am. Chem. Soc.* **1997**, *119*, 10382−10400.

(121) Widegren, J. A.; Bennett, M. A.; Finke, R. G. Is It Homogeneous or Heterogeneous Catalysis? Identification of Bulk Ruthenium Metal as the True Catalyst in Benzene Hydrogenations Starting with the Monometallic Precursor, Ru(II)(η^6-C_6Me_6)$(OAc)_2$, Plus Kinetic Characterization of the Heterogeneous Nucleation, Then Autocatalytic Surface-Growth Mechanism of Metal Film Formation. *J. Am. Chem. Soc.* **2003**, *125*, 10301−10310.

(122) Yin, X.; Shi, M.; Wu, J.; Pan, Y.-T.; Gray, D. L.; Bertke, J. A.; Yang, H. Quantitative Analysis of Different Formation Modes of Platinum Nanocrystals Controlled by Ligand Chemistry. *Nano Lett.* **2017**, *17*, 6146−6150.

(123) Besson, C.; Finney, E. E.; Finke, R. G. Nanocluster Nucleation, Growth, and Then Agglomeration Kinetic and Mechanistic Studies: A More General, Four-Step Mechanism Involving Double Autocatalysis. *Chem. Mater.* **2005**, *17*, 4925−4938.

(124) Kent, P.; Mondloch, J. E.; Finke, R. G. Synthesis of Heterogeneous $Ir^0_{\sim 600-900}/\gamma\text{-}Al_2O_3$ in One Pot From the Precatalyst Ir(1,5-COD)Cl/γ-Al_2O_3: Discovery of Two Competing Trace "Ethyl Acetate Effects" on the Nucleation Step and Resultant Product. *ACS Catal.* **2016**, *6*, 5449−5461.

(125) Xie, M.; Zhou, S.; Zhu, J.; Lyu, Z.; Chen, R.; Xia, Y. A Quantitative Analysis of the Reduction Kinetics Involved in the Synthesis of Au@Pd Concave Nanocubes. *Chem. - Eur. J.* **2019**, *25*, 16397−16404.

(126) Zhou, S.; Yang, T.-H.; Zhao, M.; Xia, Y. Quantitative Analysis of the Reduction Kinetics of a Pt(II) Precursor in the Context of Pt Nanocrystal Synthesis. *Chin. J. Chem. Phys.* **2018**, *31*, 370.

(127) Yang, T.-H.; Zhou, S.; Zhao, M.; Xia, Y. Quantitative Analysis of the Multiple Roles Played by Halide Ions in Controlling the Growth Patterns of Palladium Nanocrystals. *ChemNanoMat* **2020**, *6*, 576−588.

(128) Xia, Y.; Gilroy, K. D.; Peng, H.-C.; Xia, X. Seed-Mediated Growth of Colloidal Metal Nanocrystals. *Angew. Chem., Int. Ed.* **2017**, *56*, 60−95.

(129) Czochralski, J. Ein neues Verfahren zur Messung der Kristallisationsgeschwindigkeit der Metalle. *Z. Phys. Chem.* **1918**, *92U*, 219−221.

(130) Scheel, H. J. Historical Aspects of Crystal Growth Technology. *J. Cryst. Growth* **2000**, *211*, 1−12.

(131) Peng, H.-C.; Park, J.; Zhang, L.; Xia, Y. Toward a Quantitative Understanding of Symmetry Reduction Involved in the Seed-Mediated Growth of Pd Nanocrystals. *J. Am. Chem. Soc.* **2015**, *137*, 6643−6652.

(132) Jin, M.; Zhang, H.; Xie, Z.; Xia, Y. Palladium Nanocrystals Enclosed by {100} and {111} Facets in Controlled Proportions and Their Catalytic Activities for Formic Acid Oxidation. *Energy Environ. Sci.* **2012**, *5*, 6352−6357.

(133) Xia, X.; Zeng, J.; Oetjen, L. K.; Li, Q.; Xia, Y. Quantitative Analysis of the Role Played by Poly(vinylpyrrolidone) in Seed-Mediated Growth of Ag Nanocrystals. *J. Am. Chem. Soc.* **2012**, *134*, 1793−1801.

(134) Xia, Y.; Xia, X.; Peng, H.-C. Shape-Controlled Synthesis of Colloidal Metal Nanocrystals: Thermodynamic versus Kinetic Products. *J. Am. Chem. Soc.* **2015**, *137*, 7947−7966.

(135) Wang, Y.; He, J.; Liu, C.; Chong, W. H.; Chen, H. Thermodynamics versus Kinetics in Nanosynthesis. *Angew. Chem., Int. Ed.* **2015**, *54*, 2022−2051.

(136) Xia, X.; Xie, S.; Liu, M.; Peng, H. C.; Lu, N.; Wang, J.; Kim, M. J.; Xia, Y. On the Role of Surface Diffusion in Determining the Shape or Morphology of Noble-Metal Nanocrystals. *Proc. Natl. Acad. Sci. U. S. A.* **2013**, *110*, 6669−6673.

(137) Oura, K.; Lifshits, V. G.; Saranin, A. A.; Zotov, A. V.; Katayama, M. *Surface Science: An Introduction*; Springer: Berlin, 2013.

(138) Shustorovich, E. *Metal-Surface Reaction Energetics: Theory and Applications to Heterogeneous Catalysis, Chemisorption, and Surface Diffusion*; Wiley: Weinheim, Germany, 1991.

(139) Xiong, Y.; Cai, H.; Wiley, B. J.; Wang, J.; Kim, M. J.; Xia, Y. Synthesis and Mechanistic Study of Palladium Nanobars and Nanorods. *J. Am. Chem. Soc.* **2007**, *129*, 3665−3675.

(140) Xie, S.; Lu, N.; Xie, Z.; Wang, J.; Kim, M. J.; Xia, Y. Synthesis of Pd-Rh Core-Frame Concave Nanocubes and Their Conversion to Rh Cubic Nanoframes by Selective Etching of the Pd Cores. *Angew. Chem., Int. Ed.* **2012**, *51*, 10266−10270.

(141) Chiu, C. Y.; Li, Y.; Ruan, L.; Ye, X.; Murray, C. B.; Huang, Y. Platinum Nanocrystals Selectively Shaped Using Facet-Specific Peptide Sequences. *Nat. Chem.* **2011**, *3*, 393−399.

(142) Koczkur, K. M.; Mourdikoudis, S.; Polavarapu, L.; Skrabalak, S. E. Polyvinylpyrrolidone (PVP) in Nanoparticle Synthesis. *Dalton Trans.* **2015**, *44*, 17883−17905.

(143) Ghosh, S.; Manna, L. The Many "Facets" of Halide Ions in the Chemistry of Colloidal Inorganic Nanocrystals. *Chem. Rev.* **2018**, *118*, 7804−7864.

(144) Gisbert-González, J. M.; Feliu, J. M.; Ferre-Vilaplana, A.; Herrero, E. Why Citrate Shapes Tetrahedral and Octahedral Colloidal Platinum Nanoparticles in Water. *J. Phys. Chem. C* **2018**, *122*, 19004−19014.

(145) Liu, J.; Wang, S.; Cai, K.; Li, Y.; Liu, Z.; Liu, L.; Han, Y.; Wang, H.; Han, H.; Chen, H. A New Type of Capping Agent in Nanoscience: Metal Cations. *Small* **2019**, *15*, 1900444.

(146) Kilin, D. S.; Prezhdo, O. V.; Xia, Y. Shape-Controlled Synthesis of Silver Nanoparticles: *Ab Initio* Study of Preferential Surface Coordination with Citric Acid. *Chem. Phys. Lett.* **2008**, *458*, 113−116.

(147) Huang, H.; Ruditskiy, A.; Choi, S. I.; Zhang, L.; Liu, J.; Ye, Z.; Xia, Y. One-Pot Synthesis of Penta-twinned Palladium Nanowires and Their Enhanced Electrocatalytic Properties. *ACS Appl. Mater. Interfaces* **2017**, *9*, 31203−31212.

(148) Choi, S.-I.; Xie, S.; Shao, M.; Odell, J. H.; Lu, N.; Peng, H.-C.; Protsailo, L.; Guerrero, S.; Park, J.; Xia, X.; et al. Synthesis and Characterization of 9 nm Pt−Ni Octahedra with a Record High Activity of 3.3 A/mg_{Pt} for the Oxygen Reduction Reaction. *Nano Lett.* **2013**, *13*, 3420−3425.

(149) Aliaga, C.; Park, J. Y.; Yamada, Y.; Lee, H. S.; Tsung, C.-K.; Yang, P.; Somorjai, G. A. Sum Frequency Generation and Catalytic Reaction Studies of the Removal of Organic Capping Agents from Pt Nanoparticles by UV−Ozone Treatment. *J. Phys. Chem. C* **2009**, *113*, 6150−6155.

(150) Crespo-Quesada, M.; Andanson, J. M.; Yarulin, A.; Lim, B.; Xia, Y.; Kiwi-Minsker, L. UV-ozone Cleaning of Supported Poly(vinylpyrrolidone)-Stabilized Palladium Nanocubes: Effect of Stabilizer Removal on Morphology and Catalytic Behavior. *Langmuir* **2011**, *27*, 7909−7916.

(151) Naresh, N.; Wasim, F. G. S.; Ladewig, B. P.; Neergat, M. Removal of Surfactant and Capping Agent from Pd Nanocubes (Pd-NCs) Using Tert-butylamine: Its Effect on Electrochemical Characteristics. *J. Mater. Chem. A* **2013**, *1*, 8553−8559.

(152) Gilroy, K. D.; Puibasset, J.; Vara, M.; Xia, Y. On the Thermodynamics and Experimental Control of Twinning in Metal Nanocrystals. *Angew. Chem., Int. Ed.* **2017**, *56*, 8647−8651.

(153) Jin, M.; He, G.; Zhang, H.; Zeng, J.; Xie, Z.; Xia, Y. Shape-Controlled Synthesis of Copper Nanocrystals in an Aqueous Solution with Glucose as a Reducing Agent and Hexadecylamine as a Capping Agent. *Angew. Chem., Int. Ed.* **2011**, *50*, 10560−10564.

(154) Guo, H.; Chen, Y.; Cortie, M. B.; Liu, X.; Xie, Q.; Wang, X.; Peng, D.-L. Shape-Selective Formation of Monodisperse Copper Nanospheres and Nanocubes via Disproportionation Reaction Route and Their Optical Properties. *J. Phys. Chem. C* **2014**, *118*, 9801−9808.

(155) Yang, H.-J.; He, S.-Y.; Chen, H.-L.; Tuan, H.-Y. Monodisperse Copper Nanocubes: Synthesis, Self-Assembly, and Large-Area Dense-Packed Films. *Chem. Mater.* **2014**, *26*, 1785−1793.

(156) Loiudice, A.; Lobaccaro, P.; Kamali, E. A.; Thao, T.; Huang, B. H.; Ager, J. W.; Buonsanti, R. Tailoring Copper Nanocrystals towards C_2 Products in Electrochemical CO_2 Reduction. *Angew. Chem., Int. Ed.* **2016**, *55*, 5789−5792.

(157) Lyu, L.-M.; Kao, Y.-C.; Cullen, D. A.; Sneed, B. T.; Chuang, Y.-C.; Kuo, C.-H. Spiny Rhombic Dodecahedral CuPt Nanoframes with Enhanced Catalytic Performance Synthesized from Cu Nanocube Templates. *Chem. Mater.* **2017**, *29*, 5681−5692.

(158) Strach, M.; Mantella, V.; Pankhurst, J. R.; Iyengar, P.; Loiudice, A.; Das, S.; Corminboeuf, C.; van Beek, W.; Buonsanti, R. Insights into Reaction Intermediates to Predict Synthetic Pathways for Shape-Controlled Metal Nanocrystals. *J. Am. Chem. Soc.* **2019**, *141*, 16312−16322.

(159) Suen, N.-T.; Kong, Z.-R.; Hsu, C.-S.; Chen, H.-C.; Tung, C.-W.; Lu, Y.-R.; Dong, C.-L.; Shen, C.-C.; Chung, J.-C.; Chen, H. M. Morphology Manipulation of Copper Nanocrystals and Product Selectivity in the Electrocatalytic Reduction of Carbon Dioxide. *ACS Catal.* **2019**, *9*, 5217−5222.

(160) Hoefelmeyer, J. D.; Niesz, K.; Somorjai, G. A.; Tilley, T. D. Radial Anisotropic Growth of Rhodium Nanoparticles. *Nano Lett.* **2005**, *5*, 435−438.

(161) Zhang, Y.; Grass, M. E.; Kuhn, J. N.; Tao, F.; Habas, S. E.; Huang, W.; Yang, P.; Somorjai, G. A. Highly Selective Synthesis of Catalytically Active Monodisperse Rhodium Nanocubes. *J. Am. Chem. Soc.* **2008**, *130*, 5868−5869.

(162) Zhang, H.; Li, W.; Jin, M.; Zeng, J.; Yu, T.; Yang, D.; Xia, Y. Controlling the Morphology of Rhodium Nanocrystals by Manipulating the Growth Kinetics with a Syringe Pump. *Nano Lett.* **2011**, *11*, 898−903.

(163) Xiong, Y.; Chen, J.; Wiley, B.; Xia, Y.; Yin, Y.; Li, Z.-Y. Size-Dependence of Surface Plasmon Resonance and Oxidation for Pd Nanocubes Synthesized via a Seed Etching Process. *Nano Lett.* **2005**, *5*, 1237−1242.

(164) Niu, W.; Li, Z.-Y.; Shi, L.; Liu, X.; Li, H.; Han, S.; Chen, J.; Xu, G. Seed-Mediated Growth of Nearly Monodisperse Palladium Nanocubes with Controllable Sizes. *Cryst. Growth Des.* **2008**, *8*, 4440−4444.

(165) Niu, W.; Zhang, L.; Xu, G. Shape-Controlled Synthesis of Single-Crystalline Palladium Nanocrystals. *ACS Nano* **2010**, *4*, 1987−1996.

(166) Jin, M.; Liu, H.; Zhang, H.; Xie, Z.; Liu, J.; Xia, Y. Synthesis of Pd nanocrystals Enclosed by {100} Facets and With Sizes < 10 nm for Application in CO Oxidation. *Nano Res.* **2011**, *4*, 83−91.

(167) Laskar, M.; Skrabalak, S. E. Decoupling the Geometric Parameters of Shape-Controlled Pd Nanocatalysts. *ACS Catal.* **2014**, *4*, 1120−1128.

(168) Im, S. H.; Lee, Y. T.; Wiley, B.; Xia, Y. Large-Scale Synthesis of Silver Nanocubes: The Role of HCl in Promoting Cube Perfection and Monodispersity. *Angew. Chem., Int. Ed.* **2005**, *44*, 2154−2157.

(169) Siekkinen, A. R.; McLellan, J. M.; Chen, J.; Xia, Y. Rapid Synthesis of Small Silver Nanocubes by Mediating Polyol Reduction with a Trace Amount of Sodium Sulfide or Sodium Hydrosulfide. *Chem. Phys. Lett.* **2006**, *432*, 491−496.

(170) Zhang, Q.; Li, W.; Moran, C.; Zeng, J.; Chen, J.; Wen, L.-P.; Xia, Y. Seed-Mediated Synthesis of Ag Nanocubes with Controllable Edge Lengths in the Range of 30−200 nm and Comparison of Their Optical Properties. *J. Am. Chem. Soc.* **2010**, *132*, 11372−11378.

(171) Zhang, Q.; Li, W.; Wen, L. P.; Chen, J.; Xia, Y. Facile Synthesis of Ag Nanocubes of 30 to 70 nm in Edge Length with CF_3COOAg as a Precursor. *Chem. - Eur. J.* **2010**, *16*, 10234−10239.

(172) Wang, Y.; Zheng, Y.; Huang, C. Z.; Xia, Y. Synthesis of Ag Nanocubes 18−32 nm in Edge Length: The Effects of Polyol on Reduction Kinetics, Size Control, and Reproducibility. *J. Am. Chem. Soc.* **2013**, *135*, 1941−1951.

(173) Lin, Z. W.; Tsao, Y. C.; Yang, M. Y.; Huang, M. H. Seed-Mediated Growth of Silver Nanocubes in Aqueous Solution with Tunable Size and Their Conversion to Au Nanocages with Efficient Photothermal Property. *Chem. - Eur. J.* **2016**, *22*, 2326−2332.

(174) Zhou, S.; Li, J.; Gilroy, K. D.; Tao, J.; Zhu, C.; Yang, X.; Sun, X.; Xia, Y. Facile Synthesis of Silver Nanocubes with Sharp Corners and Edges in an Aqueous Solution. *ACS Nano* **2016**, *10*, 9861−9870.

(175) Wiley, B.; Herricks, T.; Sun, Y.; Xia, Y. Polyol Synthesis of Silver Nanoparticles: Use of Chloride and Oxygen to Promote the Formation of Single-Crystal, Truncated Cubes and Tetrahedrons. *Nano Lett.* **2004**, *4*, 1733−1739.

(176) Tao, A.; Sinsermsuksakul, P.; Yang, P. Polyhedral Silver Nanocrystals with Distinct Scattering Signatures. *Angew. Chem., Int. Ed.* **2006**, *45*, 4597−4601.

(177) Lu, X.; Tuan, H.-Y.; Chen, J.; Li, Z.-Y.; Korgel, B. A.; Xia, Y. Mechanistic Studies on the Galvanic Replacement Reaction between Multiply Twinned Particles of Ag and $HAuCl_4$ in an Organic Medium. *J. Am. Chem. Soc.* **2007**, *129*, 1733−1742.

(178) Bi, Y.; Lu, G. Morphology-Controlled Preparation of Silver Nanocrystals and Their Application in Catalysis. *Chem. Lett.* **2008**, *37*, 514−515.

(179) Zhang, Q.; Cobley, C.; Au, L.; McKiernan, M.; Schwartz, A.; Wen, L.-P.; Chen, J.; Xia, Y. Production of Ag Nanocubes on a Scale of 0.1 g per Batch by Protecting the NaHS-Mediated Polyol Synthesis with Argon. *ACS Appl. Mater. Interfaces* **2009**, *1*, 2044−2048.

(180) Zeng, J.; Zheng, Y.; Rycenga, M.; Tao, J.; Li, Z.-Y.; Zhang, Q.; Zhu, Y.; Xia, Y. Controlling the Shapes of Silver Nanocrystals with Different Capping Agents. *J. Am. Chem. Soc.* **2010**, *132*, 8552−8553.

(181) Chen, Z.; Chang, J. W.; Balasanthiran, C.; Milner, S. T.; Rioux, R. M. Anisotropic Growth of Silver Nanoparticles Is Kinetically Controlled by Polyvinylpyrrolidone Binding. *J. Am. Chem. Soc.* **2019**, *141*, 4328−4337.

(182) Ahmadi, T. S.; Wang, Z. L.; Green, T. C.; Henglein, A.; El-Sayed, M. A. Shape-Controlled Synthesis of Colloidal Platinum Nanoparticles. *Science* **1996**, *272*, 1924−1926.

(183) Petroski, J. M.; Wang, Z. L.; Green, T. C.; El-Sayed, M. A. Kinetically Controlled Growth and Shape Formation Mechanism of Platinum Nanoparticles. *J. Phys. Chem. B* **1998**, *102*, 3316−3320.

(184) Ren, J.; Tilley, R. D. Preparation, Self-Assembly, and Mechanistic Study of Highly Monodispersed Nanocubes. *J. Am. Chem. Soc.* **2007**, *129*, 3287−3291.

(185) Wu, B.; Zheng, N.; Fu, G. Small Molecules Control the Formation of Pt Nanocrystals: A Key Role of Carbon Monoxide in the Synthesis of Pt Nanocubes. *Chem. Commun.* **2011**, *47*, 1039−1041.

(186) Niesz, K.; Grass, M.; Somorjai, G. A. Precise Control of the Pt Nanoparticle Size by Seeded Growth Using $EO_{13}PO_{30}EO_{13}$ Triblock Copolymers as Protective Agents. *Nano Lett.* **2005**, *5*, 2238−2240.

(187) Song, H.; Kim, F.; Connor, S.; Somorjai, G. A.; Yang, P. Pt Nanocrystals: Shape Control and Langmuir−Blodgett Monolayer Formation. *J. Phys. Chem. B* **2005**, *109*, 188−193.

(188) Wang, C.; Daimon, H.; Lee, Y.; Kim, J.; Sun, S. Synthesis of Monodisperse Pt Nanocubes and Their Enhanced Catalysis for Oxygen Reduction. *J. Am. Chem. Soc.* **2007**, *129*, 6974−6975.

(189) Wang, C.; Daimon, H.; Onodera, T.; Koda, T.; Sun, S. A General Approach to the Size- and Shape-Controlled Synthesis of Platinum Nanoparticles and Their Catalytic Reduction of Oxygen. *Angew. Chem., Int. Ed.* **2008**, *47*, 3588−3591.

(190) Kang, Y.; Ye, X.; Murray, C. B. Size- and Shape-Selective Synthesis of Metal Nanocrystals and Nanowires Using CO as a Reducing Agent. *Angew. Chem., Int. Ed.* **2010**, *49*, 6156−6159.

(191) Kang, Y.; Li, M.; Cai, Y.; Cargnello, M.; Diaz, R. E.; Gordon, T. R.; Wieder, N. L.; Adzic, R. R.; Gorte, R. J.; Stach, E. A.; et al. Heterogeneous Catalysts Need Not Be so "Heterogeneous": Monodisperse Pt Nanocrystals by Combining Shape-Controlled Synthesis and Purification by Colloidal Recrystallization. *J. Am. Chem. Soc.* **2013**, *135*, 2741−2747.

(192) Bratlie, K. M.; Lee, H.; Komvopoulos, K.; Yang, P.; Somorjai, G. A. Platinum Nanoparticle Shape Effects on Benzene Hydrogenation Selectivity. *Nano Lett.* **2007**, *7*, 3097−3101.

(193) Lee, H.; Habas, S. E.; Kweskin, S.; Butcher, D.; Somorjai, G. A.; Yang, P. Morphological Control of Catalytically Active Platinum Nanocrystals. *Angew. Chem., Int. Ed.* **2006**, *45*, 7824−7828.

(194) Sau, T. K.; Murphy, C. J. Room Temperature, High-Yield Synthesis of Multiple Shapes of Gold Nanoparticles in Aqueous Solution. *J. Am. Chem. Soc.* **2004**, *126*, 8648−8649.

(195) Seo, D.; Park, J. C.; Song, H. Polyhedral Gold Nanocrystals with O_h Symmetry: From Octahedra to Cubes. *J. Am. Chem. Soc.* **2006**, *128*, 14863−14870.

(196) Seo, D.; Yoo, C. I.; Park, J. C.; Park, S. M.; Ryu, S.; Song, H. Directed Surface Overgrowth and Morphology Control of Polyhedral Gold Nanocrystals. *Angew. Chem., Int. Ed.* **2008**, *47*, 763−767.

(197) Chiu, C.-Y.; Chung, P.-J.; Lao, K.-U.; Liao, C.-W.; Huang, M. H. Facet-Dependent Catalytic Activity of Gold Nanocubes, Octahedra, and Rhombic Dodecahedra toward 4-Nitroaniline Reduction. *J. Phys. Chem. C* **2012**, *116*, 23757−23763.

(198) Park, J.-E.; Lee, Y.; Nam, J.-M. Precisely Shaped, Uniformly Formed Gold Nanocubes with Ultrahigh Reproducibility in Single-Particle Scattering and Surface-Enhanced Raman Scattering. *Nano Lett.* **2018**, *18*, 6475−6482.

(199) Lim, B.; Kobayashi, H.; Camargo, P. H. C.; Allard, L. F.; Liu, J.; Xia, Y. New Insights into the Growth Mechanism and Surface Structure of Palladium Nanocrystals. *Nano Res.* **2010**, *3*, 180−188.

(200) Zhang, H.; Jin, M.; Xiong, Y.; Lim, B.; Xia, Y. Shape-Controlled Synthesis of Pd Nanocrystals and Their Catalytic Applications. *Acc. Chem. Res.* **2013**, *46*, 1783−1794.

(201) Lim, B.; Jiang, M.; Tao, J.; Camargo, P. H. C.; Zhu, Y.; Xia, Y. Shape-Controlled Synthesis of Pd Nanocrystals in Aqueous Solutions. *Adv. Funct. Mater.* **2009**, *19*, 189−200.

(202) Wiley, B. J.; Chen, Y.; McLellan, J. M.; Xiong, Y.; Li, Z.-Y.; Ginger, D.; Xia, Y. Synthesis and Optical Properties of Silver Nanobars and Nanorice. *Nano Lett.* **2007**, *7*, 1032−1036.

(203) Zhang, Q.; Moran, C. H.; Xia, X.; Rycenga, M.; Li, N.; Xia, Y. Synthesis of Ag Nanobars in the Presence of Single-Crystal Seeds and a Bromide Compound, and Their Surface-Enhanced Raman Scattering (SERS) Properties. *Langmuir* **2012**, *28*, 9047−9054.

(204) Zhou, S.; Mesina, D. S.; Organt, M. A.; Yang, T.-H.; Yang, X.; Huo, D.; Zhao, M.; Xia, Y. Site-Selective Growth of Ag Nanocubes for Sharpening Their Corners and Edges, Followed by Elongation into Nanobars through Symmetry Reduction. *J. Mater. Chem. C* **2018**, *6*, 1384−1392.

(205) Li, Y.; Bian, T.; Du, J.; Xiong, Y.; Zhan, F.; Zhang, H.; Yang, D. Facile Synthesis of High-Quality Pt Nanostructures with a Controlled Aspect Ratio for Methanol Electro-oxidation. *CrystEngComm* **2014**, *16*, 8340−8343.

(206) Lu, S.-C.; Hsiao, M.-C.; Yorulmaz, M.; Wang, L.-Y.; Yang, P.-Y.; Link, S.; Chang, W.-S.; Tuan, H.-Y. Single-Crystalline Copper Nano-Octahedra. *Chem. Mater.* **2015**, *27*, 8185−8188.

(207) Long, N. V.; Chien, N. D.; Hirata, H.; Matsubara, T.; Ohtaki, M.; Nogami, M. Highly Monodisperse Cubic and Octahedral Rhodium Nanocrystals: Their Evolutions from Sharp Polyhedrons into Branched Nanostructures and Surface-Enhanced Raman Scattering. *J. Cryst. Growth* **2011**, *320*, 78−89.

(208) Lim, B.; Xiong, Y.; Xia, Y. A Water-Based Synthesis of Octahedral, Decahedral, and Icosahedral Pd Nanocrystals. *Angew. Chem., Int. Ed.* **2007**, *46*, 9279−9282.

(209) Liu, M.; Zheng, Y.; Zhang, L.; Guo, L.; Xia, Y. Transformation of Pd Nanocubes into Octahedra with Controlled Sizes by Maneuvering the Rates of Etching and Regrowth. *J. Am. Chem. Soc.* **2013**, *135*, 11752−11755.

(210) Wang, Y.; Xie, S.; Liu, J.; Park, J.; Huang, C. Z.; Xia, Y. Shape-Controlled Synthesis of Palladium Nanocrystals: A Mechanistic Understanding of the Evolution from Octahedrons to Tetrahedrons. *Nano Lett.* **2013**, *13*, 2276−2281.

(211) Figueroa-Cosme, L.; Park, J.; Bao, S.; Xia, Y. Seed-Mediated Growth of Colloidal Metal Nanocrystals: Scaling up the Production through Geometric and Stoichiometric Analyses. *ChemNanoMat* **2016**, *2*, 1033−1039.

(212) Figueroa-Cosme, L.; Gilroy, K. D.; Yang, T.-H.; Vara, M.; Park, J.; Bao, S.; da Silva, A. G. M.; Xia, Y. Synthesis of Palladium Nanoscale Octahedra through a One-Pot, Dual-Reductant Route and Kinetic Analysis. *Chem. - Eur. J.* **2018**, *24*, 6133−6139.

(213) Tsuji, M.; Maeda, Y.; Hikino, S.; Kumagae, H.; Matsunaga, M.; Tang, X.-L.; Matsuo, R.; Ogino, M.; Jiang, P. Shape Evolution of Octahedral and Triangular Platelike Silver Nanocrystals from Cubic and Right Bipyramidal Seeds in DMF. *Cryst. Growth Des.* **2009**, *9*, 4700−4705.

(214) Wang, Y.; Wan, D.; Xie, S.; Xia, X.; Huang, C. Z.; Xia, Y. Synthesis of Silver Octahedra with Controlled Sizes and Optical Properties via Seed-Mediated Growth. *ACS Nano* **2013**, *7*, 4586−4594.

(215) Bu, L.; Feng, Y.; Yao, J.; Guo, S.; Guo, J.; Huang, X. Facet and Dimensionality Control of Pt Nanostructures for Efficient Oxygen Reduction and Methanol Oxidation Electrocatalysts. *Nano Res.* **2016**, *9*, 2811−2821.

(216) Lee, C.-T.; Yang, X.; Vara, M.; Gilroy, K. D.; Xia, Y. Water-Based Synthesis of Sub-10 nm Pt Octahedra and Their Performance towards the Oxygen Reduction Reaction. *ChemNanoMat* **2017**, *3*, 879−884.

(217) Moglianetti, M.; Solla-Gullón, J.; Donati, P.; Pedone, D.; Debellis, D.; Sibillano, T.; Brescia, R.; Giannini, C.; Montiel, V.; Feliu, J. M.; et al. Citrate-Coated, Size-Tunable Octahedral Platinum Nanocrystals: A Novel Route for Advanced Electrocatalysts. *ACS Appl. Mater. Interfaces* **2018**, *10*, 41608−41617.

(218) Carbó-Argibay, E.; Rodríguez-González, B.; Pacifico, J.; Pastoriza-Santos, I.; Pérez-Juste, J.; Liz-Marzán, L. M. Chemical Sharpening of Gold Nanorods: The Rod-to-Octahedron Transition. *Angew. Chem., Int. Ed.* **2007**, *46*, 8983−8987.

(219) Li, C.; Shuford, K. L.; Chen, M.; Lee, E. J.; Cho, S. O. A Facile Polyol Route to Uniform Gold Octahedra with Tailorable Size and Their Optical Properties. *ACS Nano* **2008**, *2*, 1760−1769.

(220) Cao, C.; Park, S.; Sim, S. J. Seedless Synthesis of Octahedral Gold Nanoparticles in Condensed Surfactant Phase. *J. Colloid Interface Sci.* **2008**, *322*, 152−157.

(221) Park, K. H.; Jang, K.; Kim, H. J.; Son, S. U. Near-Monodisperse Tetrahedral Rhodium Nanoparticles on Charcoal: The Shape-Dependent Catalytic Hydrogenation of Arenes. *Angew. Chem., Int. Ed.* **2007**, *46*, 1152−1155.

(222) Zhang, N.; Shao, Q.; Pi, Y.; Guo, J.; Huang, X. Solvent-Mediated Shape Tuning of Well-Defined Rhodium Nanocrystals for Efficient Electrochemical Water Splitting. *Chem. Mater.* **2017**, *29*, 5009−5015.

(223) Zhang, Y.; Wang, M.; Zhu, E.; Zheng, Y.; Huang, Y.; Huang, X. Seedless Growth of Palladium Nanocrystals with Tunable Structures: From Tetrahedra to Nanosheets. *Nano Lett.* **2015**, *15*, 7519−7525.

(224) Gao, Y.; Jiang, P.; Song, L.; Wang, J. X.; Liu, L. F.; Liu, D. F.; Xiang, Y. J.; Zhang, Z. X.; Zhao, X. W.; Dou, X. Y.; et al. Studies on Silver Nanodecahedrons Synthesized by PVP-Assisted *N,N*-Dimethylformamide (DMF) Reduction. *J. Cryst. Growth* **2006**, *289*, 376−380.

(225) Zhou, J.; An, J.; Tang, B.; Xu, S.; Cao, Y.; Zhao, B.; Xu, W.; Chang, J.; Lombardi, J. R. Growth of Tetrahedral Silver Nanocrystals in Aqueous Solution and Their SERS Enhancement. *Langmuir* **2008**, *24*, 10407−10413.

(226) Teranishi, T.; Kurita, R.; Miyake, M. Shape Control of Pt Nanoparticles. *J. Inorg. Organomet. Polym.* **2000**, *10*, 145−156.

(227) Zheng, Y.; Liu, W.; Lv, T.; Luo, M.; Hu, H.; Lu, P.; Choi, S.-I.; Zhang, C.; Tao, J.; Zhu, Y.; et al. Seed-Mediated Synthesis of Gold Tetrahedra in High Purity and with Tunable, Well-Controlled Sizes. *Chem. - Asian J.* **2014**, *9*, 2635−2640.

(228) Ma, X.-Y.; Chen, Y.; Wang, H.; Li, Q.-X.; Lin, W.-F.; Cai, W.-B. Electrocatalytic Oxidation of Ethanol and Ethylene Glycol on Cubic, Octahedral and Rhombic Dodecahedral Palladium Nanocrystals. *Chem. Commun.* **2018**, *54*, 2562−2565.

(229) Niu, W.; Zheng, S.; Wang, D.; Liu, X.; Li, H.; Han, S.; Chen, J.; Tang, Z.; Xu, G. Selective Synthesis of Single-Crystalline Rhombic Dodecahedral, Octahedral, and Cubic Gold Nanocrystals. *J. Am. Chem. Soc.* **2009**, *131*, 697−703.

(230) Personick, M. L.; Langille, M. R.; Zhang, J.; Harris, N.; Schatz, G. C.; Mirkin, C. A. Synthesis and Isolation of {110}-Faceted Gold Bipyramids and Rhombic Dodecahedra. *J. Am. Chem. Soc.* **2011**, *133*, 6170−6173.

(231) Jeong, G. H.; Kim, M.; Lee, Y. W.; Choi, W.; Oh, W. T.; Park, Q. H.; Han, S. W. Polyhedral Au Nanocrystals Exclusively Bound by {110} Facets: The Rhombic Dodecahedron. *J. Am. Chem. Soc.* **2009**, *131*, 1672−1673.

(232) Zhao, L.; Xu, C.; Su, H.; Liang, J.; Lin, S.; Gu, L.; Wang, X.; Chen, M.; Zheng, N. Single-Crystalline Rhodium Nanosheets with Atomic Thickness. *Adv. Sci.* **2015**, *2*, 1500100.

(233) Duan, H.; Yan, N.; Yu, R.; Chang, C.-R.; Zhou, G.; Hu, H.-S.; Rong, H.; Niu, Z.; Mao, J.; Asakura, H.; et al. Ultrathin Rhodium Nanosheets. *Nat. Commun.* **2014**, *5*, 3093.

(234) Millstone, J. E.; Métraux, G. S.; Mirkin, C. A. Controlling the Edge Length of Gold Nanoprisms via a Seed-Mediated Approach. *Adv. Funct. Mater.* **2006**, *16*, 1209−1214.

(235) Millstone, J. E.; Park, S.; Shuford, K. L.; Qin, L.; Schatz, G. C.; Mirkin, C. A. Observation of a Quadrupole Plasmon Mode for a

Colloidal Solution of Gold Nanoprisms. *J. Am. Chem. Soc.* **2005**, *127*, 5312−5313.

(236) Wu, D.; Cao, M.; Cao, R. Ru-Assisted Synthesis of {111}-Faceted Pd Truncated Bipyramids: a Highly Reactive, Stable and Restorable Catalyst for Formic Acid Oxidation. *Chem. Commun.* **2014**, *50*, 12970−12972.

(237) Lu, N.; Chen, W.; Fang, G.; Chen, B.; Yang, K.; Yang, Y.; Wang, Z.; Huang, S.; Li, Y. 5-Fold Twinned Nanowires and Single Twinned Right Bipyramids of Pd: Utilizing Small Organic Molecules to Tune the Etching Degree of O_2/Halides. *Chem. Mater.* **2014**, *26*, 2453−2459.

(238) Ruan, L.; Chiu, C.-Y.; Li, Y.; Huang, Y. Synthesis of Platinum Single-Twinned Right Bipyramid and {111}-Bipyramid through Targeted Control over both Nucleation and Growth Using Specific Peptides. *Nano Lett.* **2011**, *11*, 3040−3046.

(239) Wiley, B. J.; Wang, Z.; Wei, J.; Yin, Y.; Cobden, D. H.; Xia, Y. Synthesis and Electrical Characterization of Silver Nanobeams. *Nano Lett.* **2006**, *6*, 2273−2278.

(240) Choi, C.; Cheng, T.; Flores Espinosa, M.; Fei, H.; Duan, X.; Goddard, W. A., III; Huang, Y. A Highly Active Star Decahedron Cu Nanocatalyst for Hydrocarbon Production at Low Overpotentials. *Adv. Mater.* **2018**, *31*, 1805405.

(241) Lee, S. R.; Vara, M.; Hood, Z. D.; Zhao, M.; Gilroy, K. D.; Chi, M.; Xia, Y. Rhodium Decahedral Nanocrystals: Facile Synthesis, Mechanistic Insights, and Experimental Controls. *ChemNanoMat* **2018**, *4*, 66−70.

(242) Huang, H.; Wang, Y.; Ruditskiy, A.; Peng, H.-C.; Zhao, X.; Zhang, L.; Liu, J.; Ye, Z.; Xia, Y. Polyol Syntheses of Palladium Decahedra and Icosahedra as Pure Samples by Maneuvering the Reaction Kinetics with Additives. *ACS Nano* **2014**, *8*, 7041−7050.

(243) Ruditskiy, A.; Zhao, M.; Gilroy, K. D.; Vara, M.; Xia, Y. Toward a Quantitative Understanding of the Sulfate-Mediated Synthesis of Pd Decahedral Nanocrystals with High Conversion and Morphology Yields. *Chem. Mater.* **2016**, *28*, 8800−8806.

(244) Tsuji, M.; Ogino, M.; Matsuo, R.; Kumagae, H.; Hikino, S.; Kim, T.; Yoon, S.-H. Stepwise Growth of Decahedral and Icosahedral Silver Nanocrystals in DMF. *Cryst. Growth Des.* **2010**, *10*, 296−301.

(245) Zhu, W.; Yin, A.-X.; Zhang, Y.-W.; Yan, C.-H. Highly Shape-Selective Synthesis of Monodispersed Fivefold Twinned Platinum Nanodecahedrons and Nanoicosahedrons. *Chem. - Eur. J.* **2012**, *18*, 12222−12226.

(246) Sun, J.; Guan, M.; Shang, T.; Gao, C.; Xu, Z.; Zhu, J. Selective Synthesis of Gold Cuboid and Decahedral Nanoparticles Regulated and Controlled by Cu^{2+} Ions. *Cryst. Growth Des.* **2008**, *8*, 906−910.

(247) Carbó-Argibay, E.; Rodríguez-González, B.; Pastoriza-Santos, I.; Pérez-Juste, J.; Liz-Marzán, L. M. Growth of Pentatwinned Gold Nanorods into Truncated Decahedra. *Nanoscale* **2010**, *2*, 2377−2383.

(248) Lee, J.-H.; Gibson, K. J.; Chen, G.; Weizmann, Y. Bipyramid-Templated Synthesis of Monodisperse Anisotropic Gold Nanocrystals. *Nat. Commun.* **2015**, *6*, 7571.

(249) Choi, S.-I.; Lee, S. R.; Ma, C.; Oliy, B.; Luo, M.; Chi, M.; Xia, Y. Facile Synthesis of Rhodium Icosahedra with Controlled Sizes up to 12 nm. *ChemNanoMat* **2016**, *2*, 61−66.

(250) Wang, W.; Zhou, S.; Shen, M.; Hood, Z. D.; Xiao, K.; Xia, Y. Facile Synthesis of Silver Icosahedral Nanocrystals with Uniform and Controllable Sizes. *ChemNanoMat* **2018**, *4*, 1071−1077.

(251) Peng, S.; McMahon, J. M.; Schatz, G. C.; Gray, S. K.; Sun, Y. Reversing the Size-Dependence of Surface Plasmon Resonances. *Proc. Natl. Acad. Sci. U. S. A.* **2010**, *107*, 14530−14534.

(252) Zhao, M.; Holder, J.; Chen, Z.; Xie, M.; Cao, Z.; Chi, M.; Xia, Y. Facile Synthesis of Pt Icosahedral Nanocrystals with Controllable Sizes for the Evaluation of Size-Dependent Activity toward Oxygen Reduction. *ChemCatChem* **2019**, *11*, 2458−2463.

(253) Zhou, W.; Wu, J.; Yang, H. Highly Uniform Platinum Icosahedra Made by Hot Injection-Assisted GRAILS Method. *Nano Lett.* **2013**, *13*, 2870−2874.

(254) Seo, D.; Yoo, C. I.; Chung, I. S.; Park, S. M.; Ryu, S.; Song, H. Shape Adjustment between Multiply Twinned and Single-Crystalline Polyhedral Gold Nanocrystals: Decahedra, Icosahedra, and Truncated Tetrahedra. *J. Phys. Chem. C* **2008**, *112*, 2469−2475.

(255) Xu, J.; Li, S.; Weng, J.; Wang, X.; Zhou, Z.; Yang, K.; Liu, M.; Chen, X.; Cui, Q.; Cao, M.; et al. Hydrothermal Syntheses of Gold Nanocrystals: From Icosahedral to Its Truncated Form. *Adv. Funct. Mater.* **2008**, *18*, 277−284.

(256) Rathmell, A. R.; Bergin, S. M.; Hua, Y. L.; Li, Z. Y.; Wiley, B. J. The Growth Mechanism of Copper Nanowires and Their Properties in Flexible, Transparent Conducting Films. *Adv. Mater.* **2010**, *22*, 3558−3563.

(257) Ye, E.; Zhang, S.-Y.; Liu, S.; Han, M.-Y. Disproportionation for Growing Copper Nanowires and Their Controlled Self-Assembly Facilitated by Ligand Exchange. *Chem. - Eur. J.* **2011**, *17*, 3074−3077.

(258) Ye, S.; Rathmell, A. R.; Stewart, I. E.; Ha, Y.-C.; Wilson, A. R.; Chen, Z.; Wiley, B. J. A Rapid Synthesis of High Aspect Ratio Copper Nanowires for High-Performance Transparent Conducting Films. *Chem. Commun.* **2014**, *50*, 2562−2564.

(259) Cui, F.; Yu, Y.; Dou, L.; Sun, J.; Yang, Q.; Schildknecht, C.; Schierle-Arndt, K.; Yang, P. Synthesis of Ultrathin Copper Nanowires Using Tris(trimethylsilyl)silane for High-Performance and Low-Haze Transparent Conductors. *Nano Lett.* **2015**, *15*, 7610−7615.

(260) Cui, F.; Dou, L.; Yang, Q.; Yu, Y.; Niu, Z.; Sun, Y.; Liu, H.; Dehestani, A.; Schierle-Arndt, K.; Yang, P. Benzoin Radicals as Reducing Agent for Synthesizing Ultrathin Copper Nanowires. *J. Am. Chem. Soc.* **2017**, *139*, 3027−3032.

(261) Kim, D.; Kley, C. S.; Li, Y.; Yang, P. Copper Nanoparticle Ensembles for Selective Electroreduction of CO_2 to C_2-C_3 Products. *Proc. Natl. Acad. Sci. U. S. A.* **2017**, *114*, 10560−10565.

(262) Luo, M.; Zhou, M.; Rosa da Silva, R.; Tao, J.; Figueroa-Cosme, L.; Gilroy, K. D.; Peng, H.-C.; He, Z.; Xia, Y. Pentatwinned Cu Nanowires with Ultrathin Diameters below 20 nm and Their Use as Templates for the Synthesis of Au-Based Nanotubes. *ChemNanoMat* **2017**, *3*, 190−195.

(263) Kim, M. J.; Alvarez, S.; Chen, Z.; Fichthorn, K. A.; Wiley, B. J. Single-Crystal Electrochemistry Reveals Why Metal Nanowires Grow. *J. Am. Chem. Soc.* **2018**, *140*, 14740−14746.

(264) Chen, Y.-H.; Hung, H.-H.; Huang, M. H. Seed-Mediated Synthesis of Palladium Nanorods and Branched Nanocrystals and Their Use as Recyclable Suzuki Coupling Reaction Catalysts. *J. Am. Chem. Soc.* **2009**, *131*, 9114−9121.

(265) Huang, X.; Zheng, N. One-Pot, High-Yield Synthesis of 5-Fold Twinned Pd Nanowires and Nanorods. *J. Am. Chem. Soc.* **2009**, *131*, 4602−4603.

(266) Tang, Y.; Edelmann, R. E.; Zou, S. Length Tunable Penta-Twinned Palladium Nanorods: Seedless Synthesis and Electro-oxidation of Formic Acid. *Nanoscale* **2014**, *6*, 5630−5633.

(267) Huang, H.; Zhang, L.; Lv, T.; Ruditskiy, A.; Liu, J.; Ye, Z.; Xia, Y. Five-Fold Twinned Pd Nanorods and Their Use as Templates for the Synthesis of Bimetallic or Hollow Nanostructures. *ChemNanoMat* **2015**, *1*, 246−252.

(268) Jana, N. R.; Gearheart, L.; Murphy, C. J. Wet Chemical Synthesis of Silver Nanorods and Nanowires of Controllable Aspect Ratio. *Chem. Commun.* **2001**, 617−618.

(269) Sun, Y.; Xia, Y. Large-Scale Synthesis of Uniform Silver Nanowires through a Soft, Self-Seeding, Polyol Process. *Adv. Mater.* **2002**, *14*, 833−837.

(270) Sun, Y.; Yin, Y.; Mayers, B. T.; Herricks, T.; Xia, Y. Uniform Silver Nanowires Synthesis by Reducing $AgNO_3$ with Ethylene Glycol in the Presence of Seeds and Poly(Vinyl Pyrrolidone). *Chem. Mater.* **2002**, *14*, 4736−4745.

(271) Sun, Y.; Mayers, B.; Herricks, T.; Xia, Y. Polyol Synthesis of Uniform Silver Nanowires: A Plausible Growth Mechanism and the Supporting Evidence. *Nano Lett.* **2003**, *3*, 955−960.

(272) Li, B.; Ye, S.; Stewart, I. E.; Alvarez, S.; Wiley, B. J. Synthesis and Purification of Silver Nanowires to Make Conducting Films with a Transmittance of 99%. *Nano Lett.* **2015**, *15*, 6722−6726.

(273) da Silva, R. R.; Yang, M.; Choi, S.-I.; Chi, M.; Luo, M.; Zhang, C.; Li, Z. Y.; Camargo, P. H.; Ribeiro, S. J.; Xia, Y. Facile Synthesis of

Sub-20 nm Silver Nanowires through a Bromide-Mediated Polyol Method. *ACS Nano* **2016**, *10*, 7892−7900.

(274) Wiley, B.; Sun, Y.; Xia, Y. Synthesis of Silver Nanostructures with Controlled Shapes and Properties. *Acc. Chem. Res.* **2007**, *40*, 1067−1076.

(275) Caswell, K. K.; Bender, C. M.; Murphy, C. J. Seedless, Surfactantless Wet Chemical Synthesis of Silver Nanowires. *Nano Lett.* **2003**, *3*, 667−669.

(276) Tsuji, M.; Hashimoto, M.; Nishizawa, Y.; Kubokawa, M.; Tsuji, T. Microwave-Assisted Synthesis of Metallic Nanostructures in Solution. *Chem. - Eur. J.* **2005**, *11*, 440−452.

(277) Wiley, B.; Sun, Y.; Xia, Y. Polyol Synthesis of Silver Nanostructures: Control of Product Morphology with Fe(II) or Fe(III) Species. *Langmuir* **2005**, *21*, 8077−8080.

(278) Zhang, S.-H.; Jiang, Z.-Y.; Xie, Z.-X.; Xu, X.; Huang, R.-B.; Zheng, L.-S. Growth of Silver Nanowires from Solutions: A Cyclic Penta-Twinned-Crystal Growth Mechanism. *J. Phys. Chem. B* **2005**, *109*, 9416−9421.

(279) Gou, L.; Chipara, M.; Zaleski, J. M. Convenient, Rapid Synthesis of Ag Nanowires. *Chem. Mater.* **2007**, *19*, 1755−1760.

(280) Korte, K. E.; Skrabalak, S. E.; Xia, Y. Rapid Synthesis of Silver Nanowires through a $CuCl^-$ or $CuCl_2$ Mediated Polyol Process. *J. Mater. Chem.* **2008**, *18*, 437−441.

(281) Niu, Z.; Cui, F.; Kuttner, E.; Xie, C.; Chen, H.; Sun, Y.; Dehestani, A.; Schierle-Arndt, K.; Yang, P. Synthesis of Silver Nanowires with Reduced Diameters Using Benzoin-Derived Radicals to Make Transparent Conductors with High Transparency and Low Haze. *Nano Lett.* **2018**, *18*, 5329−5334.

(282) Tsuji, M.; Matsumoto, K.; Miyamae, N.; Tsuji, T.; Zhang, X. Rapid Preparation of Silver Nanorods and Nanowires by a Microwave-Polyol Method in the Presence of Pt Catalyst and Polyvinylpyrrolidone. *Cryst. Growth Des.* **2007**, *7*, 311−320.

(283) Pietrobon, B.; McEachran, M.; Kitaev, V. Synthesis of Size-Controlled Faceted Pentagonal Silver Nanorods with Tunable Plasmonic Properties and Self-Assembly of These Nanorods. *ACS Nano* **2009**, *3*, 21−26.

(284) Zhang, J.; Langille, M. R.; Mirkin, C. A. Synthesis of Silver Nanorods by Low Energy Excitation of Spherical Plasmonic Seeds. *Nano Lett.* **2011**, *11*, 2495−2498.

(285) Jiu, J.; Sugahara, T.; Nogi, M.; Suganuma, K. Ag Nanowires: Large-Scale Synthesis via a Trace-Salt-Assisted Solvothermal Process and Application in Transparent Electrodes. *J. Nanopart. Res.* **2013**, *15*, 1588.

(286) Lee, E.-J.; Kim, Y.-H.; Hwang, D. K.; Choi, W. K.; Kim, J.-Y. Synthesis and Optoelectronic Characteristics of 20 nm Diameter Silver Nanowires for Highly Transparent Electrode Films. *RSC Adv.* **2016**, *6*, 11702−11710.

(287) Jang, H.-W.; Kim, Y.-H.; Lee, K.-W.; Kim, Y.-M.; Kim, J.-Y. Research Update: Synthesis of Sub-15-nm Diameter Silver Nanowires through a Water-Based Hydrothermal Method: Fabrication of Low-Haze 2D Conductive Films. *APL Mater.* **2017**, *5*, No. 080701.

(288) Zhang, Y.; Guo, J.; Xu, D.; Sun, Y.; Yan, F. One-Pot Synthesis and Purification of Ultralong Silver Nanowires for Flexible Transparent Conductive Electrodes. *ACS Appl. Mater. Interfaces* **2017**, *9*, 25465−25473.

(289) Hu, J. Q.; Chen, Q.; Xie, Z. X.; Han, G. B.; Wang, R. H.; Ren, B.; Zhang, Y.; Yang, Z. L.; Tian, Z. Q. A Simple and Effective Route for the Synthesis of Crystalline Silver Nanorods and Nanowires. *Adv. Funct. Mater.* **2004**, *14*, 183−189.

(290) Sun, Y.; Gates, B.; Mayers, B.; Xia, Y. Crystalline Silver Nanowires by Soft Solution Processing. *Nano Lett.* **2002**, *2*, 165−168.

(291) Johnson, C. J.; Dujardin, E.; Davis, S. A.; Murphy, C. J.; Mann, S. Growth and Form of Gold Nanorods Prepared by Seed-Mediated, Surfactant-Directed Synthesis. *J. Mater. Chem.* **2002**, *12*, 1765−1770.

(292) Liu, M.; Guyot-Sionnest, P. Mechanism of Silver(I)-Assisted Growth of Gold Nanorods and Bipyramids. *J. Phys. Chem. B* **2005**, *109*, 22192−22200.

(293) Jin, B.; Sushko, M. L.; Liu, Z.; Cao, X.; Jin, C.; Tang, R. Understanding Anisotropic Growth of Au Penta-Twinned Nanorods by Liquid Cell Transmission Electron Microscopy. *J. Phys. Chem. Lett.* **2019**, *10*, 1443−1449.

(294) Lohse, S. E.; Murphy, C. J. The Quest for Shape Control: A History of Gold Nanorod Synthesis. *Chem. Mater.* **2013**, *25*, 1250−1261.

(295) Scarabelli, L.; Sánchez-Iglesias, A.; Pérez-Juste, J.; Liz-Marzán, L. M. A "Tips and Tricks" Practical Guide to the Synthesis of Gold Nanorods. *J. Phys. Chem. Lett.* **2015**, *6*, 4270−4279.

(296) Murphy, C. J.; Thompson, L. B.; Chernak, D. J.; Yang, J. A.; Sivapalan, S. T.; Boulos, S. P.; Huang, J.; Alkilany, A. M.; Sisco, P. N. Gold Nanorod Crystal Growth: From Seed-Mediated Synthesis to Nanoscale Sculpting. *Curr. Opin. Colloid Interface Sci.* **2011**, *16*, 128−134.

(297) Salzemann, C.; Urban, J.; Lisiecki, I.; Pileni, M. P. Characterization and Growth Process of Copper Nanodisks. *Adv. Funct. Mater.* **2005**, *15*, 1277−1284.

(298) Pastoriza-Santos, I.; Sánchez-Iglesias, A.; Rodríguez-González, B.; Liz-Marzán, L. M. Aerobic Synthesis of Cu Nanoplates with Intense Plasmon Resonances. *Small* **2009**, *5*, 440−443.

(299) Sun, Y.; Xu, L.; Yin, Z.; Song, X. Synthesis of Copper Submicro/Nanoplates with High Stability and Their Recyclable Superior Catalytic Activity towards 4-Nitrophenol Reduction. *J. Mater. Chem. A* **2013**, *1*, 12361−12370.

(300) Lee, J.-W.; Han, J.; Lee, D. S.; Bae, S.; Lee, S. H.; Lee, S.-K.; Moon, B. J.; Choi, C.-J.; Wang, G.; Kim, T.-W. 2D Single-Crystalline Copper Nanoplates as a Conductive Filler for Electronic Ink Applications. *Small* **2018**, *14*, 1703312.

(301) Yin, A.-X.; Liu, W.-C.; Ke, J.; Zhu, W.; Gu, J.; Zhang, Y.-W.; Yan, C.-H. Ru Nanocrystals with Shape-Dependent Surface-Enhanced Raman Spectra and Catalytic Properties: Controlled Synthesis and DFT Calculations. *J. Am. Chem. Soc.* **2012**, *134*, 20479−20489.

(302) Jang, K.; Kim, H. J.; Son, S. U. Low-Temperature Synthesis of Ultrathin Rhodium Nanoplates via Molecular Orbital Symmetry Interaction between Rhodium Precursors. *Chem. Mater.* **2010**, *22*, 1273−1275.

(303) Zhang, J.; Chen, M.; Chen, J.; Li, H.; Wang, S.; Kuang, Q.; Cao, Z.; Xie, Z. Synthesis of Single-Crystal Hyperbranched Rhodium Nanoplates with Remarkable Catalytic Properties. *Sci. China Mater.* **2017**, *60*, 685−696.

(304) Xiong, Y.; McLellan, J. M.; Chen, J.; Yin, Y.; Li, Z.-Y.; Xia, Y. Kinetically Controlled Synthesis of Triangular and Hexagonal Nanoplates of Palladium and Their SPR/SERS Properties. *J. Am. Chem. Soc.* **2005**, *127*, 17118−17127.

(305) Xiong, Y.; Washio, I.; Chen, J.; Cai, H.; Li, Z.-Y.; Xia, Y. Poly(vinyl pyrrolidone): A Dual Functional Reductant and Stabilizer for the Facile Synthesis of Noble Metal Nanoplates in Aqueous Solutions. *Langmuir* **2006**, *22*, 8563−8570.

(306) Figueroa-Cosme, L.; Hood, Z. D.; Gilroy, K. D.; Xia, Y. A Facile, Robust and Scalable Method for the Synthesis of Pd Nanoplates with Hydroxylamine as a Reducing Agent and Mechanistic Insights from Kinetic Analysis. *J. Mater. Chem. C* **2018**, *6*, 4677−4682.

(307) Huang, X.; Tang, S.; Mu, X.; Dai, Y.; Chen, G.; Zhou, Z.; Ruan, F.; Yang, Z.; Zheng, N. Freestanding Palladium Nanosheets with Plasmonic and Catalytic Properties. *Nat. Nanotechnol.* **2011**, *6*, 28−32.

(308) Chen, S.; Carroll, D. L. Silver Nanoplates: Size Control in Two Dimensions and Formation Mechanisms. *J. Phys. Chem. B* **2004**, *108*, 5500−5506.

(309) Washio, I.; Xiong, Y.; Yin, Y.; Xia, Y. Reduction by the End Groups of Poly(vinyl pyrrolidone): A New and Versatile Route to the Kinetically Controlled Synthesis of Ag Triangular Nanoplates. *Adv. Mater.* **2006**, *18*, 1745−1749.

(310) Jiang, X. C.; Chen, C. Y.; Chen, W. M.; Yu, A. B. Role of Citric Acid in the Formation of Silver Nanoplates through a Synergistic Reduction Approach. *Langmuir* **2010**, *26*, 4400−4408.

(311) Zeng, J.; Xia, X.; Rycenga, M.; Henneghan, P.; Li, Q.; Xia, Y. Successive Deposition of Silver on Silver Nanoplates: Lateral versus Vertical Growth. *Angew. Chem., Int. Ed.* **2011**, *50*, 244−249.

(312) Rocha, T. C. R.; Winnischofer, H.; Westphal, E.; Zanchet, D. Formation Kinetics of Silver Triangular Nanoplates. *J. Phys. Chem. C* **2007**, *111*, 2885−2891.

(313) Xiong, Y.; Siekkinen, A. R.; Wang, J.; Yin, Y.; Kim, M. J.; Xia, Y. Synthesis of Silver Nanoplates at High Yields by Slowing down the Polyol Reduction of Silver Nitrate with Polyacrylamide. *J. Mater. Chem.* **2007**, *17*, 2600−2602.

(314) Cao, Z.; Fu, H.; Kang, L.; Huang, L.; Zhai, T.; Ma, Y.; Yao, J. Rapid Room-Temperature Synthesis of Silver Nanoplates with Tunable In-Plane Surface Plasmon Resonance from Visible to Near-IR. *J. Mater. Chem.* **2008**, *18*, 2673−2678.

(315) Wijaya, Y. N.; Kim, J.; Choi, W. M.; Park, S. H.; Kim, M. H. A Systematic Study of Triangular Silver Nanoplates: One-Pot Green Synthesis, Chemical Stability, and Sensing Application. *Nanoscale* **2017**, *9*, 11705−11712.

(316) Shankar, S. S.; Rai, A.; Ankamwar, B.; Singh, A.; Ahmad, A.; Sastry, M. Biological Synthesis of Triangular Gold Nanoprisms. *Nat. Mater.* **2004**, *3*, 482−488.

(317) Sun, X.; Dong, S.; Wang, E. Large-Scale Synthesis of Micrometer-Scale Single-Crystalline Au Plates of Nanometer Thickness by a Wet-Chemical Route. *Angew. Chem., Int. Ed.* **2004**, *43*, 6360−6363.

(318) Au, L.; Lim, B.; Colletti, P.; Jun, Y.-S.; Xia, Y. Synthesis of Gold Microplates Using Bovine Serum Albumin as a Reductant and a Stabilizer. *Chem. - Asian J.* **2010**, *5*, 123−129.

(319) Chen, L.; Ji, F.; Xu, Y.; He, L.; Mi, Y.; Bao, F.; Sun, B.; Zhang, X.; Zhang, Q. High-Yield Seedless Synthesis of Triangular Gold Nanoplates through Oxidative Etching. *Nano Lett.* **2014**, *14*, 7201−7206.

(320) Lyu, Z.; Xie, M.; Gilroy, K. D.; Hood, Z. D.; Zhao, M.; Zhou, S.; Liu, J.; Xia, Y. A Rationally Designed Route to the One-Pot Synthesis of Right Bipyramidal Nanocrystals of Copper. *Chem. Mater.* **2018**, *30*, 6469−6477.

(321) McEachran, M.; Kitaev, V. Direct Structural Transformation of Silver Platelets into Right Bipyramids and Twinned Cube Nanoparticles: Morphology Governed by Defects. *Chem. Commun.* **2008**, 5737−5739.

(322) Zhang, J.; Li, S.; Wu, J.; Schatz, G. C.; Mirkin, C. A. Plasmon-Mediated Synthesis of Silver Triangular Bipyramids. *Angew. Chem., Int. Ed.* **2009**, *48*, 7787−7791.

(323) Kou, X.; Zhang, S.; Tsung, C.-K.; Yeung, M. H.; Shi, Q.; Stucky, G. D.; Sun, L.; Wang, J.; Yan, C. Growth of Gold Nanorods and Bipyramids Using CTEAB Surfactant. *J. Phys. Chem. B* **2006**, *110*, 16377−16383.

(324) Kou, X.; Ni, W.; Tsung, C.-K.; Chan, K.; Lin, H.-Q.; Stucky, G. D.; Wang, J. Growth of Gold Bipyramids with Improved Yield and Their Curvature-Directed Oxidation. *Small* **2007**, *3*, 2103−2113.

(325) Burgin, J.; Florea, I.; Majimel, J.; Dobri, A.; Ersen, O.; Tréguer-Delapierre, M. 3D Morphology of Au and Au@Ag Nanobipyramids. *Nanoscale* **2012**, *4*, 1299−1303.

(326) Huang, X.; Tang, S.; Zhang, H.; Zhou, Z.; Zheng, N. Controlled Formation of Concave Tetrahedral/Trigonal Bipyramidal Palladium Nanocrystals. *J. Am. Chem. Soc.* **2009**, *131*, 13916−13917.

(327) Jin, M.; Zhang, H.; Xie, Z.; Xia, Y. Palladium Concave Nanocubes with High-Index Facets and Their Enhanced Catalytic Properties. *Angew. Chem., Int. Ed.* **2011**, *50*, 7850−7854.

(328) Zhang, J.; Zhang, L.; Xie, S.; Kuang, Q.; Han, X.; Xie, Z.; Zheng, L. Synthesis of Concave Palladium Nanocubes with High-Index Surfaces and High Electrocatalytic Activities. *Chem. - Eur. J.* **2011**, *17*, 9915−9919.

(329) Bai, Y.; Long, R.; Wang, C.; Gong, M.; Li, Y.; Huang, H.; Xu, H.; Li, Z.; Deng, M.; Xiong, Y. Activation of Specific Sites on Cubic Nanocrystals: A New Pathway for Controlled Epitaxial Growth towards Catalytic Applications. *J. Mater. Chem. A* **2013**, *1*, 4228−4235.

(330) Vara, M.; Xia, Y. Facile Synthesis of Pd Concave Nanocubes: From Kinetics to Mechanistic Understanding and Rationally Designed Protocol. *Nano Res.* **2018**, *11*, 3122−3131.

(331) Ren, J.; Tilley, R. D. Shape-Controlled Growth of Platinum Nanoparticles. *Small* **2007**, *3*, 1508−1512.

(332) Zhang, Z.-c.; Hui, J.-f.; Liu, Z.-C.; Zhang, X.; Zhuang, J.; Wang, X. Glycine-Mediated Syntheses of Pt Concave Nanocubes with High-Index {*hk*0} Facets and Their Enhanced Electrocatalytic Activities. *Langmuir* **2012**, *28*, 14845−14848.

(333) Ma, Y.; Kuang, Q.; Jiang, Z.; Xie, Z.; Huang, R.; Zheng, L. Synthesis of Trisoctahedral Gold Nanocrystals with Exposed High-Index Facets by a Facile Chemical Method. *Angew. Chem., Int. Ed.* **2008**, *47*, 8901−8904.

(334) Zhang, J.; Langille, M. R.; Personick, M. L.; Zhang, K.; Li, S.; Mirkin, C. A. Concave Cubic Gold Nanocrystals with High-Index Facets. *J. Am. Chem. Soc.* **2010**, *132*, 14012−14014.

(335) Song, Y.; Miao, T.; Zhang, P.; Bi, C.; Xia, H.; Wang, D.; Tao, X. {331}-Faceted Trisoctahedral Gold Nanocrystals: Synthesis, Superior Electrocatalytic Performance and Highly Efficient SERS Activity. *Nanoscale* **2015**, *7*, 8405−8415.

(336) Huo, D.; Ding, H.; Zhou, S.; Li, J.; Tao, J.; Ma, Y.; Xia, Y. Facile Synthesis of Gold Trisoctahedral Nanocrystals with Controllable Sizes and Dihedral Angles. *Nanoscale* **2018**, *10*, 11034−11042.

(337) Hong, J. W.; Lee, S.-U.; Lee, Y. W.; Han, S. W. Hexoctahedral Au Nanocrystals with High-Index Facets and Their Optical and Surface-Enhanced Raman Scattering Properties. *J. Am. Chem. Soc.* **2012**, *134*, 4565−4568.

(338) Ma, L.; Wang, C.; Xia, B. Y.; Mao, K.; He, J.; Wu, X.; Xiong, Y.; Lou, X. W. Platinum Multicubes Prepared by Ni^{2+}-Mediated Shape Evolution Exhibit High Electrocatalytic Activity for Oxygen Reduction. *Angew. Chem., Int. Ed.* **2015**, *54*, 5666−5671.

(339) Xu, D.; Lv, H.; Jin, H.; Liu, Y.; Ma, Y.; Han, M.; Bao, J.; Liu, B. Crystalline Facet-Directed Generation Engineering of Ultrathin Platinum Nanodendrites. *J. Phys. Chem. Lett.* **2019**, *10*, 663−671.

(340) Lim, B.; Lu, X.; Jiang, M.; Camargo, P. H. C.; Cho, E. C.; Lee, E. P.; Xia, Y. Facile Synthesis of Highly Faceted Multioctahedral Pt Nanocrystals through Controlled Overgrowth. *Nano Lett.* **2008**, *8*, 4043−4047.

(341) Huo, D.; Cao, Z.; Li, J.; Xie, M.; Tao, J.; Xia, Y. Seed-Mediated Growth of Au Nanospheres into Hexagonal Stars and the Emergence of a Hexagonal Close-Packed Phase. *Nano Lett.* **2019**, *19*, 3115−3121.

(342) Tian, N.; Zhou, Z. Y.; Sun, S. G.; Ding, Y.; Wang, Z. L. Synthesis of Tetrahexahedral Platinum Nanocrystals with High-Index Facets and High Electro-Oxidation Activity. *Science* **2007**, *316*, 732−735.

(343) Li, J.; Wang, L.; Liu, L.; Guo, L.; Han, X.; Zhang, Z. Synthesis of Tetrahexahedral Au Nanocrystals with Exposed High-Index Surfaces. *Chem. Commun.* **2010**, *46*, 5109−5111.

(344) Zheng, Y.; Tao, J.; Liu, H.; Zeng, J.; Yu, T.; Ma, Y.; Moran, C.; Wu, L.; Zhu, Y.; Liu, J.; et al. Facile Synthesis of Gold Nanorice Enclosed by High-Index Facets and Its Application for CO Oxidation. *Small* **2011**, *7*, 2307−2312.

(345) Niu, W.; Duan, Y.; Qing, Z.; Huang, H.; Lu, X. Shaping Gold Nanocrystals in Dimethyl Sulfoxide: Toward Trapezohedral and Bipyramidal Nanocrystals Enclosed by {311} Facets. *J. Am. Chem. Soc.* **2017**, *139*, 5817−5826.

(346) Sun, Y.; Mayers, B.; Xia, Y. Transformation of Silver Nanospheres into Nanobelts and Triangular Nanoplates through a Thermal Process. *Nano Lett.* **2003**, *3*, 675−679.

(347) Bai, J.; Qin, Y.; Jiang, C.; Qi, L. Polymer-Controlled Synthesis of Silver Nanobelts and Hierarchical Nanocolumns. *Chem. Mater.* **2007**, *19*, 3367−3369.

(348) Zhang, J.; Du, J.; Han, B.; Liu, Z.; Jiang, T.; Zhang, Z. Sonochemical Formation of Single-Crystalline Gold Nanobelts. *Angew. Chem., Int. Ed.* **2006**, *45*, 1116−1119.

(349) Zhao, N.; Wei, Y.; Sun, N.; Chen, Q.; Bai, J.; Zhou, L.; Qin, Y.; Li, M.; Qi, L. Controlled Synthesis of Gold Nanobelts and Nanocombs in Aqueous Mixed Surfactant Solutions. *Langmuir* **2008**, *24*, 991−998.

(350) Anderson, L. J.; Payne, C. M.; Zhen, Y.-R.; Nordlander, P.; Hafner, J. H. A Tunable Plasmon Resonance in Gold Nanobelts. *Nano Lett.* **2011**, *11*, 5034−5037.

(351) Lu, T.; Wei, H.; Yang, X.; Li, J.; Wang, X.; Zhang, T. Microemulsion-Controlled Synthesis of One-Dimensional Ir Nanowires and Their Catalytic Activity in Selective Hydrogenation of *o*-Chloronitrobenzene. *Langmuir* **2015**, *31*, 90−95.

(352) Halder, A.; Ravishankar, N. Ultrafine Single-Crystalline Gold Nanowire Arrays by Oriented Attachment. *Adv. Mater.* **2007**, *19*, 1854−1858.

(353) Zhu, C.; Peng, H.-C.; Zeng, J.; Liu, J.; Gu, Z.; Xia, Y. Facile Synthesis of Gold Wavy Nanowires and Investigation of Their Growth Mechanism. *J. Am. Chem. Soc.* **2012**, *134*, 20234−20237.

(354) Zhao, M.; Figueroa-Cosme, L.; Elnabawy, A. O.; Vara, M.; Yang, X.; Roling, L. T.; Chi, M.; Mavrikakis, M.; Xia, Y. Synthesis and Characterization of Ru Cubic Nanocages with a Face-Centered Cubic Structure by Templating with Pd Nanocubes. *Nano Lett.* **2016**, *16*, 5310−5317.

(355) Zhao, M.; Elnabawy, A. O.; Vara, M.; Xu, L.; Hood, Z. D.; Yang, X.; Gilroy, K. D.; Figueroa-Cosme, L.; Chi, M.; Mavrikakis, M.; et al. Facile Synthesis of Ru-Based Octahedral Nanocages with Ultrathin Walls in a Face-Centered Cubic Structure. *Chem. Mater.* **2017**, *29*, 9227−9237.

(356) Zhao, M.; Xu, L.; Vara, M.; Elnabawy, A. O.; Gilroy, K. D.; Hood, Z. D.; Zhou, S.; Figueroa-Cosme, L.; Chi, M.; Mavrikakis, M.; et al. Synthesis of Ru Icosahedral Nanocages with a Face-Centered-Cubic Structure and Evaluation of Their Catalytic Properties. *ACS Catal.* **2018**, *8*, 6948−6960.

(357) Zhao, M.; Lyu, Z.; Xie, M.; Hood, Z. D.; Cao, Z.; Chi, M.; Xia, Y. Pd-Ru Alloy Nanocages with a Face-Centered Cubic Structure and Their Enhanced Activity toward the Oxidation of Ethylene Glycol and Glycerol. *Small Methods* **2020**, *4*, 1900843.

(358) Wang, S.-B.; Zhu, W.; Ke, J.; Lin, M.; Zhang, Y.-W. Pd−Rh Nanocrystals with Tunable Morphologies and Compositions as Efficient Catalysts toward Suzuki Cross-Coupling Reactions. *ACS Catal.* **2014**, *4*, 2298−2306.

(359) Ye, W.; Kou, S.; Guo, X.; Xie, F.; Sun, H.; Lu, H.; Yang, J. Controlled Synthesis of Bimetallic Pd−Rh Nanoframes and Nanoboxes with High Catalytic Performances. *Nanoscale* **2015**, *7*, 9558−9562.

(360) Xiong, Y.; Wiley, B.; Chen, J.; Li, Z.-Y.; Yin, Y.; Xia, Y. Corrosion-Based Synthesis of Single-Crystal Pd Nanoboxes and Nanocages and Their Surface Plasmon Properties. *Angew. Chem., Int. Ed.* **2005**, *44*, 7913−7917.

(361) Chen, J.; Wiley, B.; McLellan, J.; Xiong, Y.; Li, Z.-Y.; Xia, Y. Optical Properties of Pd−Ag and Pt−Ag Nanoboxes Synthesized via Galvanic Replacement Reactions. *Nano Lett.* **2005**, *5*, 2058−2062.

(362) Zhu, J.; Chen, Z.; Xie, M.; Lyu, Z.; Chi, M.; Mavrikakis, M.; Jin, W.; Xia, Y. Iridium-Based Cubic Nanocages with 1.1-nm-Thick Walls: A Highly Efficient and Durable Electrocatalyst for Water Oxidation in an Acidic Medium. *Angew. Chem., Int. Ed.* **2019**, *58*, 7244−7248.

(363) Zhang, L.; Roling, L. T.; Wang, X.; Vara, M.; Chi, M.; Liu, J.; Choi, S. I.; Park, J.; Herron, J. A.; Xie, Z.; et al. Platinum-Based Nanocages with Subnanometer-Thick Walls and Well-Defined, Controllable Facets. *Science* **2015**, *349*, 412−416.

(364) Wang, X.; Vara, M.; Luo, M.; Huang, H.; Ruditskiy, A.; Park, J.; Bao, S.; Liu, J.; Howe, J.; Chi, M.; et al. Pd@Pt Core-Shell Concave Decahedra: A Class of Catalysts for the Oxygen Reduction Reaction with Enhanced Activity and Durability. *J. Am. Chem. Soc.* **2015**, *137*, 15036−15042.

(365) Wang, X.; Figueroa-Cosme, L.; Yang, X.; Luo, M.; Liu, J.; Xie, Z.; Xia, Y. Pt-Based Icosahedral Nanocages: Using a Combination of {111} Facets, Twin Defects, and Ultrathin Walls to Greatly Enhance Their Activity toward Oxygen Reduction. *Nano Lett.* **2016**, *16*, 1467−1471.

(366) Lu, X.; Au, L.; McLellan, J.; Li, Z.-Y.; Marquez, M.; Xia, Y. Fabrication of Cubic Nanocages and Nanoframes by Dealloying Au/Ag Alloy Nanoboxes with an Aqueous Etchant Based on $Fe(NO_3)_3$ or NH_4OH. *Nano Lett.* **2007**, *7*, 1764−1769.

(367) Skrabalak, S. E.; Chen, J.; Au, L.; Lu, X.; Li, X.; Xia, Y. Gold Nanocages for Biomedical Applications. *Adv. Mater.* **2007**, *19*, 3177−3184.

(368) Skrabalak, S. E.; Chen, J.; Sun, Y.; Lu, X.; Au, L.; Cobley, C. M.; Xia, Y. Gold Nanocages: Synthesis, Properties, and Applications. *Acc. Chem. Res.* **2008**, *41*, 1587−1595.

(369) Cobley, C. M.; Xia, Y. Engineering the Properties of Metal Nanostructures via Galvanic Replacement Reactions. *Mater. Sci. Eng., R* **2010**, *70*, 44−62.

(370) Sun, X.; Kim, J.; Gilroy, K. D.; Liu, J.; König, T. A. F.; Qin, D. Gold-Based Cubic Nanoboxes with Well-Defined Openings at the Corners and Ultrathin Walls Less than Two Nanometers Thick. *ACS Nano* **2016**, *10*, 8019−8025.

(371) Xie, S.; Choi, S.-I.; Lu, N.; Roling, L. T.; Herron, J. A.; Zhang, L.; Park, J.; Wang, J.; Kim, M. J.; Xie, Z.; et al. Atomic Layer-by-Layer Deposition of Pt on Pd Nanocubes for Catalysts with Enhanced Activity and Durability toward Oxygen Reduction. *Nano Lett.* **2014**, *14*, 3570−3576.

(372) Jin, M.; Zhang, H.; Wang, J.; Zhong, X.; Lu, N.; Li, Z.; Xie, Z.; Kim, M. J.; Xia, Y. Copper Can Still Be Epitaxially Deposited on Palladium Nanocrystals to Generate Core−Shell Nanocubes Despite Their Large Lattice Mismatch. *ACS Nano* **2012**, *6*, 2566−2573.

(373) Xie, S.; Liu, X. Y.; Xia, Y. Shape-Controlled Syntheses of Rhodium Nanocrystals for the Enhancement of Their Catalytic Properties. *Nano Res.* **2015**, *8*, 82−96.

(374) Zhang, H.; Jin, M.; Liu, H.; Wang, J.; Kim, M. J.; Yang, D.; Xie, Z.; Liu, J.; Xia, Y. Facile Synthesis of Pd−Pt Alloy Nanocages and Their Enhanced Performance for Preferential Oxidation of CO in Excess Hydrogen. *ACS Nano* **2011**, *5*, 8212−8222.

(375) Zeng, J.; Zhu, C.; Tao, J.; Jin, M.; Zhang, H.; Li, Z. Y.; Zhu, Y.; Xia, Y. Controlling the Nucleation and Growth of Silver on Palladium Nanocubes by Manipulating the Reaction Kinetics. *Angew. Chem., Int. Ed.* **2012**, *51*, 2354−2358.

(376) Chen, J.; McLellan, J. M.; Siekkinen, A.; Xiong, Y.; Li, Z.-Y.; Xia, Y. Facile Synthesis of Gold−Silver Nanocages with Controllable Pores on the Surface. *J. Am. Chem. Soc.* **2006**, *128*, 14776−14777.

(377) Yavuz, M. S.; Cheng, Y.; Chen, J.; Cobley, C. M.; Zhang, Q.; Rycenga, M.; Xie, J.; Kim, C.; Song, K. H.; Schwartz, A. G.; et al. Gold Nanocages Covered by Smart Polymers for Controlled Release with Near-Infrared Light. *Nat. Mater.* **2009**, *8*, 935−939.

(378) Sun, X.; Yang, X.; Zhang, Y.; Ding, Y.; Su, D.; Qin, D. Pt−Ag Cubic Nanocages with Wall Thickness Less than 2 nm and Their Enhanced Catalytic Activity toward Oxygen Reduction. *Nanoscale* **2017**, *9*, 15107−15114.

(379) Ruditskiy, A.; Xia, Y. Toward the Synthesis of Sub-15 nm Ag Nanocubes with Sharp Corners and Edges: The Roles of Heterogeneous Nucleation and Surface Capping. *J. Am. Chem. Soc.* **2016**, *138*, 3161−3167.

(380) Chen, Z.; Balankura, T.; Fichthorn, K. A.; Rioux, R. M. Revisiting the Polyol Synthesis of Silver Nanostructures: Role of Chloride in Nanocube Formation. *ACS Nano* **2019**, *13*, 1849−1860.

(381) Eichler, A. CO Oxidation on Transition Metal Surfaces: Reaction Rates from First Principles. *Surf. Sci.* **2002**, *498*, 314−320.

(382) Wu, J.; Gross, A.; Yang, H. Shape and Composition-Controlled Platinum Alloy Nanocrystals Using Carbon Monoxide as Reducing Agent. *Nano Lett.* **2011**, *11*, 798−802.

(383) Xi, Z.; Cheng, X.; Gao, Z.; Wang, M.; Cai, T.; Muzzio, M.; Davidson, E.; Chen, O.; Jung, Y.; Sun, S.; et al. Strain Effect in Palladium Nanostructures as Nanozymes. *Nano Lett.* **2020**, *20*, 272−277.

(384) Li, L.; Zhang, N.; He, H.; Zhang, G.; Song, L.; Qiu, W. Shape-Controlled Synthesis of Pd Nanocrystals with Exposed {110} Facets and Their Catalytic Applications. *Catal. Today* **2019**, *327*, 28−36.

(385) Xiong, Y.; Xia, Y. Shape-Controlled Synthesis of Metal Nanostructures: The Case of Palladium. *Adv. Mater.* **2007**, *19*, 3385−3391.

(386) Wu, J.; Qi, L.; You, H.; Gross, A.; Li, J.; Yang, H. Icosahedral Platinum Alloy Nanocrystals with Enhanced Electrocatalytic Activities. *J. Am. Chem. Soc.* **2012**, *134*, 11880−11883.

(387) Xie, S.; Xu, Q.; Huang, X. Defect-Rich Metal Nanocrystals in Catalysis. *ChemCatChem* **2016**, *8*, 480−485.

(388) Choi, S.-I.; Herron, J. A.; Scaranto, J.; Huang, H.; Wang, Y.; Xia, X.; Lv, T.; Park, J.; Peng, H.-C.; Mavrikakis, M.; et al. A Comprehensive Study of Formic Acid Oxidation on Palladium Nanocrystals with Different Types of Facets and Twin Defects. *ChemCatChem* **2015**, *7*, 2077−2084.

(389) Luo, M.; Ruditskiy, A.; Peng, H.-C.; Tao, J.; Figueroa-Cosme, L.; He, Z.; Xia, Y. Penta-Twinned Copper Nanorods: Facile Synthesis via Seed-Mediated Growth and Their Tunable Plasmonic Properties. *Adv. Funct. Mater.* **2016**, *26*, 1209−1216.

(390) Zhang, H.; Xia, X.; Li, W.; Zeng, J.; Dai, Y.; Yang, D.; Xia, Y. Facile Synthesis of Five-Fold Twinned, Starfish-Like Rhodium Nanocrystals by Eliminating Oxidative Etching with a Chloride-Free Precursor. *Angew. Chem., Int. Ed.* **2010**, *49*, 5296−5300.

(391) Zhang, Q.; Xie, J.; Yang, J.; Lee, J. Y. Monodisperse Icosahedral Ag, Au, and Pd Nanoparticles: Size Control Strategy and Superlattice Formation. *ACS Nano* **2009**, *3*, 139−148.

(392) Pastoriza-Santos, I.; Liz-Marzán, L. M. Formation and Stabilization of Silver Nanoparticles through Reduction by *N,N*-Dimethylformamide. *Langmuir* **1999**, *15*, 948−951.

(393) Pastoriza-Santos, I.; Liz-Marzán, L. M. Synthesis of Silver Nanoprisms in DMF. *Nano Lett.* **2002**, *2*, 903−905.

(394) Giersig, M.; Pastoriza-Santos, I.; Liz-Marzán, L. M. Evidence of an Aggregative Mechanism during the Formation of Silver Nanowires in *N,N*-Dimethylformamide. *J. Mater. Chem.* **2004**, *14*, 607−610.

(395) Yavuz, M. S.; Li, W.; Xia, Y. Facile Synthesis of Gold Icosahedra in an Aqueous Solution by Reacting $HAuCl_4$ with *N*-Vinyl Pyrrolidone. *Chem. - Eur. J.* **2009**, *15*, 13181−13187.

(396) Du, J.; Chen, Z.; Ye, S.; Wiley, B. J.; Meyer, T. J. Copper as a Robust and Transparent Electrocatalyst for Water Oxidation. *Angew. Chem., Int. Ed.* **2015**, *54*, 2073−2078.

(397) Lee, J.; Lee, P.; Lee, H.; Lee, D.; Lee, S. S.; Ko, S. H. Very Long Ag Nanowire Synthesis and Its Application in a Highly Transparent, Conductive and Flexible Metal Electrode Touch Panel. *Nanoscale* **2012**, *4*, 6408−6414.

(398) Nikoobakht, B.; El-Sayed, M. A. Preparation and Growth Mechanism of Gold Nanorods (NRs) Using Seed-Mediated Growth Method. *Chem. Mater.* **2003**, *15*, 1957−1962.

(399) Cherns, D. Direct Resolution of Surface Atomic Steps by Transmission Electron Microscopy. *Philos. Mag.* **1974**, *30*, 549−556.

(400) Shi, Y.; Lyu, Z.; Liu, J.; Chase, E.; Xia, Y. Facile Synthesis of Pd−Cu Bimetallic Twin Nanocubes and a Mechanistic Understanding of the Shape Evolution. *ChemNanoMat* **2020**, *6*, 386−391.

(401) Berriman, R. W.; Herz, R. H. Twinning and the Tabular Growth of Silver Bromide Crystals. *Nature* **1957**, *180*, 293−294.

(402) Qiao, X.; Chen, X.; Huang, C.; Li, A.; Li, X.; Lu, Z.; Wang, T. Detection of Exhaled Volatile Organic Compounds Improved by Hollow Nanocages of Layered Double Hydroxide on Ag Nanowires. *Angew. Chem., Int. Ed.* **2019**, *58*, 16523−16527.

(403) Thoka, S.; Madasu, M.; Hsia, C.-F.; Liu, S.-Y.; Huang, M. H. Aqueous-Phase Synthesis of Size-Tunable Copper Nanocubes for Efficient Aryl Alkyne Hydroboration. *Chem. - Asian J.* **2017**, *12*, 2318−2322.

(404) Lyu, Z.; Xie, M.; Aldama, E.; Zhao, M.; Qiu, J.; Zhou, S.; Xia, Y. Au@Cu Core−Shell Nanocubes with Controllable Sizes in the Range of 20−30 nm for Applications in Catalysis and Plasmonics. *ACS Appl. Nano Mater.* **2019**, *2*, 1533−1540.

(405) Yoo, H.; Jang, M. H. Size-Controlled Synthesis of Gold Bipyramids Using an Aqueous Mixture of CTAC and Salicylate Anions as the Soft Template. *Nanoscale* **2013**, *5*, 6708−6712.

(406) Yu, Y.; Zhang, Q.; Liu, B.; Lee, J. Y. Synthesis of Nanocrystals with Variable High-Index Pd Facets through the Controlled Heteroepitaxial Growth of Trisoctahedral Au Templates. *J. Am. Chem. Soc.* **2010**, *132*, 18258−18265.

(407) Yu, N.-F.; Tian, N.; Zhou, Z.-Y.; Huang, L.; Xiao, J.; Wen, Y.-H.; Sun, S.-G. Electrochemical Synthesis of Tetrahexahedral Rhodium Nanocrystals with Extraordinarily High Surface Energy and High Electrocatalytic Activity. *Angew. Chem., Int. Ed.* **2014**, *53*, 5097−5101.

(408) Liu, R.; Sen, A. Unified Synthetic Approach to Silver Nanostructures by Galvanic Displacement Reaction on Copper: From Nanobelts to Nanoshells. *Chem. Mater.* **2012**, *24*, 48−54.

(409) Xia, X.; Figueroa-Cosme, L.; Tao, J.; Peng, H.-C.; Niu, G.; Zhu, Y.; Xia, Y. Facile Synthesis of Iridium Nanocrystals with Well-Controlled Facets Using Seed-Mediated Growth. *J. Am. Chem. Soc.* **2014**, *136*, 10878−10881.

(410) Pong, B.-K.; Lee, J.-Y.; Trout, B. L. First Principles Computational Study for Understanding the Interactions between ssDNA and Gold Nanoparticles: Adsorption of Methylamine on Gold Nanoparticulate Surfaces. *Langmuir* **2005**, *21*, 11599−11603.

(411) Strasser, P.; Koh, S.; Anniyev, T.; Greeley, J.; More, K.; Yu, C.; Liu, Z.; Kaya, S.; Nordlund, D.; Ogasawara, H.; et al. Lattice-Strain Control of the Activity in Dealloyed Core−Shell Fuel Cell Catalysts. *Nat. Chem.* **2010**, *2*, 454−460.

(412) Sneed, B. T.; Young, A. P.; Tsung, C.-K. Building Up Strain in Colloidal Metal Nanoparticle Catalysts. *Nanoscale* **2015**, *7*, 12248−12265.

(413) Xia, X.; Wang, Y.; Ruditskiy, A.; Xia, Y. 25th Anniversary Article: Galvanic Replacement: A Simple and Versatile Route to Hollow Nanostructures with Tunable and Well-Controlled Properties. *Adv. Mater.* **2013**, *25*, 6313−6333.

(414) Zhao, M.; Wang, X.; Yang, X.; Gilroy, K. D.; Qin, D.; Xia, Y. Hollow Metal Nanocrystals with Ultrathin, Porous Walls and Well-Controlled Surface Structures. *Adv. Mater.* **2018**, *30*, 1801956.

(415) Francis, M.; Curtin, W. Mechanical Work Makes Important Contributions to Surface Chemistry at Steps. *Nat. Commun.* **2015**, *6*, 6261.

(416) Wang, X.; Choi, S.-I.; Roling, L. T.; Luo, M.; Ma, C.; Zhang, L.; Chi, M.; Liu, J.; Xie, Z.; Herron, J. A.; et al. Palladium−Platinum Core-Shell Icosahedra with Substantially Enhanced Activity and Durability towards Oxygen Reduction. *Nat. Commun.* **2015**, *6*, 7594.

(417) Han, Y.; Yan, Y.; Wu, Z.; Jiang, Y.; Li, X.; Xu, Q.; Yang, X.; Zhang, H.; Yang, D. Facile Synthesis of Pd@Ru Nanoplates with Controlled Thickness as Efficient Catalysts for Hydrogen Evolution Reaction. *CrystEngComm* **2018**, *20*, 4230−4236.

(418) Bard, A. J.; Parsons, R.; Jordan, J. *Standard Potentials in Aqueous Solution*; CRC Press: Boca Raton, FL, 1985.

(419) Choi, S.-I.; Young, A.; Lee, S. R.; Ma, C.; Luo, M.; Chi, M.; Tsung, C.-K.; Xia, Y. Pd@Rh Core−Shell Nanocrystals with Well-Defined Facets and Their Enhanced Catalytic Performance towards CO Oxidation. *Nanoscale Horiz.* **2019**, *4*, 1232−1238.

(420) Haynes, W. M. *CRC Handbook of Chemistry and Physics*; CRC Press: Boca Raton, FL, 2016.

(421) Zhang, T.; Li, S.-C.; Zhu, W.; Ke, J.; Yu, J.-W.; Zhang, Z.-P.; Dai, L.-X.; Gu, J.; Zhang, Y.-W. Iridium Ultrasmall Nanoparticles, Worm-Like Chain Nanowires, and Porous Nanodendrites: One-Pot Solvothermal Synthesis and Ctalytic CO Oxidation Activity. *Surf. Sci.* **2016**, *648*, 319−327.

(422) Xia, X.; Zhang, J.; Lu, N.; Kim, M. J.; Ghale, K.; Xu, Y.; McKenzie, E.; Liu, J.; Ye, H. Pd−Ir Core−Shell Nanocubes: A Type of Highly Efficient and Versatile Peroxidase Mimic. *ACS Nano* **2015**, *9*, 9994−10004.

(423) Wang, X.; Luo, M.; Huang, H.; Chi, M.; Howe, J.; Xie, Z.; Xia, Y. Facile Synthesis of Pt−Pd Alloy Nanocages and Pt Nanorings by Templating with Pd Nanoplates. *ChemNanoMat* **2016**, *2*, 1086−1091.

(424) Park, J.; Zhang, L.; Choi, S. I.; Roling, L. T.; Lu, N.; Herron, J. A.; Xie, S.; Wang, J.; Kim, M. J.; Mavrikakis, M.; et al. Atomic Layer-by-Layer Deposition of Platinum on Palladium Octahedra for Enhanced Catalysts toward the Oxygen Reduction Reaction. *ACS Nano* **2015**, *9*, 2635−2647.

(425) Lim, B.; Wang, J.; Camargo, P. H. C.; Jiang, M.; Kim, M. J.; Xia, Y. Facile Synthesis of Bimetallic Nanoplates Consisting of Pd Cores and Pt Shells through Seeded Epitaxial Growth. *Nano Lett.* **2008**, *8*, 2535−2540.

(426) Yang, X.; Roling, L. T.; Vara, M.; Elnabawy, A. O.; Zhao, M.; Hood, Z. D.; Bao, S.; Mavrikakis, M.; Xia, Y. Synthesis and Characterization of Pt−Ag Alloy Nanocages with Enhanced Activity and Durability toward Oxygen Reduction. *Nano Lett.* **2016**, *16*, 6644−6649.

(427) Chen, Z.; Waje, M.; Li, W.; Yan, Y. Supportless Pt and PtPd Nanotubes as Electrocatalysts for Oxygen-Reduction Reactions. *Angew. Chem., Int. Ed.* **2007**, *46*, 4060−4063.

(428) Mayers, B.; Jiang, X.; Sunderland, D.; Cattle, B.; Xia, Y. Hollow Nanostructures of Platinum with Controllable Dimensions Can be Synthesized by Templating Against Selenium Nanowires and Colloids. *J. Am. Chem. Soc.* **2003**, *125*, 13364−13365.

(429) Ahn, J.; Kim, J.; Qin, D. Orthogonal Deposition of Au on Different Facets of Ag Cuboctahedra for the Fabrication of Nanoboxes with Complementary Surfaces. *Nanoscale* **2020**, *12*, 372−379.

(430) Yang, X.; Yang, M.; Pang, B.; Vara, M.; Xia, Y. Gold Nanomaterials at Work in Biomedicine. *Chem. Rev.* **2015**, *115*, 10410−10488.

(431) Chen, J.; Yang, M.; Zhang, Q.; Cho, E. C.; Cobley, C. M.; Kim, C.; Glaus, C.; Wang, L. V.; Welch, M. J.; Xia, Y. Gold Nanocages: A Novel Class of Multifunctional Nanomaterials for Theranostic Applications. *Adv. Funct. Mater.* **2010**, *20*, 3684−3694.

(432) Karelovic, A.; Galdames, G.; Medina, J. C.; Yévenes, C.; Barra, Y.; Jiménez, R. Mechanism and Structure Sensitivity of Methanol Synthesis from CO_2 over SiO_2-Supported Cu Nanoparticles. *J. Catal.* **2019**, *369*, 415−426.

(433) Chinchen, G. C.; Spencer, M. S.; Waugh, K. C.; Whan, D. A. Promotion of Methanol Synthesis and the Water-Gas Shift Reactions by Adsorbed Oxygen on Supported Copper Catalysts. *J. Chem. Soc., Faraday Trans. 1* **1987**, *83*, 2193−2212.

(434) Gokhale, A. A.; Dumesic, J. A.; Mavrikakis, M. On the Mechanism of Low-Temperature Water Gas Shift Reaction on Copper. *J. Am. Chem. Soc.* **2008**, *130*, 1402−1414.

(435) Zhang, Z.; Wang, S.-S.; Song, R.; Cao, T.; Luo, L.; Chen, X.; Gao, Y.; Lu, J.; Li, W.-X.; Huang, W. The Most Active Cu Facet for Low-Temperature Water Gas Shift Reaction. *Nat. Commun.* **2017**, *8*, 488.

(436) Wang, Q.; Feng, J.; Zheng, L.; Wang, B.; Bi, R.; He, Y.; Liu, H.; Li, D. Interfacial Structure-Determined Reaction Pathway and Selectivity for 5-(Hydroxymethyl)furfural Hydrogenation over Cu-Based Catalysts. *ACS Catal.* **2020**, *10*, 1353−1365.

(437) Kajaste, R.; Hurme, M.; Oinas, P. Methanol-Managing Greenhouse Gas Emissions in the Production Chain by Optimizing the Resource Base. *AIMS Energy* **2018**, *6*, 1074−1102.

(438) Yant, W. P.; Schrenk, H. H.; Sayers, R. R. Methanol Antifreeze and Methanol Poisoning. *Ind. Eng. Chem.* **1931**, *23*, 551−555.

(439) Sunley, G. J.; Watson, D. J. High Productivity Methanol Carbonylation Catalysis Using Iridium: The Cativa Process for the Manufacture of Acetic Acid. *Catal. Today* **2000**, *58*, 293−307.

(440) Olsbye, U.; Svelle, S.; Bjørgen, M.; Beato, P.; Janssens, T. V. W.; Joensen, F.; Bordiga, S.; Lillerud, K. P. Conversion of Methanol to Hydrocarbons: How Zeolite Cavity and Pore Size Controls Product Selectivity. *Angew. Chem., Int. Ed.* **2012**, *51*, 5810−5831.

(441) Tian, P.; Wei, Y.; Ye, M.; Liu, Z. Methanol to Olefins (MTO): From Fundamentals to Commercialization. *ACS Catal.* **2015**, *5*, 1922−1938.

(442) Fu, Q.; Weber, A.; Flytzani-Stephanopoulos, M. Nanostructured Au−CeO_2 Catalysts for Low-Temperature Water−Gas Shift. *Catal. Lett.* **2001**, *77*, 87−95.

(443) Mendes, D.; Mendes, A.; Madeira, L. M.; Iulianelli, A.; Sousa, J. M.; Basile, A. The Water-Gas Shift Reaction: From Conventional Catalytic Systems to Pd-Based Membrane Reactors—A Review. *Asia-Pac. J. Chem. Eng.* **2010**, *5*, 111−137.

(444) Axet, M. R.; Philippot, K. Catalysis with Colloidal Ruthenium Nanoparticles. *Chem. Rev.* **2020**, *120*, 1085−1145.

(445) Zhao, M.; Xia, Y. Crystal-Phase and Surface-Structure Engineering of Ruthenium Nanocrystals. *Nat. Rev. Mater.* **2020**, *5*, 440−459.

(446) Li, W.-Z.; Liu, J.-X.; Gu, J.; Zhou, W.; Yao, S.-Y.; Si, R.; Guo, Y.; Su, H.-Y.; Yan, C.-H.; Li, W.-X.; et al. Chemical Insights into the Design and Development of Face-Centered Cubic Ruthenium Catalysts for Fischer−Tropsch Synthesis. *J. Am. Chem. Soc.* **2017**, *139*, 2267−2276.

(447) Liu, J.-X.; Wang, P.; Xu, W.; Hensen, E. J. M. Particle Size and Crystal Phase Effects in Fischer−Tropsch Catalysts. *Engineering* **2017**, *3*, 467−476.

(448) Saadatjou, N.; Jafari, A.; Sahebdelfar, S. Ruthenium Nanocatalysts for Ammonia Synthesis: A Review. *Chem. Eng. Commun.* **2015**, *202*, 420−448.

(449) Kusada, K.; Kobayashi, H.; Yamamoto, T.; Matsumura, S.; Sumi, N.; Sato, K.; Nagaoka, K.; Kubota, Y.; Kitagawa, H. Discovery of Face-Centered-Cubic Ruthenium Nanoparticles: Facile Size-Controlled Synthesis Using the Chemical Reduction Method. *J. Am. Chem. Soc.* **2013**, *135*, 5493−5496.

(450) Chen, G.; Zhang, J.; Gupta, A.; Rosei, F.; Ma, D. Shape-controlled synthesis of Ruthenium Nanocrystals and Their Catalytic Applications. *New J. Chem.* **2014**, *38*, 1827−1833.

(451) Schulz, H. Short History and Present Trends of Fischer−Tropsch synthesis. *Appl. Catal., A* **1999**, *186*, 3−12.

(452) Chen, J.; Liu, Z.-P. Origin of Selectivity Switch in Fischer−Tropsch Synthesis over Ru and Rh from First-Principles Statistical Mechanics Studies. *J. Am. Chem. Soc.* **2008**, *130*, 7929−7937.

(453) Joo, S. H.; Park, J. Y.; Renzas, J. R.; Butcher, D. R.; Huang, W.; Somorjai, G. A. Size Effect of Ruthenium Nanoparticles in Catalytic Carbon Monoxide Oxidation. *Nano Lett.* **2010**, *10*, 2709−2713.

(454) Rodriguez, J.; Wayne Goodman, D. High-Pressure Catalytic Reactions over Single-Crystal Metal Surfaces. *Surf. Sci. Rep.* **1991**, *14*, 1−107.

(455) Goodman, D. W. Model Studies in Catalysis Using Surface Science Probes. *Chem. Rev.* **1995**, *95*, 523−536.

(456) Guerrero, M.; T Than Chau, N.; Noël, S.; Denicourt-Nowicki, A.; Hapiot, F.; Roucoux, A.; Monflier, E.; Philippot, K. About the Use of Rhodium Nanoparticles in Hydrogenation and Hydroformylation Reactions. *Curr. Org. Chem.* **2013**, *17*, 364−399.

(457) Favier, I.; Pla, D.; Gomez, M. Palladium Nanoparticles in Polyols: Synthesis, Catalytic Couplings, and Hydrogenations. *Chem. Rev.* **2020**, *120*, 1146−1183.

(458) Kielhorn, J.; Melber, C.; Keller, D.; Mangelsdorf, I. Palladium − A Review of Exposure and Effects to Human Health. *Int. J. Hyg. Environ. Health* **2002**, *205*, 417−432.

(459) Crespo-Quesada, M.; Yarulin, A.; Jin, M.; Xia, Y.; Kiwi-Minsker, L. Structure Sensitivity of Alkynol Hydrogenation on Shape- and Size-Controlled Palladium Nanocrystals: Which Sites Are Most Active and Selective? *J. Am. Chem. Soc.* **2011**, *133*, 12787−12794.

(460) He, Y.-F.; Feng, J.-T.; Du, Y.-Y.; Li, D.-Q. Controllable Synthesis and Acetylene Hydrogenation Performance of Supported Pd Nanowire and Cuboctahedron Catalysts. *ACS Catal.* **2012**, *2*, 1703−1710.

(461) Crespo-Quesada, M.; Yoon, S.; Jin, M.; Prestianni, A.; Cortese, R.; Cárdenas-Lizana, F.; Duca, D.; Weidenkaff, A.; Kiwi-Minsker, L. Shape-Dependence of Pd Nanocrystal Carburization during Acetylene Hydrogenation. *J. Phys. Chem. C* **2015**, *119*, 1101−1107.

(462) Collins, G.; Schmidt, M.; O'Dwyer, C.; Holmes, J. D.; McGlacken, G. P. The Origin of Shape Sensitivity in Palladium-Catalyzed Suzuki−Miyaura Cross Coupling Reactions. *Angew. Chem., Int. Ed.* **2014**, *53*, 4142−4145.

(463) Long, R.; Mao, K.; Ye, X.; Yan, W.; Huang, Y.; Wang, J.; Fu, Y.; Wang, X.; Wu, X.; Xie, Y.; et al. Surface Facet of Palladium Nanocrystals: A Key Parameter to the Activation of Molecular Oxygen for Organic Catalysis and Cancer Treatment. *J. Am. Chem. Soc.* **2013**, *135*, 3200−3207.

(464) Claus, P.; Hofmeister, H. Electron Microscopy and Catalytic Study of Silver Catalysts: Structure Sensitivity of the Hydrogenation of Crotonaldehyde. *J. Phys. Chem. B* **1999**, *103*, 2766−2775.

(465) Lim, K. H.; Mohammad, A. B.; Yudanov, I. V.; Neyman, K. M.; Bron, M.; Claus, P.; Rösch, N. Mechanism of Selective Hydrogenation of α,β-Unsaturated Aldehydes on Silver Catalysts: A Density Functional Study. *J. Phys. Chem. C* **2009**, *113*, 13231−13240.

(466) Dai, W.-L.; Cao, Y.; Ren, L.-P.; Yang, X.-L.; Xu, J.-H.; Li, H.-X.; He, H.-Y.; Fan, K.-N. Ag−SiO_2−Al_2O_3 Composite as Highly Active Catalyst for the Formation of Formaldehyde from the Partial Oxidation of Methanol. *J. Catal.* **2004**, *228*, 80−91.

(467) Bao, X.; Muhler, M.; Schlögl, R.; Ertl, G. Oxidative Coupling of Methane on Silver Catalysts. *Catal. Lett.* **1995**, *32*, 185−194.

(468) Özbek, M. O.; van Santen, R. A. The Mechanism of Ethylene Epoxidation Catalysis. *Catal. Lett.* **2013**, *143*, 131−141.

(469) Van Santen, R. A.; Kuipers, H. P. C. E. The Mechanism of Ethylene Epoxidation. *Adv. Catal.* **1987**, *35*, 265−321.

(470) Hess, C.; Lercher, J.; Naraschewski, F.; Kondratenko, E.; Baerns, M.; Trunschke, A.; Grasselli, R.; Carreon, M.; Guliants, V.; Schunk, S. *Nanostructured Catalysts: Selective Oxidations*; Royal Society of Chemistry: London, 2011.

(471) Lee, J. K.; Verykios, X. E.; Pitchai, R. Support and Crystallite Size Effects in Ethylene Oxidation Catalysis. *Appl. Catal.* **1989**, *50*, 171−188.

(472) Christopher, P.; Linic, S. Engineering Selectivity in Heterogeneous Catalysis: Ag Nanowires as Selective Ethylene Epoxidation Catalysts. *J. Am. Chem. Soc.* **2008**, *130*, 11264−11265.

(473) Claus, P.; Kraak, P.; Schödel, R. Selective Hydrogenation of α,β-Unsaturated Aldehydes to Allylic Alcohols over Supported Monometallic and Bimetallic Ag Catalysts. *Stud. Surf. Sci. Catal.* **1997**, *108*, 281−288.

(474) Bron, M.; Teschner, D.; Wild, U.; Steinhauer, B.; Knop-Gericke, A.; Volckmar, C.; Wootsch, A.; Schlögl, R.; Claus, P. Oxygen-Induced Activation of Silica Supported Silver in Acrolein Hydrogenation. *Appl. Catal., A* **2008**, *341*, 127−132.

(475) Dupont, J.; Fonseca, G. S.; Umpierre, A. P.; Fichtner, P. F. P.; Teixeira, S. R. Transition-Metal Nanoparticles in Imidazolium Ionic Liquids: Recycable Catalysts for Biphasic Hydrogenation Reactions. *J. Am. Chem. Soc.* **2002**, *124*, 4228−4229.

(476) Mévellec, V.; Roucoux, A.; Ramirez, E.; Philippot, K.; Chaudret, B. Surfactant-Stabilized Aqueous Iridium(0) Colloidal Suspension: An Efficient Reusable Catalyst for Hydrogenation of Arenes in Biphasic Media. *Adv. Synth. Catal.* **2004**, *346*, 72−76.

(477) Stowell, C. A.; Korgel, B. A. Iridium Nanocrystal Synthesis and Surface Coating-Dependent Catalytic Activity. *Nano Lett.* **2005**, *5*, 1203−1207.

(478) Cano, I.; Tschan, M. J. L.; Martínez-Prieto, L. M.; Philippot, K.; Chaudret, B.; van Leeuwen, P. W. N. M. Enantioselective Hydrogenation of Ketones by Iridium Nanoparticles Ligated with Chiral Secondary Phosphine Oxides. *Catal. Sci. Technol.* **2016**, *6*, 3758−3766.

(479) Krebs, R. E.; Dejur, R. *The History and Use of Our Earth's Chemical Elements: A Reference Guide*; Greenwood Press, 2006.

(480) Lee, I.; Zaera, F. Nanoparticle Shape Selectivity in Catalysis: Butene Isomerization and Hydrogenation on Platinum. *Top. Catal.* **2013**, *56*, 1284−1298.

(481) Zaera, F.; Somorjai, G. A. Hydrogenation of Ethylene over Platinum (111) single-crystal Surfaces. *J. Am. Chem. Soc.* **1984**, *106*, 2288−2293.

(482) Beccat, P.; Bertolini, J. C.; Gauthier, Y.; Massardier, J.; Ruiz, P. Crotonaldehyde and Methylcrotonaldehyde Hydrogenation over Pt(111) and $Pt_{80}Fe_{20}(111)$ Single Crystals. *J. Catal.* **1990**, *126*, 451−456.

(483) Weiss, P. S.; Eigler, D. M. Site Dependence of the Apparent Shape of a Molecule in Scanning Tunneling Micoscope Images: Benzene on Pt{111}. *Phys. Rev. Lett.* **1993**, *71*, 3139−3142.

(484) Bratlie, K. M.; Montano, M. O.; Flores, L. D.; Paajanen, M.; Somorjai, G. A. Sum Frequency Generation Vibrational Spectroscopic and High-Pressure Scanning Tunneling Microscopic Studies of Benzene Hydrogenation on Pt(111). *J. Am. Chem. Soc.* **2006**, *128*, 12810−12816.

(485) Bratlie, K. M.; Flores, L. D.; Somorjai, G. A. In Situ Sum Frequency Generation Vibrational Spectroscopy Observation of a Reactive Surface Intermediate during High-Pressure Benzene Hydrogenation. *J. Phys. Chem. B* **2006**, *110*, 10051−10057.

(486) Bratlie, K. M.; Kliewer, C. J.; Somorjai, G. A. Structure Effects of Benzene Hydrogenation Studied with Sum Frequency Generation Vibrational Spectroscopy and Kinetics on Pt(111) and Pt(100) Single-Crystal Surfaces. *J. Phys. Chem. B* **2006**, *110*, 17925−17930.

(487) Tsung, C.-K.; Kuhn, J. N.; Huang, W.; Aliaga, C.; Hung, L.-I.; Somorjai, G. A.; Yang, P. Sub-10 nm Platinum Nanocrystals with Size and Shape Control: Catalytic Study for Ethylene and Pyrrole Hydrogenation. *J. Am. Chem. Soc.* **2009**, *131*, 5816−5822.

(488) Lee, I.; Delbecq, F.; Morales, R.; Albiter, M. A.; Zaera, F. Tuning Selectivity in Catalysis by Controlling Particle Shape. *Nat. Mater.* **2009**, *8*, 132−138.

(489) Thomas, J. M.; Evans, E. L.; Williams, J. O.; Linnett, J. W. Microscopic Studies of Enhanced Reactivity at Structural Faults in Solids. *Proc. R. Soc. A* **1972**, *331*, 417−427.

(490) Haruta, M.; Yamada, N.; Kobayashi, T.; Iijima, S. Gold Catalysts Prepared by Coprecipitation for Low-Temperature Oxidation of Hydrogen and of Carbon Monoxide. *J. Catal.* **1989**, *115*, 301−309.

(491) Qian, K.; Luo, L.; Bao, H.; Hua, Q.; Jiang, Z.; Huang, W. Catalytically Active Structures of SiO_2-Supported Au Nanoparticles in Low-Temperature CO Oxidation. *Catal. Sci. Technol.* **2013**, *3*, 679−687.

(492) Si, R.; Flytzani-Stephanopoulos, M. Shape and Crystal-Plane Effects of Nanoscale Ceria on the Activity of Au-CeO_2 Catalysts for the Water-Gas Shift Reaction. *Angew. Chem., Int. Ed.* **2008**, *47*, 2884−2887.

(493) Wang, W.; Gu, J.; Hua, W.; Jia, X.; Xi, K. A Novel High Efficiency Composite Catalyst: Single Crystal Triangular Au Nanoplates Supported by Functional Reduced Graphene Oxide. *Chem. Commun.* **2014**, *50*, 8889−8891.

(494) Zhang, Q.; Wang, H. Facet-Dependent Catalytic Activities of Au Nanoparticles Enclosed by High-Index Facets. *ACS Catal.* **2014**, *4*, 4027−4033.

(495) Baldyga, L. M.; Blavo, S. O.; Kuo, C.-H.; Tsung, C.-K.; Kuhn, J. N. Size-Dependent Sulfur Poisoning of Silica-Supported Monodisperse Pt Nanoparticle Hydrogenation Catalysts. *ACS Catal.* **2012**, *2*, 2626−2629.

(496) Seh, Z. W.; Kibsgaard, J.; Dickens, C. F.; Chorkendorff, I.; Norskov, J. K.; Jaramillo, T. F. Combining Theory and Experiment in Electrocatalysis: Insights into Materials Design. *Science* **2017**, *355*, eaad4998.

(497) Cheng, F.; Chen, J. Metal−Air Batteries: From Oxygen Reduction Electrochemistry to Cathode Catalysts. *Chem. Soc. Rev.* **2012**, *41*, 2172−2192.

(498) Wu, B.; Zheng, N. Surface and Interface Control of Noble Metal Nanocrystals for Catalytic and Electrocatalytic Applications. *Nano Today* **2013**, *8*, 168−197.

(499) Shao, M.; Chang, Q.; Dodelet, J.-P.; Chenitz, R. Recent Advances in Electrocatalysts for Oxygen Reduction Reaction. *Chem. Rev.* **2016**, *116*, 3594−3657.

(500) Borup, R.; Meyers, J.; Pivovar, B.; Kim, Y. S.; Mukundan, R.; Garland, N.; Myers, D.; Wilson, M.; Garzon, F.; Wood, D.; Zelenay, P.; More, K.; Stroh, K.; Zawodzinski, T.; Boncella, J.; McGrath, J. E.; Inaba, M.; Miyatake, K.; Hori, M.; Ota, K.; Ogumi, Z.; Miyata, S.; Nishikata, A.; Siroma, Z.; Uchimoto, Y.; Yasuda, K.; Kimijima, K.-i.; Iwashita, N. Scientific Aspects of Polymer Electrolyte Fuel Cell Durability and Degradation. *Chem. Rev.* **2007**, *107*, 3904−3951.

(501) Peighambardoust, S. J.; Rowshanzamir, S.; Amjadi, M. Review of the Proton Exchange Membranes for Fuel Cell Applications. *Int. J. Hydrogen Energy* **2010**, *35*, 9349−9384.

(502) Nørskov, J. K.; Rossmeisl, J.; Logadottir, A.; Lindqvist, L.; Kitchin, J. R.; Bligaard, T.; Jónsson, H. Origin of the Overpotential for Oxygen Reduction at a Fuel-Cell Cathode. *J. Phys. Chem. B* **2004**, *108*, 17886−17892.

(503) Stamenkovic, V. R.; Fowler, B.; Mun, B. S.; Wang, G.; Ross, P. N.; Lucas, C. A.; Markovic, N. M. Improved Oxygen Reduction Activity on $Pt_3Ni(111)$ via Increased Surface Site Availability. *Science* **2007**, *315*, 493−497.

(504) Dong, J.-C.; Zhang, X.-G.; Briega-Martos, V.; Jin, X.; Yang, J.; Chen, S.; Yang, Z.-L.; Wu, D.-Y.; Feliu, J. M.; Williams, C. T.; et al. In situ Raman Spectroscopic Evidence for Oxygen Reduction Reaction Intermediates at Platinum Single-Crystal Surfaces. *Nat. Energy* **2019**, *4*, 60−67.

(505) Wu, J.; Yang, H. Platinum-Based Oxygen Reduction Electrocatalysts. *Acc. Chem. Res.* **2013**, *46*, 1848−1857.

(506) Wang, L.; Holewinski, A.; Wang, C. Prospects of Platinum-Based Nanostructures for the Electrocatalytic Reduction of Oxygen. *ACS Catal.* **2018**, *8*, 9388−9398.

(507) Wang, Y.-J.; Zhao, N.; Fang, B.; Li, H.; Bi, X. T.; Wang, H. Carbon-Supported Pt-Based Alloy Electrocatalysts for the Oxygen Reduction Reaction in Polymer Electrolyte Membrane Fuel Cells: Particle Size, Shape, and Composition Manipulation and Their Impact to Activity. *Chem. Rev.* **2015**, *115*, 3433−3467.

(508) Wang, Y.-J.; Long, W.; Wang, L.; Yuan, R.; Ignaszak, A.; Fang, B.; Wilkinson, D. P. Unlocking the Door to Highly Active ORR Catalysts for PEMFC Applications: Polyhedron-Engineered Pt-Based Nanocrystals. *Energy Environ. Sci.* **2018**, *11*, 258−275.

(509) Xia, Y.; Zhao, M.; Wang, X.; Huo, D. Toward Affordable and Sustainable Use of Precious Metals in Catalysis and Nanomedicine. *MRS Bull.* **2018**, *43*, 860−869.

(510) Wang, J.; Cui, Y.; Wang, D. Design of Hollow Nanostructures for Energy Storage. *Adv. Mater.* **2019**, *31*, 1801993.

(511) He, D. S.; He, D.; Wang, J.; Lin, Y.; Yin, P.; Hong, X.; Wu, Y.; Li, Y. Ultrathin Icosahedral Pt-Enriched Nanocage with Excellent Oxygen Reduction Reaction Activity. *J. Am. Chem. Soc.* **2016**, *138*, 1494−1497.

(512) Tahir, M.; Pan, L.; Idrees, F.; Zhang, X.; Wang, L.; Zou, J.-J.; Wang, Z. L. Electrocatalytic Oxygen Evolution Reaction for Energy Conversion and Storage: A Comprehensive Review. *Nano Energy* **2017**, *37*, 136−157.

(513) Suen, N.-T.; Hung, S.-F.; Quan, Q.; Zhang, N.; Xu, Y.-J.; Chen, H. M. Electrocatalysis for the Oxygen Evolution Reaction: Recent Development and Future Perspectives. *Chem. Soc. Rev.* **2017**, *46*, 337−365.

(514) Trasatti, S. Electrocatalysis in the Anodic Evolution of Oxygen and Chlorine. *Electrochim. Acta* **1984**, *29*, 1503−1512.

(515) Cherevko, S.; Geiger, S.; Kasian, O.; Kulyk, N.; Grote, J.-P.; Savan, A.; Shrestha, B. R.; Merzlikin, S.; Breitbach, B.; Ludwig, A.; et al. Oxygen and Hydrogen Evolution Reactions on Ru, RuO_2, Ir, and IrO_2 Thin Film Electrodes in Acidic and Alkaline Eectrolytes: A Comparative Study on Activity and Stability. *Catal. Today* **2016**, *262*, 170−180.

(516) Stoerzinger, K. A.; Rao, R. R.; Wang, X. R.; Hong, W. T.; Rouleau, C. M.; Shao-Horn, Y. The Role of Ru Redox in pH-Dependent Oxygen Evolution on Rutile Ruthenium Dioxide Surfaces. *Chem.* **2017**, *2*, 668−675.

(517) Reier, T.; Oezaslan, M.; Strasser, P. Electrocatalytic Oxygen Evolution Reaction (OER) on Ru, Ir, and Pt Catalysts: A Comparative Study of Nanoparticles and Bulk Materials. *ACS Catal.* **2012**, *2*, 1765−1772.

(518) Alia, S. M.; Rasimick, B.; Ngo, C.; Neyerlin, K. C.; Kocha, S. S.; Pylypenko, S.; Xu, H.; Pivovar, B. S. Activity and Durability of Iridium Nanoparticles in the Oxygen Evolution Reaction. *J. Electrochem. Soc.* **2016**, *163*, F3105−F3112.

(519) Pi, Y.; Zhang, N.; Guo, S.; Guo, J.; Huang, X. Ultrathin Laminar Ir Superstructure as Highly Efficient Oxygen Evolution Electrocatalyst in Broad pH Range. *Nano Lett.* **2016**, *16*, 4424−4430.

(520) Reier, T.; Pawolek, Z.; Cherevko, S.; Bruns, M.; Jones, T.; Teschner, D.; Selve, S.; Bergmann, A.; Nong, H. N.; Schlogl, R.; Mayrhofer, K. J. J.; Strasser, P. Molecular Insight in Structure and Activity of Highly Efficient, Low-Ir Ir−Ni Oxide Catalysts for Electrochemical Water Splitting (OER). *J. Am. Chem. Soc.* **2015**, *137*, 13031−13040.

(521) Vesborg, P. C. K.; Seger, B.; Chorkendorff, I. Recent Development in Hydrogen Evolution Reaction Catalysts and Their Practical Implementation. *J. Phys. Chem. Lett.* **2015**, *6*, 951−957.

(522) Eftekhari, A. Electrocatalysts for Hydrogen Evolution Reaction. *Int. J. Hydrogen Energy* **2017**, *42*, 11053−11077.

(523) Zhu, J.; Hu, L.; Zhao, P.; Lee, L. Y. S.; Wong, K.-Y. Recent Advances in Electrocatalytic Hydrogen Evolution Using Nanoparticles. *Chem. Rev.* **2020**, *120*, 851−918.

(524) Sheng, W.; Myint, M.; Chen, J. G.; Yan, Y. Correlating the Hydrogen Evolution Reaction Activity in Alkaline Electrolytes with the Hydrogen Binding Energy on Monometallic Surfaces. *Energy Environ. Sci.* **2013**, *6*, 1509−1512.

(525) Zheng, J.; Sheng, W.; Zhuang, Z.; Xu, B.; Yan, Y. Universal Dependence of Hydrogen Oxidation and Evolution Reaction Activity of Platinum-Group Metals on pH and Hydrogen Binding Energy. *Sci. Adv.* **2016**, *2*, No. e1501602.

(526) Mahmood, N.; Yao, Y.; Zhang, J.-W.; Pan, L.; Zhang, X.; Zou, J.-J. Electrocatalysts for Hydrogen Evolution in Alkaline Electrolytes: Mechanisms, Challenges, and Prospective Solutions. *Adv. Sci.* **2018**, *5*, 1700464.

(527) Trasatti, S. Work Function, Electronegativity, and Electrochemical Behaviour of Metals: III. Electrolytic Hydrogen Evolution in Acid Solutions. *J. Electroanal. Chem. Interfacial Electrochem.* **1972**, *39*, 163−184.

(528) Nørskov, J. K.; Bligaard, T.; Logadottir, A.; Kitchin, J. R.; Chen, J. G.; Pandelov, S.; Stimming, U. Trends in the Exchange Current for Hydrogen Evolution. *J. Electrochem. Soc.* **2005**, *152*, J23−J26.

(529) Skúlason, E.; Tripkovic, V.; Björketun, M. E.; Gudmundsdóttir, S.; Karlberg, G.; Rossmeisl, J.; Bligaard, T.; Jónsson, H.; Nørskov, J. K. Modeling the Electrochemical Hydrogen Oxidation and Evolution Reactions on the Basis of Density Functional Theory Calculations. *J. Phys. Chem. C* **2010**, *114*, 18182−18197.

(530) Bianchini, C.; Shen, P. K. Palladium-Based Electrocatalysts for Alcohol Oxidation in Half Cells and in Direct Alcohol Fuel Cells. *Chem. Rev.* **2009**, *109*, 4183−4206.

(531) Antolini, E.; Gonzalez, E. R. Alkaline Direct Alcohol Fuel Cells. *J. Power Sources* **2010**, *195*, 3431−3450.

(532) Xu, C. W.; Wang, H.; Shen, P. K.; Jiang, S. P. Highly Ordered Pd Nanowire Arrays as Effective Electrocatalysts for Ethanol Oxidation in Direct Alcohol Fuel Cells. *Adv. Mater.* **2007**, *19*, 4256−4259.

(533) Wang, E.; Xu, J.; Zhao, T. Density Functional Theory Studies of the Structure Sensitivity of Ethanol Oxidation on Palladium Surfaces. *J. Phys. Chem. C* **2010**, *114*, 10489−10497.

(534) Yang, Y.-Y.; Ren, J.; Li, Q.-X.; Zhou, Z.-Y.; Sun, S.-G.; Cai, W.-B. Electrocatalysis of Ethanol on a Pd Electrode in Alkaline Media: An in situ Attenuated Total Reflection Surface-Enhanced Infrared Absorption Spectroscopy Study. *ACS Catal.* **2014**, *4*, 798−803.

(535) Wang, Y.; Zou, S.; Cai, W.-B. Recent Advances on Electro-Oxidation of Ethanol on Pt- and Pd-based Catalysts: From Reaction Mechanisms to Catalytic Materials. *Catalysts* **2015**, *5*, 1507−1534.

(536) Zhang, H.-X.; Wang, H.; Re, Y.-S.; Cai, W.-B. Palladium Nanocrystals Bound by {110} or {100} Facets: From One Pot Synthesis to Electrochemistry. *Chem. Commun.* **2012**, *48*, 8362−8364.

(537) Lin, J.-L.; Ren, J.; Tian, N.; Zhou, Z.-Y.; Sun, S.-G. *In situ* FTIR Spectroscopic Studies of Ethylene Glycol Electrooxidation on Pd Electrode in Alkaline Solution: The Effects of Concentration. *J. Electroanal. Chem.* **2013**, *688*, 165−171.

(538) Wang, H.; Jiang, B.; Zhao, T.-T.; Jiang, K.; Yang, Y.-Y.; Zhang, J.; Xie, Z.; Cai, W.-B. Electrocatalysis of Ethylene Glycol Oxidation on Bare and Bi-Modified Pd Concave Nanocubes in Alkaline Aolution: An Interfacial Infrared Spectroscopic Investigation. *ACS Catal.* **2017**, *7*, 2033−2041.

(539) Zhou, Y.; Liu, J.; Ye, J.; Zou, Z.; Ye, J.; Gu, J.; Yu, T.; Yang, A. Poisoning and Regeneration of Pd Catalyst in Direct Formic Acid Fuel Cell. *Electrochim. Acta* **2010**, *55*, 5024−5027.

(540) Ren, M.; Kang, Y.; He, W.; Zou, Z.; Xue, X.; Akins, D. L.; Yang, H.; Feng, S. Origin of Performance Degradation of Palladium-

Based Direct Formic Acid Fuel Cells. *Appl. Catal., B* **2011**, *104*, 49−53.

(541) Zhao, X.; Yin, M.; Ma, L.; Liang, L.; Liu, C.; Liao, J.; Lu, T.; Xing, W. Recent Advances in Catalysts for Direct Methanol Fuel Cells. *Energy Environ. Sci.* **2011**, *4*, 2736−2753.

(542) Jiang, K.; Zhang, H.-X.; Zou, S.; Cai, W.-B. Electrocatalysis of Formic Acid on Palladium and Platinum Surfaces: From Fundamental Mechanisms to Fuel Cell Applications. *Phys. Chem. Chem. Phys.* **2014**, *16*, 20360−20376.

(543) Zhang, X.; Yin, H.; Wang, J.; Chang, L.; Gao, Y.; Liu, W.; Tang, Z. Shape-Dependent Electrocatalytic Activity of Monodispersed Palladium Nanocrystals Toward Formic Acid Oxidation. *Nanoscale* **2013**, *5*, 8392−8397.

(544) Hoshi, N.; Kida, K.; Nakamura, M.; Nakada, M.; Osada, K. Structural Effects of Electrochemical Oxidation of Formic Acid on Single Crystal Electrodes of Palladium. *J. Phys. Chem. B* **2006**, *110*, 12480−12484.

(545) Gao, D.; Aran-Ais, R. M.; Jeon, H. S.; Roldan Cuenya, B. Rational Catalyst and Electrolyte Design for CO_2 Electroreduction Towards Multicarbon Products. *Nat. Catal.* **2019**, *2*, 198−210.

(546) Arán-Ais, R. M.; Gao, D.; Roldan Cuenya, B. Structure-and Electrolyte-Sensitivity in CO_2 Electroreduction. *Acc. Chem. Res.* **2018**, *51*, 2906−2917.

(547) Hori, Y.; Takahashi, I.; Koga, O.; Hoshi, N. Electrochemical Reduction of Carbon Dioxide at Various Series of Copper Single Crystal Electrodes. *J. Mol. Catal. A: Chem.* **2003**, *199*, 39−47.

(548) De Gregorio, G. L.; Burdyny, T.; Loiudice, A.; Iyengar, P.; Smith, W. A.; Buonsanti, R. Facet-Dependent Selectivity of Cu Catalysts in Electrochemical CO_2 Reduction at Commercially Viable Current Densities. *ACS Catal.* **2020**, *10*, 4854−4862.

(549) Cheng, T.; Xiao, H.; Goddard, W. A. Nature of the Active Sites for CO Reduction on Copper Nanoparticles; Suggestions for Optimizing Performance. *J. Am. Chem. Soc.* **2017**, *139*, 11642−11645.

(550) Calle-Vallejo, F.; Koper, M. T. Theoretical Considerations on the Electroreduction of CO to C_2 Species on Cu (100) Electrodes. *Angew. Chem., Int. Ed.* **2013**, *52*, 7282−7285.

(551) Montoya, J. H.; Shi, C.; Chan, K.; Nørskov, J. K. Theoretical Insights into a CO Dimerization Mechanism in CO_2 Electroreduction. *J. Phys. Chem. Lett.* **2015**, *6*, 2032−2037.

(552) Luo, W.; Nie, X.; Janik, M. J.; Asthagiri, A. Facet Dependence of CO_2 Reduction Paths on Cu Electrodes. *ACS Catal.* **2016**, *6*, 219−229.

(553) Reske, R.; Mistry, H.; Behafarid, F.; Roldan Cuenya, B.; Strasser, P. Particle Size Effects in the Catalytic Electroreduction of CO_2 on Cu Nanoparticles. *J. Am. Chem. Soc.* **2014**, *136*, 6978−6986.

(554) Birdja, Y. Y.; Pérez-Gallent, E.; Figueiredo, M. C.; Göttle, A. J.; Calle-Vallejo, F.; Koper, M. T. M. Advances and Challenges in Understanding the Electrocatalytic Conversion of Carbon Dioxide to Fuels. *Nat. Energy* **2019**, *4*, 732−745.

(555) Jeon, H. S.; Kunze, S.; Scholten, F.; Roldan Cuenya, B. Prism-Shaped Cu Nanocatalysts for Electrochemical CO_2 Reduction to Ethylene. *ACS Catal.* **2018**, *8*, 531−535.

(556) Reller, C.; Krause, R.; Volkova, E.; Schmid, B.; Neubauer, S.; Rucki, A.; Schuster, M.; Schmid, G. Selective Electroreduction of CO_2 Toward Ethylene on Nano Dendritic Copper Catalysts at High Current Density. *Adv. Energy Mater.* **2017**, *7*, 1602114.

(557) Scholten, F.; Sinev, I.; Bernal, M.; Roldan Cuenya, B. Plasma-Modified Dendritic Cu Catalyst for CO_2 Electroreduction. *ACS Catal.* **2019**, *9*, 5496−5502.

(558) Huang, J.; Hormann, N.; Oveisi, E.; Loiudice, A.; De Gregorio, G. L.; Andreussi, O.; Marzari, N.; Buonsanti, R. Potential-Induced Nanoclustering of Metallic Catalysts During Electrochemical CO_2 Reduction. *Nat. Commun.* **2018**, *9*, 3117.

(559) Li, Y.; Cui, F.; Ross, M. B.; Kim, D.; Sun, Y.; Yang, P. Structure-Sensitive CO_2 Electroreduction to Hydrocarbons on Ultrathin 5-Fold Twinned Copper Nanowires. *Nano Lett.* **2017**, *17*, 1312−1317.

(560) Cao, N.; Zheng, G. Aqueous Electrocatalytic N_2 Reduction Under Ambient Conditions. *Nano Res.* **2018**, *11*, 2992−3008.

(561) Bao, D.; Zhang, Q.; Meng, F.-L.; Zhong, H.-X.; Shi, M.-M.; Zhang, Y.; Yan, J.-M.; Jiang, Q.; Zhang, X.-B. Electrochemical Reduction of N_2 under Ambient Conditions for Artificial N_2 Fixation and Renewable Energy Storage Using N_2/NH_3 Cycle. *Adv. Mater.* **2017**, *29*, 1604799.

(562) Davydova, E. S.; Mukerjee, S.; Jaouen, F.; Dekel, D. R. Electrocatalysts for Hydrogen Oxidation Reaction in Alkaline Electrolytes. *ACS Catal.* **2018**, *8*, 6665−6690.

(563) Poerwoprajitno, A. R.; Gloag, L.; Cheong, S.; Gooding, J. J.; Tilley, R. D. Synthesis of Low-and High-Index Faceted Metal (Pt, Pd, Ru, Ir, Rh) Nanoparticles for Improved Activity and Stability in Electrocatalysis. *Nanoscale* **2019**, *11*, 18995−19011.

(564) Zalitis, C. M.; Kucernak, A. R.; Sharman, J.; Wright, E. Design Principles for Platinum Nanoparticles Catalysing Electrochemical Hydrogen Evolution and Oxidation Reactions: Edges are Much More Active than Facets. *J. Mater. Chem. A* **2017**, *5*, 23328−23338.

(565) Markovića, N. M.; Sarraf, S. T.; Gasteiger, H. A.; Ross, P. N. Hydrogen Electrochemistry on Platinum Low-Index Single-Crystal Surfaces in Alkaline Solution. *J. Chem. Soc., Faraday Trans.* **1996**, *92*, 3719−3725.

(566) Schmidt, T. J.; Ross, P. N.; Markovic, N. M. Temperature Dependent Surface Electrochemistry on Pt Single Crystals in Alkaline Electrolytes: Part 2. The Hydrogen Evolution/Oxidation Reaction. *J. Electroanal. Chem.* **2002**, *524*, 252−260.

(567) Lavrich, D. J.; Wetterer, S. M.; Bernasek, S. L.; Scoles, G. Physisorption and Chemisorption of Alkanethiols and Alkyl Sulfides on Au(111). *J. Phys. Chem. B* **1998**, *102*, 3456−3465.

(568) Rossi, L. M.; Fiorio, J. L.; Garcia, M. A. S.; Ferraz, C. P. The Role and Fate of Capping Ligands in Colloidally Prepared Metal Nanoparticle Catalysts. *Dalton Trans.* **2018**, *47*, 5889−5915.

(569) Lopez-Sanchez, J. A.; Dimitratos, N.; Hammond, C.; Brett, G. L.; Kesavan, L.; White, S.; Miedziak, P.; Tiruvalam, R.; Jenkins, R. L.; Carley, A. F.; et al. Facile Removal of Stabilizer-Ligands from Supported Gold Nanoparticles. *Nat. Chem.* **2011**, *3*, 551−556.

(570) Rioux, R. M.; Song, H.; Grass, M.; Habas, S.; Niesz, K.; Hoefelmeyer, J. D.; Yang, P.; Somorjai, G. A. Monodisperse Platinum Nanoparticles of Well-Defined Shape: Synthesis, Characterization, Catalytic Properties and Future Prospects. *Top. Catal.* **2006**, *39*, 167−174.

(571) Peng, H.-C.; Xie, S.; Park, J.; Xia, X.; Xia, Y. Quantitative Analysis of the Coverage Density of Br^- Ions on Pd{100} Facets and Its Role in Controlling the Shape of Pd Nanocrystals. *J. Am. Chem. Soc.* **2013**, *135*, 3780−3783.

(572) Peng, H.-C.; Li, Z.; Aldahondo, G.; Huang, H.; Xia, Y. Seed-Mediated Synthesis of Pd Nanocrystals: The Effect of Surface Capping on the Heterogeneous Nucleation and Growth. *J. Phys. Chem. C* **2016**, *120*, 11754−11761.

(573) Shao, M.; Odell, J.; Humbert, M.; Yu, T.; Xia, Y. Electrocatalysis on Shape-Controlled Palladium Nanocrystals: Oxygen Reduction Reaction and Formic Acid Oxidation. *J. Phys. Chem. C* **2013**, *117*, 4172−4180.

(574) Wang, Y.; Choi, S. I.; Zhao, X.; Xie, S. F.; Peng, H.-C.; Chi, M. F.; Huang, C. Z.; Xia, Y. N. Polyol Synthesis of Ultrathin Pd Nanowires via Attachment-Based Growth and Their Enhanced Activity towards Formic Acid Oxidation. *Adv. Funct. Mater.* **2014**, *24*, 131−139.

(575) Kabiraz, M. K.; Kim, J.; Lee, W.-J.; Ruqia, B.; Kim, H. C.; Lee, S.-U.; Kim, J.-R.; Paek, S.-M.; Hong, J. W.; Choi, S.-I. Ligand Effect of Shape-Controlled β-Palladium Hydride Nanocrystals on Liquid-Fuel Oxidation Reactions. *Chem. Mater.* **2019**, *31*, 5663−5673.

(576) Tsunoyama, H.; Ichikuni, N.; Sakurai, H.; Tsukuda, T. Effect of Electronic Structures of Au Clusters Stabilized by Poly(*N*-vinyl-2-pyrrolidone) on Aerobic Oxidation Catalysis. *J. Am. Chem. Soc.* **2009**, *131*, 7086−7093.

(577) Zhong, R.-Y.; Sun, K.-Q.; Hong, Y.-C.; Xu, B.-Q. Impacts of Organic Stabilizers on Catalysis of Au Nanoparticles from Colloidal Preparation. *ACS Catal.* **2014**, *4*, 3982−3993.

(578) Harjanto, S.; Cao, Y.; Shibayama, A.; Naitoh, I.; Nanami, T.; Kasahara, K.; Okumura, Y.; Liu, K.; Fujita, T. Leaching of Pt, Pd and

Rh from Automotive Catalyst Residue in Various Chloride Based Solutions. *Mater. Trans.* **2006**, *47*, 129−135.

(579) Goodman, E. D.; Schwalbe, J. A.; Cargnello, M. Mechanistic Understanding and the Rational Design of Sinter-Resistant Heterogeneous Catalysts. *ACS Catal.* **2017**, *7*, 7156−7173.

(580) Kim, C.; Min, M.; Chang, Y. W.; Yoo, K. H.; Lee, H. Chemical and Thermal Stability of Pt Nanocubes Synthesized with Various Surface-Capping Agents. *J. Nanosci. Nanotechnol.* **2010**, *10*, 233−239.

(581) Collins, G.; Schmidt, M.; McGlacken, G. P.; O'Dwyer, C.; Holmes, J. D. Stability, Oxidation, and Shape Evolution of PVP-Capped Pd Nanocrystals. *J. Phys. Chem. C* **2014**, *118*, 6522−6530.

(582) Gilroy, K. D.; Elnabawy, A. O.; Yang, T.-H.; Roling, L. T.; Howe, J.; Mavrikakis, M.; Xia, Y. Thermal Stability of Metal Nanocrystals: An Investigation of the Surface and Bulk Reconstructions of Pd Concave Icosahedra. *Nano Lett.* **2017**, *17*, 3655−3661.

(583) Albrecht, W.; Bladt, E.; Vanrompay, H.; Smith, J. D.; Skrabalak, S. E.; Bals, S. Thermal Stability of Gold/Palladium Octopods Studied In Situ in 3D: Understanding Design Rules for Thermally Stable Metal Nanoparticles. *ACS Nano* **2019**, *13*, 6522−6530.

(584) Zeng, X.-M.; Huang, R.; Shao, G.-F.; Wen, Y.-H.; Sun, S.-G. High-Index-Faceted Platinum Nanoparticles: Insights into Structural and Thermal Stabilities and Shape Evolution from Atomistic Simulations. *J. Mater. Chem. A* **2014**, *2*, 11480−11489.

(585) Sung, Y.-E.; Chrzanowski, W.; Zolfaghari, A.; Jerkiewicz, G.; Wieckowski, A. Structure of Chemisorbed Sulfur on a Pt (111) Electrode. *J. Am. Chem. Soc.* **1997**, *119*, 194−200.

(586) Wang, T.; Lee, C.; Schmidt, L. D. Shape and Orientation of Supported Pt Particles. *Surf. Sci.* **1985**, *163*, 181−197.

(587) Zhang, X.; Meng, J.; Zhu, B.; Yuan, W.; Yang, H.; Zhang, Z.; Gao, Y.; Wang, Y. Unexpected Refacetting of Palladium Nanoparticles Under Atmospheric N_2 Conditions. *Chem. Commun.* **2018**, *54*, 8587−8590.

(588) Huang, X.; Zhao, Z.; Chen, Y.; Zhu, E.; Li, M.; Duan, X.; Huang, Y. A Rational Design of Carbon-Supported Dispersive Pt-Based Octahedra as Efficient Oxygen Reduction Reaction Catalysts. *Energy Environ. Sci.* **2014**, *7*, 2957−2962.

(589) Zhou, Z.-Y.; Huang, Z.-Z.; Chen, D.-J.; Wang, Q.; Tian, N.; Sun, S.-G. High-Index Faceted Platinum Nanocrystals Supported on Carbon Black as Highly Efficient Catalysts for Ethanol Electrooxidation. *Angew. Chem., Int. Ed.* **2010**, *49*, 411−414.

(590) Ho, V. T. T.; Pan, C.-J.; Rick, J.; Su, W.-N.; Hwang, B.-J. Nanostructured $Ti_{0.7}Mo_{0.3}O_2$ Support Enhances Electron Transfer to Pt: High-Performance Catalyst for Oxygen Reduction Reaction. *J. Am. Chem. Soc.* **2011**, *133*, 11716−11724.

(591) Schubert, M. M.; Hackenberg, S.; van Veen, A. C.; Muhler, M.; Plzak, V.; Behm, R. J. CO Oxidation over Supported Gold Catalysts—"Inert" and "Active" Support Materials and Their Role for the Oxygen Supply during Reaction. *J. Catal.* **2001**, *197*, 113−122.

(592) Zhou, Y.; Neyerlin, K.; Olson, T. S.; Pylypenko, S.; Bult, J.; Dinh, H. N.; Gennett, T.; Shao, Z.; O'Hayre, R. Enhancement of Pt and Pt-Alloy Fuel Cell Catalyst Activity and Durability *via* Nitrogen-Modified Carbon Supports. *Energy Environ. Sci.* **2010**, *3*, 1437−1446.

(593) Wang, H.; Xu, S.; Tsai, C.; Li, Y.; Liu, C.; Zhao, J.; Liu, Y.; Yuan, H.; Abild-Pedersen, F.; Prinz, F. B.; et al. Direct and Continuous Strain Control of Catalysts with Tunable Battery Electrode Materials. *Science* **2016**, *354*, 1031−1036.

(594) Li, Y.; Li, Y.; Zhu, E.; McLouth, T.; Chiu, C.-Y.; Huang, X.; Huang, Y. Stabilization of High-Performance Oxygen Reduction Reaction Pt Electrocatalyst Supported on Reduced Graphene Oxide/Carbon Black Composite. *J. Am. Chem. Soc.* **2012**, *134*, 12326−12329.

(595) Cho, K. Y.; Yeom, Y. S.; Seo, H. Y.; Kumar, P.; Lee, A. S.; Baek, K.-Y.; Yoon, H. G. Molybdenum-Doped PdPt@Pt Core−Shell Octahedra Supported by Ionic Block Copolymer-Functionalized Graphene as a Highly Active and Durable Oxygen Reduction Electrocatalyst. *ACS Appl. Mater. Interfaces* **2017**, *9*, 1524−1535.

(596) Kongkanand, A.; Kuwabata, S.; Girishkumar, G.; Kamat, P. Single-Wall Carbon Nanotubes Supported Platinum Nanoparticles with Improved Electrocatalytic Activity for Oxygen Reduction Reaction. *Langmuir* **2006**, *22*, 2392−2396.

(597) Tian, X.; Luo, J.; Nan, H.; Zou, H.; Chen, R.; Shu, T.; Li, X.; Li, Y.; Song, H.; Liao, S.; et al. Transition Metal Nitride Coated with Atomic Layers of Pt as a Low-Cost, Highly Stable Electrocatalyst for the Oxygen Reduction Reaction. *J. Am. Chem. Soc.* **2016**, *138*, 1575−1583.

(598) Liu, Y.; Mustain, W. E. High Stability, High Activity Pt/ITO Oxygen Reduction Electrocatalysts. *J. Am. Chem. Soc.* **2013**, *135*, 530−533.

(599) Zhang, L.; Xia, Y. Scaling up the Production of Colloidal Nanocrystals: Should We Increase or Decrease the Reaction Volume? *Adv. Mater.* **2014**, *26*, 2600−2606.

(600) Niu, G.; Ruditskiy, A.; Vara, M.; Xia, Y. Toward Continuous and Scalable Production of Colloidal Nanocrystals by Switching from Batch to Droplet Reactors. *Chem. Soc. Rev.* **2015**, *44*, 5806−5820.

(601) Zhang, L.; Niu, G.; Lu, N.; Wang, J.; Tong, L.; Wang, L.; Kim, M. J.; Xia, Y. Continuous and Scalable Production of Well-Controlled Noble-Metal Nanocrystals in Milliliter-Sized Droplet Reactors. *Nano Lett.* **2014**, *14*, 6626−6631.

(602) Niu, G.; Zhang, L.; Ruditskiy, A.; Wang, L.; Xia, Y. A Droplet-Reactor System Capable of Automation for the Continuous and Scalable Production of Noble-Metal Nanocrystals. *Nano Lett.* **2018**, *18*, 3879−3884.

(603) Lin, X. Z.; Terepka, A. D.; Yang, H. Synthesis of Silver Nanoparticles in a Continuous Flow Tubular Microreactor. *Nano Lett.* **2004**, *4*, 2227−2232.

(604) Boleininger, J.; Kurz, A.; Reuss, V.; Sönnichsen, C. Microfluidic Continuous Flow Synthesis of Rod-Shaped Gold and Silver Nanocrystals. *Phys. Chem. Chem. Phys.* **2006**, *8*, 3824−3827.

(605) Lohse, S. E.; Eller, J. R.; Sivapalan, S. T.; Plews, M. R.; Murphy, C. J. A Simple Millifluidic Benchtop Reactor System for the High-throughput Synthesis and Functionalization of Gold Nanoparticles with Different Sizes and Shapes. *ACS Nano* **2013**, *7*, 4135−4150.

(606) Chen, R.; Cao, Z.; Lyu, Z.; Xie, M.; Shi, Y.; Xia, Y. Continuous and Scalable Synthesis of Pt Multipods with Enhanced Electrocatalytic Activity toward the Oxygen Reduction Reaction. *ChemNanoMat* **2019**, *5*, 599−605.

(607) Maroun, F.; Ozanam, F.; Magnussen, O. M.; Behm, R. J. The Role of Atomic Ensembles in the Reactivity of Bimetallic Electrocatalysts. *Science* **2001**, *293*, 1811−1814.

(608) Chen, M.; Kumar, D.; Yi, C. W.; Goodman, D. W. The Promotional Effect of Gold in Catalysis by Palladium-gold. *Science* **2005**, *310*, 291−293.

(609) Lin, W.; Zei, M.; Eiswirth, M.; Ertl, G.; Iwasita, T.; Vielstich, W. Electrocatalytic Activity of Ru-Modified Pt (111) Electrodes toward CO Oxidation. *J. Phys. Chem. B* **1999**, *103*, 6968−6977.

(610) Tedsree, K.; Li, T.; Jones, S.; Chan, C. W. A.; Yu, K. M. K.; Bagot, P. A. J.; Marquis, E. A.; Smith, G. D. W.; Tsang, S. C. E. Hydrogen Production from Formic Acid Decomposition at Room Temperature Using a Ag−Pd Core−Shell Nanocatalyst. *Nat. Nanotechnol.* **2011**, *6*, 302−307.

(611) Moseley, P.; Curtin, W. A. Computational Design of Strain in Core−Shell Nanoparticles for Optimizing Catalytic Activity. *Nano Lett.* **2015**, *15*, 4089−4095.

(612) Yan, Y.; Du, J. S.; Gilroy, K. D.; Yang, D.; Xia, Y.; Zhang, H. Intermetallic Nanocrystals: Syntheses and Catalytic Applications. *Adv. Mater.* **2017**, *29*, 1605997.

(613) Li, Q.-J.; Sheng, H.; Ma, E. Strengthening in Multi-Principal Element Alloys with Local-Chemical-Order Roughened Dislocation Pathways. *Nat. Commun.* **2019**, *10*, 3563.

(614) Nunez, M.; Lansford, J. L.; Vlachos, D. G. Optimization of the Facet Structure of Transition-Metal Catalysts Applied to the Oxygen Reduction Reaction. *Nat. Chem.* **2019**, *11*, 449−456.